Copyright

by

Seung Han Kim

2010

The Dissertation Committee for Seung Han Kim Certifies that this is the approved version of the following dissertation:

Large Tunnels for Transportation Purposes and Face Stability of Mechanically Driven Tunnels in Soft Ground

Committee:

Fulvio Tonon, Supervisor

Karin Bäppler

Chadi El Mohtar

Loukas Kallivokas

Jorge G. Zornberg

Large Tunnels for Transportation Purposes and Face Stability of Mechanically Driven Tunnels in Soft Ground

by

Seung Han Kim, B.S.; M.S.

Dissertation

Presented to the Faculty of the Graduate School of

The University of Texas at Austin

in Partial Fulfillment

of the Requirements

for the Degree of

Doctor of Philosophy

The University of Texas at Austin

August 2010

Dedication

To my family.

Acknowledgements

I would like to express sincere gratitude to my supervisor Dr. Fulvio Tonon
for his guidance, support, and encouragement throughout this research.
I would also appreciate to other dissertation committee members,
Dr. Jorge Zornberg, Dr. Chadi El Mohtar, Dr. Loukas Kallivokas and Dr. Karin Bäppler.

Large Tunnels for Transportation Purposes and Face Stability of Mechanically Driven Tunnels in Soft Ground

Publication No._____

Seung Han Kim, Ph.D.

The University of Texas at Austin, 2010

Supervisor: Fulvio Tonon

With the advent of the large diameter tunnel boring machine (TBM), mechanically driven large diameter tunnel is becoming a more attractive option. During operation, a large diameter tube allows for stacked deck configuration with shafts dropped to platform level (no station caverns). The extensive information has been compiled on innovative TBM tunneling projects such as the Barcelona Line 9, where the concept of continuous station has been used for the first time, stormwater management and roadway tunnel in Malaysia, where the floodwater bypass tunnel and the road tunnel are incorporated in a single bore tunnel. The decision making process that led to the construction of large bore tunnel is also presented.

A detailed study has been carried out to determine the necessary face support pressure in drained conditions (with ideal membrane), and undrained conditions. The effects of tunnel diameter, cover-to-diameter ratio, at-rest lateral earth pressure

coefficient, and soil shear strength parameters on the local and global stability of the excavation face of mechanically-driven tunnels have been investigated. The relation between the face support pressure and the calculated tunnel face displacement gave the minimum face support pressure that should be applied on the tunnel face to avoid abrupt movement of the tunnel face. Simple expressions have been developed for the support pressure as a function of tunnel diameter, cover depth, lateral earth pressure coefficient, and soil strength parameters. The required face support pressures are compared to the analytical solutions available from the literature. It has been found that analytical stability solutions generally underestimate the required face support pressure and excessive deformation will take place in the ground near the tunnel heading when these solutions are used.

By using plastic limit analysis, a rigid and deformable prism-and-wedge model has been developed; in undrained conditions, upper bound solutions against collapse load are derived for face pressure. Deformable blocks enabled to take into account the effect of non-uniform support pressure due to the unit weight of the supporting medium. The upper bound solution derived as a function of tunnel diameter and cover depth, normalized undrained shear strength ratio, and unit weight of the ground and the supporting medium was compared with a solution available from the literature. Largest face support pressure was obtained when the uniform face support pressure was applied and it was smallest when identical unit weight was used for the ground and the supporting medium.

Table of Contents

List of Figures

List of Tables

CHAPTER 1. INTRODUCTION

1.1. MOTIVATION AND OBJECTIVE

Since tunneling at a larger scale started in the 19th century, underground space development has played a very important role in forming the metropolitan area. The advent of powerful and reliable tunnel boring machines enabled the effective and safe construction of large tunnels even in a difficult ground condition. The diameter of a tunnel boring machine increased dramatically in last decades and the increased diameter of the tunnel enabled multi-purpose usage and multi-deck configuration within a single bore. The Duplex Tunnel in Paris Socatop A86 Highway that was proposed in late 90's was the first implementation of the multi-deck configuration, and afterward several large-diameter multi-deck tunnels have been proposed and constructed all over the world. However, complete documentation over the case histories where this configuration was realized was unavailable. In this dissertation, case histories on large-bore stacked-deck mechanically driven tunnels are presented.

The stability of tunnel face is one of the most critical components that should be secured for the successful tunneling. It is especially true for the tunneling in urban environment and even more when large diameters are contemplated, where the excessive settlement and ground deformation may lead to catastrophic and costly consequences. Many researchers and engineers have successfully presented various theoretical and empirical/experimental methods to evaluate the tunnel face stability and to assess the required face support pressure. The analytical approaches may be used to assess the face support pressure, but they do not provide any information about surface settlement and face deformation characteristics. Currently, only a three-dimensional numerical

analysis is in a position to provide complete information on face stability, required face support pressure and ground deformation and subsidence. However, an attempt to evaluate the required face support pressure using a series of numerical simulations was not made yet due to the restriction on available time and resources. In this dissertation, using a three-dimensional finite element simulation technique, the face stability was evaluated and equations that evaluate the face support pressure necessary to avoid excessive deformation of the ground near the tunnel heading were developed.

The bound theorems of limit analysis estimate the range (upper and lower bound) of collapse loads for a plastic material that obeys associated plastic flow rule. The true collapse load lies between the statically admissible lower bound solution (safe) and (kinematically admissible) upper bound solution (unsafe). Various upper bound solutions have been published, but no solution is capable of considering the effect of non-uniform face support pressure. In this dissertation, for the ground that follows Tresca yield criterion (e.g., clay in undrained conditions); the collapse load was evaluated using the upper bound solution. To take into account the effect of the face support pressure gradient, deformable blocks were used for the prism-and-wedge model.

1.2. ORGANIZATION OF DISSERTATION

In Chapter 2, the case histories on large diameter/multi-purpose tunnels are summarized. It includes Stormwater Management And Road Tunnel (Kuala Lumpur, Malaysia), Subway Line 9 Tunnel (Barcelona, Spain), Highway M30 Tunnel (Madrid, Spain), Socatop A86 Duplex Tunnel (Paris, France), 4th Elbe Tunnel (Hamburg, Germany), Lefortovo Tunnel and Silberwald Tunnel (Moscow, Russia), Chongming

Tunnel (Shanghai, China), Dulles Tyson Corner Tunnel (Washington, DC), and State Route 99 Tunnel (Seattle, WA).

In Chapter 3, the deformation characteristics of the ground near the tunnel heading are investigated and equations that give the face support pressure to avoid excessive deformation of the ground ahead of the tunnel face are presented for drained ground (Section 5.1) and undrained ground (Section 5.2). In Sections 5.1.5 and 5.2.5, the face support pressure values obtained as a result of the numerical simulation are compared with the values available from the literature. Popular analytical or experimental/empirical face stability solutions are summarized in Section 3.2.

In Chapter 4, upper bound solutions against collapse load are derived using a prism-and-wedge model. The undrained shear strength of the ground is assumed to be either uniform or non-uniform. Deformable soil blocks are used to take into account the effect of non-uniform face support pressure due to the unit weight of the supporting medium (Section 4.3).

CHAPTER 2. LARGE DIAMETER ROAD/MULTI-PURPOSE TBM DRIVEN TUNNELS

2.1. INTRODUCTION

Tunnels are feasible alternatives to cross through or under physical barriers such as mountains, bodies of water, existing artificial structures, such as roads or railways, viaducts, buildings, and other developed underground spaces. In addition, tunnels are often used to satisfy environmental requirements and to reduce potential negative impact and disturbance on surface area.

Before a surface road, viaduct, bridge, or tunnel is constructed, a number of technical and socio-economic issues, such as geological conditions, constructability, seismicity, costs (construction, operation and maintenance), environmental impact, aesthetics, land use restrictions, and life expectancy are comparatively evaluated during the feasibility study and preliminary design stage. When the tunnel option is compared with other possible options, such as surface roads, viaducts, and bridges, it has been often found that the tunnels are one of the options with higher initial cost and higher risk options. However, when life-cycle cost is considered, the tunnel option is often times very advantageous (Table 2.1).

Table 2.1 Comparison of the cost over various types of infrastructures for transportation purposes (Tunnels and Tunnelling North America, 2005(12))

		Type of infrastructures for transportation purposes		At grade (baseline)	Elevated structure/via-duct/bridge	Tunnel (cut-and-cover)	Tunnel (NATM & TBM)
		Life span (years):		100	50	100	150
		Details	Weight (Range)				
Project cost	Soft cost	EIS/EIR	4.5 (3-8)	1	1.4	1.4	0.3
		Design fee	13.5 (12-15)	1	1.4	1.6	1.4
		Right of way	11.5 (6-15)	1	1.8	1	0.3
		Productivity loss	3.5 (2-5)	1	1	1.5	0.3
		Construction management	13.5 (12-15)	1	2	1.6	0.7
	Construction cost	Traffic relocation and maintenance	16.5 (8-25)	1	1	1.5	0.3
		Utility relocation and support	11.5 (8-15)	1	1.2	2	0.3
		Structures	25 (15-35)	1	7	10	11
		Total project cost		1.00	2.83	3.66	3.19
		Annual project cost after considering life span		1.00	5.66	3.66	2.13
Annual cost		Environmental pollution	25 (20-30)	1	1.2	0.05	0.05
		Loss of property taxes	25 (20-30)	1	1	0.2	0.2
		Social divide	15 (10-20)	1	0.8	0	0
		Maintenance cost	35 (30-40)	1	2	1.3	1.1
		Total annual cost		1.00	1.37	0.52	0.45
		Annual cost after considering life span		1.00	2.74	0.52	0.30

* Interest not included; Based on international experience in urban areas

Environmental benefits, such as reduced air, noise, and visual pollution to the surface area, reduced land acquisition cost, and opportunities for real estate development often offset the high construction and operational costs of the tunnel option in an urban area, where land values are high. Undoubtedly, in urban environments, a tunnel is found to be the only option for a given route and purpose of a proposed infrastructure. In

addition, with the advent of powerful and dependable tunnel boring machines (Figure 2.1) and accumulating previous experience, a tunnel is becoming a more feasible option.

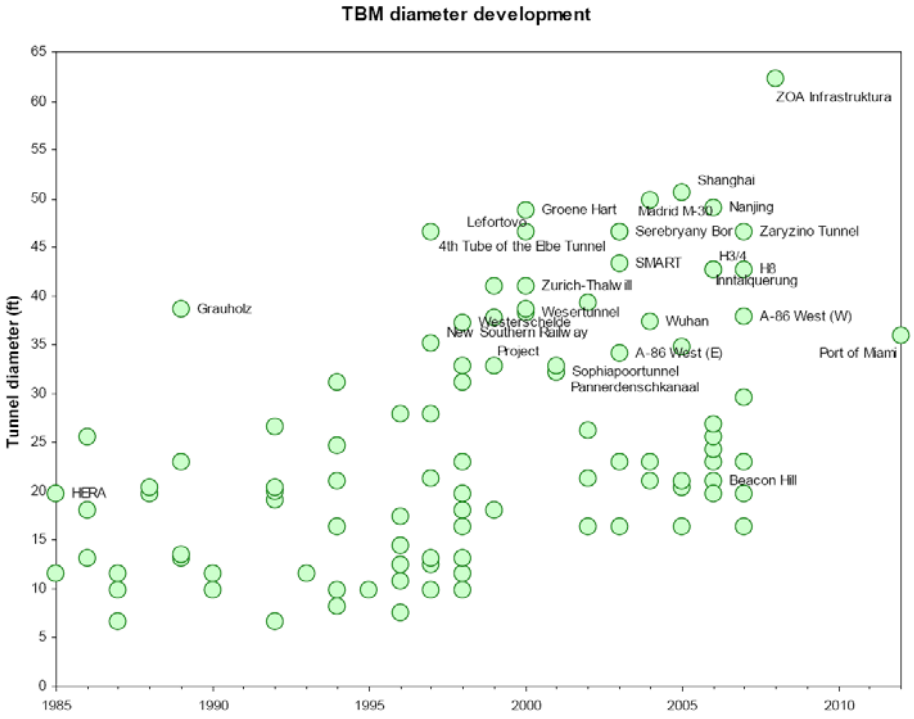

Figure 2.1 Increasing TBM diameter over the past 20 years (Cascadia Center, 2008)

In the United States, a number of large diameter multi-deck tunnel construction plans for transportation purpose have been proposed. Two case histories, Dulles Tyson Corner Tunnel and State Route 99, are presented in this dissertation. A decision making process and a brief comparison between the single-bore double-deck tunnel and twin-bore single-deck tunnel is provided.

2.2. CASE HISTORY I: STORMWATER MANAGEMENT AND ROAD TUNNEL, KUALA LUMPUR

2.2.1. Planning and purpose of the tunnel

The Stormwater Management and Road Tunnel (SMART) is a 9.7-km long, 11.83 m inner diameter and 13.21 m outer diameter dual purpose tunnel with a flashflood drainage/storage water tunnel and 2.6-km long, cars only, double-deck toll road tunnel incorporated in the middle of a water tunnel. It was an innovative solution for the city's flooding problem and traffic congestion at the city center.

The Klang River runs through the northern part of Kuala Lumpur, also known as the Upper Klang Valley, where the river's major two tributaries, Ampang and Gombak Rivers, join the Klang River. The area enclosed in a dotted line in
Figure 2.2a indicates the region that had had severe flooding problems during the Monsoon season (April to October). Inadequate expansion of the drainage system to accommodate the growing intensity of development, resulted in a dramatic increase in the number of flooding events and their magnitude every year.

To mitigate the flooding problem of the city, the Government implemented the Klang River Basin Flood Mitigation (KRBFM) Project. The SMART project was one of countermeasures to the flood problem implemented as a part of KRBFM. The KRBFM project also includes: construction of floodwater detention facilities and flood walls; channel improvement of the Klang and Gomabt Rivers; building of the Batu dam; and raising of the Klang Gate dam. The SMART project's flood mitigation scheme is providing an underground flow channel allowing floodwater to bypass from the upper Klang River to the Kerayong River, as shown in Figure 1.1b. Alternative options to

construction of an expensive large diameter tunnel included construction of a surface flow channel or enlargement of the reservoir capacity. However, they were not feasible, due to the prohibitive land acquisition cost in the heavily populated downtown area.

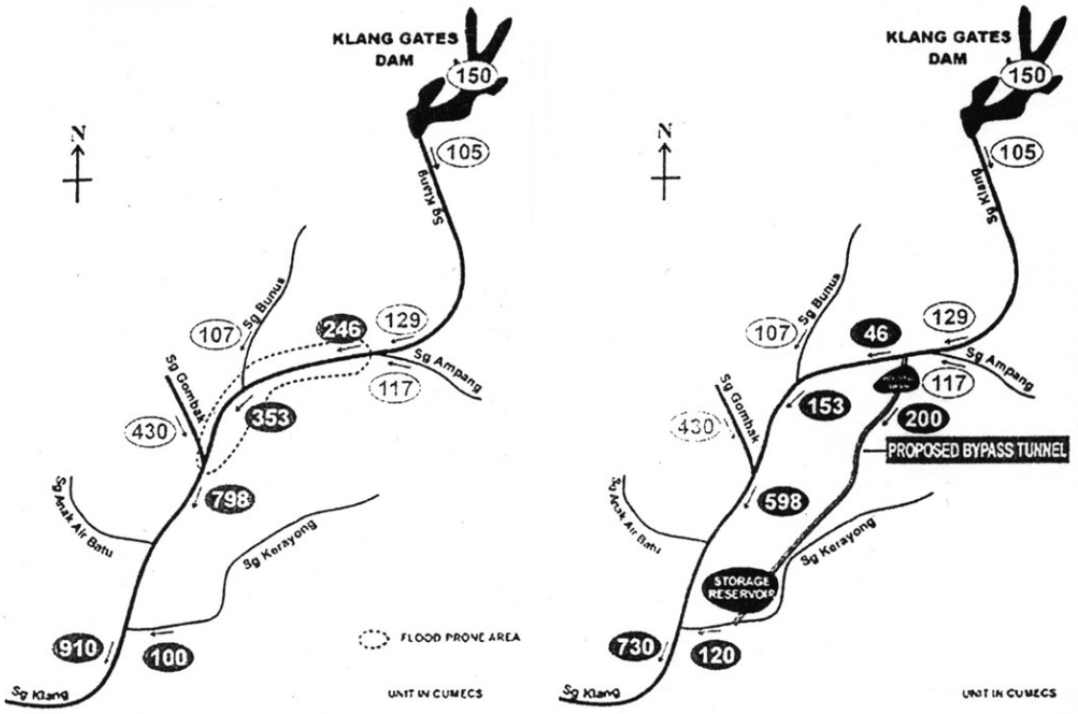

(a) Upper Klang Valley flooding area (b) Proposed Klang River bypass tunnel

Figure 2.2 Klang River bypass tunnel (after Abdullah, 2004b)

Supported by the Prime Minister, building a bypass tunnel seemed a feasible solution, if construction funding could be raised. It was not justifiable to invest huge public funds on a flood mitigation tunnel that might be used to full capacity for less than once a year or that would stay empty most of the time except during high monsoon season. Malaysia's two largest construction companies, MMC Berhad and Gamuda Berhad, submitted an innovative joint-venture proposal to include a toll road section in a

multi-deck, large, single-bore tunnel. This solution would alleviate the flood problem by diverting the floodwater and the city's chronic traffic congestion around the northern part of the city center by providing a bypass route to the traffic. Furthermore, by attracting private investment, this solution would cut the burden on public funds by 35 %. The overall cost of the project was 2 billion Malaysian Ringgits (MR), or 520 million USD. The estimated construction cost of the water tunnel, without the road section, was 1.8 billion MR, and the additional construction cost of the road section was estimated at 200 million MR. 700 million MR of the 2 billion MR would be funded by the toll road project.

The floodwater drainage element was overseen by the Drainage and Irrigation Department, and the highway element by the National Highways Department. There was a four-year contract of MR 1.3 billion (equivalent to 340 million USD) for design-build-delivery of the floodwater mitigation facility between the Department of Irrigation and Drainage and the MMC-Gamuda JV and a forty-year build-operate-transfer agreement between the National Highway Department and the SMART JV concessionaire. The SMART project was planned in 2001, construction started in 2003, and excavation of the South Drive was completed in April 2006 and of the North Drive in March 2007. The excavation and construction of the South Drive was carried out by MMC-Gamuda JV and was subcontracted to the Wayss & Freytag of Germany for the North Drive. The road section was opened to the public in March 2007, three months behind the previously scheduled Dec 2006 opening. The list of major participants is summarized in Table 2.2.

Table 2.2 List of major participants

Participant	Position and responsibility
Drainage and Irrigation Department	Owner of Diversion tunnel and flood mitigation facilities
Highway Authority	Owner of Toll road section and road facilities
MMC-Gamuda JV	Contractor
SMART JV (Syarikat Mengurus Air Banjir & Terowong Sdn Bhd)	Toll road operation (40 year BOT), covers cost of MR 700 million
Sepakat Setia Perunding (SSP) and Mott-MacDonald	Design and project supervision
Wayss & Freytag AG	Excavation and road deck construction for North Drive
MMC-Gamuda JV	Excavation and road deck construction for South Drive
Herrenknecht AG	TBM and plant supplier
Eastern Pretech and ACPI	Manufacturing precast segment linings
Sunway	Manufacturing road deck base panels

2.2.2. Geological conditions

The geological condition close to the surface of the city is well represented by the city's name, Kuala Lumpur. Kuala means the 'river convergence,' and Lumpur means 'mud.' Soft Quaternary alluvial deposit, 4 to 5-m thick, overlies medium to strong limestone. The average standard penetration number for the overlying material is 4. Although the Kuala Lumpur limestone is typically made up of 90~100 % calcite and is considered competent with an average Q value of 22 and the UCS value of 50 MPa, on average, and 120 MPa, at maximum, the karstic nature of the geology and the presence of loosely filled mine tailings made the tunneling difficult (Darby) as follows:

- The rockhead level varies, rapidly displaying steep pinnacles and deep valleys;
- Cavities are comparable in size to the TBM and are interconnected;
- Sinkholes or excessive settlement could result from groundwater dewatering;
- Void infilling materials are inconsistent: water, soft mud, or dense soil.

The groundwater table presents 1.5-2.0 m below the surface. Permeability of the rock is low, but interconnected karstic voids could provide extensive and rapid drawdown of groundwater. When excavating the interconnected karstic ground, groundwater lowering could cause a sinkhole, even at a significant distance from the site of excavation. Furthermore, the karstic nature of bedrock allows alluvium soil to intrude into the karstic void, which made tunneling more challenging. Since the tunnel was constructed beneath the most sensitive urban areas, including the Royal Selangor Golf Club, SG Besi Air Field, and Star light rail transit system, predetermining the location and the size of the void was a crucial factor to guarantee problem-free excavation. From north to south, as shown in Figure 2.3, the tunnel runs through 2.5 km of alluvium deposit, 0.7 km of mixed ground and, then, mainly limestone ground, except the southernmost region of 200 m of residual soils of granite.

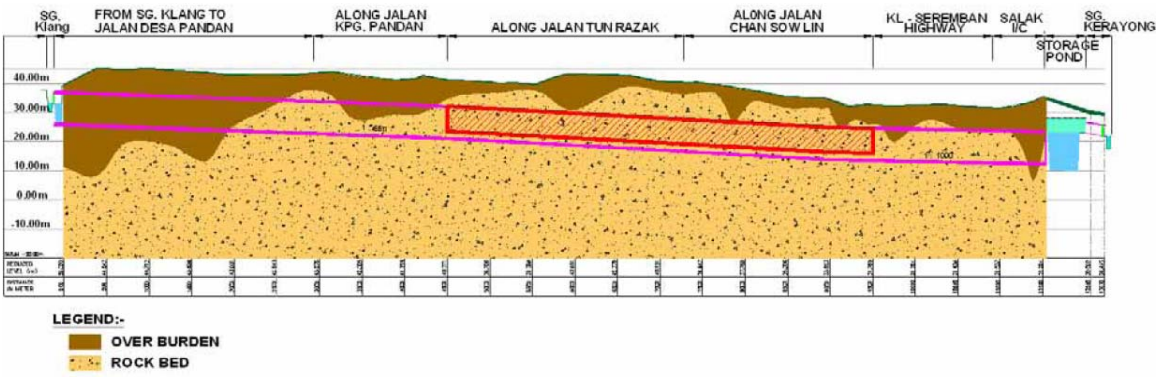

Figure 2.3 Subsurface conditions for the SMART (after Darby and Wilson, 2005)

Extensive site investigation was carried out. Rock cores were recovered and packer tests were carried out. Four geotechnical survey techniques (cross-hole seismic survey, ground penetration radar, micro-gravity survey, and 2D resistivity survey) were attempted. Among these, the resistivity survey was found to be the most effective

method in identifying karstic void and detecting anomalies. The resistivity survey provided clear contrast between a filled karstic void and limestone bedrock. The resistivity survey, unlike the other techniques, was powerful in filtering out interferences from traffic vibration, noise, and the existence of metal pipelines and electrical cables. This technique was applied to the whole tunnel alignment and any anomalies identified were inspected by boring from the surface and treated well ahead of the TBM's approach. As a complementary measure to identify the presence of karstic void near the highway section of the tunnel, a microgravity survey was carried out on five parallel lines along the tunnel alignment.

2.2.3. Tunnel alignment and cross section

As described in Figure 2.4, the tunnel is located between the Holding Pond and the Storage Reservoir and is 9.7-km long. The tunnel features a 2.6-km long, multi-deck section in the middle of the alignment between the North Junction Box (NJB) and the South Junction Box (SJB), and it houses a double-deck toll road and a permanent invert channel. The tunnel is divided into three levels by upper and lower decks, incorporating a permanent invert channel at the invert and double-deck highway. There are Y-shaped on- and off-ramps for traffic in the NJB and SJB that allow the roads to join and leave the main tunnel corridor. Between the NJB and the SJB, there are two ventilation shafts: the North Ventilation Shaft (NVS) and the South Ventilation Shaft (SVS). These four structures, two ventilation shafts and two junction boxes, provide ventilation for the road tunnel and emergency escape routes.

The tunnel's horizontal alignment is a winding shape. Because the private property ownership in Malaysia extends to the center of the earth, the tunnel had to

follow a corridor beneath public roads to minimize the necessity of land acquisition. The tunnel horizon was established based on the need of gravity flow and gradient as well as length restrictions of on- and off-ramps of the highway. Having sufficient cover depth would have been beneficial to avoid risks caused by shallow cover depth, especially in the treacherous karstic ground conditions of Kuala Lumpur. Nevertheless, cover depth was limited to about 1-1.5 times diameter to allow gravity flow of the floodwater from the Klang River to the Kerayong River and to observe the gradient and length limitation of highway on- and off-ramps.

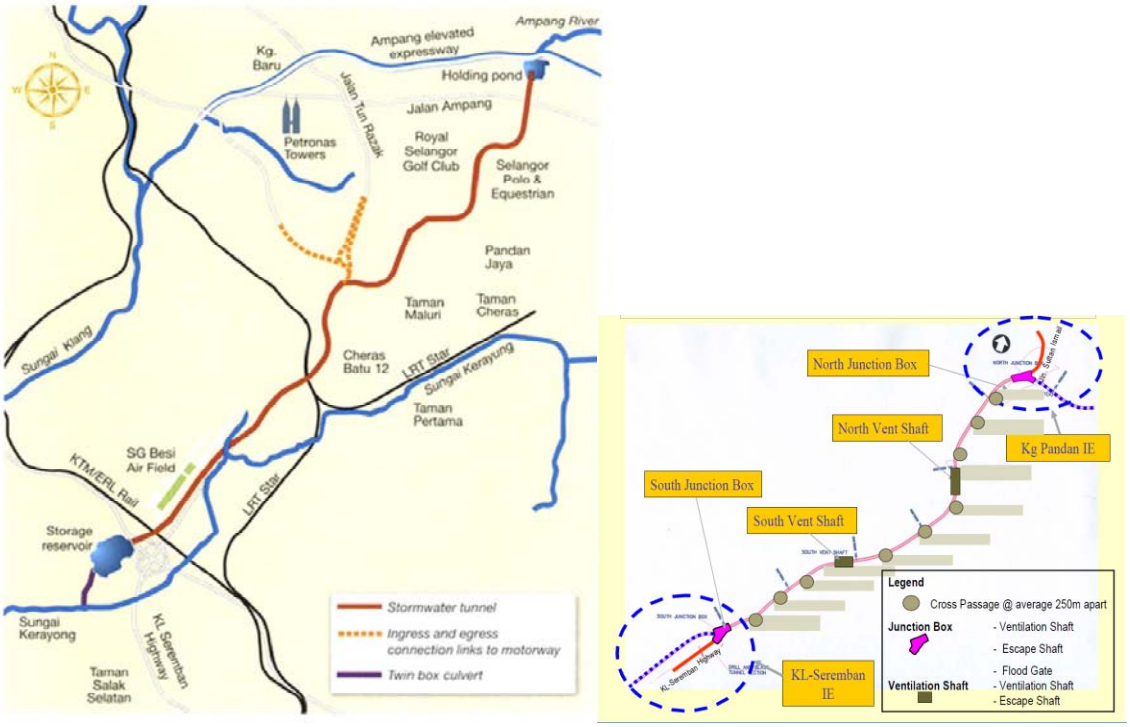

Figure 2.4 SMART tunnel alignment and its project location
(after Tunnels and Tunnelling International, 2005)

Figure 2.5 shows the composition and dimension of the multi-deck section. The upper deck provides two 60 km/h 3.35-m wide traffic lanes and one 2.0-m wide emergency lane flowing south (leaving the city center), and the lower deck has the same arrangement for traffic flowing north (bound to city center). The maximum vehicle height is restricted to 2.55 m, both for upper and lower decks. In a severe storm situation, the road deck can be used as a floodwater flow channel or floodwater retention facility. The flow area for the multi-deck section is 18.97 m^2 in Modes I or II and 80.18 m^2 in Mode III. (Details of the operation mode will be dealt with in the next section). The stretch that does not include the road deck has 109.92-m^2 flow area. The tunnel was designed to cope with storm magnitudes of 100 year ARI (average returning interval), using 3-hour storm duration for peak flow rate.

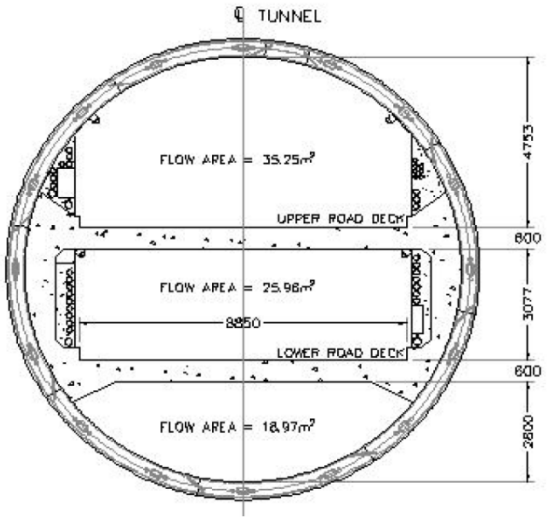

Figure 2.5 SMART tunnel alignment and its cross section
(after Darby and Wilson, 2005)

2.2.4. Operation mode

The lower and upper road decks are open to traffic a majority of the time and, when required for full capacity flood control during a heavy storm, the road decks are closed to traffic and the whole tube diverts the floodwater. The tunnel can be operated in three modes, as described in Figure 2.6. Most of the time, the tunnel is in Mode I, that is, the road section is open to traffic and minimal seasonal flow exists in the permanent invert channel. The tunnel is in Mode II typically about 15 times/year. In Mode II, floodwater flows through the permanent invert channel. Protected from the floodwater by double flood gates, placed in series at each end of the road section, the road deck is still open to traffic. The maximum flow rate that can be handled in Mode II is 80 m^3/sec. Mode III is activated less than once a year. In Mode III, the road deck is closed to traffic and, by opening the double flood gates at either end of the road section, the entire cross section of the tunnel is used to divert the floodwater. The full drainage capacity in Mode III is 290 m^3/sec. If the toll-road section is closed for more than the agreed number of days per year for full capacity flood mitigation purposes, compensation payment is issued to the SMART JV and its concessionaire. The total retention capacity of the SMART system is about 3,000,000 m^3. This is the combined capacity of the Holding Pond (600,000 m^3), the Storage Reservoir (1,400,000 m^3) and the 9.7-km long tunnel. The retention capacity of the tunnel is about 1,000,000 m^3 in Mode III and about 750,000 m^3 in Mode II. The retention capacity of the SMART system can handle a storm that lasts 6 hours with a magnitude of 100 year ARI

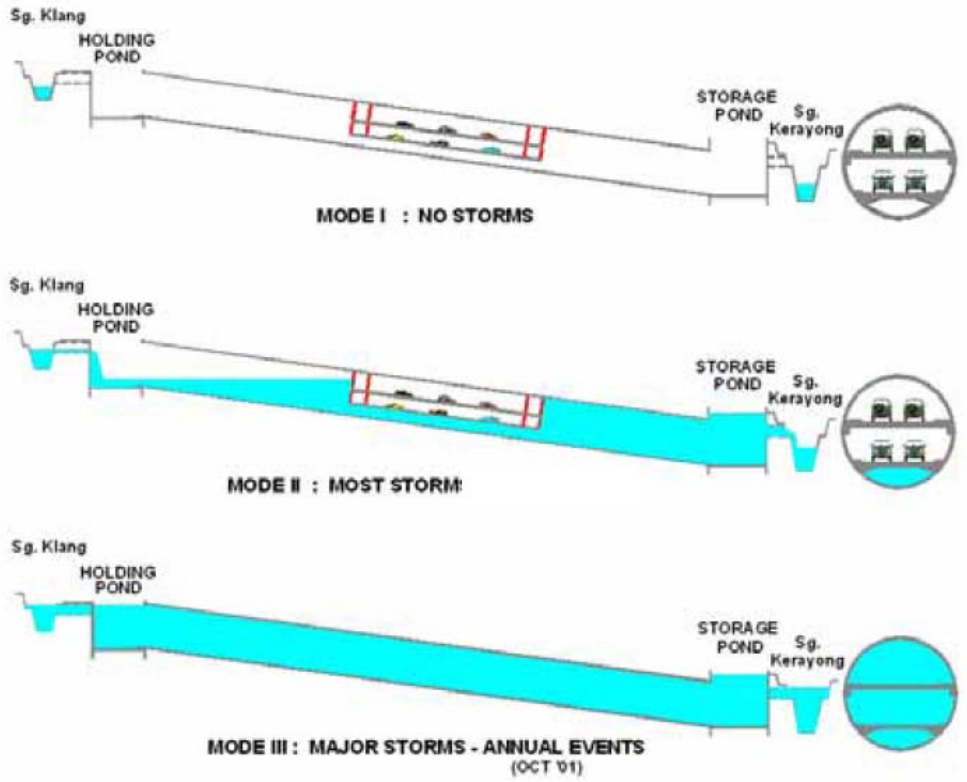

Figure 2.6 SMART's three modes of operation (after Darby and Wilson, 2005)

When the Mode III operation is necessary, the operators close the hydraulic flap gates installed at the on- and off-ramps, watertight doors for the four ventilation shafts, and watertight fire doors for nine cross passages. After the final walkthrough check, which takes fifteen minutes, operators open the double flood gates at either end of the road section. Usually the floodwater diversion through the tunnel does not exceed 8 hours, and another 10 hours are necessary for dewatering. After the road facility is used for the full-capacity, flood mitigation process, and before it can be reopened to traffic, it takes about 48 hours to wash down a film of thin mud built on the surface of the road tunnel. The wash-down water is collected in sumps at both sides of the road deck and pumped out for treatment. The internal surface of the road deck is coated with epoxy

material to ease the wash-down process. If the flood control requires the capacity of the lower deck only, floodwater is directed only to the lower deck, in order to facilitate the road section's reopening. Apart from restoring the road section for normal traffic use following the flood diversion process, the stormwater management system is designed to be ready in 24 hours for handling another storm.

2.2.5. Flood relief procedure

Floodwater bypassing from the Klang River to the Kerayong River is carried out by several hydraulic structures. The list of hydraulic structures in SMART and its capacity is summarized in Table 2.3.

The central control station determines the mode of tunnel operation based on weather conditions and data collected from flow monitoring gauges installed along the Klang River and in the catchment basin. Flow that exceeds 70 m^3/sec at the confluence of the Klang and Ampang Rivers is diverted into the Holding Pond (Figure 2.7) by a diversion weir and an offtake structure. When the flood control system is in operation, the diversion weir is closed and the offtake structure is opened. The diversion weir, fitted with four 6-m wide and 5-m tall tilting gates, controls the flow rate by adjusting the tilt of the tilting gate (Figure 2.8). When the river is not being diverted, the tilting gates sit on the riverbed allowing normal flow for the river. Under heightened flood alert conditions, the tilting gates are raised to build up the water level in the forebay higher than the spill height of the offtake structure. During diversion, the downstream flow rate of the river can be adjusted by controlling the tilting gates. To prevent scouring of the riverbed, the tilting gate of the diversion weir has a steep convex shape, and a 14-m long stilling basin is installed downstream of the diversion weir. The offtake structure,

fitted with eight 6.0-m wide, 3.5-m tall vertical roller gates, passes a maximum of 300 m^3/sec into the Holding Pond by opening the gates. The gates are kept closed when diversion is not necessary. Upstream of the offtake structure, sets of floating trash booms block the floating debris from flowing into the pond.

Table 2.3 List of the hydraulic structures in SMART

Location	Structure	Elevation (m, above sea level in LSD)	Flow rate (m^3/sec)	Retention capacity (m^3)
Holding Pond	Diversion weir	33.0 m at invert		
	Offtake structure	33.5 m at invert	Max. 300 $m^{3/}$sec	
	Holding Pond	27.3 m at floor; Water level: 29.7 m (normal); 38.0 m (maximum); 34.0 m (minimum to allow spilling)		600,000 m^3 (Floor area: 94,000 m^2)
	Bellmouth intake shaft	34.0 m at the crest of ogee weir spillway 15.17 m at the floor of stilling well	Max. 300 m^3/sec	
Main tunnel		21.55 m at upstream invert 8.22 m at downstream invert	Up to 70 m^3/sec (mode I) 70-150 m^3/sec (mode II) 150-290 m^3/sec (mode III)	750,000 m^3 (mode II) 1,000,000 m^3 (mode III)
Storage Reservoir	Chamber width	8.22 m at invert		
	Storage Reservoir	Water level: 20.0 m (normal); 28.0 m (maximum)	1,400,000 m^3	Floor area: 220,000 m^2
	Twin box culvert	20.0 m at invert of upstream 19.5 m at invert of downstream	Max. 200 m^3/sec	
	Stilling basin and outfall structure	Stilling basin floor: 16.8 m Riverbed at discharge point: 18.1 m	Max. 200 m^3/sec	
Overall system's flood mitigation capacity		Maximum floodwater intake capacity: 300 m^3/sec Maximum floodwater flow rate in tunnel: 300 m^3/sec Maximum floodwater discharge capacity to the Kerayong River: 200 m^3/sec Maximum floodwater retention capacity: 3,000,000 m^3 under the mode III; 2,750,000 m^3 under the mode II		

The floor of the offtake structure (33.5-m LSD, land surveying datum) is located 0.5 m above the riverbed (33.0-m LSD). This is to prevent the inflow of sediment from

the riverbed to the Holding Pond. To dissipate the energy of flow as it passes the gate of the offtake structure, a steep concave glacis leading to a stilling basin, which is 8.2-m deeper than the floor of the Holding Pond, is provided. When the level of the Holding Pond reaches 34-m LSD, floodwater is spilled into the tunnel through a bellmouth shaft (Figure 2.9). The bellmouth shaft has eight 6-m wide straight weirs, where the crest is at 34-m LSD. These settings are arranged radially around the shaft. The bellmouth is protected by screens to prevent the inflow of trash material, and baffles are installed to promote sedimentation. The peak flow rate of the bellmouth structure is 300 m^3/sec. At the bottom of the bellmouth shaft is a stilling well whose invert elevation is 15.17-m LSD.

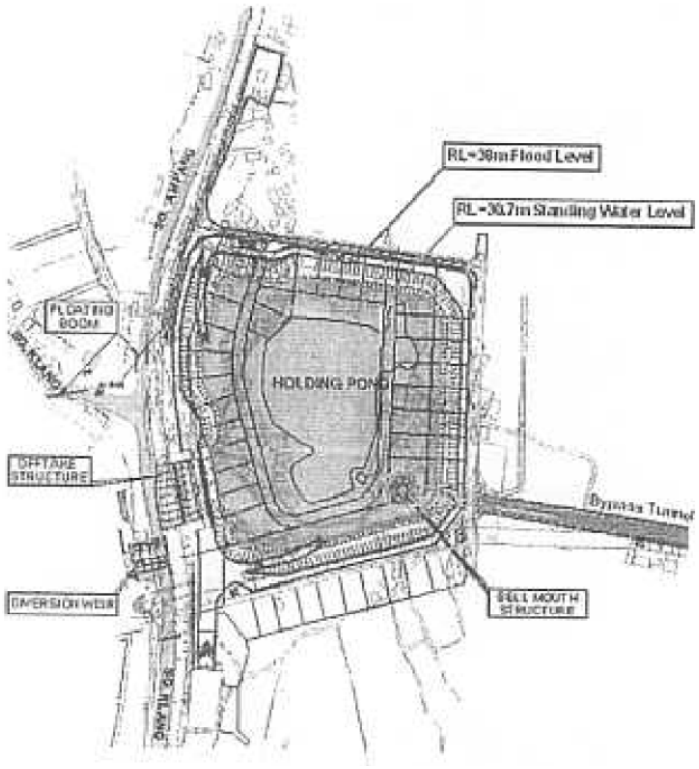

Figure 2.7 Holding Pond (after Abdullah, 2004b)

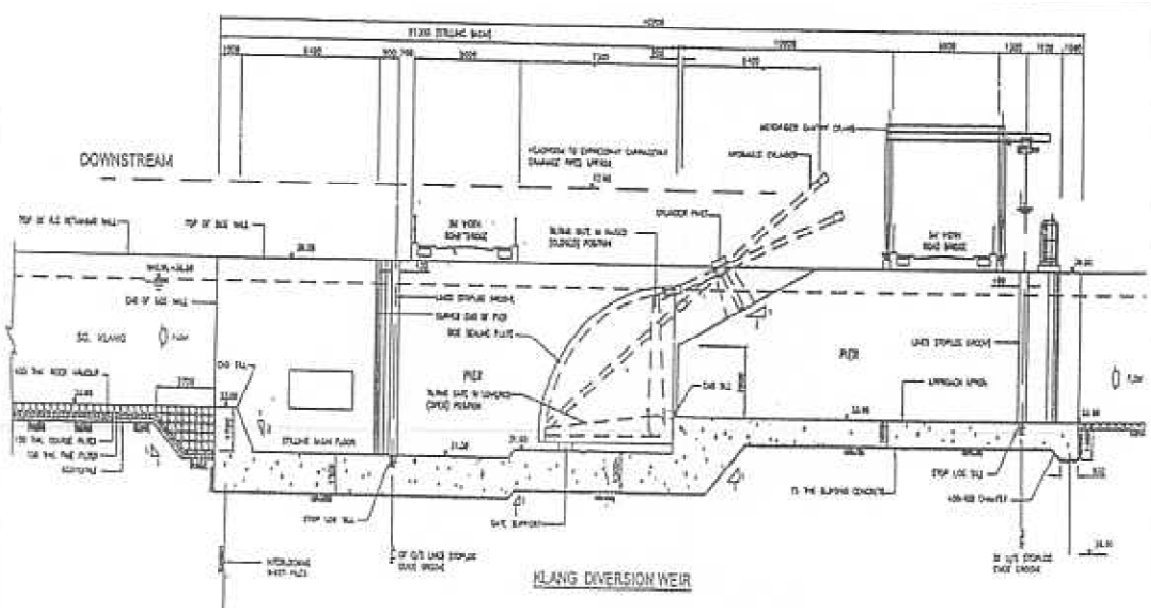

Figure 2.8 Klang river diversion weir (after Abdullah, 2004b)

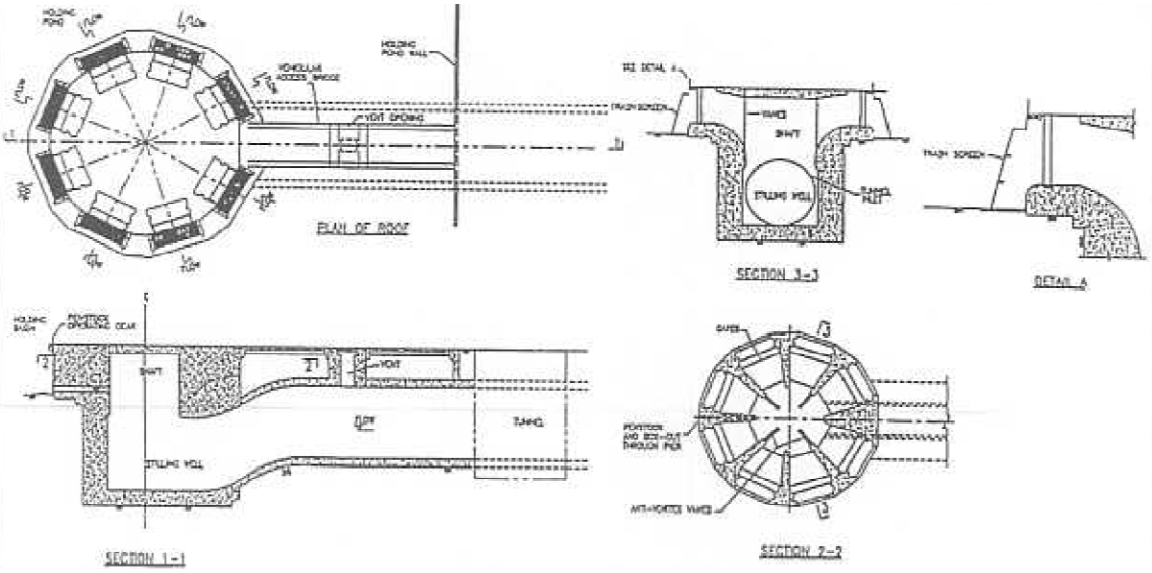

Figure 2.9 Bellmouth intake structure (after Abdullah, 2004b)

In the tunnel, the average flow velocity is around 3 m/sec, and the flow velocities at various locations are provided in Table 2.4. To avoid forming entrained air pockets,

several vent points that allow escape of air are located at the inlet, junction boxes, and ventilation shafts.

Table 2.4 Flow velocities in the tunnel (Abdullah, 2004b)

Section	Flow area (m^2)	Velocity (m/sec)	
		Steady flow	Transient flow
Tunnel without road section	109.9	3.0	4.9
Upper road deck	35.25	2.5~3.2	4.7
Lower road deck	25.96	2.5~2.6	4.6
Permanent invert channel	18.97	2.1~3.0	4.9

The floodwater in the tunnel is discharged into the Storage Reservoir through a chamber. The chamber connects the main tunnel and the Storage Reservoir (Figure 2.10). In the chamber, there are four submersible pumps and a 5.5-m wide, 10-m high vertical roller bulkhead gate. The bulkhead gate is required since the normal water elevation of the Storage Reservoir is 20-m LSD, while the elevation of the tunnel invert is 8.22-m LSD. The bulkhead gate is kept closed to prevent backflow of water into the tunnel. Only when the SMART is activated and when the water elevation in the Storage Pond is lower than about 24-m LSD at the earlier stage of flood flow operation, is the bulkhead gate opened to discharge the floodwater. As the Storage Pond water level builds up, the flow cannot be discharged effectively by gravity only. Then, the bulkhead gate is closed and pumps start to drive the water out from the chamber. In the case of gate or pump failure, an emergency weir located at the top of the chamber structure provides drainage to the tunnel. As the reservoir fills, water is released to the Kerayong River through 500-m long, twin box culvert channels, each 5-m wide and 5.5-m high. Figure 2.11 shows a plan view around the Storage Pond and the Kerayong River. The flow is released at about 1,800 m above the Kerayong River's confluence point with the

Klang River. To avoid downstream flooding, the release of water is regulated. No more than 200 m^3/sec should be discharged into the Kerayong River. As shown in Figure 2.12, the twin box culvert channels have 5.5-m wide and 4.0-m tall vertical roller gates at both ends of the channels to control the discharge of water. To prevent scour of the riverbed close to the release conduit, a stilling basin protected by stone and with floor elevation at 16.8 m was constructed in the conduit and riverbed.

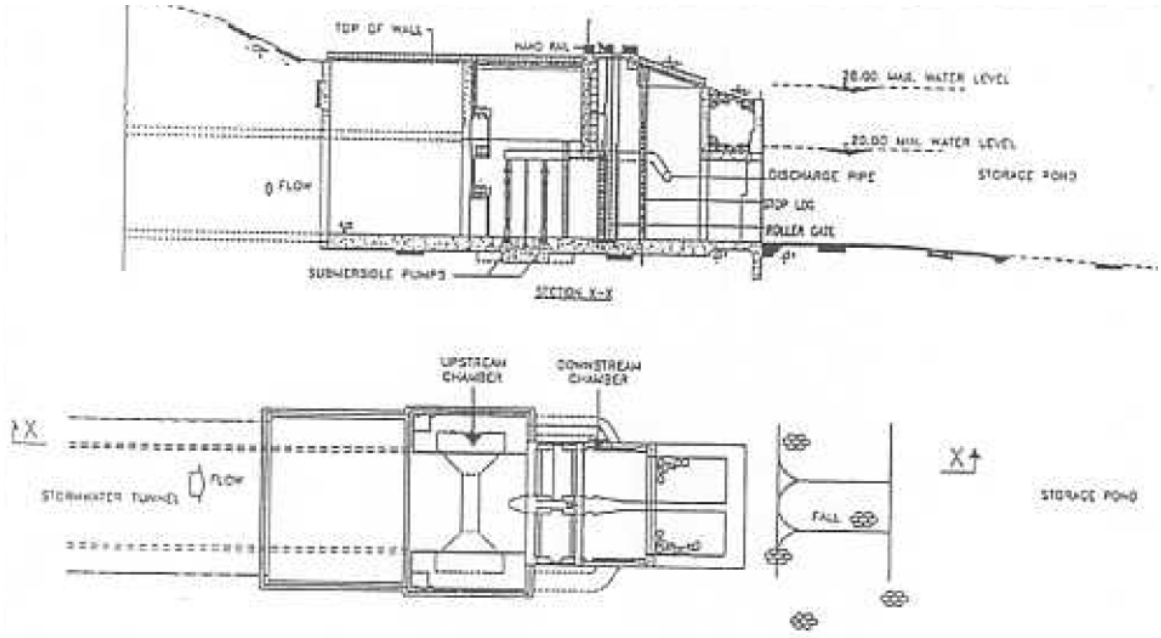

Figure 2.10 Discharge structure at the Storage Reservoir (after Abdullah, 2004b)

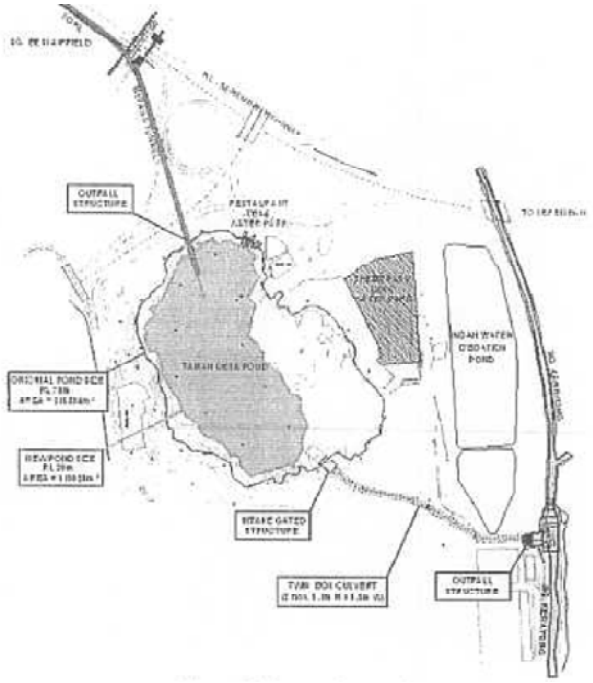

Figure 2.11 Storage Reservoir and twin box culvert (after Abdullah, 2004b)

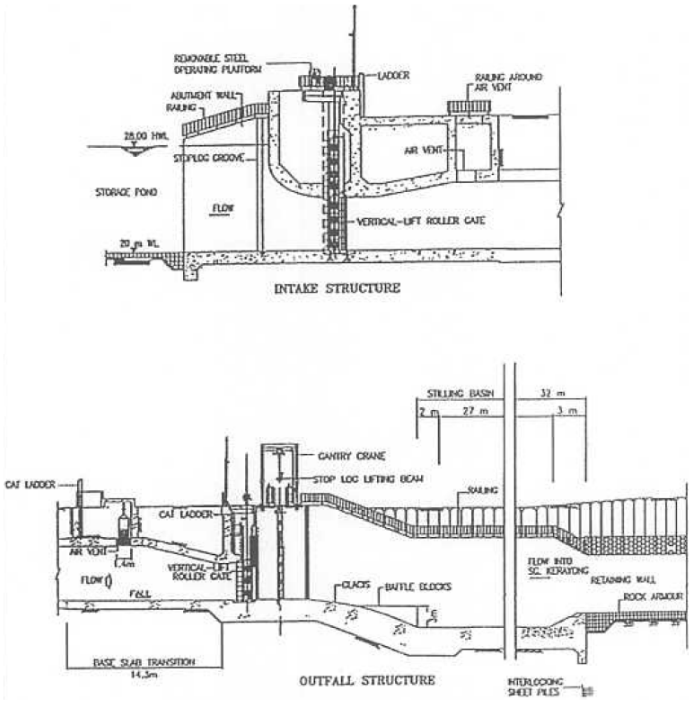

Figure 2.12 Twin box culvert intake and outlet structure (after Abdullah, 2004b)

2.2.6. Road section management

The middle 2.7-km section is earmarked as a toll road facility. The toll road is operatated by SMART JV (Syarikat Mengurus Air Banjir & Terowong Sendirian Berhad). Specifications for the road section are summarized in Table 2.5. Two ingress/egress ramps are provided for vehicles at Kampong Pandan in the north and at KL Seremban Highway in the south. The road deck is protected from floodwater by double flood gates at both ends of the road section. A set of double flood gates is comprised of an emergency gate and two service gates installed at upper and lower decks. The emergency gates, located at the outer side of road section, are 7-m high and 9.5-m wide and weigh 40 tons. The upper and the lower deck service gates, located at the roadside of each emergency gate, are 4-m high and 9.5-m wide and weigh 26 tons, each. The details of the flood gates are shown in Figure 2.13 and the scheme by which the flood gates protect the road section from flooding is shown in

Figure 2.14a. The upper and lower decks have their own separate service gates to allow for the Mode III operation that uses only the lower deck. To prevent flooding of the area near the on- and off-ramps, each ramp is protected by a 31.1-m wide, 3.3-m tall roll-on-roll-off type hydraulic flap gate weighing 37 tons installed in the gatehouse of the North and South Junction Boxes. Nine cross passages are protected from flooding by watertight fire doors installed on the sidewalls of the road section. Ventilation ducts and emergency exits of the ventilation shafts and the junction boxes are protected by watertight flap doors. All fittings inside the road section are operable in a submerged condition as well as in the dry, and they do not require replacement parts after a full flood. Every fixture in the road section, such as lighting, linear heat detection cable, surveillance cameras, and road signs, is designed to remain in place and survive the harsh

flooding environment of at least 24 hours with 2.5 bar hydrostatic pressure and peak water velocity of 4.7 m/sec. Every fixture that cannot survive the flooding environment has been provided with protective casing or housed in a dry area behind the water-tight gates in the cross passages at 250 m intervals. For example, casings for lightings were designed to stricter criteria than the highest IP (ingress protection) rating of 68, and power cables and optic communication cables were installed in watertight ducts or multi cable transits (MCT) in the in situ concrete sidewalls. To ensure the water tightness of the road deck, which is subjected to an up-lift water pressure of 2 bar when Mode II is in operation, all construction joints and the gaps between the segmental lining and road deck were sealed with a post injection grouting system.

Table 2.5 Road section specification

Description	Specification
Composition of roadway	Two 3.35 m traffic lanes and one 2.0 m emergency lane per deck, cars only; (upper deck: southbound, lower deck: northbound; Height of upper deck: 3.2 m,vehicle height restriction 2.55 m)
Maximum vehicle speed	60 km/h
Ingress/egress ramps	North junction box to Kampong Pandan South junction box to KL Seremban Highway
Road section flood gate	1 emergency gate and 2 service gates at each end of the road section
Ramp flood gates	2 roll-on roll-off type hydraulic flap gates at each endof the road section
Emergency cross passages	Nine at 250 m intervals
Road tunnel environment	Designed to control three car fires (10 MW) Watertight up to 2.5 bar pressure

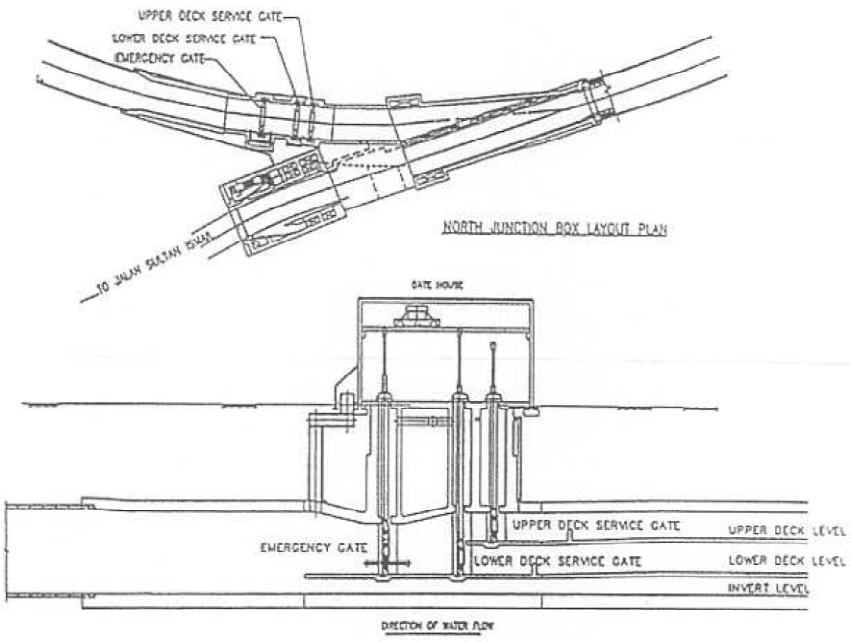

Figure 2.13 Road deck flooding gate (after Abdullah, 2004b)

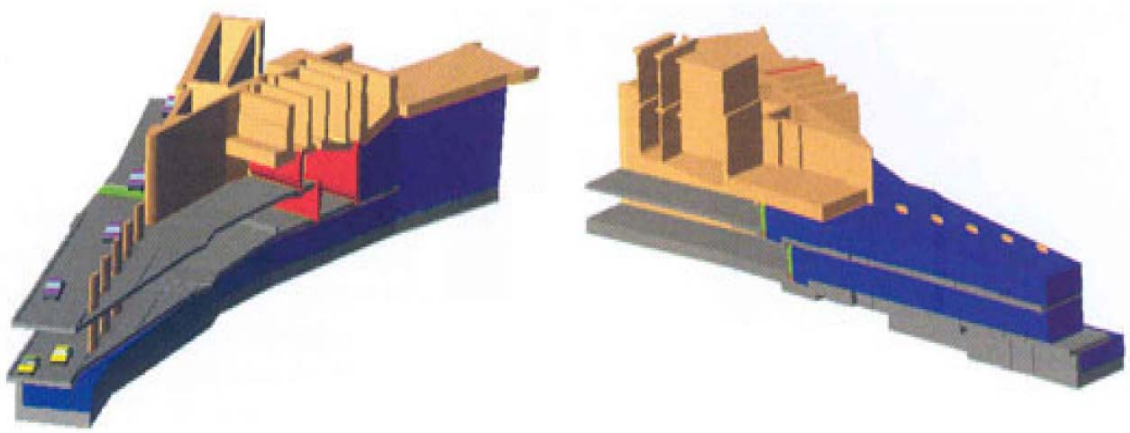

(a) Mode II: closed floodgates (b) Mode III: closed flapdoors

Figure 2.14 Operation scheme of the flood gates and the highway ramp flap gate (after Master Builder, 2005)

2.2.7. Excavation method selection

The first construction plan was to bore the 5.5 km northern part of the tunnel mechanically and the 4.2 km southern part using the conventional cut-and-cover and drill-and-blast method. However the option of using the cut-and-cover and drill-and-blast techniques was discarded for the following reasons:

- The tunnel runs under a densely urbanized area.
- Dewatering of the ground was not permissible and it was difficult to preserve the groundwater level in Kuala Lumpur's karstic limestone ground.
- There was a risk of encountering a mud- or water-filled karstic void, unexpectedly.
- Slow and costly, extensive systematic grouting from the surface was required.
- Objection to blasting was expected and the limitation on the vibration and hours of blasting was strict.
- Doing open-cut work without worsening traffic congestion in an already congested area was impossible.
- The excavation depth was considerable, due to the large diameter of the tunnel.

The decision was made to excavate the whole tunnel corridor mechanically since a closed-mode pressurized TBM is effective in protecting the natural groundwater and in avoiding karstic void drainage and ground settlement. Once it was determined to excavate mechanically, both the slurry TBM and EPB TBM were considered. It was necessary to cope with very tight radius curves, shallow overburden depth, sudden drops in rockhead, unexpected karstic voids, and mixed ground conditions. Slurry technique rather than EPB technique was selected for the following reasons.

- Slurry machines of the required size had been used several times, whereas EPB machines of that size or greater had been used only once, for the Groenhart tunnel.
- The Mixshield technique provides the flexiblity of switching the drive method between limestone and alluvial sediments.
- Slurry machines can respond more rapidly to sudden changes in excavation chamber pressure.
- It is difficult to control the groundwater ingress into the plenum when the excavation chamber is filled with rock.

2.2.8. TBM specification

Five TBM manufactures, Herrenknecht, Hitachi, Kawasaki, Mitsubishi and NFM, submitted quotes for the bid. Among them, the proposal from Herrenknecht had the competitive edge to build and deliver both machines within 12 months and to supply all necessary tunneling equipment as part of a single package. Orders for two Herrenknecht slurry Mixshield machines were signed in Mar 2003. Herrenknecht supplied two refurbished Mixshield TBMs, two separation plants, compressed air stations, ventilation chiller plants, and spare parts inventory, including cutting tools. The two TBMs were refurbished after the Westerschelde tunnel project in the Netherlands. The North Drive TBM S-252(Tuah) was delivered in early Feb 2004. After it was assembled for launch, it started excavation in May 2004 and completed excavation in March 2007, 8 months behind the original schedule. The South Drive TBM S-253 (Gamilang) was delivered in Apr 2004, started boring in Sep 2004, and completed excavation in May 2006. The TBM was manufactured in the Herrenknecht plant in Schwanau, Germany and was shipped to Kuala Lumpur by a heavy lift ship. The TBM specifications are summarized in Table 2.6.

Table 2.6 Specification of the Mixshield TBM

Description		Specification
Total installed power		8,200 kW
Total length		71 m
Total weight		2,500 tons
Slurry circulation rate		2,400 m^3/hr
Cutterhead	Diameter	13.26 m
	Rotating speed	0-3 rpm, left and right
	Hydraulic motors	18
	Construction	1 center part and 4 outer segments
	Tool Composition	76 17" disc cutters, 16 buckets and 196 scrapers,
	Installed power	4,000 kW
	Nominal torque	24,400 kNm
	Breakout torque	31,500 kNm
	Axial displacement	400 mm
	Main bearing	3 rows roller bearing with 5.6 m outer diameter
Thrust cylinders	Thrust force	94,500 kN
	Advance speed	0-50 mm/min
	No. of thrust cylinders	48 cylinders (16 triple cylinders)
	Dimension	280/240 mm diameter, 2,500 mm stroke
	Maximum pressure	350 bar
Shield	Diameter	13.21 m at front, 13.19 m at rear
	Length	10.24 m
	Working pressure	Max 3 bar (at the crown of the shield)
Tailskin	Diameter	13.18 m
	Articulation	Passive articulation with articulation cylinders
	Sealing system	3 rows of brushes
Obstacle removing equipment installed in the plenum		Rock crusher that can handle up to 1.2 m diameter boulder Two flushing lines wash out excavated material at the slow moving center of the cutterhead.
Maximum negotiable curve		200 m radius
Air lock		4 bar 2 man air locks (4+2 persons), 4 bar 1 material air lock

To minimize the risks associated with the karstic and mixed ground conditions of Kuala Lumpur, several risk mitigation schemes were employed:

- The face support pressure in karstic void was calculated using the Mohkam Model (Klados and Kok, 2004).
- Extensive site investigation and geophysical surveys were conducted and an intensive settlement or heave monitoring system was installed.
- Slurry composition was adjusted according to the ground conditions.
- Each TBM was equipped with two 350 m^3 bentonite slurry tanks as a provision against rapid slurry loss.
- A cutterhead tilt-indicator revealed the presence of a karstic void or mixed ground conditions.
- Two drill rigs to investigate ahead of the face and invert of the tunnel were installed.
- A seismic, soft ground probing system to identify the ground conditions ahead of the face was installed. The seismic probing system was not functional during the entire tunnel alignment project, because the sensors broke down frequently in the harsh limestone excavation process.

Both TBMs were operated under hydrostatic pressure of 1.2-1.8 bar. The compressed air was delivered to the excavation chamber using four diesel compressors, each capable of producing 160 m^3/hr of 70 bar compressed air. Since the limestone was not very abrasive, the tool wear was moderate. Disc inspection was done twice a week to check for flat spot wear, and chamber interventions were made at 100-200 m intervals. Disc inspection and chamber interventions were carried out in the zone of competent rock or a suitable location using the resistivity survey results to eliminate the need for applying air pressure or excessive grouting on the tunnel face. A cutter head drive unit with 400 mm extension-retraction capability facilitated cutting tool change. The performance of a TBM depends on the combined performance of all support facilities i.e., separation

plant, grout plant, segment feeder and erector, etc. The approximate combined output was 10 m of excavation per day. The positioning of the TBM was accomplished using a VMT guidance system that constantly monitors current position and provides corrective feedback to the TBM operator. To maintain smooth downhill gravity flow gradient, the level and line tolerance was kept within ± 50 mm. To negotiate tight 250 m radius curves, each TBM was equipped with a spherical main bearing and copy cutters on the cutting wheel.

2.2.9. Slurry treatment plant

Two slurry treatment plants, one for each TBM, were used. They were supplied as part of the Herrenknecht package. The first bentonite separation plant for the North Drive TBM was a refurbished Schauenburg plant used for the 4th Elbe tunnel project, and was assembled adjacent to the working shaft in May 2004. The second plant for the South Drive TBM was a new Schauenburg plant and was installed at a 500 m distance from the access box. Each plant had 2,800 m^3 of bentonite slurry in the system. The fresh bentonite slurry was stored in two 1,000 m^3 tanks in the plant, one 350 m^3 tank in the TBM, and the circulation pipelines. The diameter of the circulation pipeline was 500 mm and the optimum slurry circulation velocity in the pipelines was 3.6 m/sec. Each slurry separation plant had a treatment capacity of 2,400 m^3/hr. The maximum distance between the TBM and treatment plants was 5.3 km for the North Drive and 4.1 km for the South Drive.

The slurry separation plants produced fresh bentonite slurry, separated excavated materials from slurry for reuse, and disposed of bentonite slurry in bad condition. To produce fresh bentonite, 40 kg of bentonite were mixed with 1 m^3 of water. The amount

of bentonite was increased to 60-70 kg, when excavating in sandy ground. The used bentonite slurry underwent two separating processes. First, particles larger than 0.5 mm were removed by three decks made of screen, with 30 mm, 6 mm, and 0.5 mm openings. Subsequently, particles larger than 0.03-0.04 mm were removed using hydrocyclones. Depending on the quality of slurry, flow was then diverted to the holding tank for reuse or to the waste disposal process. The reusable slurry was stored in the holding tank, where it was mixed with fresh bentonite, and recirculated into the TBM plenum. The slurry sent for the disposal process was stored in a 1,000 m^3 waste slurry holding tank until its solids were separated by centrifuge and waste water was clarified by flocculent treatment. For bentonite slurry to be reusable, the treated slurry must have specific gravity less than 1.25 and pH of less than 9 or 10. Slurry consumption was high due to chemical reaction between the bentonite and the limestone and the forward migration of annular grouting material into the excavation chamber. To keep the bentonite slurry in good condition, 120-200 m^3 of bentonite slurry was extracted per each 1.7 m ring advance and replaced by fresh bentonite slurry. Chips formed during excavation of limestone were sharp enough to cause damage to rubber components in the separation plant, and the 6 mm screen was replaced by 4.5 mm screen to alleviate the situation.

2.2.10. Tunnel excavation

The 5.5 km-long North Drive excavation and road deck construction in the North Drive was awarded to one of the leading soft ground tunnel excavation contractors, Wayss & Freytag, in May 2003, for a value of $102 million. The North Drive TBM was delivered in early Feb 2004 and, after it was assembled for launch, started excavation in May 2004. In Dec 2004, the TBM broke through into the North Junction Box,

completing the excavation of 740 m of the North Drive road deck section. The TBM was relaunched in Feb 2005 for the remaining 4.5 km North Drive excavation. Wayss & Freytag had been on site from Aug 2003 to February 2006, when the subcontract was terminated due to the under-performance in excavation. By Jan 23, 2006, Gamuda-MMC JV had almost completed its South Drive excavation, while the progress in the North Drive was about 46% complete. Once the subcontract with Wayss & Freytag was terminated, Gamuda-MMC JV took over the remaining 2.8 km stretch of the North section. They replaced many tools and discs on the cutterhead and repaired the separation plant before resuming excavation of the remaining 2.8 km section in the third week of April 2006. The North section of the tunnel achieved its breakthrough in March 2007. It was eight months behind the original schedule and three months behind the schedule revised after the termination of subcontract.

The 4.2-km long South Drive was excavated by Gamuda-MMC JV, a relatively inexperienced tunnel builder. The South Drive TBM arrived in April 2004 and started boring in September 2004. In July 2005, it was relaunched for its final 2-km long drive. In May 2006, the South Drive excavation was completed. During the boring of the 3,968 m, or 2,334 rings, southern part of the SMART project, a world record advance-rate for a large TBM in karstic ground was achieved: 66 rings per week and 13 rings per 24 hours.

During construction, fresh air was supplied through a 2 m diameter flexible duct using two 250 kW fans and a heat exchanger capable of maintaining 27°C around the ring build area.

Probing and grouting were carried out both from within the TBM and from the surface. Two drill rigs were available in each TBM to investigate the presence of

cavities or anomalies ahead of the face and invert of the tunnel. One drill rig probed the ground horizontally through the cutterhead at the lower one third of the tunnel face and the other drill rig at -7° inclination reaching about 1.5 m below the invert. Probing, which took about four hours, was carried out at two-day intervals. The drilled length was 40 m and normally, two day intervals yielded overlapping distance of about 15 m.

2.2.11. Lining

One-pass lining was constructed using 1.7-m long, 500-mm thick reinforced precast concrete segments. Precast segments were designed by Mott MacDonald. One ring weighed about 82 tons and the composition of a ring was six standard segments, 2 counter keys, and a keystone (Figure 2.15). To expedite the ring building, it was decided to use a smaller number of larger segments than that usual for a tunnel of this size. 50 conventional spear bolts per ring were used to connect the segments. Two bolts were used to connect segments across the radial joints, and four bolts per segment were used to connect adjacent rings. To negotiate tight, 250 m radius curves, 2×55 mm taper was given. The average time for ring building, using a vacuum segment erector, was about 35-40 minutes. Water tightness was achieved using EPDM sealing gaskets designed to resist up to 32 m of water head (Darby and Wilson, 2005). Cracks on concrete lining were repaired using acrylic gel injections.

Perfect annulus grouting was important because: voids left behind the segmental lining could cause excessive settlement; the segmental lining had to support the weight of the road deck; water pressure under operation Modes II and III could cause an expansion on the lining. To ensure that no voids were left behind the lining, the annular grouting was done by controlling pressure rather than volume. Annular grout was injected

through four annular grouting injection pipelines. The actual amount of grout intake was much higher than the theoretical value of 16 m^3 per one ring advance with 220-m wide annulus. Secondary grouting was applied to improve top-up grouting quality 15 m and 65 m behind the injection.

The segments used for the North and South Drives were identical. A total of 43,120 plus 5,390 key segments were needed to line the 9.7 km bore. High precision, small tolerance casting molds for 10 ring sets, or 90 segments and keys, were manufactured by CBE of France. The molds and test segments were surveyed according to the tolerance specification of ±0.3 mm before full production using the 3D scanner by VMT. To assure a continuous supply, the production of precast segments was split between two subcontractors, ACPI and Eastern Pretech. The segment reinforcement quantity was moderate (90 kg/m^3). Grade C50 concrete, water reduction admixture (Rheobuild 1000), and water/concrete ratio less than 0.4 were used to achieve early strength for demolding. The segments were cured under tarpaulin for 72 hours and in the yard for 28 days. The weight of a standard segment was 10.3 tons.

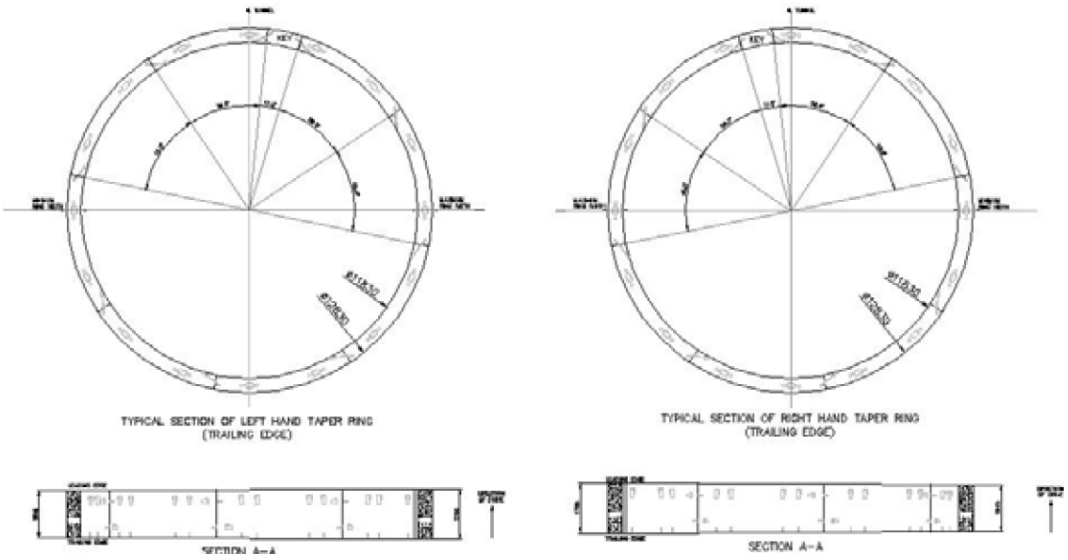

Figure 2.15 Composition of the segment lining (after Klados and Parks, 2005)

2.2.12. Road deck construction

The total length of the highway section is 2.6 km and lies between the NJB and SJB. Both the North and South Drives were excavated from the NVS. The length of the highway section is 0.74 km in the North Drive (from NVS to NJB) and 1.9 km in the South Drive (from NVS to SJB). The north section road deck construction had begun after the North Drive TBM broke through into the NJB in Dec 2004. On the other hand, because of the longer road section and tight schedule, the road deck construction for the south section started right behind the trailing of the TBM. The 1.9 km South Drive road deck was constructed concurrently with the tunnel excavation.

The road deck was designed to withstand up-lift pressure of a maximum of 2 bars in Mode II and imposed traffic load of 10 kN/m^2, and at the same time, the geometry of the tunnel cross section was designed to provide maximum flow rate. To have maximum flow rate through the permanent invert channel, any structure that might

impede the flow was not allowed in the permanent invert channel, and the side wall and lower road deck were constructed at the same time, as a single unit, by pouring concrete at one time for a designated length. 7.5-m long panels were used to build one form for haunch panels at both side walls of the tunnel, and 6.55-m wide, 1.7-m long, 100-mm thick precast panels were used for the main span of road deck. The thickness of the lower and upper road decks are 600 mm and 550 mm, respectively. The road deck panels are tapered by 21 mm on both edges to negotiate the 250 m radius curves without the need of packing.

The road deck was constructed in the following order. The starter bars, which tie the road deck to the tunnel lining, were installed. After that, sets of formworks, precast elements and base panels, and rebar were assembled and adjusted to the tunnel alignment and road camber. In the North Drive, the cast length per one pour was 22.5 m (three 7.5-m long panels), while it was 37.5 m (five 7.5-m long panels) in the South Drive to meet the tight schedule requirements. No dowels or fixing between base panels were used. Concrete was poured for the lower deck first and next for the sidewall and upper deck. The upper deck and sidewall were cast at about 120 m behind the lower decks. After concreting, two days were given for curing before forms were struck and the new section was supported by temporary props for ten days.

To minimize leakage from the invert to the lower road deck, every construction joint and gap between segmental lining and road deck were sealed with a post injection grouting system capable of regrouting repeatedly through the same installed hose system. To minimize leakage through the circular joint between lining and the road deck side wall, sets of gaskets were installed behind the sidewall in the compressed zone.

The Precast road deck base panels are 6.55-m wide, 1.625-m long, and 100-mm thick. They were cast at Sunway Casting Factory. 100-mm thick base panels were then bound with 450-mm high lattices, which would become cast sections of 600-mm thick road deck. At either side of the precast panel, 1m rebar extensions secure the precast span element to the cast in situ haunch walls in tunnel. To negotiate the 250 m radius curve, both the leading and trailing edges of the panels were taped by 21 mm. To avoid applying extra load to the fresh road deck during construction, precast segments and other supplies were supplied via service trains in advance of deck construction, and concrete was pumped from the surface through a pipe.

2.2.13. Ramp, cross passage construction

Ingress/egress highway ramps where the road decks leave the tunnel alignment were constructed at the NJB and SJB by the cut-and-cover method. These Y-shaped junction boxes allow bifurcation of the highway section from the main tunnel and house large hydraulic flap gates. The 800-m long northern ramp is connected to two major arteries, Jalan Sultan Ismail and Jalan Tun Razak. At the southern end of the road deck, 1-km long cut-and-cover structure was constructed to connect the road section of the tunnel with the KL Seremban Highway, which is a 1.8-km long, four lane (2 lanes in each direction) highway constructed as a part of the SMART project. At the end of the KL Seremban Highway, a 16-lane toll booth plaza was constructed (8 lanes in each direction). Waterproofing of the cut-and-cover structure was achieved by injecting acrylic resin into the construction joints, after the construction, and by applying bentonite sheets on the outside of the structure, before backfilling.

For the highway section, nine cross passages, shown in Figure 2.16, were constructed to connect the two road decks at 250 m intervals. Excavation of cross passages started after precast lining construction was completed. One segment was broken out, and from there, excavation started using hydraulic fracturing and the drill-and-blast technique. Support of the excavated cavity was provided by wire mesh and dry-mix shotcrete. Before excavating the cross passage between the two road decks of the toll road section, curtain grouting was applied to the ground from the surface, well in advance of excavation as a preventative measure.

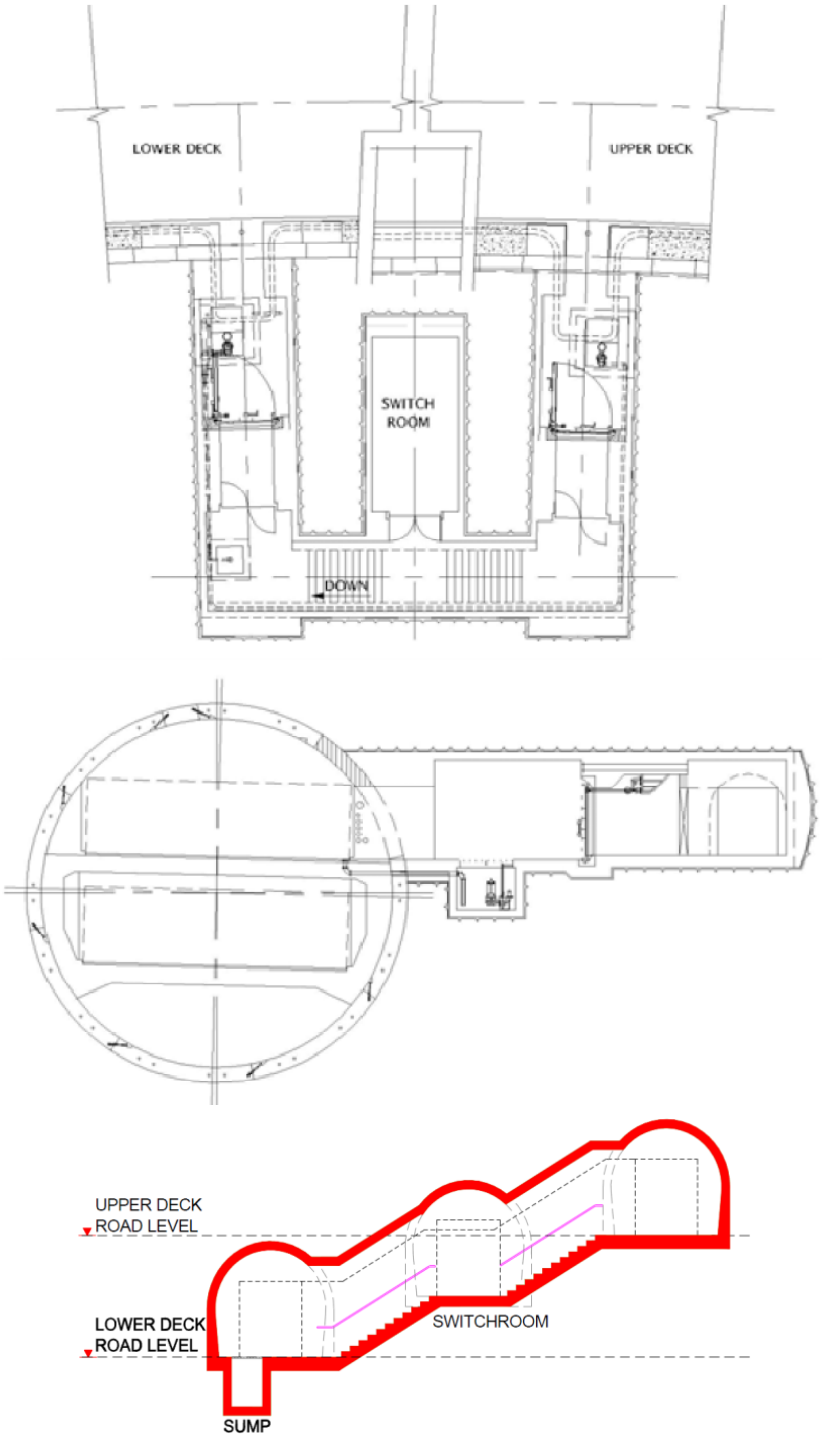

Figure 2.16 Cross passage (available from http://www.smarttunnel.com.my/construction/images/news/special/SR05.pdf)

2.2.14. Open cut work

In between the NJB and SJB, two ventilation shafts, the North and the South ventilation shafts, were constructed. The North Ventilation Shaft was a launch shaft. Therefore, it was 140-m long, 35-m deep, and 25-m wide to accommodate the assembly and operation of two machines and their backups. Later it was backfilled except for the ventilation shaft. The South Ventilation Shaft is a 35-m deep, 35-m long, and 18-m wide structure, which was excavated and backfilled ahead of the TBM's approach. Excavation of the vertical shaft was mainly carried out using drill-and-blast and hydraulic breakers. Since the limestone was relatively competent, the ground was supported by 50 mm of shotcrete, wire mesh, and pattern bolting. Even though contiguous bore pile walls, ground anchors, and extensive jet grouting and sealing supported the ground, settlement of all buildings and structures close to the excavation was monitored. Curtain grouting was installed for the shafts to prevent extensive ingress of water.

The TBMs for the North and South Drives broke through into the North and South Junction boxes. The TBMs were then pushed to the starter wall for relaunch by sliding them on Teflon-rubber bearings of a steel cradle resting on concrete strip footings. Other than 500 mm diameter slurry pipes and the other supply line connected to the separation plant, back-up equipment, such as segment handling, grout supply, ventilation system, and crew access, were relocated to facilitate road deck and cross passage construction.

2.2.15. Ventilation and safety facilities

The four ventilation shafts located at NJB, NVS, SVS, and SJB are about 20m wide, 30-m long, and 42-m tall, of which 12 m is above ground and 30 m is below ground

(Figure 2.17). Each ventilation shaft provides emergency exit stairs and firefighters' lifts. A saccardo injection system was employed for tunnel ventilation for four ventilation shafts along the road section of the tunnel. Six fans were axially installed in each shaft, three of which inject fresh air and three for exhaust. All active components of the ventilation system are located above maximum water level or behind the flood doors. With the traffic-induced air flow, fans do not need to run continuously, rather they are automatically activated when sensors detect higher pollution level. In the event of a fire, the fans can be operated manually to supply fresh air in the direction of traffic flow and to pressurize the unfired deck to prevent smoke flow into the unfired road deck. To force smoke away from fire, each ventilation shaft is capable of supply 105 m^3/sec of fresh air at a speed of 20 m/sec at the nozzle in the direction of traffic flow.

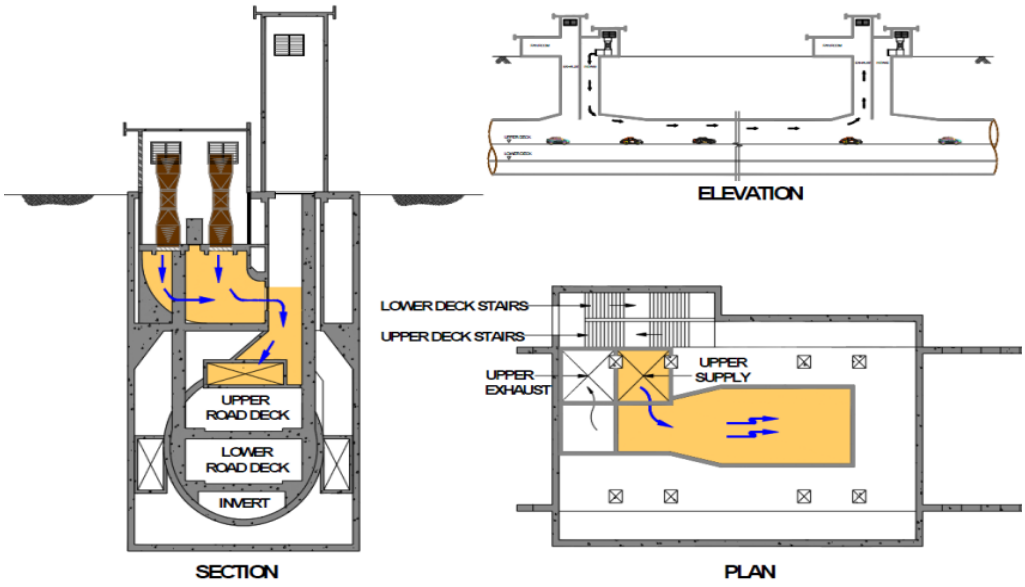

(a) Ventilation for upper deck

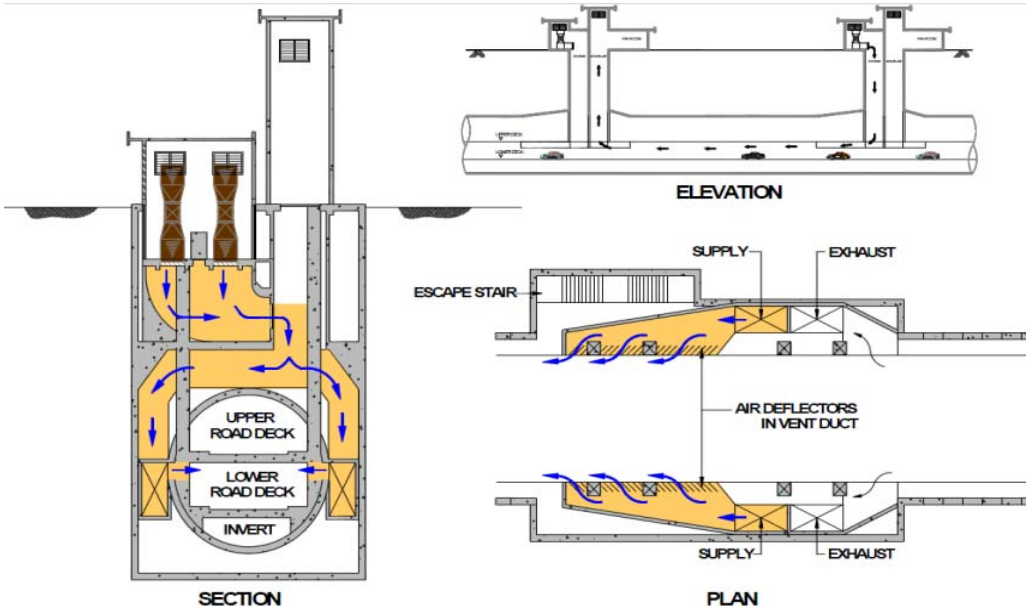

(b) Ventilation for lower deck (from http://www.smarttunnel.com.my/construction/images/news/special/SR05.pdf)

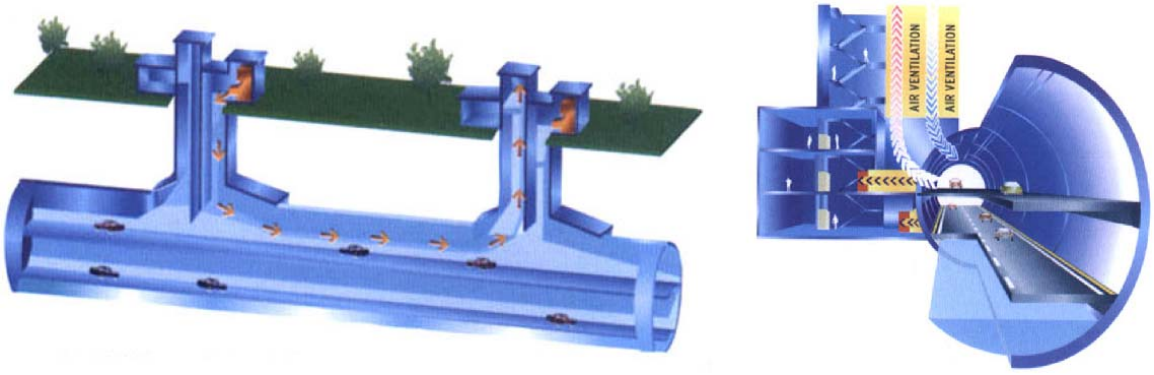

(c) Illustration of Saccardo ventilation system (Tunnels and Tunnelling International, 2005(05))

Figure 2.17 Ventilation system

With the aid of a failsafe operation scheme, the floodgates at the end of the road deck cannot be opened without closing the on and off ramp gates. Due to the height limitation of the road deck, fire engines and emergency vehicles were specially designed

and customized for accessibility into the road section. Emergency phones are provided at safe areas. FM radios and mobile phones can be used for both the safety and convenience of the users.

2.3. CASE HISTORY II: METRO LINEA 9 TUNNEL, BARCELONA

2.3.1. Planning and purpose of the tunnel

Barcelona, located on the north-east corner of the Iberian Peninsula, is the capital of Catalunya and the second largest city of Spain. For more than 80 years, Barcelona has had a big metro, tram, and bus network for the metropolitan area, together with suburban railways services. However, with the increase of the population and the expansion of the metropolitan area, the need for better transport options increased and, in 1997, the Metropolitan Transport Authority (ATM: Autoritat del Transport Metropolità) designed the Infrastructure Master Plan for Public Transport 2001-2010. The plan involved several projects such as improving the transit network, expansion of existing lines, installing lifts in every station for disabled people, and replacing old rolling stock, etc. Among these, the most expensive project was building a new metro line, L9 to connect the Barcelona Airport and the industrial area of Zona Franca with the northern part of Barcelona. Although Line 9 does not pass through the city center, it links all of the city's five metro lines and six railways very effectively. When completed, the Barcelona Metro will be one and a half times its current length. The expected traffic through Line 9 is about 90 million trips a year.

Initially, proposed in 1999, Line 9 was planned to be a 41 km line (34 km of which would be in a tunnel) with 43 stations and required an investment of USD 1.6 billion. However, the plan has been revised several times and, currently, has a 43-km

long section and 53 stations (Figure 2.18). The construction of a deep tunnel was necessary since it passes under all the other shallow metro networks of the city and connects all the existing metros in Barcelona. Because two thirds of the route passes beneath the heavily populated area, an innovative shaft station was proposed to minimize the impact on the surface and consumption of surface area.

Line 9 is a good complement to the existing metro network, acting as a mesh that links all other metros and railway systems in Barcelona. Active development is expected for the Zona Franca area, which is an industrial zone situated in the southwest part of Barcelona. Currently, about 60% of those working in Zona Franca travel by private car, and as a result, a quarter of the surface area of Zona Franca is used as a parking space. With the completion of L9, and the reduced need for private transport, the road will be less congested and a parking section can be redeveloped to create new space for industry.

Critics emphasize that from the airport end, L9 does not offer the best mode of transport, because it does not directly connect with the city center, whereas the bus and train do. Additional concerns have been raised about the deep alignment and stations of L9. The depth of the station increases the access time and reduces the safety in case of emergency. Some stations are located 70 m beneath the surface, and people may prefer using alternative transport modes, especially when their travel distance is not as long. Furthermore, the deep alignment adversely affects construction costs, so the project has become extremely expensive. Because Barcelona is not the capital of Spain, it does not receive the same financing for construction of infrastructures from the Spanish Government as Madrid. The total investment in this long, deep metro line has been

about 2.4 billion Euros. Some of the financing has come from the European Union Fund that supports construction of mass transport systems serving airports.

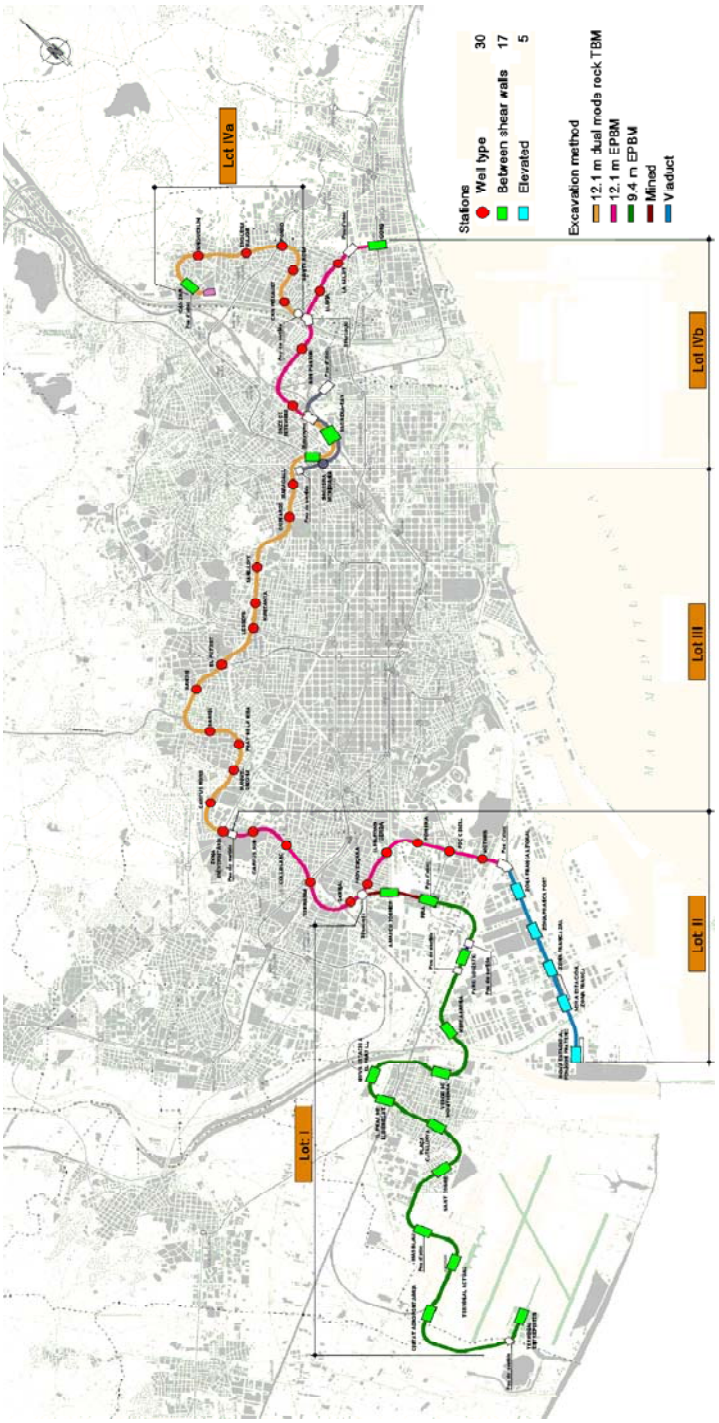

Figure 2.18 Route of the Barcelona Metro line 9

2.3.2. Project participant

The major participants in the project are summarized in Table 2.7.

Table 2.7 List of major participants

Participant	Role and responsibility
Catalunya Regional Government	Owner
GISA (Gestió d'Infraestructures S.A)	The project client: the construction agency for the Catalunya Government
ATM (Autoritat del Transport Metropolità)	Planning and evalution
TMB (Transports Metropolitans de Barcelona)	Metro operation and maintenance
Paymacotas S.A.U.	Consulting and engineering supervision
UTE Aeroport JV	Construction of Section I (Joint Venture leaded by FCC and composed by OHL, Ferrovial – Agroman, Scrynser y Copisa)
Gorg JV	Construction of Section II and IVb (Joint Venture leaded by Dragados and composed by Nesco, Comsa, ACS and Sorigué)
Línea 9 JV	Construction of Section III and IVa (Joint Venture led by FCC and composed by Copcisa, OHL, Ferrovial – Agroman y Copisa)

2.3.3. Alignment

Line 9 is 42.6-km long from north to south and connects all existing metro lines and railways at fifteen stations. As shown in Fig 2.20, at both ends of the line it bifurcates into two different branches. At the northern end, the line splits towards Santa Coloma de Gramanet and towards Badalona. At the southern end, the line splits towards the industrial area of Zona Franca and the Aeroport de Barcelona. The corridor of Line 9 includes 34 km of tunnel, and underground construction has been divided into

five sections (Table 2.8) based on the geological conditions to allocate proper excavation equipment. The geological conditions of the Line 9 site are summarized in Section 2.3.4. Herrenknecht EPB shield machines were employed for Sections I, II, and IVb, and a NFM-Wirth dual-mode rock TBM was employed for Sections III and IVa. The section, including five stations from the Zona Franca Litoral Station to the Nova Estacio al Poligon Pratenc Station, is designed as an elevated structure. The section, including thirteen stations from Amadeu Torner to Terminal Enterprise, is designed as an 8.32 m ID tunnel, and the remaining sections, a total of 30 stations, are incorporated in a 10.9 m ID tunnel. The tunnel is deep because it crosses all other existing metro lines. The depth of the tunnel reaches as far as 25 m to 90 m under the densely populated city area (Sections II, III, IVa and IVb), in order to avoid disturbing the existing metro tunnel and other underground structures. On the other hand, in Section I, where the tunnel corridor passes under relatively less densely developed areas, the tunnel depth at the crown is about 15 m. The alignment has 280 m of a tight radius curve and a maximum slope of 4%.

Table 2.8 Sections of Line 9

Section	Stations	Machine	Structure	Contractor	Geology	Length
I	Airport ~ Amadeu Torner	Herrenknecht	Tunnel (9.4 m OD, 8.3 m ID)	UTE Aeroport JV	Soil	15 km 9.8km
II	Zona Franca ~ Zona Universitària	Herrenknecht	Tunnel (12.06 m OD, 10.9 m ID)	Gorg JV	Soil	12.3km
III	Zona Universitària ~ Sagrera TAV	NFM-Wirth	Tunnel (11.9 m OD, 10.9 m ID)	Línea 9 JV	Hard rock /soil	9.4km
IVa	Can Peixauet ~ Can Zam	NFM-Wirth	Tunnel (11.9 m OD, 10.9 m ID)	Línea 9 JV	Hard rock/soil	4.3Km
IVb	Sagrera TAV ~ Gorg	Herrenknecht	Tunnel (12.06 m OD, 10.9 m ID)	Gorg JV	Soil	5.0Km

2.3.4. Geology

Barcelona lies on the so-called Barcelona Plain that extends from the Collserola range in the northwest to the Mediterranean Sea in the southeast. It has two rivers, Besòs and Llobregat, in the northeast and southwest, respectively, where fluvial deltaic deposits are formed. The Barcelona area is composed of a Paleozoic crystalline bedrock underlying a Quaternary series of alluvial deposit. The Paleozoic crystalline bedrock is composed of slates, limestone, slightly metamorphosed micro-conglomerates, and intruded batholitic granodiorite. These rocks are highly weathered when they are close to the surface. The thickness of highly weathered rock, which behaves like a sandy cohesionless soil, varies from a few meters to almost 40 m. The Line 9 tunnel depth varies from 15 m to 60 m and most of the tunnel was built beneath the ground water table. Although the bedrock was considered impermeable, a highly fractured and weathered zone exists, and the maximum ground pressure on the tunnel crown reaches about 2.5 bar. Once the alignment was determined, a detailed geological study of the deep subsurface condition was carried out and extensive, long core recovery drillings were executed. The alignment was divided into five sections according to the ground conditions: Sections I, II, III, IVa and IVb. Detailed geological descriptions for each section are provided below.

- Section I: The tunnel runs in the alluvial Quaternary deposits consisting of silty sands with some portions of sandy silts, silts, and silty clays. In this section the tunnel runs beneath the Holocene deposits of the Llobregat River. The groundwater level is located 5m below surface, on average.
- Section II: In the southern part, the tunnel runs through the Llobregat deltaic deposit, and, as it goes to north, it enters into the Quaternary deposit consisting of silt and clay overlaying Miocene breccias.

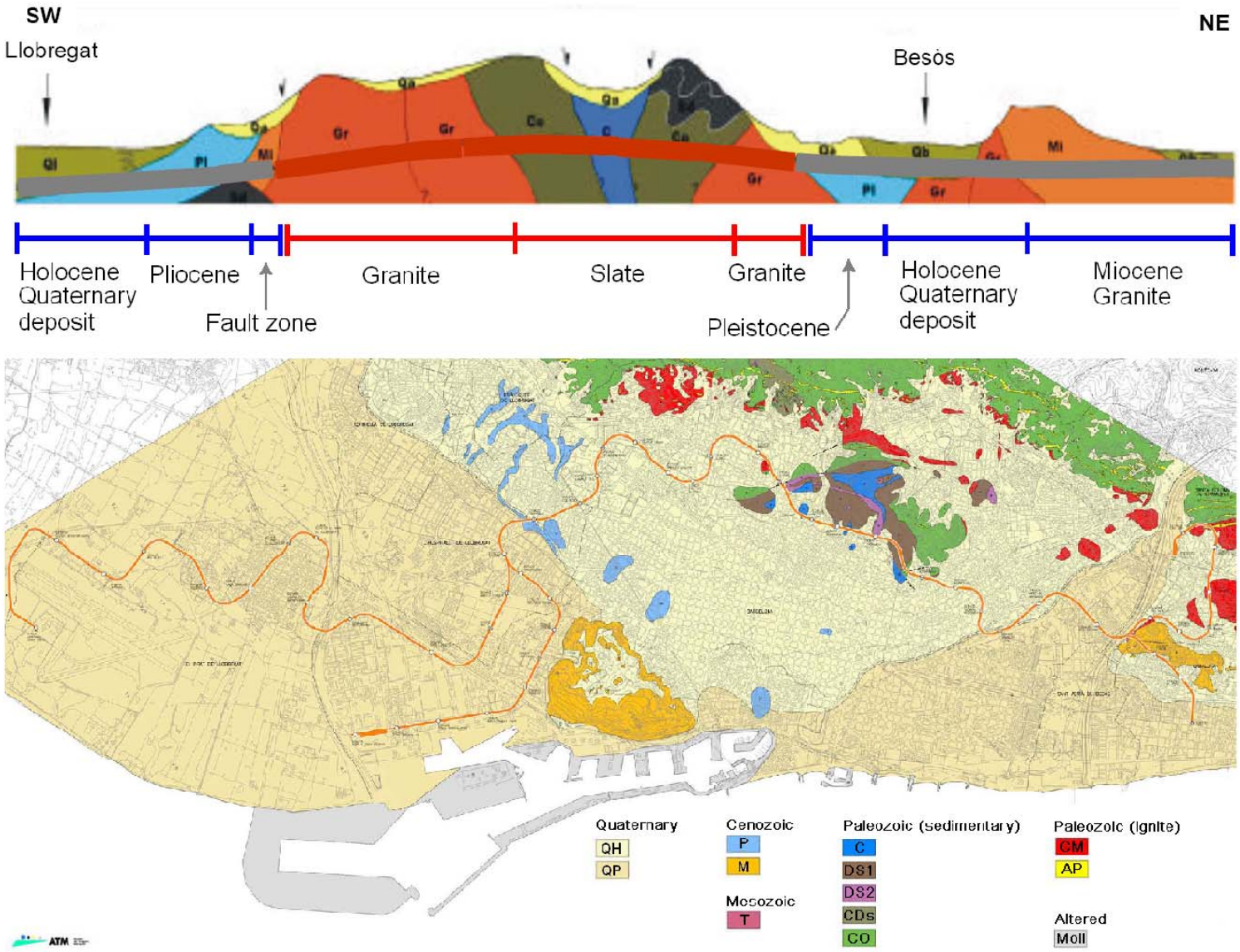

Figure 2.19 Geology of project site

- Section III: Mixed ground conditions exist in this section. They range from hard rock to severely weathered rock and soft soil. Due to its numerous fault zones and rock/soil transition zone, a dual-mode TBM was employed.
- Section IVa: Mixed ground conditions were observed here. The ground is mainly composed of Miocenic conglomerate, fresh granite (UCS value of 150-250 MPa), severely weathered granite, and hornfels.
- Section IVb: The ground near Sagrera Station is an alluvial plain of the Besòs River that shows similar characteristics to that of the Llobregat. The north of Llefia Station is composed of Miocenic conglomerate.

2.3.5. Configuration of tunnel cross section

The underground corridor of Line 9 consists of two types of structures:

- Double deck configuration in a single bore tunnel with 12.1 m OD and 10.9 m ID (Figure 2.20 and Figure 2.21)
- Twin track in a single bore tunnel with 9.4 m OD and 8.31 m ID tunnel (Figure 2.22)

The most notable aspect of Line 9 comes from the double deck in a single bore scheme. Its typical cross section consists of stacked tracks, as shown in Figure 2.20 and Figure 2.21. Owing to the large diameter (10.9 m ID) of the tunnel, two tracks could be superimposed using the tunnel's double-deck configuration. A concrete slab constructed close to the springline divides the tunnel into upper and lower decks. Both sides of slab are connected by a two-way cross passage in order to allow evacuation in case of emergency. In addition, this configuration allows the integration of platforms in the tunnel section without excavating huge caverns. The track runs at the center of each deck between the stations, but as the tracks become close to a station, the position of the

tracks is pushed close to the sidewall, making space for a platform at the upper and lower decks. Figure 2.22 shows a track in Section I where a relatively shallow and small diameter single bore tunnel was built in a less populated area.

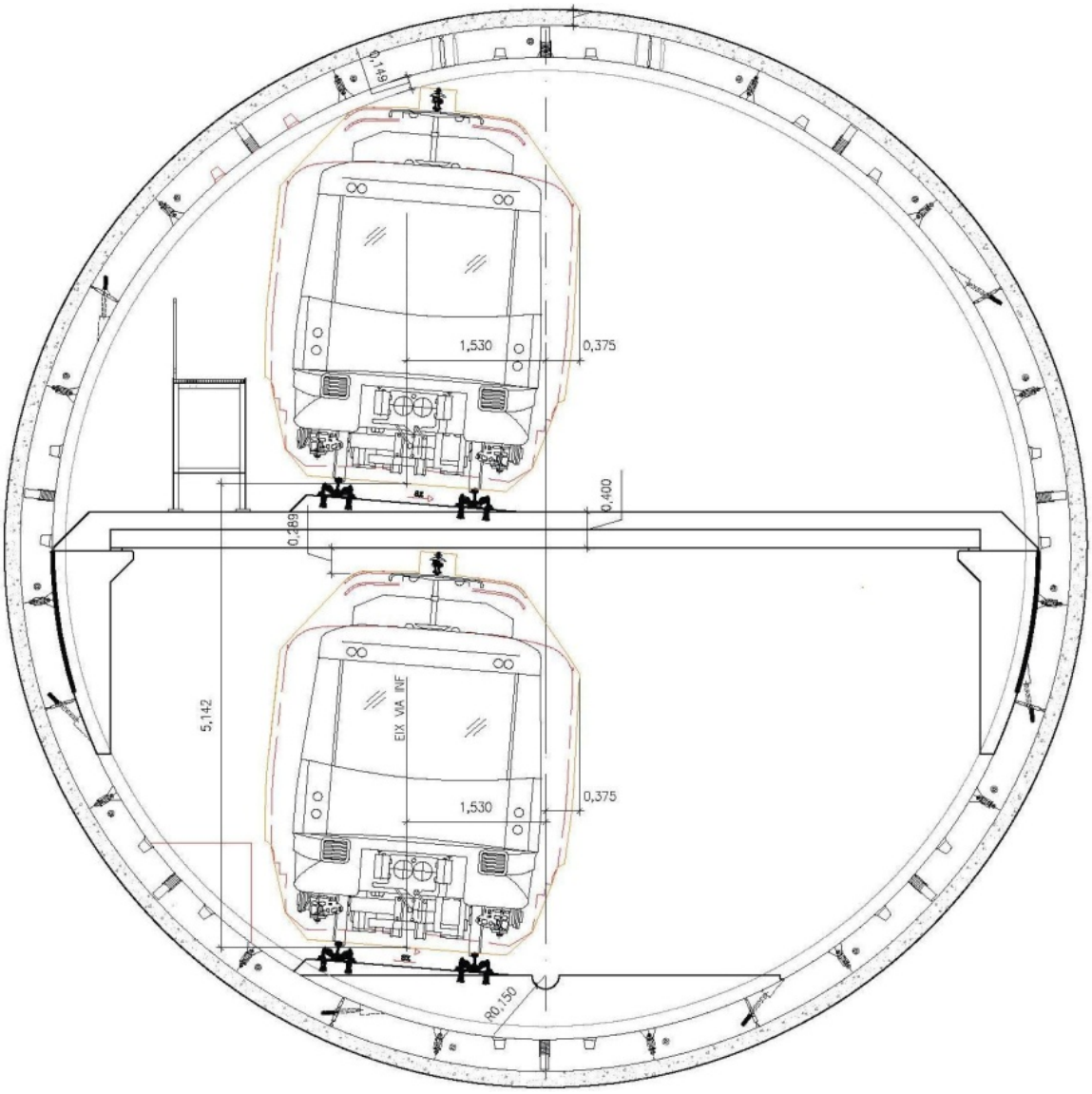

Figure 2.20 Cross section of double-deck tunnel with prefabricated horizontal slab

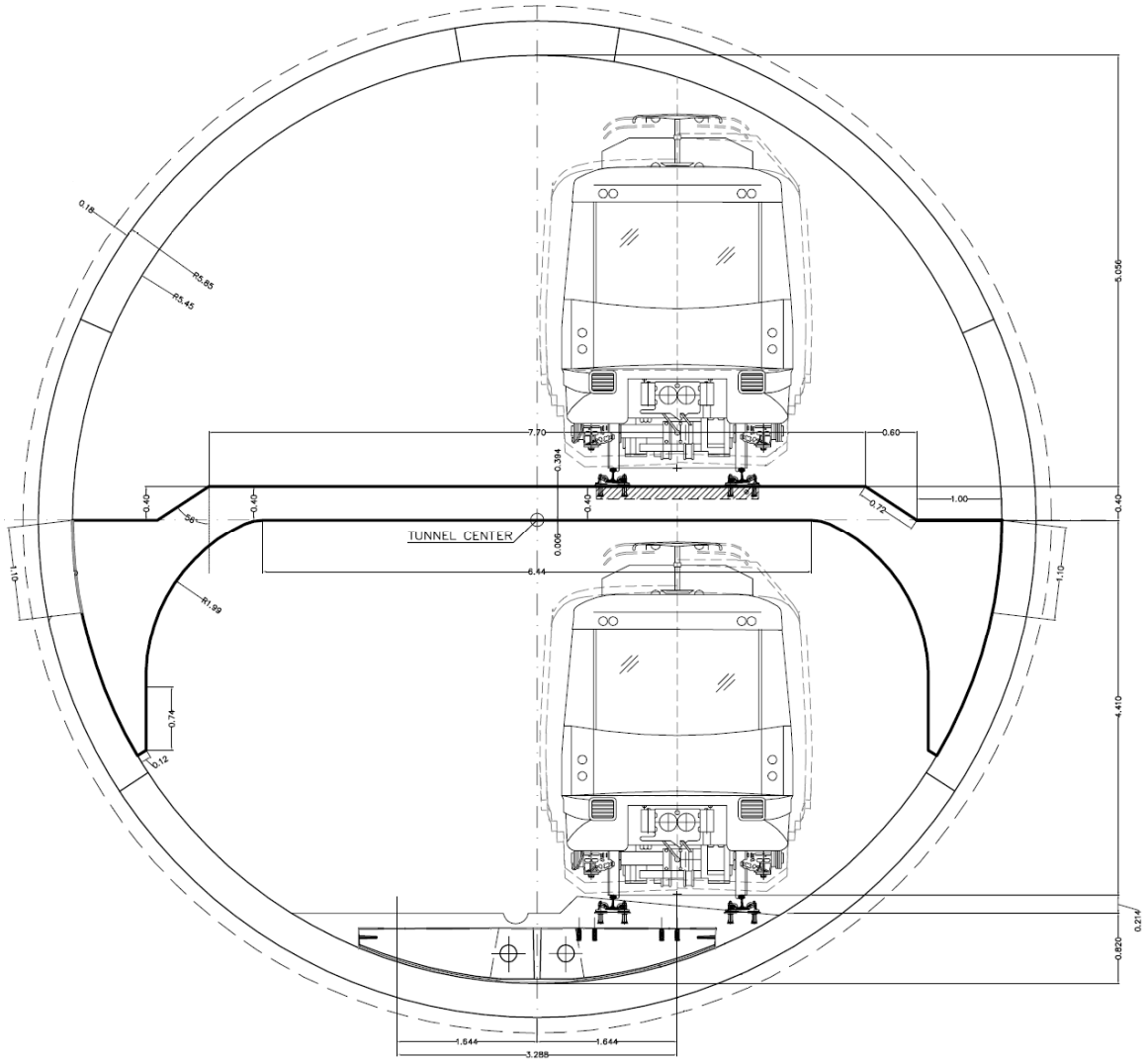

Figure 2.21 Cross section of double-deck tunnel with in situ horizontal slab

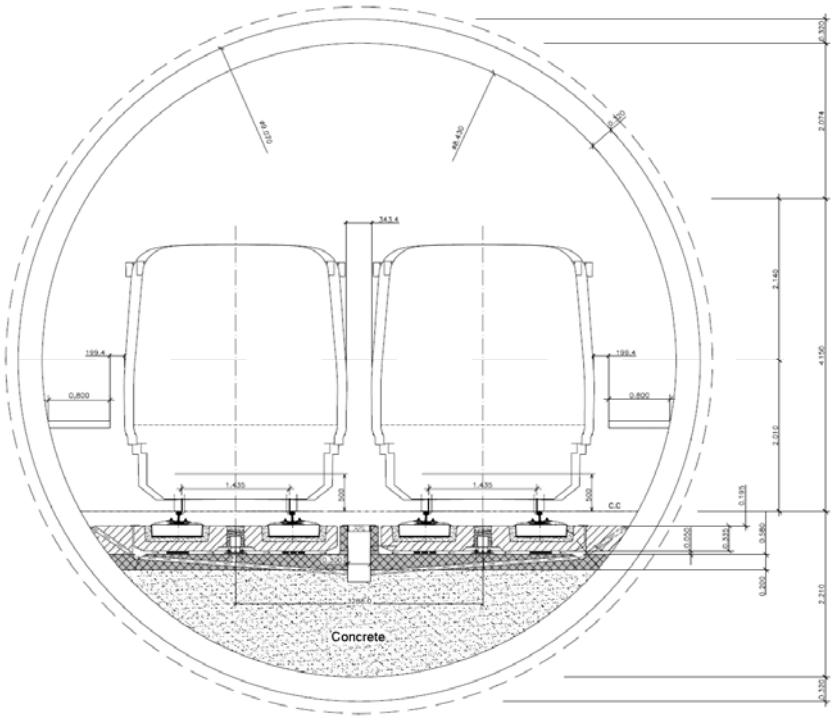

Figure 2.22 Cross section of twin track tunnel

2.3.6. Configuration of station

Line 9 has 47 underground stations: 30 well-type stations and 17 cut-and-cover stations between slurry walls. Stations were constructed using an open-cut method for twelve stations located in a shallow depth (15 m), under less populated areas, in Section I and for stations where large numbers of passengers are expected, such as Sagrera-TAV Station. Unlike these 17 stations, 30 stations in the remaining sections of Line 9 are located deep (25-90 m) under the metropolitan area, and, as a result, an unprecedented method was developed associated with a double-deck tunnel configuration. The densely urbanized city area has only limited capabilities to accommodate space for open-cut station construction without causing massive disturbance and cost. Therefore, it was decided to use a vertical shaft as a station whose internal diameter is 24 m. 30 well-type

vertical shaft stations were constructed for Sections II, III, IVa and IVb. The vertical shafts were excavated to the depth of tunnel alignment prior to the TBM excavation. The drill-and-blast method was used for the hard rock section and a slurry wall technique was used for the soft ground section. The station has two halls at the surface and at the platforms. Two halls are linked by elevators and an emergency stair case. The tunnel and the vertical shaft are connected at the center of the station. Figure 2.25 show the plan and transverse cross-sectional view of a well-type station. An opening 16-m long and 7-m high connects the platforms and the shaft. Upper and lower platforms are connected by emergency stairs that are installed at both ends. For passengers' safety, tracks are separated by a transparent screen door. Figure 2.26 shows the well-type station under construction. At the lower part of the picture, the access route to the platform is shown. Figure 2.27 captures the access route linking the tunnel and vertical shaft before the platform and deck are installed. In Figure 2.28, the transverse cross section of a cut-and-cover station is shown.

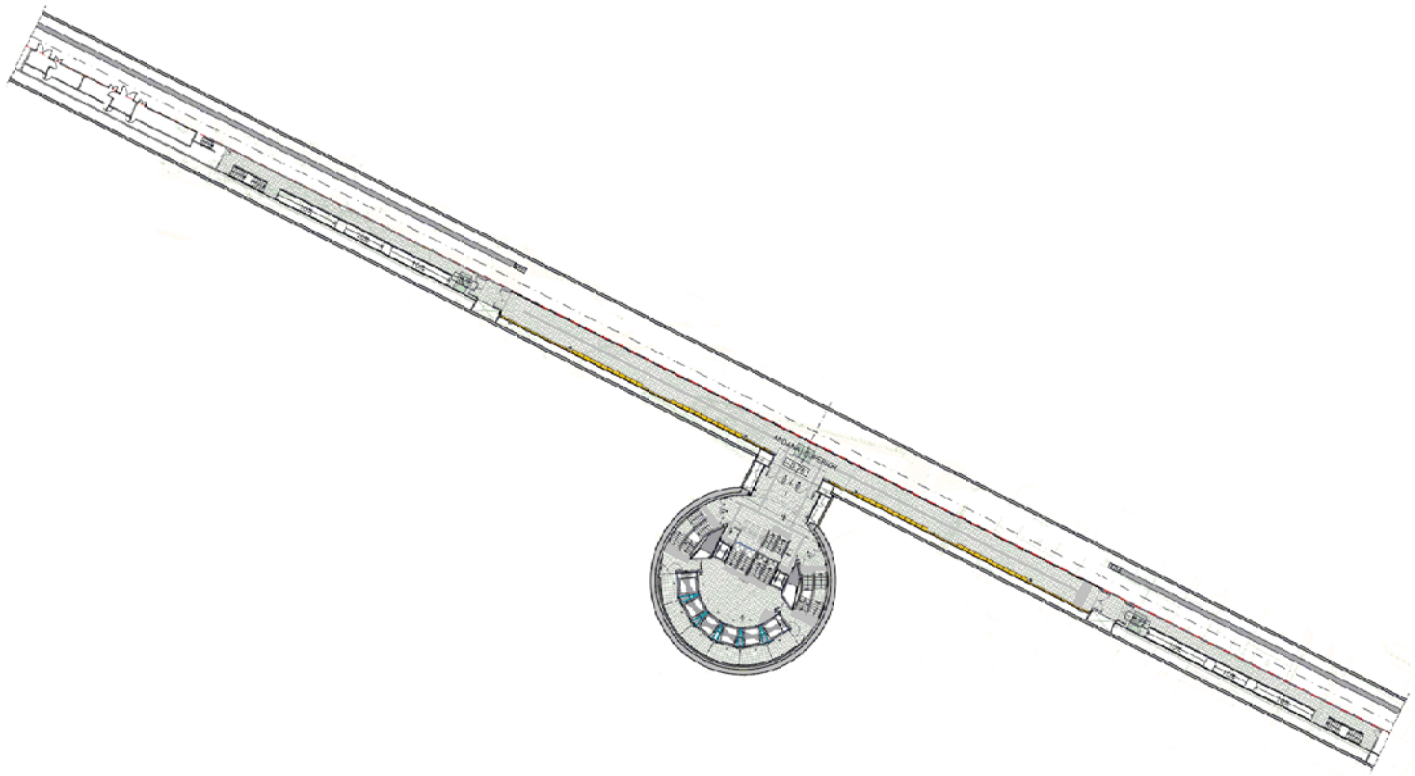

(a) plan view of well-type station and tunnel

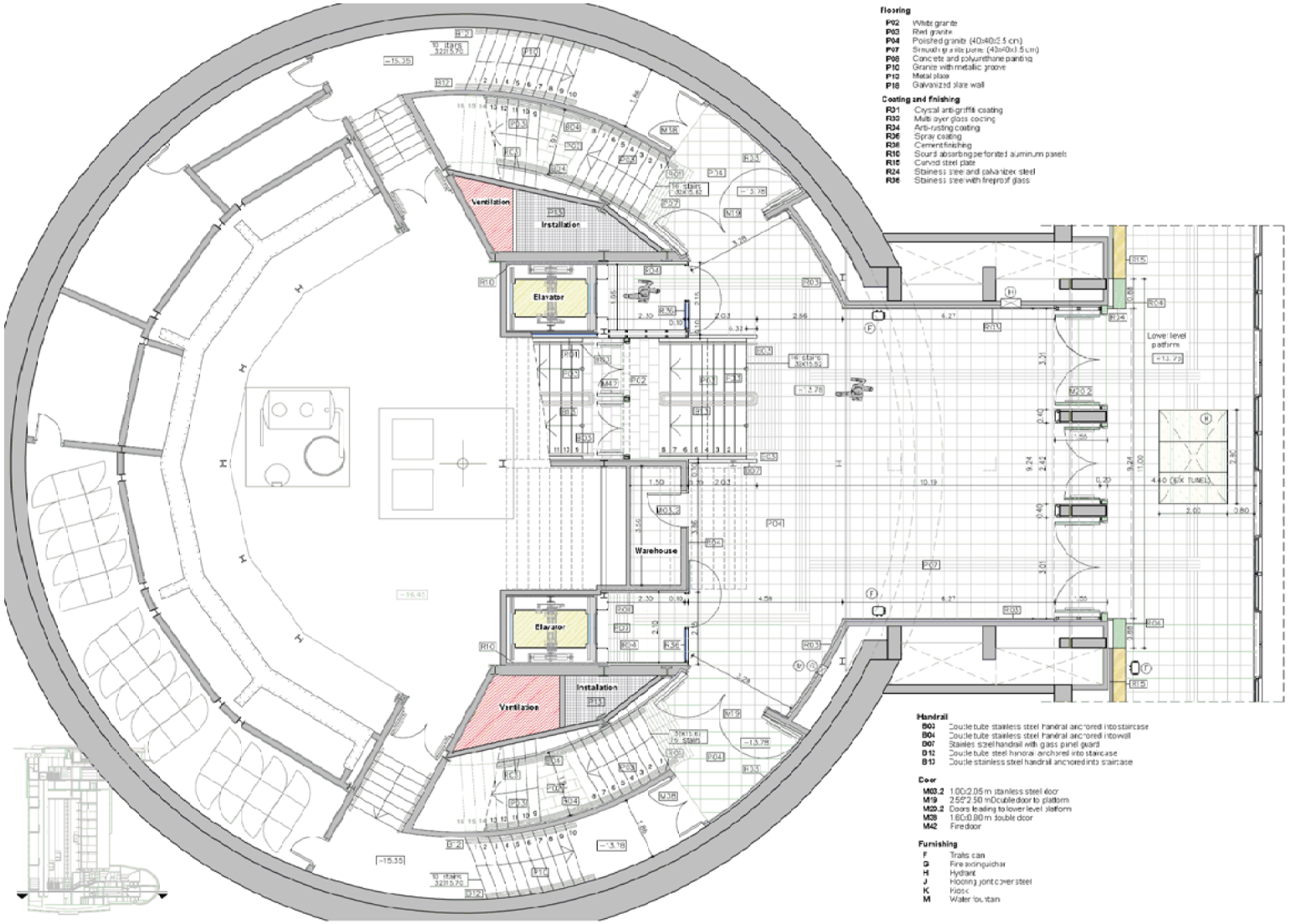

(b) Detailed planar drawing of well-type station at platform level

Figure 2.23 Plan view of well-type station

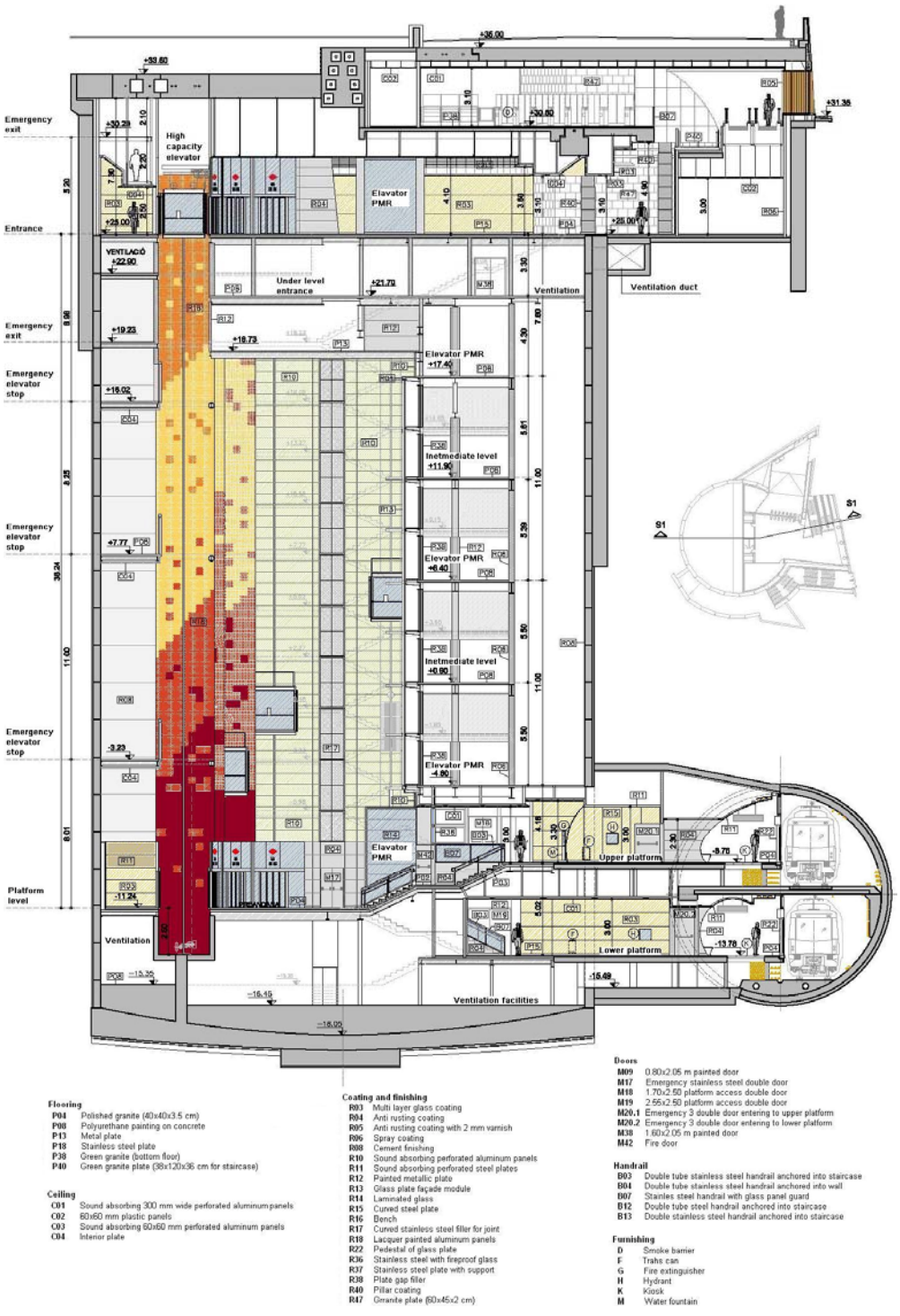

Figure 2.24 Transverse cross section perpendicular to tunnel axis

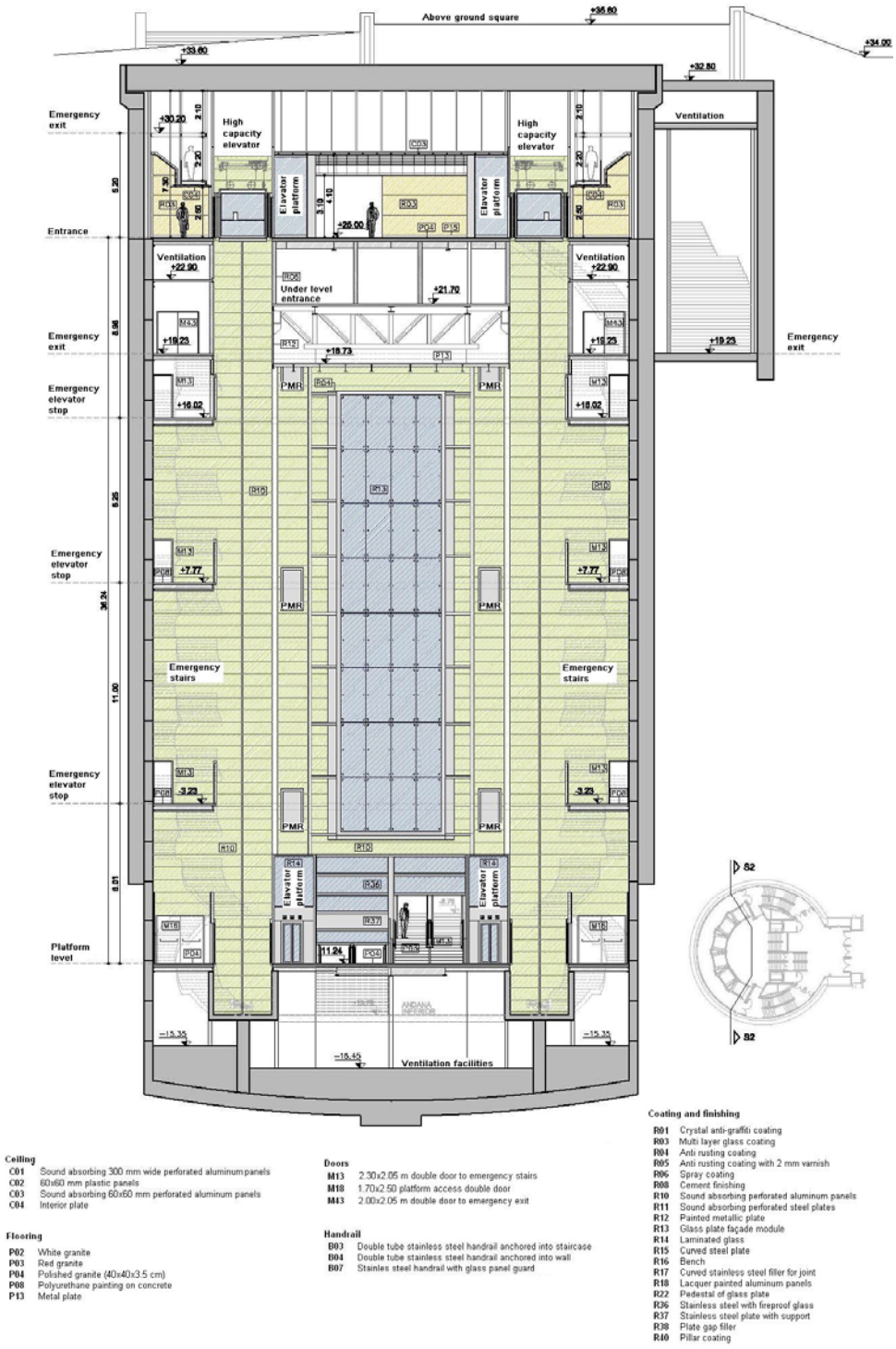

Figure 2.25 Transverse cross section parallel to tunnel

Figure 2.26 Photo taken at the bottom of well-type station

Figure 2.27 Photo of access route linking tunnel and station

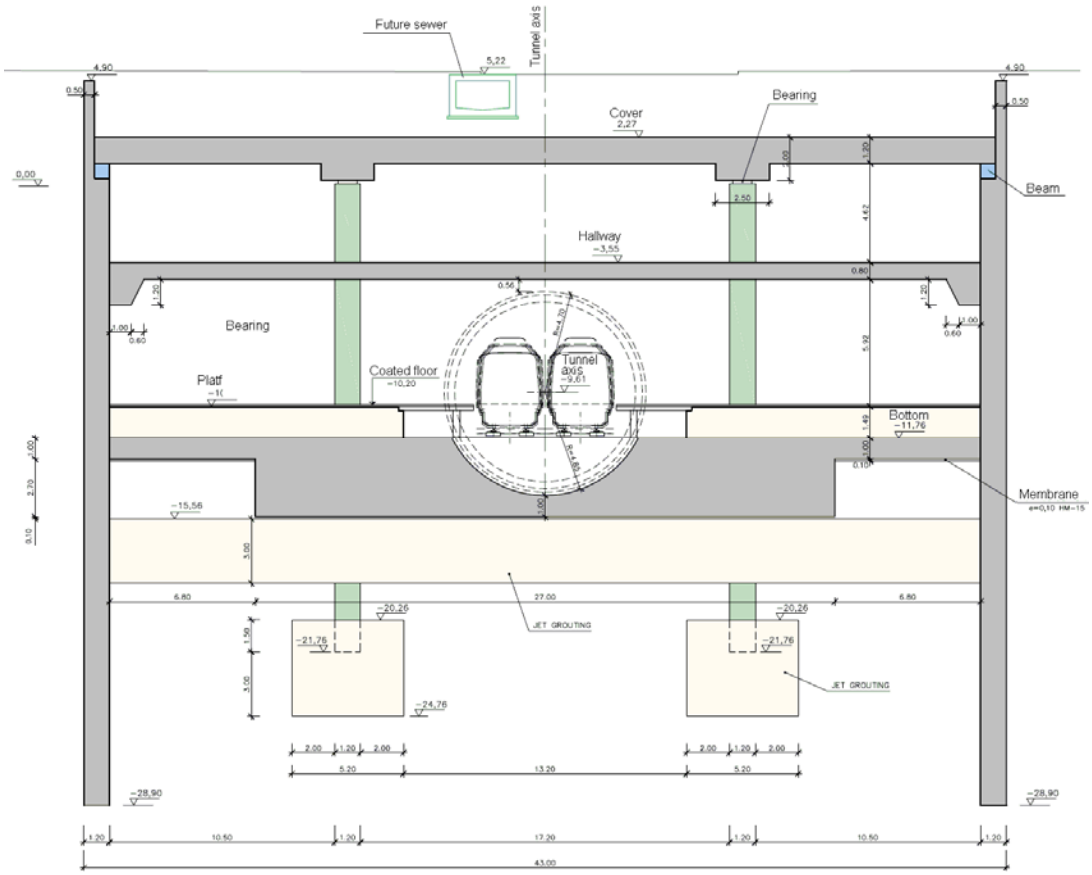

Figure 2.28 Side view of cut-and-cover station

2.3.7. TBMs and shafts

A double-deck tunnel with an integrated platform inevitably requires a large diameter bore, and the existence of other metros and underground structures in the metropolitan area led the tunnel alignment to the depth of 25 m to 90 m. Excavating the tunnel using the open-cut method was unthinkable for this depth and it was determined to excavate the entire tunnel corridor using TBMs. The excavation, initiated in June 2003 is expected to be completed by 2013-2014. As already discussed in Section 2.3.4, the suitable type of TBM was assigned for each section according to its predominant geological conditions. For the mostly rock sections, an 11.95 m diameter NFM-Wirth

dual-mode TBM was used, and for the mostly soft soil sections, a 12.06 m diameter and 9.4 m diameter Herrenknecht EPB shield machine was used.

2.3.7.1. NFM-Wirth dual-mode TBM

The high-thrust, high-torque NFM-Wirth dual-mode TBM (named Bessi) used for the mostly rock sections, Sections III and IVa, has an 11.9 m OD and erects a one-pass lining using 350 mm thick precast segments, leaving the 10.9 m ID bore. The cutterhead was equipped with 76 disc cutters with 14" and 17" diameters and scraper tools. The opening ratio of the cutterhead is 26%. Under stable geological conditions with no significant ground water inflow, the TBM is operated in an open mode, whereas it is operated in a closed mode under unstable and difficult ground conditions. The mode switching from the open mode to the closed mode is achieved by replacing the belt conveyor with a 1.2 m diameter screw conveyor to extract the spoil material from the chamber in a controlled manner. In order to allow the loading of spoil onto the belt conveyor, the cutterhead rotates clockwise, only. The maximum confinement pressure available in the plenum under the closed mode is 3 bar. Bentonite slurry was supplied to reduce material friction and to improve the ground flow through the cutting wheel opening. The TBM was featured with lateral hydraulic cylinders to prevent shield-roll. Detailed TBM parameters are shown in Table 2.9.

A problem that the dual-mode hard-rock TBM encountered was the segment stabilization immediately behind the tail shield. The amount of injected annular grout was 90 % of the theoretical volume between the excavation surface and the outer rim of lining, and the top-up grouting was carried out 8-12 m behind the shield for the tunnel shoulder. As a result, the grouting could not provide immediate external support to the

lining, and the ring showed a tendency to deform into elliptical shapes. The contractor solved this problem by adding a slump-reducing admixture. In addition, due to the decompression on the face of the excavation, spalling and rock fracturing took place and oversized blocks fell through the cutterhead openings. The contractor closed up the cutting wheel to solve this problem.

Figure 2.29 NEF-Wirth dual-mode TBM

Table 2.9 Specification of NFM-Wirth dual-mode TBM

Manufacturer	NFM-Wirth
Nominal diameter	11,950 mm
Segment ring (ID – thickness)	10,900 – 350 mm
Shield length	12,590 mm
Cutting wheel opening ratio	26%
Cutterhead RPM	0 – 3.7
Cutting wheel drive	Electric
Installed power	7,335 kW
Cutting wheel nominal torque	28,930 kNm
Cutting wheel exceptional torque	37,000 kNm
Thrust cylinders	30
Total nominal thrust	90,000 kN
Total exceptional thrust	110,000 KN
Minimum turning radius	200 m

2.3.7.2. Herrenknecht EPBM for Sections II, IVb

The 12.06 m OD Herrenknecht EPB shield machine was used to excavate the mostly soft soil sections, Sections II and IVb. It erected a one-pass lining using 400-mm thick precast segments, leaving a 10.9 m ID bore. The cutterhead was driven by 24 hydraulic motors that generate 38,000 kNm of torque, which is in the higher range for this kind of machine. It was used to deal with the stiff Miocene clay and consolidated clay matrix. The opening ratio of the cutterhead is 36%. Installation of 17" disc cutters was possible when needed to excavate rock sections. The maximum available pressure was 4 bar of dynamic pressure and 6 bar of static pressure. To facilitate the smooth progression of the shield, the shield had a conical shape with 30 mm diameter reduction in the tail and over 12,600 mm shield length. Annular grouting was done by bentonite slurry and fine sand mix with other additives and injected through 10 holes at the middle and back of the tail shield. The amount of injected annular grout was 90% of the theoretical volume loss between the excavation perimeter and the outer rim of the segmental lining. Detailed EPBM parameters are shown in Table 2.10.

The 11.9 m diameter NFM-Wirth TBM used by the Linea 9 JV started its excavation in June 2003, through the hard-rock mixed-ground section from the Can Zam Station to just past the Can Peixauet Station (Section IVa, Figure 2.18). Then, it was disassembled and transported to Zona Universitaria Station (Figure 2.18). Once it was reassembled, it excavated through the hard-rock mixed-ground section until it reached the Sagrera TAV Station (Section III). The 12.06 m diameter Herrenknecht EPBM used by the Gorg JV started its excavation in August 2003, from Gorg Station to Segrera TAV Station (Section IVb, Figure 2.18). Then it was disassembled and transported to Zona Franca Station. Once it was reassembled, it excavated through the soft-ground section

until it reached Zona University (Section II, Figure 2.18). The 9.4 m Herrenknecht EPBM used by the UTE Aeroport JV started its excavation in May 2006, from the Fira Station to the Terminal Entrepistes Station (Section I, Figure 2.18). It broke through into the reception shaft near the Terminal Entrepistes Station.

A problem that the EPBM encountered was the very low water content of the clay matrix. The natural water content was between 2% and 4% and the plastic limit was about 15%. This dry and hard material generated very high cutting wheel torque and the spoils could not be extracted by the screw from the plenum. It required large quantities of water, 25-45 m^3 per ring advance. Abrasive wear was severe due to the existence of gravel in the clay matrix and the scrapers and their fixing bolts were damaged due to the impact. Several tool changes under hyperbaric conditions were required. This problem was solved by changing the geometry of the scraper and by increasing the diameter of the bolt.

Figure 2.30 Herrenknecht EPBM for Section II and IVb

Table 2.10 Specification of Herrenknecht EPBM for Sections II and IVb

Model no.	Herrenknecht S-221
Nominal diameter	12,060 mm
Segment ring ID and thickness	10,900-mm ID and 400-mm thick
Shield length	12,600 mm
Cutting wheel opening ratio	33%
RPM	0 – 2.6
Cutting wheel drive	Hydraulic (4,000 kW)
Installed power	5,320 kW
Cutting wheel nominal torque	38,000 kNm
Cutting wheel exceptional torque	45,626 kNm
Thrust cylinders	38
Total nominal thrust	110,000 kN
Total exceptional thrust	138,000 kN
maximum EPB pressure MPa	Max. 6 bar
Minimum turning radius	200 m

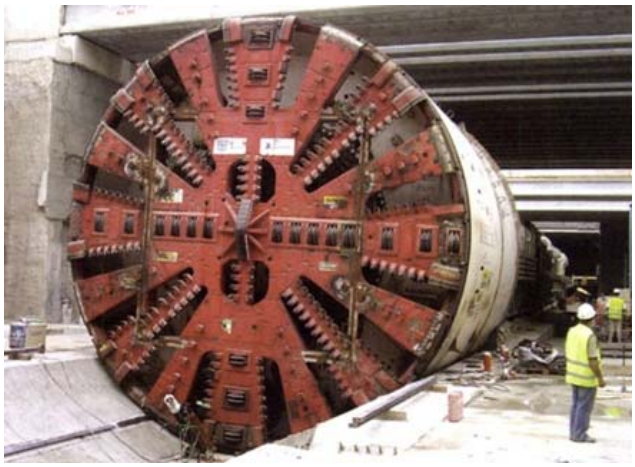

Figure 2.31 Herrenknecht EPBM for Section I
(from Tunnels and Tunnelling International, 2007(05))

Table 2.11 Specification of Herrenknecht EPBM for Section I

Model no.	Herrenknecht S-461
Nominal diameter	9,370 mm
Inner diameter	8.4 m
Cutting wheel drive	3,600 kW
Cutting wheel nominal torque	22,617 kNm

To prevent any surface disturbances, settlement monitoring was carried out using various techniques throughout the tunnel alignment. The techniques used for Line 9 include classic manual leveling, real time monitoring of adjacent buildings and structures, borehole monitoring using piezometers and inclinometers, and satellite monitoring. The satellite monitoring system identified 180,000 reflective points over the area of 160 km^2 and the track settlement of predetermined points.

2.3.7.3. Well-stations

The well-type station is constructed in a vertical shaft. The diameter of the vertical shaft is typically 24 m OD (Figure 2.23), but differs from station to station according to the depth of the tunnel and geological and geographical conditions. The vertical shafts were constructed prior to the passage of the TBM. The circular diaphragm walls were constructed down to the design level and the ground between the walls was partially excavated to slightly above the tunnel crown to provide even pressure on the face of the TBM. The area corresponding to the opening that connects the platforms and the shaft remained un-reinforced. When the TBM touches this area, it continues to bore through it. An elliptical hole was created on the intersection between the diaphragm wall and the tunnel is supported by the segmental linings. Procedures for excavating the remaining ground at the bottom of the shaft, completing the connection by

removing the segments and constructing the stations follow, successively. The typical size of the opening for the station is 16-m long and 7-m high (Figure 2.27).

2.3.8. Installation of precast segment lining and horizontal slab

A one-pass lining scheme using a universal ring is employed. The composition and thickness of the ring differs from section to section and is summarized in Table 2.12. One ring is made up of six or seven segments and a key block (6+1 or 7+1) and is tapered at both sides. Details are shown in Figure 2.32 and Figure 2.33. A key segment is in trapezoidal shape at both sides and the adjacent two segments are also in trapezoidal shapes, but inclined at one side only. The slant at the sides was given in the radial direction as well as the longitudinal direction to prevent damage due to friction between segments (Figure 2.33). For a straight section, the key segment was alternatively placed at top and bottom. Precast concrete segments are reinforced by rebars and steel fibers to increase load bearing capacity and to reduce longitudinal crack development. Supplied by Maccaferri, 45 kg of steel fibers are added per 1 m^3 of concrete batch. Segments feature EPDM gaskets for watertightness.

Table 2.12 Composition and dimension of universal lining

Section	Machine	Reinforcement	Composition	Thickness	Length
I	9.4 m OD EPBM	No data	6+1	320 mm	1.5 m
II, IVb	12.1 m OD EPBM	Rebar and steel fiber	6+1	400 mm	1.8 m
III, IVa	11.9 m OD Rock TBM	Rebar and steel fiber	7+1	350 mm	1.8 m

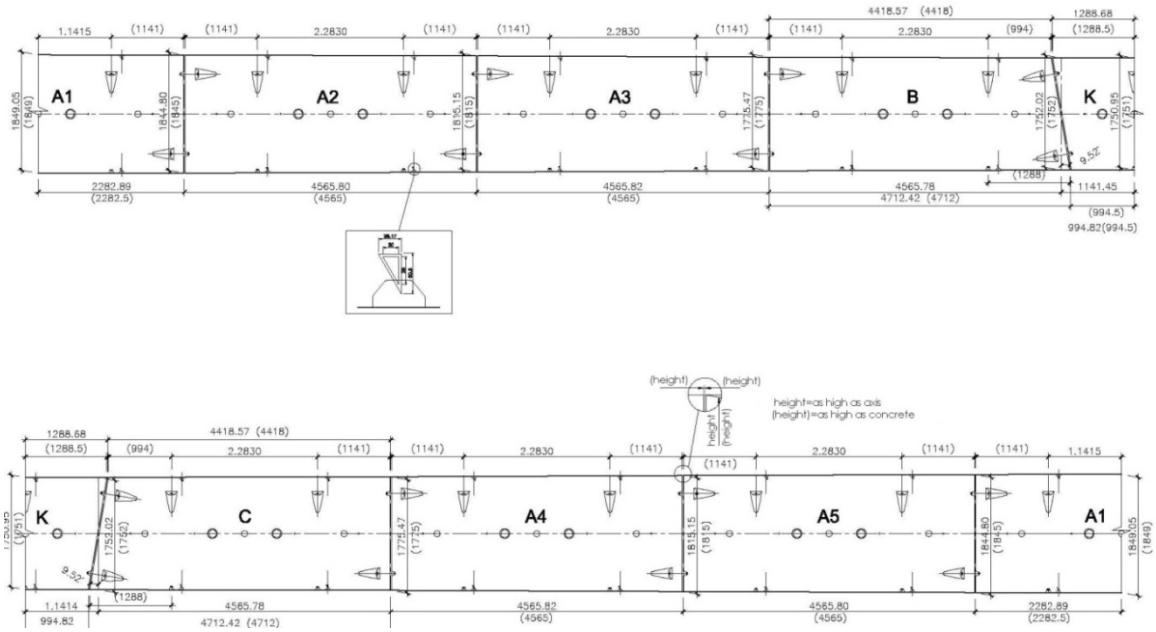

Figure 2.32 Ring details (drawn based on dimensions of intrados)

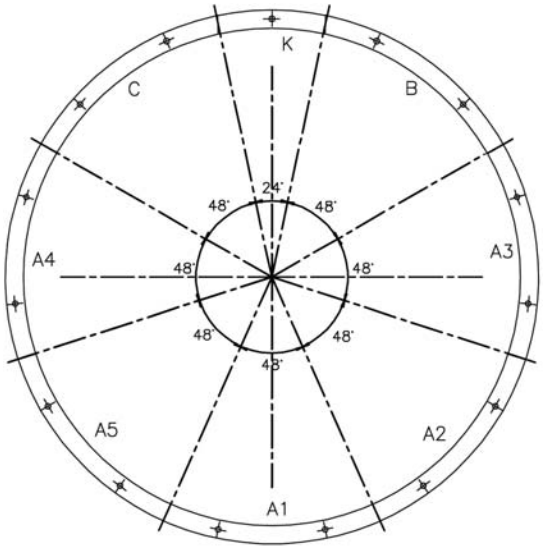

(a) Segment composition and numbering

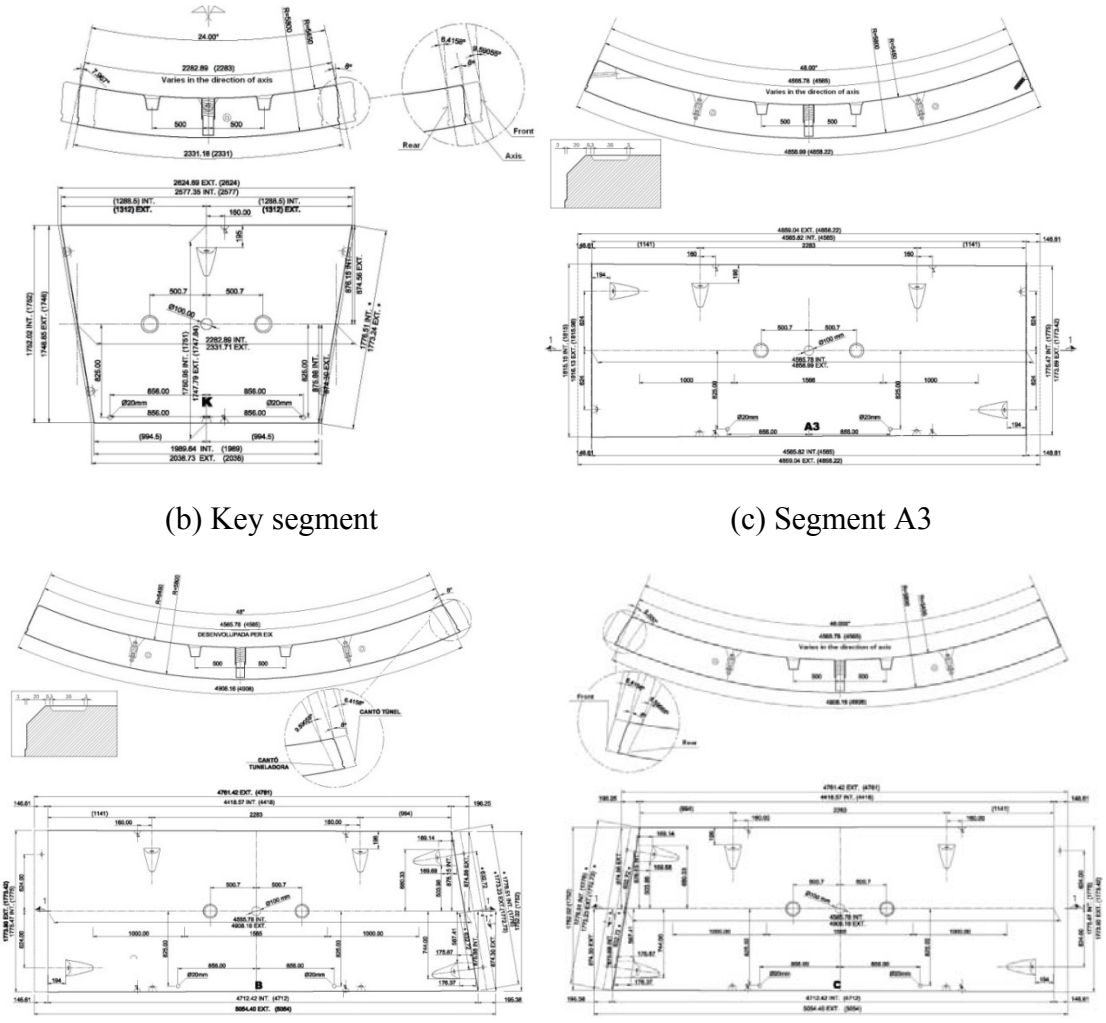

(b) Key segment

(c) Segment A3

(d) Segment B

(e) Segment C

Figure 2.33 Segment lining

The construction of the horizontal slab was done either by the cast-in-situ method or by assembling prefabricated elements. The selection of the horizontal-slab-construction method is made according to the contractors' available personnel, machinery, and subcontractors. For both cast-in-situ type and prefabricated-type horizontal slabs, the thickness is 400 mm and the bottom of the slab is located at the

center of the tunnel. A 1.1-m long, 2-cm thick expandable polystyrene (EPS) sheet is installed at each side of the slab. This lightweight geo-foam fill material absorbs vibration induced by trains passing through the upper deck, and lessens damage to the tunnel lining. Figure 2.34 and Figure 2.35 show the prefabricated horizontal slab.

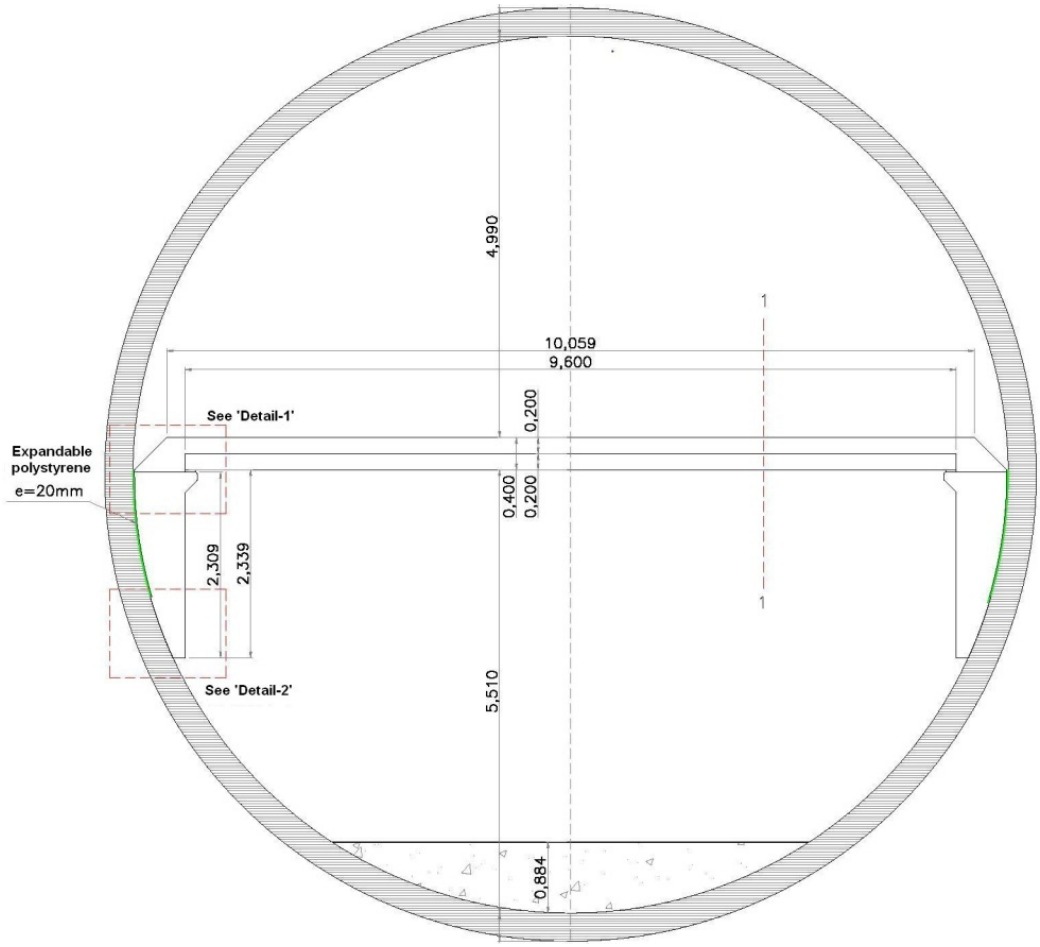

Figure 2.34 Dimension of prefabricated horizontal slab

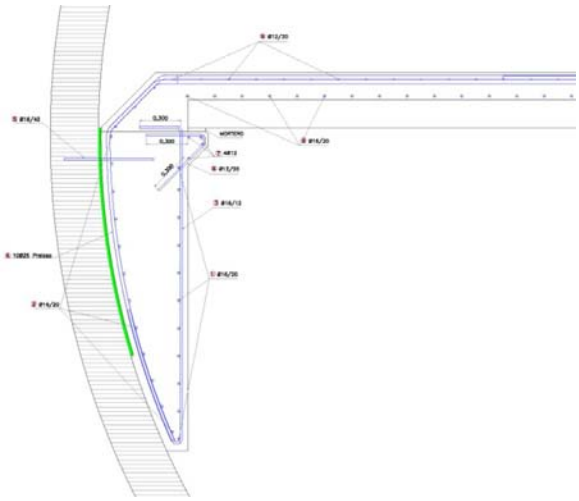

(a) Reinforcement and fastening of slab element

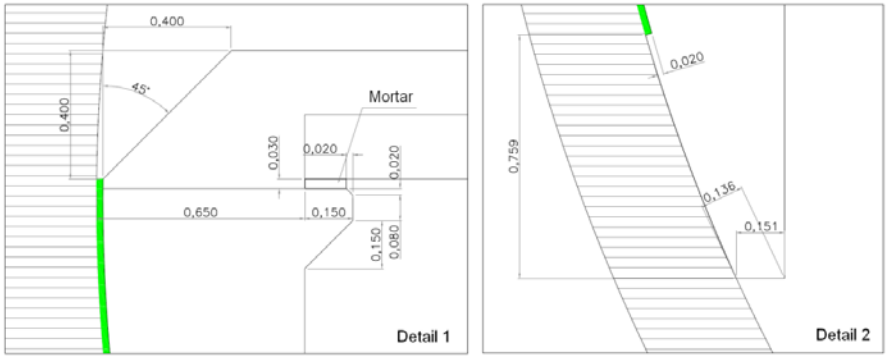

(b) Detailed dimension of prefabricated slab

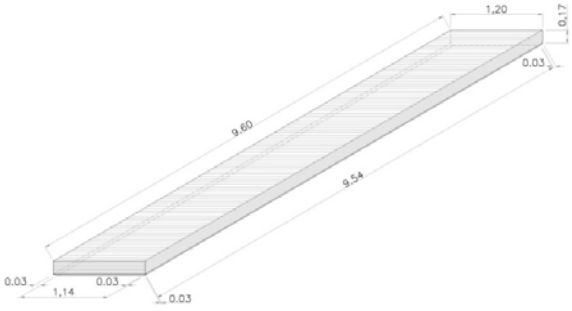

(c) Three-dimensional view of base panel

(d) Transverse cross section of the slab

Figure 2.35 Details of prefabricated horizontal slab

Crossovers are constructed at several points allowing trains to switch tracks. Figure 2.36 shows the points where crossovers are constructed in the tunnel.

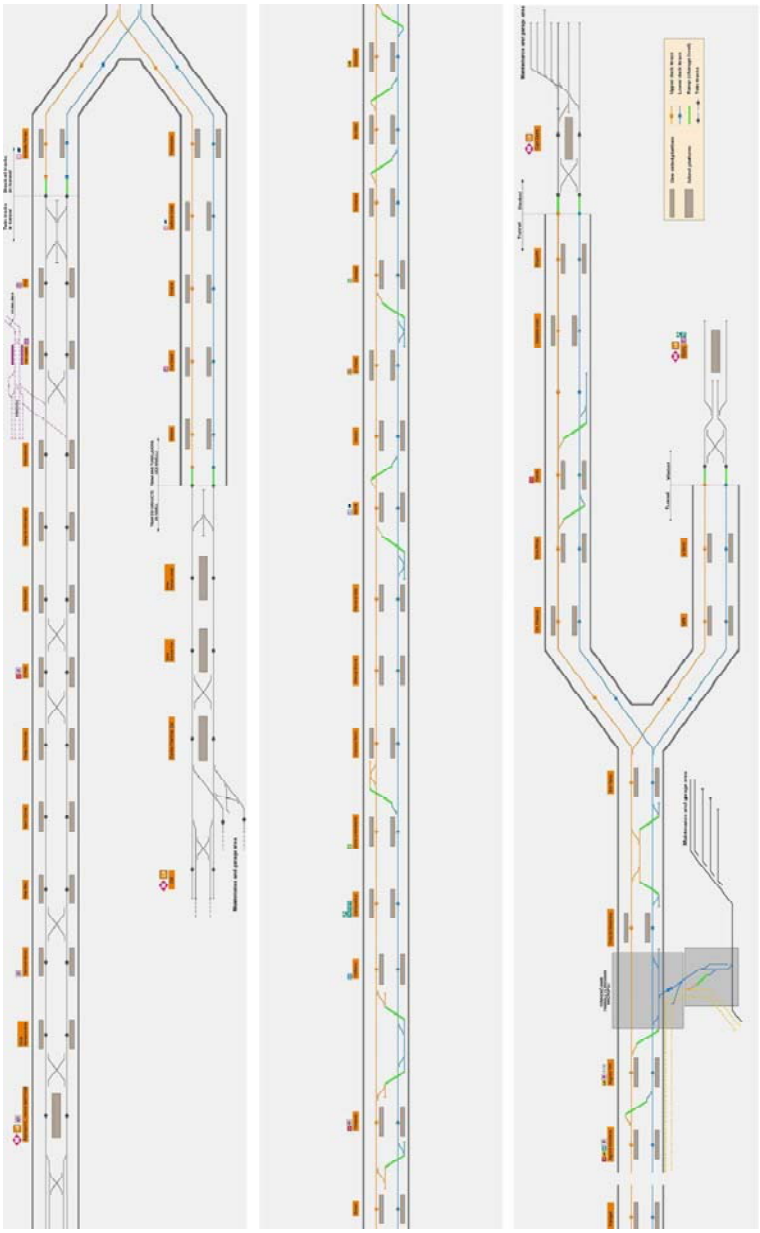

Figure 2.36 Location of cross-overs

The cross-over is a junction where tracks on lower and upper decks meet each other enabling trains to be redirected from one track to another track. When a tunnel features a single track configuration within a bore, huge cavern or cross over tunnels are necessary. For example in the Channel Tunnel, a 170-m long 18-m wide huge cavern had to be constructed to house a cross-over. On the other hand, a bore of this diameter is large provide enough space for cross-overs without additional excavation. A typical design of cross-over is (prepared for another project) presented in Figure 2.37.

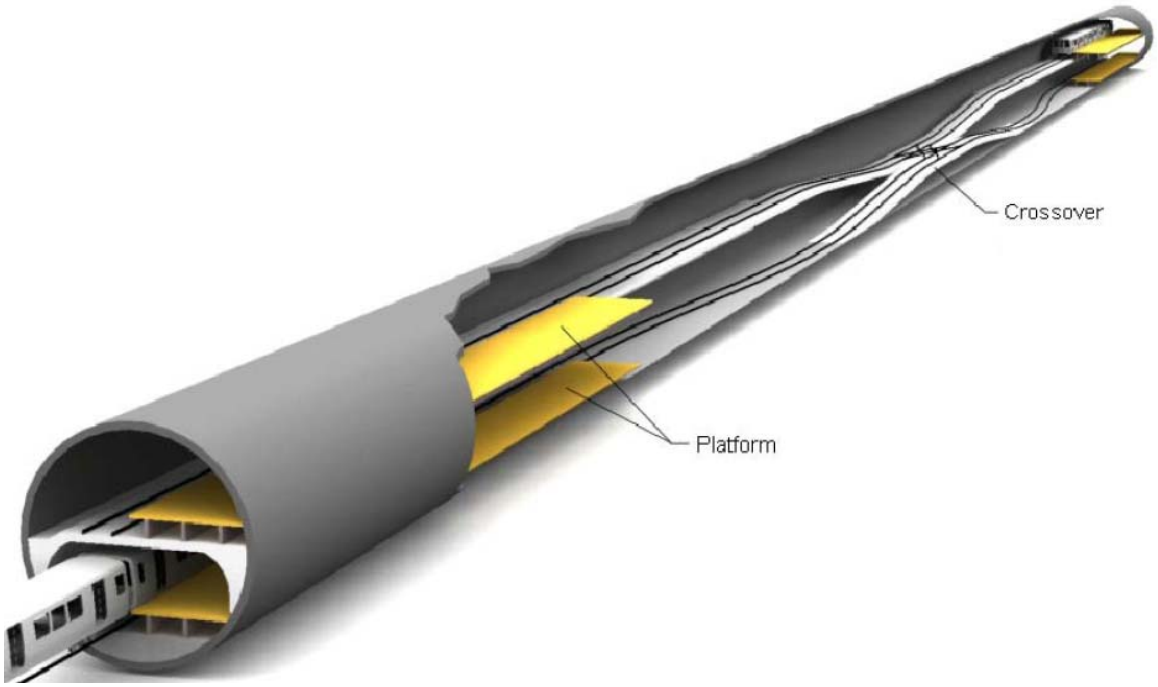

Figure 2.37 Conceptual drawing of typical cross-over (from Dragados and Dr. G Sauer Corporation, 2006)

2.3.9. Ventilation and safety facilities

The number of expected passengers per day is summarized for major stations in Table 2.13. Stations that require a large space for multiple railways and large numbers

of transfer passengers are constructed by cut-and-cover technique. Many citizens of Barcelona travel on foot when they go to subway stations, rather than using a bicycle or other means of transportation. Therefore the catchment area is small and is regarded as a 400 to 500-m radius. However, the catchment area can become even smaller when considering the fairly high access-and-exit time to and from the stations as deep as 70 meters underground. Even with multiple powerful elevators and emergency stair cases, such a depth can cause safety concerns to the public in case of emergency. Evacuation of passengers to the surface and access of personnel from the surface will be more difficult. Stations, such as Lesseps and Guinardó, which will be the most populated stations with passengers, could have capacity problems, both in platform areas and elevator halls. In order to prevent platform areas of well-type stations from overcrowding, elevators are synchronized with train arrivals. The elevators are automatically sent to the lower level when the train arrives to minimize passengers' waiting time and congestion. The trains were manufactured by a consortium led by ALSTOM. One train set consists of five coaches. It is 85.8-m long, 3.9-m high, and 2.7-m wide, and weighs 173 tons, when empty. It runs on a 1,435 mm standard-gage track with the normal operation speed of 33 km/h and the maximum speed of 80 km/h. It has no driver on board and the whole operation is controlled by a centralized control center. The train-to-train headway time can be reduced up to 60 seconds during rush hours by optimizing fleet deployment.

Table 2.13 Number of passengers expected in major stations (Almar, 2006)

Station	Passenger/day	Type	Link to other transit
Gorg	3,447	Cut-and-cover	
Llefia	7,687	Well-type	
Can Zam	1,086	Cut-and-cover	

Singuerlin	7,791	Well-type	
Sagrera TAV	20,597	Cut-and-cover	L4, High speed train, Suburban railway
Sagrera	20,590	Cut-and-cover	L1, L4, L5, Suburban railway
Guinardó	13,979	Well-type	L4
Lesseps	23,128	Well-type	L3
El Putxep	12,253	Well-type	L7
Zona Universitaria	8,383	Well-type	
Parc Logistic	15,593	Cut-and-cover	
Terminal Entre Pistas	4,420	Cut-and-cover	

2.3.10. Acknowledgement

Figure 2.18 to Figure 2.28 and Figure 2.32 to Figure 2.36 were provided by Xavier Delgado of GISA

2.4. CASE HISTORY III: HIGHWAY M30 TUNNEL, MADRID

2.4.1. Project overview

Madrid's inner ring road, Calle M-30, has served as one of the city's major arteries since it was built in 1980. It is the innermost ring road that encircles the central districts of Madrid. Outer ring roads are named M-40, M-45, and M-50. However, this vital infrastructure had numerous, unforeseen, shortcomings. Due to insufficient capacity and the poorly designed alignment of Calle M-30, drivers experienced chronic traffic congestion and high accident rates. Furthermore, residential areas near the highway suffered from noise and air pollution. The uniform development of the city area on each side of the highway was marred, because the highway acted as a barrier. To resolve these issues, the Madrid City Council proposed a plan to improve Calle M-30.

The project included road-surface refurbishment, re-design of high-capacity ramps and intersections, relocation of a considerable portion of the road underground, increase of the traffic capacity, and recovery of the environmental areas surrounding the ring road (Figure 2.38). Currently, the total length of the M-30 is 98.8 km, 56.7 km of which is in different types of tunnels. The surface area formerly occupied by a paved road is now used for public parks, affordable housing, parking space, and a bicycle road. The improvements were expected to save 14 million hours of travel time (Tunnels and Tunnelling International, 2006(06)) and 2.5 million liters of fuel per year (Madrid City Government, 2007). A significant, 45% reduction in the accident rate was also projected (Madrid City Government, 2007). The overall cost was 3.8 billion Euro (US$5.7bn) and the project was funded by a public-private partnership (PPP) between the Madrid City Council and ACS/Ferrovial. Construction started September 2004 and was completed April 2007 (Turner, 2007). The project was divided into four regions and fifteen sections, according to the nature of the work. The section numbers are shown in Figure 2.38 and the features of each section are summarized in Table 2.14.

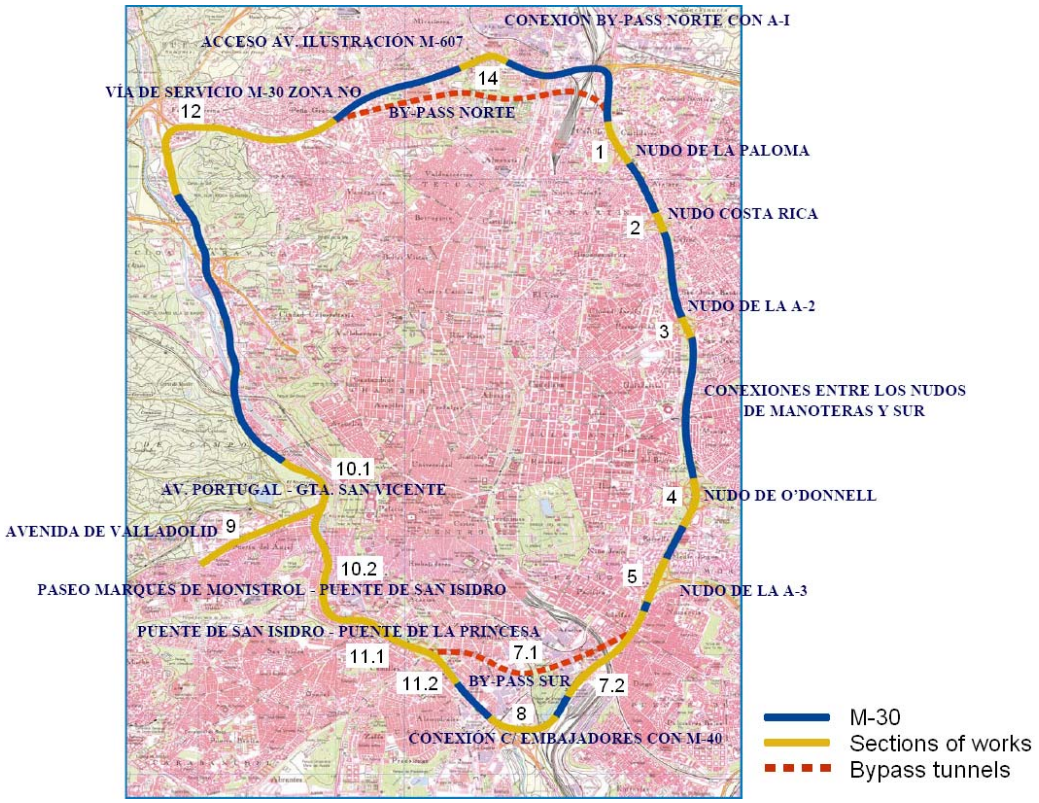

Figure 2.38 Project location (from Madrid City Government, 2007)

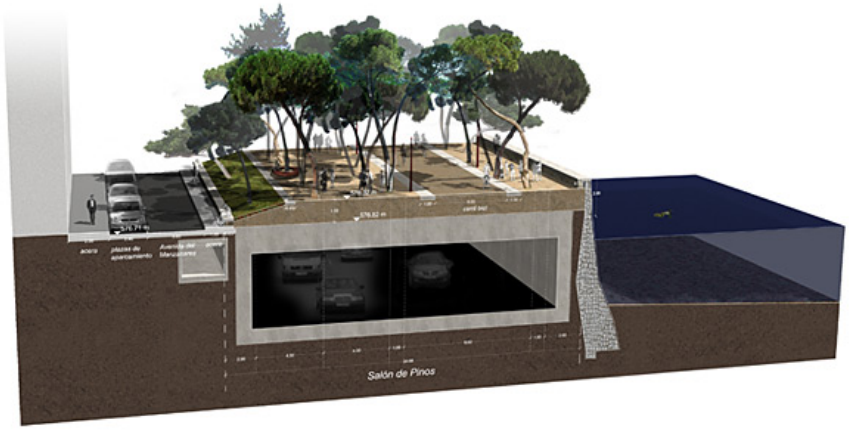

Figure 2.39 Development of green area after relocation of the paved road (from http://2.bp.blogspot.com/_d9q1ZhPUK6s/SXsVJqx6zAI/AAAAAAAAB-I/PwQ7V56SWfc/s1600-h/124.jpg)

Table 2.14 Calle M-30 sections (information from Turner, 2007)

	Section no.	Nature of work	Total length	Tunnel length	Cost (Mil €)
East	1	Refurbishment of the intersection between the M30 and Pio XII and Burgos Avenues.	5,508 m	1,546 m (cut-and-cover) 175 m (conventional method)	56
	2	Refurbishment of Calle Costa Rica and Plaza de J.M. Soler and their intersections with the M30.	2,078 m	892 m (cut-and-cover) 175 m (conventional method)	27
	3	Refurbishment of the M30 intersection with the Avenida de América (A-2)	4,460 m	510 m (cut-and-cover)	25
	4	Improvement of the intersection between the M-23 – O'Donnell and M30.	6,800 m	150 m (cut-and-cover)	18
	5	Improvement of the intersection between M30 and the A-3.	16,800 m	1,400 m (cut-and-cover) 430 m (conventional method)	217
South	7.1	Left lane of the intersection between Paseo de Santa Maria de la Cabeza and the A-3 from the south bypass of the M30.	8,344 m	7,212 m (15 m diameter-bored) 632 m (cut-and-cover)	792
	7.2	Right lane of the intersection between Paseo de Santa Maria de la Cabeza and the A-3 from the south bypass of the M30.			
	8	Connection between calle Embajadores and M40 ring road.	5,800 m	2,460 m (cut-and-cover)	144
West	9	Burial underground of Avenida de Portugal from Paseo de Extremadura to M30.	2,983 m	2,674 m (cut-and-cover)	177
	10.1	Burial underground of the crossroad Puente del Rey – Avenida de Portugal between Puente de Segovia and Marqués de Monistrol Avenue.	12,759 m	12,719 m (cut-and-cover) 40 m (conventional method)	618
	10.2	Burial underground of M30 from Puente de Segovia to Puente de San Isidro.	12,212 m	11,852 (cut-and-cover) 360 (conventional method)	450
North	11.1	Burial undergound of M30 from Puente de Segovia to Puente de Praga.	3,426 m	n/a	32
	11.2	Burial underground of M30 from Puente de Praga to Nudo Sur.	10,525 m	4,817 (cut-and-cover) 4,187 (conventional method)	722
	12	Service route for the M30 in the northwest area and addition of three lanes in the intersections with M30 area.	1,650 m	n/a	25
	14	Construction of a new access to the Avenida de la Ilustración with the Colmenar M-607 road.	5,479 m	4,463 (conventional method)	474

The new sections of the motorway totaled 98.8 km, 56.7 km of which are in tunnels. The tunnel was constructed using either the cut-and-cover method (39.7 km, at 11 sections), the conventional method (9.8 km, at 7 sections) or the TBM (7.2 km, at 2 sections). The typical cross sections are shown in Figure 2.40 and Figure 2.41 for cut-and-cover and conventional tunnels and in Figure 2.42 for TBM driven tunnels. In Sections 7.1 and 7.2, one of the major challenges for construction of the bypass tunnel was to minimize the negative impact on its densely developed surrounding area and its link with the A3, which was the Spain's most congested road. The bypass tunnel, 3.6-km long twin-bore, 13.45 m ID, three-lane tunnel was to be excavated using two earth-pressure-balanced tunnel-boring machines (EPB TBM).

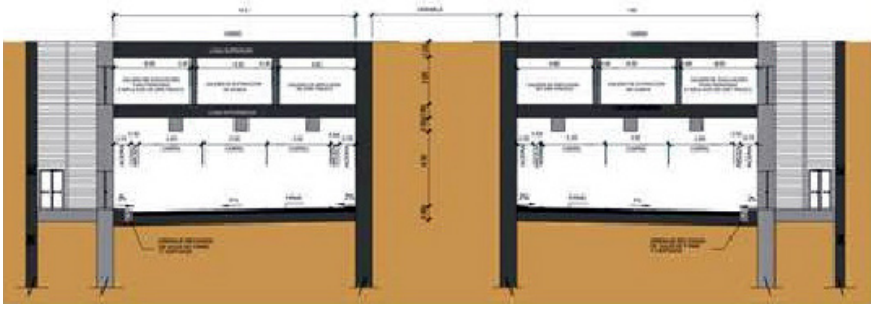

Figure 2.40 Typical cross section of cut-and-cover tunnel
(from http://www.roadtraffic-technology.com/projects/m30_madrid)

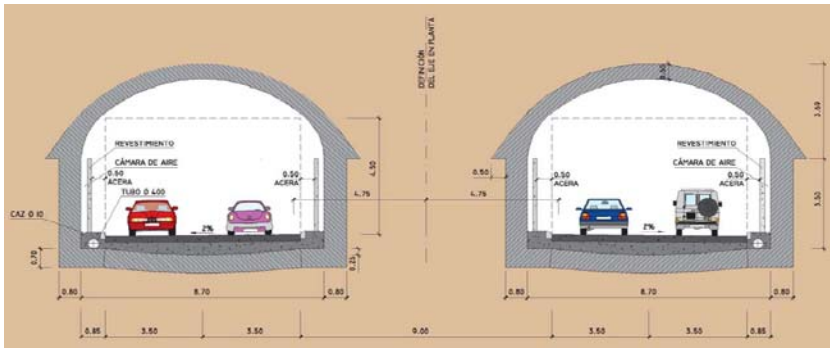

Figure 2.41 Typical cross section of conventional tunnel (from Romo-Alcañiz, 2007)

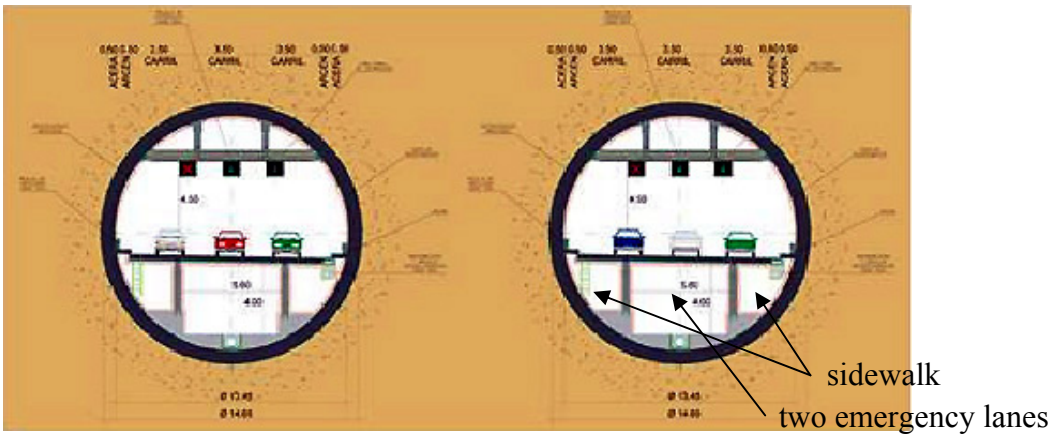

Figure 2.42 Typical cross section of bored tunnel
(from http://www.roadtraffic-technology.com/projects/m30_madrid)

2.4.2. Feature of twin-bore tunnel

The twin-bore tunnel in Section 7 consists of a 3,652-m long south bore that serves the traffic flowing east and the 3,526-m long north bore that serves the traffic flowing west. The inner diameter of each tube is 13.45 m and the outer diameter is 14.65 m. A 2-m wide, 600-mm thick precast concrete segment was used. One ring was composed of nine segments and a key segment. The segments were manufactured at an off-site factory, 40 km away from Madrid. As already shown in Figure 2.42, the cross section of the tunnel consists of three traffic lanes (3.5-m wide, each), 0.5-m wide hard shoulders, 0.8-m wide sidewalks, and a 0.1-m thick sacrificial concrete layer that protects the tunnel lining from vehicles. The road deck was constructed on a horizontal slab. The horizontal slab was installed simultaneously with the tunnel excavation. A 600-mm thick, 1.3-m wide pre-stressed, prefabricated concrete slab segment was used. The road deck is located 1 m below the tunnel center and the clearance height of the road deck is 4.5 m. Below the road deck is the service gallery. It incorporates two sidewalks and two emergency lanes where ambulance or other emergency vehicles can

pass. The space above the road deck is used for the ventilation. This area also accommodates other electrical and mechanical facilities. Eight cross passages were constructed to connect two tubes (Figure 2.44). They were hand-mined after the main tunnel's excavation. Five cross passages are pedestrian-only and three cross passages are large enough to allow vehicular access (Tunnels and Tunnelling International 2006, June and 2006, December). Figure 2.45 shows the shaft that serves as a ventilation duct and an exit route to the surface in case of an emergency. The fresh air is supplied through the lower gallery and the polluted air is extracted through the opening at the ventilation gallery above the highway. The ventilation is produced by jet fans installed in the vertical shaft. Emergency staircases and elevators were constructed in the vertical shaft.

Figure 2.43 Installation of the horizontal slab (from Romo-Alcañiz, 2007)

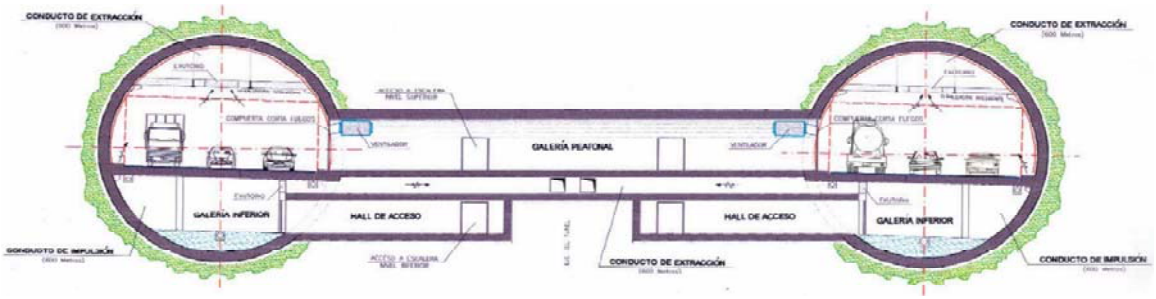

Figure 2.44 Cross passage (from Romo-Alcañiz, 2007)

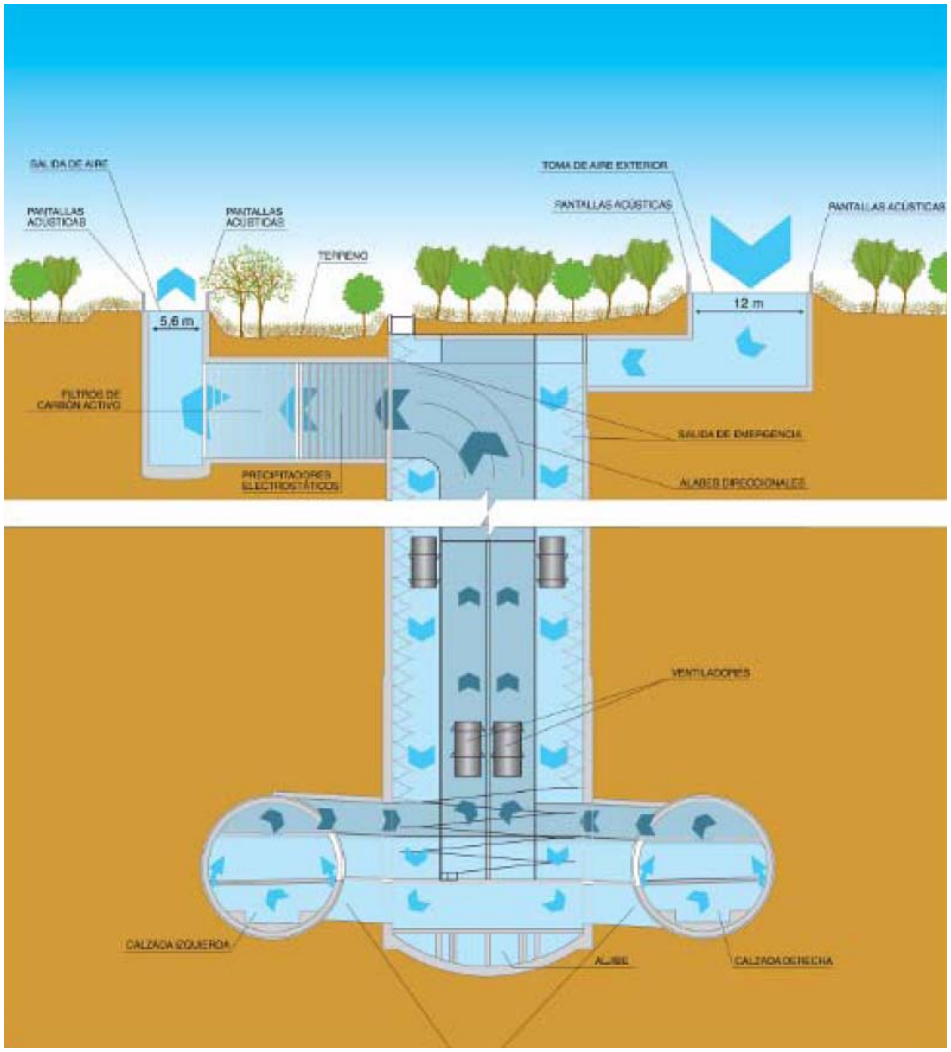

Figure 2.45 Ventilation and emergency shaft (from Romo-Alcañiz, 2007)

2.4.3. Geological conditions of South Bypass tunnels

The average overburden of the South Bypass tunnels was around 30 m, with the maximum value of 65 m. The surface of the project area is alluvial deposits, mainly consisting of soft silts and clays. This layer reaches a depth of 20-25 m. The next layer is a 25 to 30-m thick fissured marly clay layer called peñuela. Finally, there is a layer of hard clay with occasional bands of hard gypsum layer (peñuela yesifera). The geological profile is given in Figure 2.46. The effective friction angle, cohesion, and Young's modulus of the peñuela clay is c'=28°, φ'=60 kPa, and E=220 MPa. The fines content is 85 to 95%. The tunnels were constructed below the ground water table and the maximum hydrostatic water pressure was about 4 bar.

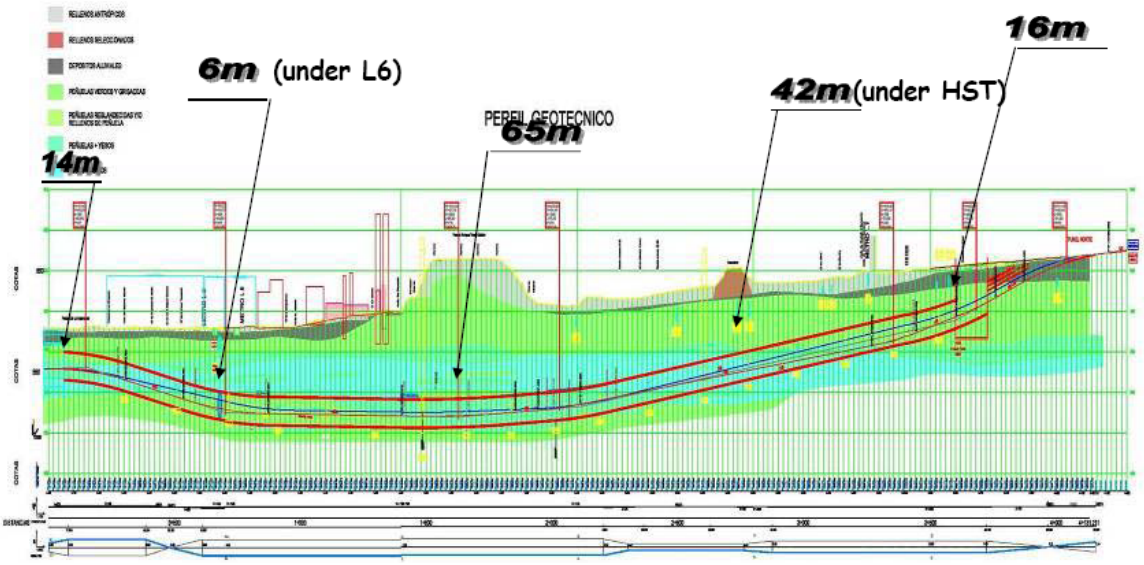

Figure 2.46 Geological profile (from Romo-Alcañiz, 2007)

2.4.4. TBM specifications

The geological conditions of Madrid are very suitable for EPB tunnel excavation, as was proved by previous metro tunneling experiences where Herrenknecht 9.5 m OD, EPB TBMs have been used (World Tunneling 1998, Tunnels and Tunnelling International, 2006(6)). Two EPB shields were used for the excavation of the South Bypass tunnels. For the south bore, a 15.1 m diameter Mitsubishi EPBM was used and, for the north bore, a 15.2 m diameter Herrenknecht EPBM was used. The outer diameters of the precast segment ring for north and south bores were identical—14.65 m. The technical specifications of both EPBMs are summarized in Table 2.15. Figure 2.48 shows the progress of each TBM in the south and the north bores. The Herrenknecht EPBM in the north bore started its excavation November 16, 2005 and completed July 12, 2006. The average daily progress was 14.8 m. The Mitsubishi EPBM in the south bore started its excavation March 29, 2006 and completed October 29, in the same year. The average daily progress was 17.1 m.

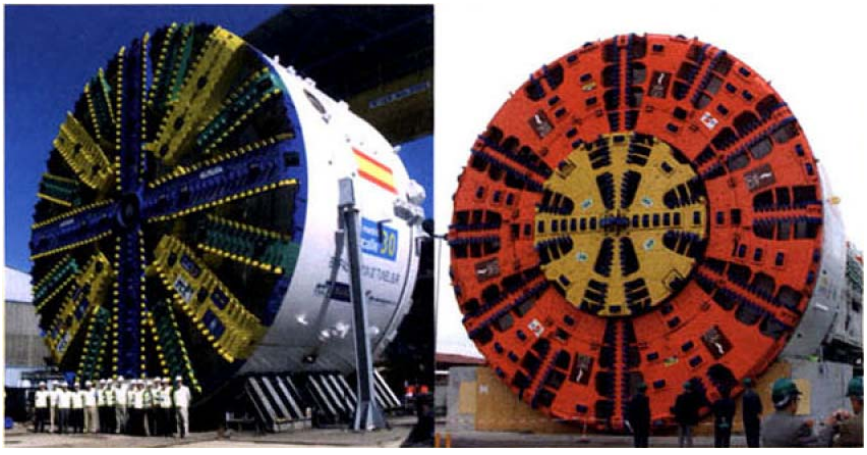

Figure 2.47 Photos of two TBMs (left: Mitsubishi O15 EPBM, right: Herrenknecth S-300) (from Tunnels and Tunnelling International, 2006(06))

Table 2.15 TBM specifications

Description		South bore Mitsubishi EPBM	North bore Herrenknecht EPBM
Total installed power		10 MW	15.8 MW
Total weight			4,000 tons
Cutterhead	Diameter	15.1 m	15.2 m dual cutterhead (with 7 m inner cutterhead)
	Rotating speed	1.05 rpm	Max. 1.5 rpm
	Tool Composition	44 triple 17" disc cutters, one center cutter, 226 teeth, 472 picks, 4 copy cutters	57 double 17" disc cutters, 332 bits, 24 scrapers
	Installed power		10.7 MW
	Torque	12,700 mTon	12,527 mT (outer) 10,890 mT (inner)
	Opening ratio	43 %	> 30%
Thrust cylinders	Thrust force	285,000 kN	276,390 kN
	No. of thrust jacks	57	57
Shield	Articulation	Active articulation	Not installed
	Length	12.22 m	11.51 m
	Working pressure		6 bar
Mucking		One 1,500 mm screw conveyer	One 700 mm screw at the center and two 1,200 mm screws at the bottom

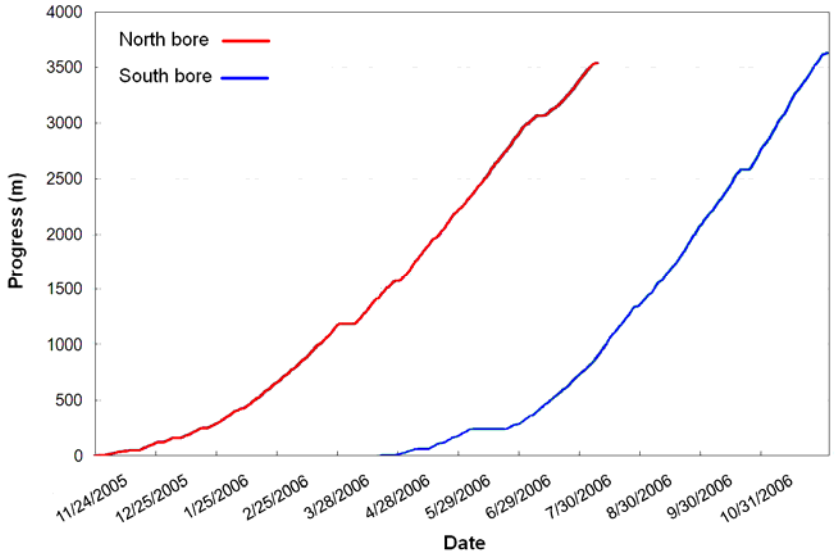

Figure 2.48 TBM progress chart (from Romo-Alcañiz, 2007)

2.5. CASE HISTORY IV: SOCATOP A86 TUNNEL, PARIS

2.5.1. Introduction

The A86 west tunnels, in Paris, are privately-funded, toll-highway tunnels that are composed of two tunnels: the East Tunnel and the West Tunnel. A86 was constructed as a part of the Socatop A86 ring-road project that skirts Greater Paris (Figure 2.49).The West Tunnel is for heavy vehicles and the East Tunnel is for the lighter vehicles. The West Tunnel is a conventional single-deck two-lane tunnel, with a clearance height of 4.5 m. The East Tunnel, which is also called A86 Duplex, is a 10.5-km long double-deck traffic tunnel, with an 11.9 m outer diameter. It was excavated with an 11.9 m diameter Mixshield. The A86 Duplex connects Malmaison and Versailles and shortens the travel time from 45 minutes to 10 minutes. The A86 Duplex is designed to serve only light vehicles. Vehicles taller than 2 m are supposed to use another route.

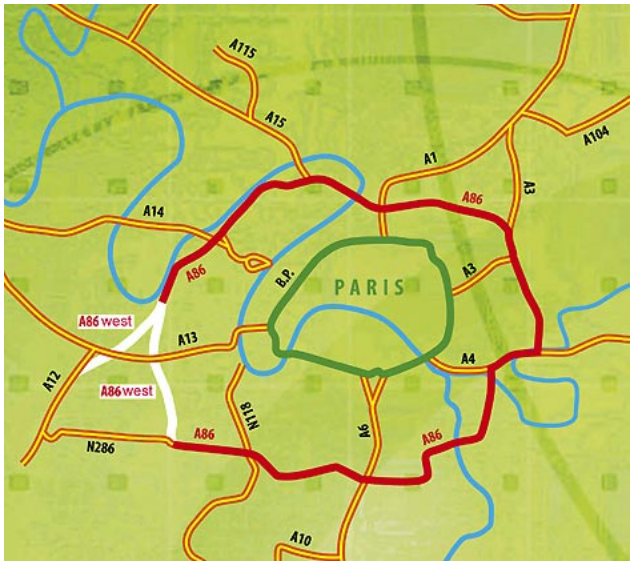

Figure 2.49 A86 Duplex

2.5.2. Project history

Prior to construction of the A86 Duplex, the need for an additional highway had been raised for more than thirty years because of chronic traffic congestion at the Socatop A86 Highway and its intersection around western suburban Paris. However, due to the historical importance and environmental sensitivity of the region, the construction of the surface highway was not undertaken. It was determined to go underground and the proposal of A86 Duplex solution was accepted (http://www.roadtraffic-technology.com /projects/a86).

In 1996, the Mixshield was ordered from Herrenknecht and preliminary work started. However, a series of rejections from environmental groups, hearings, and arbitration delayed arrival of the TBM until June 2000. The first bore was begun in December 2000. The design was revised to meet enhanced fire-safety requirements after the Mont Blanc tunnel fire accident that claimed 39 lives in March 1999.

The total construction cost for the tunnel was 1.8 billion Euros (US $2.8 billion). No public funds were spent and the tunnel will be financed entirely by the projected tolls (Reid, 2008).

2.5.3. Features of the tunnel

The A86 Duplex has a 10.4 m inner diameter and features a double deck. Each has three 2.8-m wide lanes, plus a 2.5-m wide emergency lane. Figure 2.50 shows the typical cross section of the tunnel. The outer diameter is 11.9 m. The ceiling height of the road deck is 2.55 m and the clearance height of each road deck was set at 2 m. Each road deck has an individual ventilation system. One ring was composed of seven

precast segments and a key segment 30 cm thick. The tunnel has 13 emergency refuge areas with interconnecting staircases (Figure 2.50).

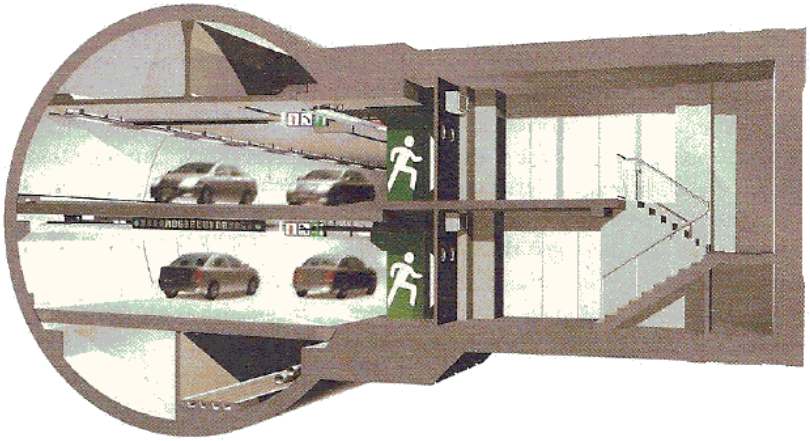

Figure 2.50 Cross section view (from Civil Engineering, 2008(06))

Figure 2.51 Photos of the upper and lower road deck

2.5.4. Geological conditions

The geology of the site is represented by limestone and limestone-marl layers, with occasional presence of clay and sand layers, underlain by the Seine riverside chalk. The tunnel is located within limestone, except for the regions close to the portals and the interchange with the A13 Highway. For cohesive ground and soft rock, EPB and open

excavation modes were chosen. A slurry mode was chosen to drive in the water-bearing sand strata. The overburden ranged from 10 to 100 m.

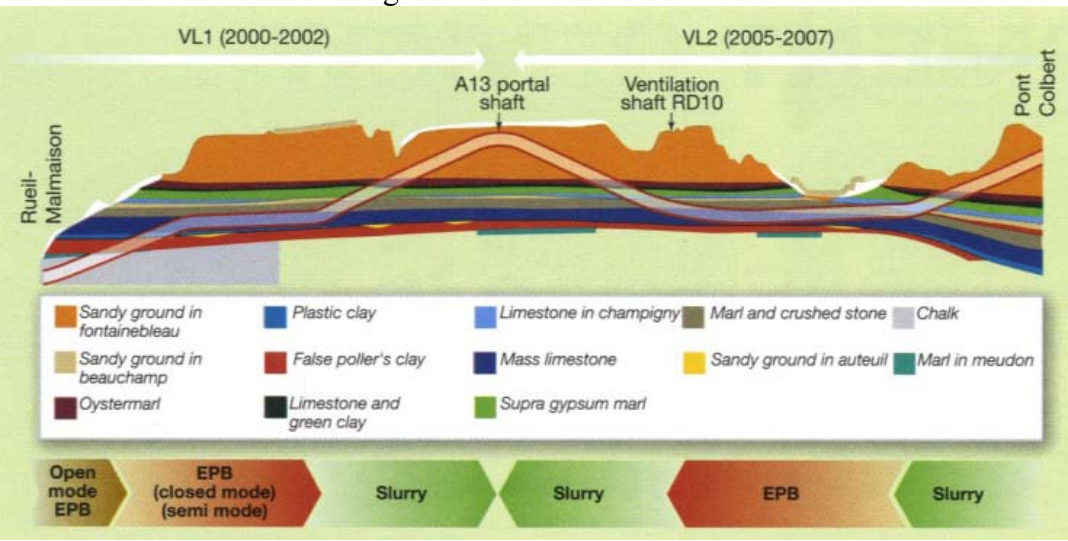

Figure 2.52 Geological conditions and the different TBM modes used on the drive (from Tunnels and Tunnelling International 2008(06))

Figure 2.52 shows the geological conditions of the ground in the tunneling site and the operation mode of the Mixshield, depending on the ground conditions. Where the ground mainly consists of the chalk, clay, and limestone, an open mode was used. For the mixed ground of the limestone, marl, and crushed stone, the TBM was operated in an EPB mode. A slurry mode was used for the water-bearing sandy ground.

2.5.5. TBM specifications

The tunnel was constructed using a convertible 11.56 m diameter, Herrenknecht Mixshield TBM to cope with heterogeneous geological conditions. The components of the TBM were configured differently for various geological conditions, from soft clays to hard rocks. The TBM can be converted from open-mode to closed-mode to EPB-mode

inside the tunnel and vice versa (Herrenknecht and Bäppler, 2008). The average daily advance rate was 30 m (http://www.roadtraffic-technology.com /projects/a86).

Since the Mixshield had a closed-type cutterhead, the conversion of the excavation mode between the EPB and slurry modes was possible without any modifications except for the conversion of the back-up and mucking systems (Herrenknecht and Bäppler, 2008). The installed power in the cutterhead was 4,000 kW and the torque was 16,400 kNm.

2.5.6. Excavation

The construction of the A86 Duplex was divided into two drives: first, a 4.5-km long section from Rueli-Malmaison to Vaucressin and, second, a 6.0-km long section to Pont Colbert. The excavation of the first section was started in December 2000 and completed in 2003, and fittings, such as pavement, the safety system, and the ventilation system, were completely installed in 2006. The TBM was mainly operated in the closed EPB mode and slurry-supported mode. The first section of the tunnel was open to the public in 2008. After the boring of the first section of the tunnel, the TBM was dismantled and moved to the launch shaft of the second section of the tunnel. The excavation of the first section was started in June 2005 and completed in August 2007. The scheduled opening is in 2010. For the excavation of the cross passages, a ground-freezing technique was used to eliminate the need for a dewatering process and to assure successful excavation. The freeze pipes were installed from within the main tunnel or from auxiliary shaft.

Figure 2.53 Wheeled gantry installing the horizontal slab
(from Tunnels and Tunnelling International 2002(10))

2.5.7. Tunnel fire accident

After the 1999 Mont Blanc tunnel fire accident, strict safety regulations were established for the construction of A86 Duplex. The TBM and the tunnel were equipped with several fire detection and fire-fighting measures, such as a water curtain on the TBM back-up and fire extinguishers, ventilation system, and breathing apparatus on the TBM and on the carriageway. Fire-safety equipment was checked on a weekly basis and regular fire drills were conducted with all personnel. Despite this effort, a major fire accident occurred March 5, 2002. There was no loss of life or major injury, but three months of production were lost.

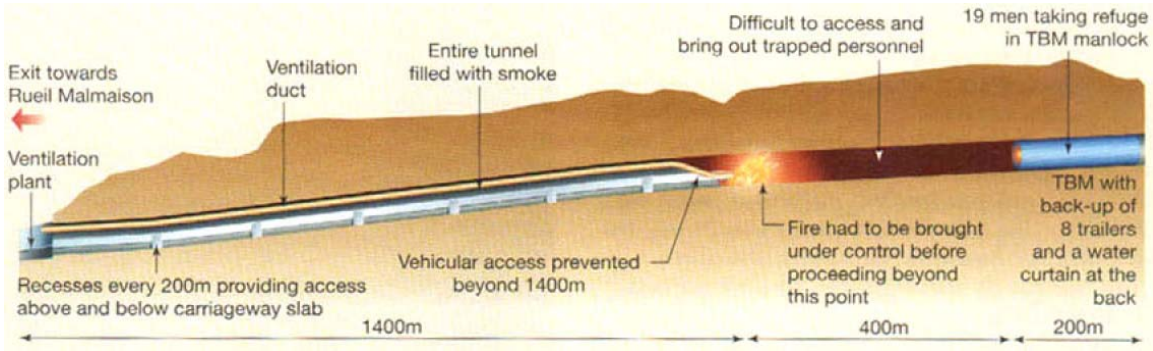

Figure 2.54 View of the fire incident (Tunnels and Tunnelling International 2003(11))

This major fire occurred during the excavation of the first drive, at 22:30, at station 1,540 m (Figure 2.54). The diesel engine of the service train caught fire when it was approaching the end of a long uphill haul. The fire could not be stopped by a powder extinguisher system operated by the train driver and soon spread to the train's fuel tank and the TBM mucking conveyor belt. As the plastic conveyor belt burned, the tunnel quickly filled with fumes. The fire alarm was raised and the water curtain on the TBM back-up was activated. Nineteen workers were present behind the water curtain and, as rehearsed two times, they escaped 500 m back to the TBM and took refuge in the man-lock, where personnel air supplies were stocked. The workers' location was detected at 2:50, on March 6, and their evacuation was completed by 5:30. The rescue mission was difficult because tunnel lighting, electric cables, telephone lines, radio transmitters, the ventilation system, and vehicles were disabled due to the fire. Since there were no major injuries, the rescued personnel were sent to the hospital and released the next day. The fire was completely extinguished in the later afternoon on March 6, and the rescue and fire-fighting operation was officially closed on March 8.

Protected by the water curtain at the end of the TBM back-up, the TBM and back-up were undamaged. However, the precast lining and the horizontal slab over an 80 m

length were damaged. In some cases, reinforcement bars were revealed due to spalling of the concrete. The stability of the tunnel lining was examined by a series of coring, sclerometric tests, resonance tests, and finite element analyses. The tunnel was in a stable limestone area and, despite the reduced lining thickness, the tunnel lining was found to be structurally safe. The damaged concrete was water-jetted to sound concrete, and, later, it was cleaned with hot water with detergent. The lining was repaired after the completion of the tunnel excavation. Deformed rebars in the concrete segment were replaced by welding, and spalled concrete segments were resurfaced using a special concrete, based on experience from the Channel Tunnel fire (Tunnels and Tunnelling International, 2004(03)). The steel platform, overhead crane, cables, conveyor belts, and ventilation duct were replaced. After the fire, to achieve secure communication measures in the tunnel, fire resistant cables and wires were used, and several upgrades of the fire-fighting equipment were installed (Tunnels and Tunnelling International 2003(11)).

2.5.8. Safety and ventilation system

The ventilation system is within the conduit beneath the bottom slab in the lower-road deck and above the ceiling in the upper-road deck. Both ventilation systems operate independently. A ventilation shaft is constructed every 1,200 m and five shafts were constructed along the route. The shafts serve as escape shafts and have elevators and spiral staircases (Figure 2.55). The emergency refuge areas are spaced every 200 m along the route. A sealed interconnecting staircase connects upper- and lower-road decks. During an incident, the unaffected road deck acts as an emergency access route.

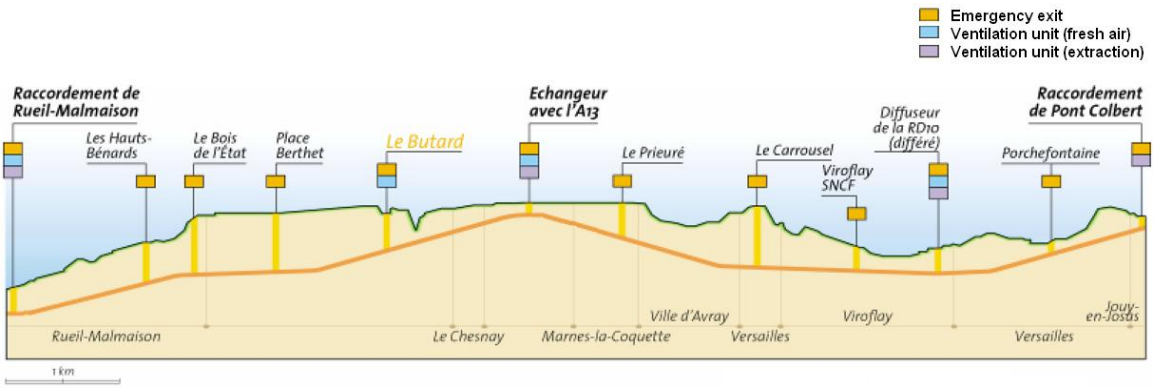

Figure 2.55 Location of vertical shafts for emergency access and ventilation (after Vuorisalo, 2008)

The tunnel uses a HI-FOG fire-extinguish system, which has proven to be very effective in extinguishing fires, in dropping the temperature, and in suppressing the generation of smoke and toxic fumes. The sprinkler uses a high pressure nozzle to produce a fine mist of water droplets (50-120 micron). The traffic is monitored by the 350 cameras and automatic speed and traffic density data collector. The speed limit of the tunnel is 70 km/h.

The traffic moves in the northbound direction on the upper-road deck and in the southbound on the lower deck. Due to the limited clearance height and the width, extensive studies on driver behavior in tunnels have been carried out by social scientists, psychiatrists, and ethnologists. As a result, bright colors were chosen for the walls and roadway surface and a white lighting system that mimics natural sunlight was used rather than the yellowish, sodium-vapor lamps that are typical for tunnel lighting (see Figure 2.51) (Civil Engineering, 2008(6)).

2.6. CASE HISTORY V: 4TH ELBE TUNNEL, HAMBURG

2.6.1. Old Elbe tunnel and New Elbe tunnel 1st-3rd bores

The River Elbe is one of the major rivers in central Europe. It flows from the Czech Republic to the German coast on the North Sea, 100 km northwest of Hamburg. The river crosses the City of Hamburg, dividing the city center on the north from the port of Hamburg on the south (Figure 2.56). The river is about 400-m wide in this area. Both sides of the river were connected only by a bridge before the old Elbe Tunnel, technically sensational at the time, was completed in 1911. It is a twin bore tunnel for pedestrian and (horse-drawn) vehicles. Each bore is 449-m long. The external and internal diameters are 5.92 and 5.64 m, respectively, and the distance between the two tunnels' axes is 8.0 m. The tunnel does not have the ramp typical of modern tunnels. Instead, it features two vertical shafts of 22 m ID that incorporate stairs and vehicle lifts (Figure 2.56). The tunnel crown was about 15 m below the reference level (about 6 m below the river bed). The tunnel was bored by a closed shield. The shield was about 15 cm thick, and the entire tunnel was pressurized 2 to 2.5 bar of the compressed air, depending on the tidal height, to prevent the ingress of water. 4,400 workers manually excavated the tunnel face and, due to decompression sickness (also known as caisson disease), three men died (Craig, 2000). A 25-cm wide, rolled iron-segment ring was used (Figure 2.57) and the gap was filled with concrete. The total cost of the construction was 10.7 million Gold Marks. The tunnel opened to the public in 1911. It is still in operation and attracts many tourists (Zell et al., 1999).

Figure 2.56 View of vehicle elevator
(from http://commons.wikimedia.org/wiki/File:Hamburg_Alter_Elbtunnel_01_KMJ.jpg)

Figure 2.57 Tunnel lining iron segment assembly (from Zell et al., 1999)

With the growth of the Port of Hamburg, traffic across the River Elbe increased. The New Elbe Tunnel was constructed between 1968 and 1975, as part of Autobahn A7. It is a triple tube tunnel with two lanes each. The tunnel is divided into three parts: the

northern slope, the river undercrossing, and the south bank. The northern slope of the tunnel was excavated by shielded TBMs. Three platform-type open shields were used to excavate 1,113-m long, 10.3 m ID triple bores. The shield was 11.08 m in outer diameter and 9 m in length. Hydraulic excavators cut the soil at the tunnel face. The mucking was done by the conveyor belts and trailer system. The average daily advance rate was 7.9 m. The groundwater was fully lowered to ensure a dry condition in the launch shaft. For the remainder of the shield-driving section, the groundwater level was lowered to a level at which the compressed air pressure would not exceed 1.5 bar at any point. A tunnel ring was 1.125-m long and was composed of 15 precast segments plus a key. The part of the tunnel that crosses under the river is 1,057-m long and is inclined by 45° with respect to the river's axis. It was constructed by an immersed-tunnel method. Seven 132 x 42 x 8.4 m (length x width x height) elements and one 121 x 41.7 x 84 m tunnel element were prefabricated in a building dock on the south bank. The finished tunnel elements were floated and dragged by barge to a predetermined position and then submerged into a previously excavated trench. The tunnel in the south bank area is 800-m long. It was constructed by a cut-and-cover method (Zell et al., 1999). The cross section of the tunnel at each section is shown in Figure 2.58. The ground of the northern slope area is mainly stiff tertiary clay. The riverbed and relatively low south bank consist of glacial deposits whose settlements were difficult to predict. To prevent the formation of shear cracks, due to differential settlement, intermediate joints were provided at every 27 m (Grantz, 2001).

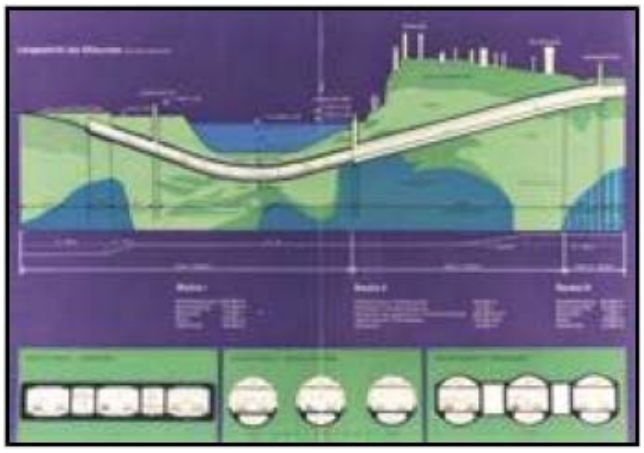

Figure 2.58 Tunnel cross section (from Zell et al., 1999)

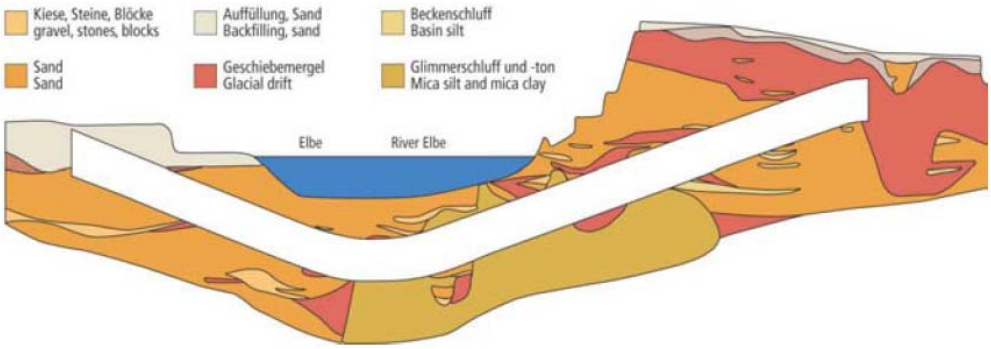

Figure 2.59 Geological condition
(from http://www.ita-aites.org/cms/uploads/RTEmagicC_1e7417468d.jpeg.jpeg)

2.6.2. 4th Elbe tunnel

To ease traffic congestion of the existing three bores of the New Elbe Tunnel, an additional 4th bore was constructed. A Herrenknecht Mixshield was used to cope with the heterogeneous ground condition of the riverbed and northern slope areas. The geology consists of glacial deposits, sands in the south and marl and clay in the north. Blocks and boulders of all sizes were present everywhere (Becker, 2001). The average monthly progress was 84 m, including downtime, and 156 m, excluding the downtime.

The outer diameter of the Mixshield (S-108) was 14.2 m. It was the biggest TBM at the time. The installed power for the cutterhead was 3,400 kW and the torque was 25,780 kNm. The slurry separation plant incorporated three steps in slurry recycling procedures, screening and removal of clay particles by hydrocyclones and, finally, by centrifuges. Its hourly capacity was 2,400 m^3/hr. The total length of the 4th bore is 3.1 km. 2.6 km was bored by the TBM and the additional 500 m at the north and south portals were constructed by using the cut-and-cover method. The tunnel includes two 3.75-m wide traffic lanes and a 2.0-m wide hard shoulder. It is the only bore that has a hard shoulder among the four bores of the New Elbe tunnel. Prefabricated 2-m long, 700-mm thick segmental lining was used. One ring was composed of eight segments plus one key. 1,280 rings were erected in the tunnel. The tunnel is 42 m below sea level; thus two EPDM-Kautshuk sealings, each of which can resist 10 bar of water pressure, were used (Zell et al., 1999). The excavation was started in October 1997 and completed in March 2000. After the completion of the excavation, the TBM was disassembled and sent to Schwanau, Germany and refurbished for the next projects in Moscow, Russia.

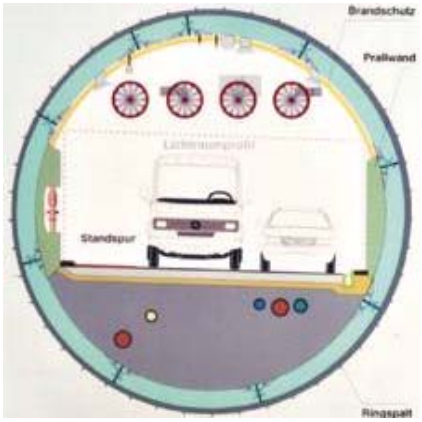

Figure 2.60 Cross section of the tunnel
(from http://www.ita-aites.org/cms/uploads/RTEmagicC_1e7417468d.jpeg.jpeg)

2.7. CASE HISTORY VI: LEFORTOVO TUNNEL, MOSCOW

2.7.1. Introduction

Lefortovo Tunnel is a 3.3-km long single-bore double-deck traffic tunnel on Moscow's third ring road in the Lefortovo District of eastern Moscow. A 2.5-km long drive was bored and the rest of the tunnel was built by cut-and-cover technique. It was bored using the Herrenknecht Mixshield that had been used to excavate the 4th Elbe tunnel. The entire tunneling system, including the TBM, slurry separation plant, grout mixing plant, ventilation equipment, segment fabricating plant, segment moulds, segment moving vehicles, muck loaders, crane, and fleet of locos and dump trucks were dismantled and transferred to Moscow, Russia.

Figure 2.61 Tunnel plan (http://www.rfsworld.com/stayconnected)

2.7.2. Planning

The Lefortovo Tunnel was constructed to connect the missing link of the third ring road of Moscow. Originally, construction of twin tubes was planned to serve the traffic flowing in both directions. However, due to political factors and financial problems during the design stage, the plan was changed and the project was split into two separate projects. As a result, instead of building the originally planned twin-bore tunnel, a single bore tunnel that serves traffic flowing northbound was constructed. The southbound highway was constructed on the surface and in a cut-and-cover tunnel (Figure 2.61). The government had to pay the redesign costs for the alternative cut-and-cover tunnel and surface highway. The configuration of the bored tunnel had to be changed because the cross passages could not be constructed. In addition to the design costs, various social costs were generated. When the government had selected driven tunnels, the original intention was to minimize disruption on the surface area and the environmental impact. Eight buildings had to be demolished to accommodate the alternative highway. The construction cost per unit length of the twin-bore tunnel would have been cheaper than that for the single-bore tunnel.

2.7.3. Features of the tunnel

The inner diameter of the tunnel is 12.75 m. The tunnel includes three 3.5-m wide traffic lanes. The clearance height is 4.5 m. This 3.3-km long single-bore tunnel has no cross passages or emergency lane. Instead, it has an evacuation passage constructed beneath the road deck. The main road deck and the evacuation passage are interconnected by stainless steel slides at 500 m intervals. The prefabricated segmental

lining that was designed for 4th Elbe tunnel was re-used. One ring was 2-m long and 700-mm thick. It consists of eight segments, and one key was used.

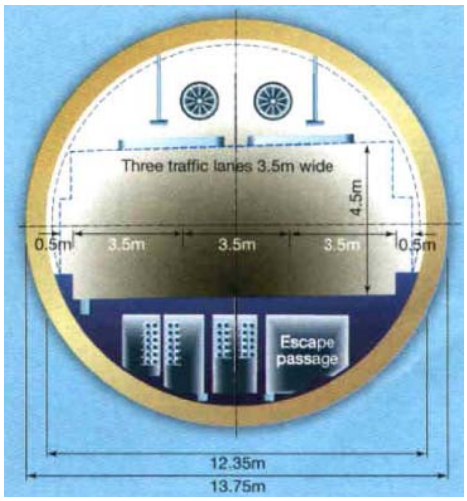

Figure 2.62 Cross sectional view (from Tunnels and Tunnelling International, 2002(12))

Figure 2.63 Slide for emergency escape
(from Tunnels and Tunnelling International, 2002(12))

2.7.4. Geological conditions

The geology of the project site consists of water bearing sands, silts, and clays, with thin layers of laminated limestone. The water pressure at the tunnel invert was up to 3.5 bar (Tunnels and Tunnelling International, 2002(12)). The project site has few boulders, one of the factors that enabled rapid excavation, compared to the 4th Elbe tunnel.

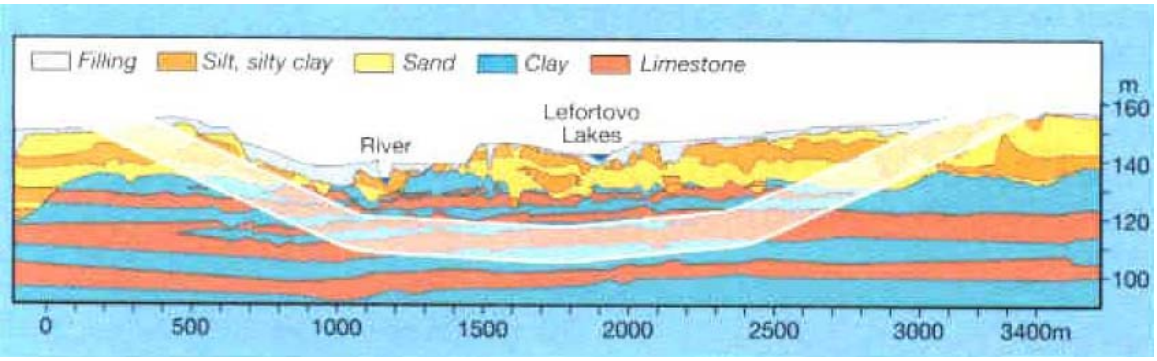

Figure 2.64 Geological conditions (from Tunnels and Tunnelling International, 2002(12))

2.7.5. TBM specifications

During the refurbishment, a new cutting wheel with a center cutter (2.65 m in diameter) was installed in the Mixshield to reflect the predicted geological conditions of the project area. The power installed to the cutterhead was 3,200 kW, + 315 kW for the center cutter. The cutterhead was equipped with scrapers, disc cutter, and buckets (Herrenknecht and Bäppler, 2006). The thrust force was 120 MN.

The largest slurry separation plant was used to recycle used bentonite slurry. The recycling process consisted of three steps: removal of gravel to sand particles by a series of vibrating screens, removal of clay particles by hydrocyclones, and filter pressing. It was the largest separation plant at the time and the flow capacity was 2,800

m^3/hr. Because the advance rate was almost twice what had been expected, the slurry separation plant had to operate full-time. Even though six filter presses had been installed in the separation plant, it was the filter pressing process that showed the slowest progress rate and reduced the combined efficiency of the entire slurry separation plant. As a result, the number of separation plants was increased to ten for the next tunneling project site, Silberwald, Russia. The entire tunneling system was refurbished and transferred to Moscow, where the geological conditions are similar (Tunnels and Tunnelling International, 2002(12)).

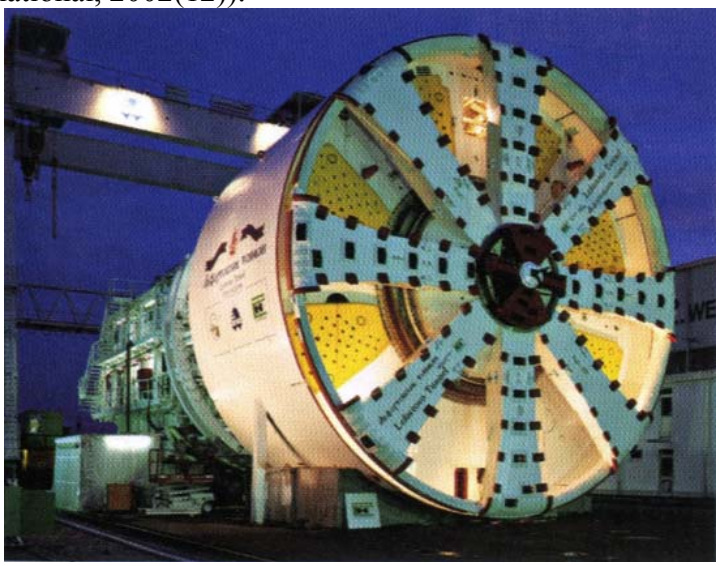

Figure 2.65 TBM refurbished as S-164 before it was shipped to Moscow
(from Tunnels and Tunnelling International 2008(06))

2.7.6. Construction

With the refurbished TBM and back-up units, including the slurry separation plant, German engineers and technicians were also sent to Moscow to train the Russian tunneling team. Before the excavation began, it was expected that the advance rate would be about 100 m/month, based both on the experience in the 4th Elbe tunnel in

Hamburg, where the average monthly progress had been 84 m, as well as the fact that it was the first use of such a large TBM in Russia. In fact, the average advance rate was 180 m/month, including all downtime, such as time for routing maintenance, crew entry, and replacement of the cutter tool. The best daily and monthly progress achieved was 12 m and 226 m, respectively (Tunnels and Tunnelling International 2003(03)). The total cost originally expected for the twin tube tunnel was around 2 billion US dollars. Due to the speed of excavation, the cost for the single-bore tunnel was 600 million US dollars.

2.8. CASE HISTORY VII: SILBERWALD TUNNEL, MOSCOW

2.8.1. Introduction

With the completion of the boring of the Lefortovo Tunnel in eastern Moscow, the entire tunneling system was dismantled and moved to the Silberwald tunneling site. The Silberwald Tunnel (Silver Forest Tunnel) is a 2.1-km long twin-tube double-deck tunnel for the missing link on the M-9 radial highway of west Moscow. The depth of the tunnel varies between 22 and 40 m. Of the 2.1 m tunnel length, a 1.51-km long section was driven by a TBM and the remainder was constructed by the cut-and-cover technique. The tunnel was to be constructed using a TBM to minimize the impact on the conservation area, Silver Forest, under which the tunnel runs. The geology consisted of highly-fissured medium-strength limestone, fine to coarse sand with boulders up to 1 m, and cohesive clay (Tunnels and Tunnelling International, 2005(05)).

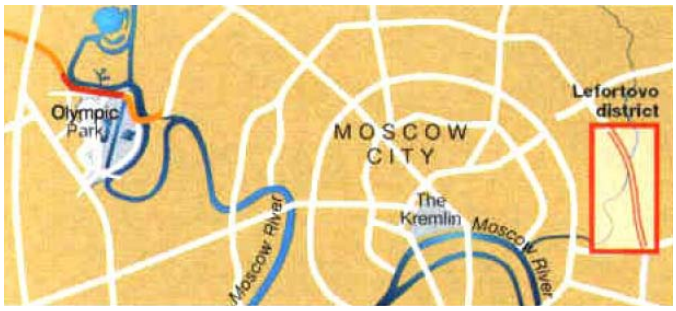

Figure 2.66 Location of the Lefortovo and Silberwald tunnel (from Tunnels and Tunnelling International, 2002(12))

2.8.2. Features of the tunnel

The tunnel consists of two 14.2 m diameter main bores and a 6.28 m diameter service tunnel which was constructed in between the two main bores and was excavated prior to the excavation of the two main bores. Concrete lining rings consisted of eight segments plus key, each ring is 2,000 m in width. Each main bore incorporates a three-lane highway on the upper deck. The lower conduit was reserved for a future extension of the existing subway line, Filevskaya. The subway extension project has not yet been realized (http://www.rustunnel.ru/news/3046.html:Russian).

The main bores do not have emergency lanes. Instead, the service tunnel is used for emergency access through cross passages that connect the service tunnel and the main bores at five points along the route.

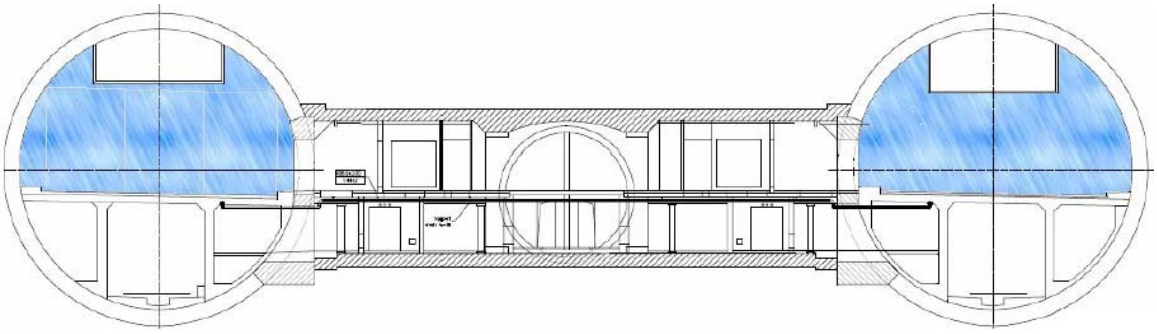

Figure 2.67 Tunnel section and cross passage (from Fogtec, 2008)

2.8.3. Construction

The TBM launched in April 2004 and the boring of the first drive was completed in March 2005. Excavation for the second tube started in December 2005 and finished in 2006 December. The excavation of the service tunnel was carried out using a 6.28 m diameter Herrenknecht Mixshield (S-290). The advance rate achieved was 78 m per week, and the average monthly progress, including the downtime, was about 120 m/month. The tunnel was opened to the public in December 2007. Another tunneling project (a 2.4-km long, single-bore tunnel in southern Moscow, the Zaryzino Tunnel) was proposed using the same TBM after refurbishment. However the proposal was never realized.

2.9. CASE HISTORY VIII: CHONGMING TUNNEL, SHANGHAI

2.9.1. Introduction

The Shanghai Yangtze River Tunnel is the largest-diameter driven tunnel in the world and is also the longest tunnel driven under a river. This tunnel is part of the 25.5-km long Shanghai-Chongming Highway that consists of the tunnel and a cable bridge. The length of the bored tunnel is 7.47 km and the remaining 1.5 km of the tunnel, including the approach ramp, was constructed using the cut-and-cover method. The tunnel opened to the public in October 2009. Ferries were used to cross the river before completion of the project. The new tunnel reduces travel time from two hours to thirty minutes.

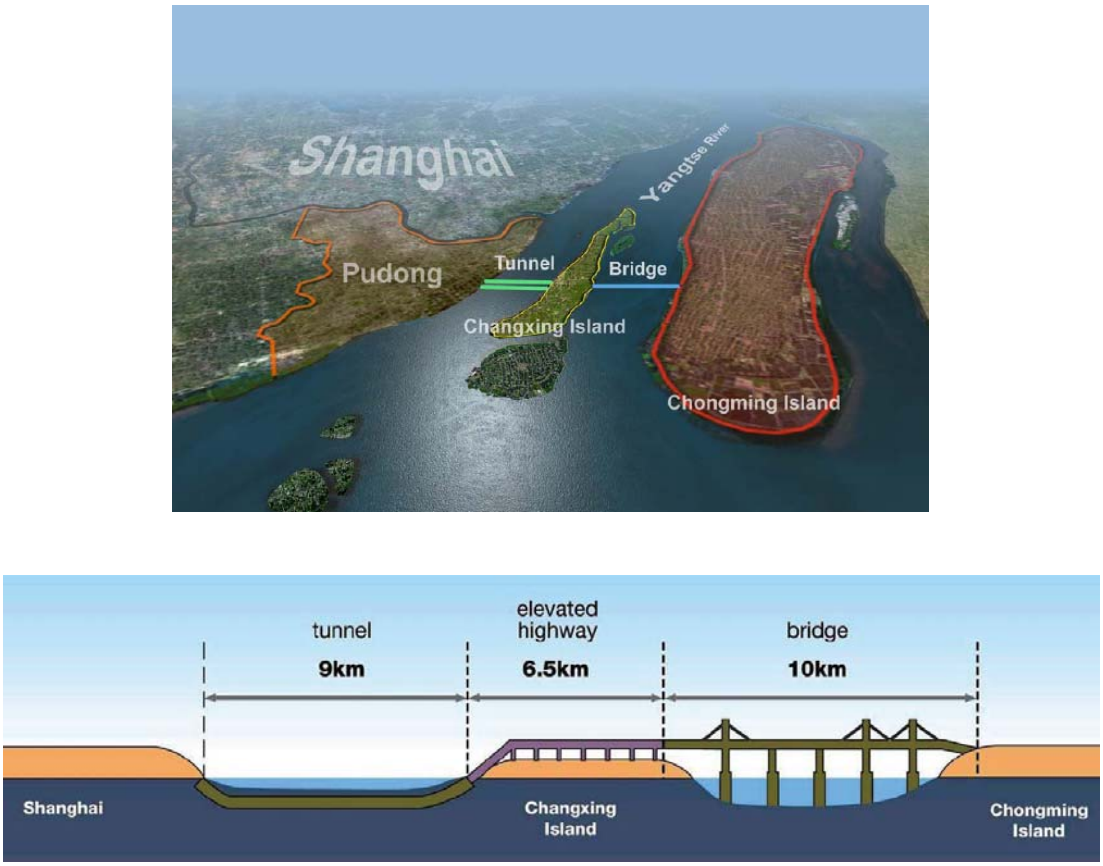

Figure 2.68 Project overview (from Münchener Rück, 2006)

2.9.2. Planning

The project was proposed by the Shanghai Municipal Planning Project Administration and approved by China's State Council, the country's highest decision-making body (Tunnel and Tunnelling International, 2003(03)).

The manufacture of the TBM was awarded to Herrenknecht in May 2006. The Mixshield was assembled at the Shanghai Pudong facility of Herrenknecht's Chinese partner, Shanghai Tunnel Engineering Co Ltd (STEC) (Tunnels and Tunnelling, 2006(06)). The assembly facility was located 6 km away from the launch shaft.

The preliminary design was carried out by Halcrow of England. The Shanghai Urban Planning and Design Research Institute took over the design and supervised construction. To accommodate a three-lane highway, a 15.43 m outer diameter was planned.

2.9.3. Features of the tunnel

The 15.43 m OD bores incorporate double-deck configuration. The upper deck is used as three-lane highway tunnel. The lower deck incorporates a rescue lane, safety systems, and a future metro link. A 650-mm thick precast segment was used. One ring was 2-m long and consisted of 9 segments plus a key.

The twin tubes are connected by eight cross passages at an interval of 800 m. The cross passages are 2.74-m wide hand-mined openings. The distance between centers of the two bores is about 23 m.

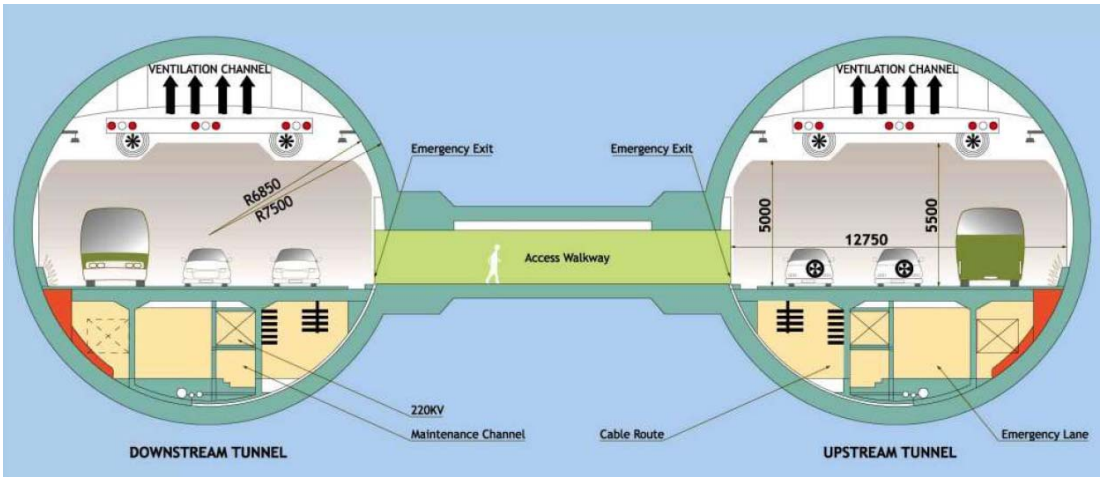

Figure 2.69 Configuration of the tunnel (from Münchener Rück, 2006)

2.9.4. TBM specifications

To cope with the difficult ground conditions, a Mixshield was to be used. The geology comprises sand, weak clay, and rubble. The maximum tunnel depth is 65 m and the maximum ground water level above the tunnel was expected to be 47 m. The TBMs were designed for a maximum working pressure of 6.5 bar. The six main spokes of the cutting wheel were accessible under atmospheric pressure for cutter tool replacement. The power installed to the cutterhead was 3,500 kW and provided the torque with 39,945 kNm.

2.9.5. Construction

The boring of the first drive was started in September 2006 and completed in May 2008, using the Herrenknecht S-317 Mixshield. The second drive was started in January 2007 and completed in September 2008, using the Herrenknecht S-318 Mixshield. The excavation was started from Pudong to Changxing Island. The best advance rates achieved were 26 m/day and 142 m/week (Tunnels and Tunnelling International, 2008(10)). The tunnel excavation was finished about a year earlier than the scheduled completion date.

The construction of the cross passages was carried out by hand-mining. The ground freezing technique was used and cast iron segments were used in place of 650-mm thick, precast concrete lining at the junction of the main tunnel and the cross passage.

2.10. DULLES TYSON CORNER TUNNEL

The 37-km long Dulles Corridor Metrorail project was proposed to extend the existing Orange Line of the Washington, DC Metro to the Dulles International Airport

(Figure 2.70). The project consisted of two phases: Phase 1 (West Falls Station to the Dulles access road at Wiehle Avenue; 18.5 km) and Phase 2 (the Dulles access road at Wiehle Avenue to Dulles International Airport; 18.7 km).

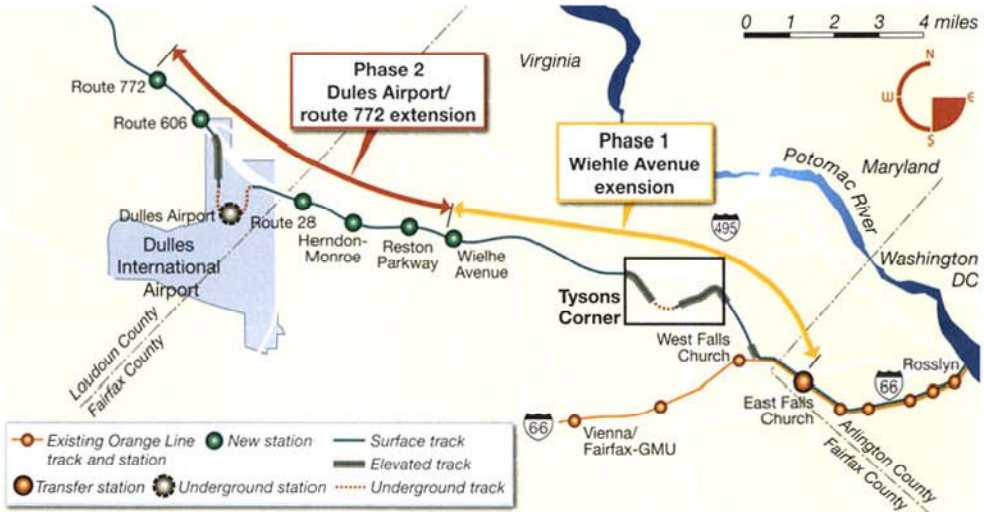

Figure 2.70 Dulles Metrorail Project overview
(Tunnels and Tunnelling International, 2008(03))

The extension line was originally planned to be built on-surface or on an elevated structure. At Tyson Corner, the tracks and stations were to be constructed on a viaduct and elevated structures. However, the Tyson Corner area was in the midst of active development and expansion. The home owners and other property owners did not want the construction of an aerial structure in the city center because it would negatively impact development of the area. The residents and property owners who protested construction of the aerial structure in Tyson Corner privately funded and established a not-for-profit, grassroots organization, Tyson Tunnel Inc. and hired engineers (Tunnels and Tunnelling International, 2008(03)). In January 2007, Tyson Tunnel Inc. proposed,

in an unsolicited fashion, a 5.4-km long large-bore tunnel as an alternative to the viaduct structure to cover the portion of the Phase 1 alignment at Tyson Corner (Figure 2.71).

Figure 2.71 View of the proposed tunnel at Tyson corner (Carter and Burgess Inc., 2007)

Once the tunnel option had been proposed, the ASCE Dulles Metrorail Project Technical Review Board carried out a feasibility study and concluded that construction of the large-bore, double-deck tunnel was technically feasible. But, after more than a year of dispute, the tunnel option was finally denied. Instead, the original viaduct option was chosen. The construction period for a tunnel had been deemed too long and the risks associated with the uncertain underground excavation too high to be acceptable, even though the construction of a large-bore tunnel may have been technically feasible. In Sections 2.10.1 to 2.10.5, the summary of the proposed tunnel and the decision-making process that led to the original viaduct option are presented.

2.10.1. Benefits and drawbacks of the tunnel option

The tunnel option requires higher construction/operation cost and a longer construction period compared to surface structures. It requires various safety and operation systems, such as for ventilation, drainage, pumping, and lighting,. However, bored tunnels have only a minimal impact on the surface area during and after construction. The tunnel option is superior from the urban landscape point of view.

Since Tyson Corner was a rapidly growing city center, the viaduct option eliminated some future real estate development opportunities. Therefore, it is possible that preserving those opportunities might have offset the high construction and operation costs of the tunnel option. Additionally, if the area consumed by the aerial structure were used to serve local traffic demand, the traffic congestion that was worsening in the area would have been mitigated.

2.10.2. Ground condition and selection of the TBM

Tyson Tunnel Inc. did not carry out any independent boring or geotechnical investigations. In order to prepare the alternative tunnel option proposal, they used the boring and testing data that had been prepared for the design and review of the viaduct structure. Therefore, out of the 226 boring data, about 200 borings did not extend to the depth of the tunnel invert (Carter and Burgess, 2007). Moreover, because the boring had been carried out before the large tunnel option was suggested, the gap between the boring points was too large to be used for the preliminary design of the tunnel and to give a reliable prediction of the TBM advance-rate, which was crucial to assess the risks associated with the extended construction period.

According to the geotechnical data prepared for the design of the viaduct, the geology is composed of schist, granite, and phyllonite bedrock overlain by residual soils and decomposed rock, as shown in Figure 2.72. The residual soil ranges from silty sand to clayey silt and the fines content is over 40%. Occasionally, unweathered rock zones, where SPT values exceed 100 blows per foot, exist within the decomposed rock. It was predicted that mixed-face subsurface conditions existed, and that the non-homogeneous excavation face would increase machine wear and damage. The ground conditions were predominantly defined as decomposed rock and mixed-face. Due to the lack of geotechnical data, Tyson Tunnel Inc. did not propose the type of TBM that should be employed.

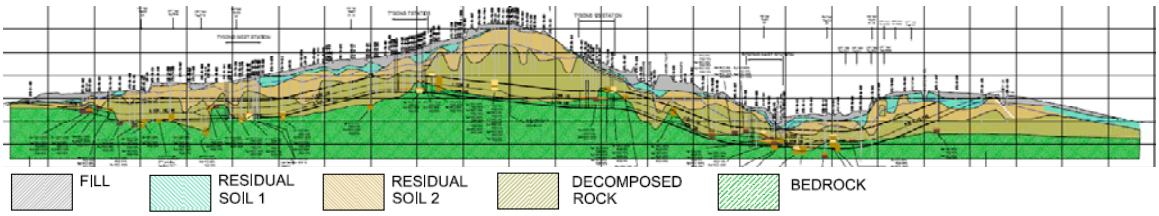

Figure 2.72 Geological profile (Dr. G Sauer Corporation, 2006)

2.10.3. Schedule and construction cost

Construction of the aerial structure was expected to take 60 months, whereas construction of the tunnel was predicted to require more than 54 to 70 months (Carter and Burgess, 2007). This estimate did not include the bidding process, environmental studies, hearings, additional subsurface exploration, or the design and review process. Therefore, if the large tunnel option were chosen, postponement of the completion date of the Dulles Corridor Metrorail extension project would have been inevitable. Both the construction cost and schedule are largely influenced by the TBM advance rate. Carter and Burgess (2007) developed a chart that shows the relationship between the total cost of a bored tunnel and the advance rate (Figure 2.73). The cost was estimated based on a 5-day production week and a 24-hours/day construction schedule.

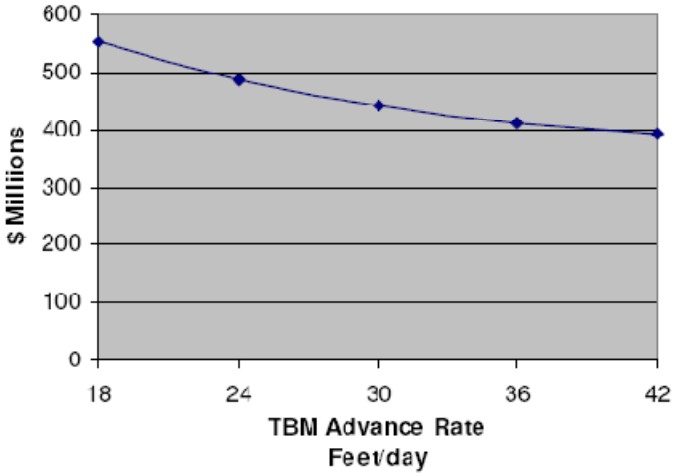

Figure 2.73 Total cost of bored tunnel according to the TBM advance rate (Carter and Burgess, 2007)

To save time and cost to manufacture the TBM, refurbishment of the existing Mixshield (S-252) used for the SMART project in Kuala Lumpur, Malaysia was proposed. Because the diameter of the S-252 was 13.21 m, a cutterhead and a shield bigger by 0.35 m in diameter was needed for proper refurbishment. However, the reliability of the refurbished and adjusted TBM was questionable. Ultimately, the proposal to refurbish the TBM used for the SMART project was not accepted because the failure of the TBM during excavation would have led to a significant delay in the entire construction schedule.

2.10.4. Feature of the tunnel and station

The proposed tunnel had a 13.2 m OD and 12.3 m ID. A 46-cm thick precast segmental lining was to be used for the double-deck configuration (see Figure 2.75). Four mined stations at a depth of 18 to 32 m were planned. Table 2.16 presents the depth of the tunnel at the lower level platform. The side view of the mined station is

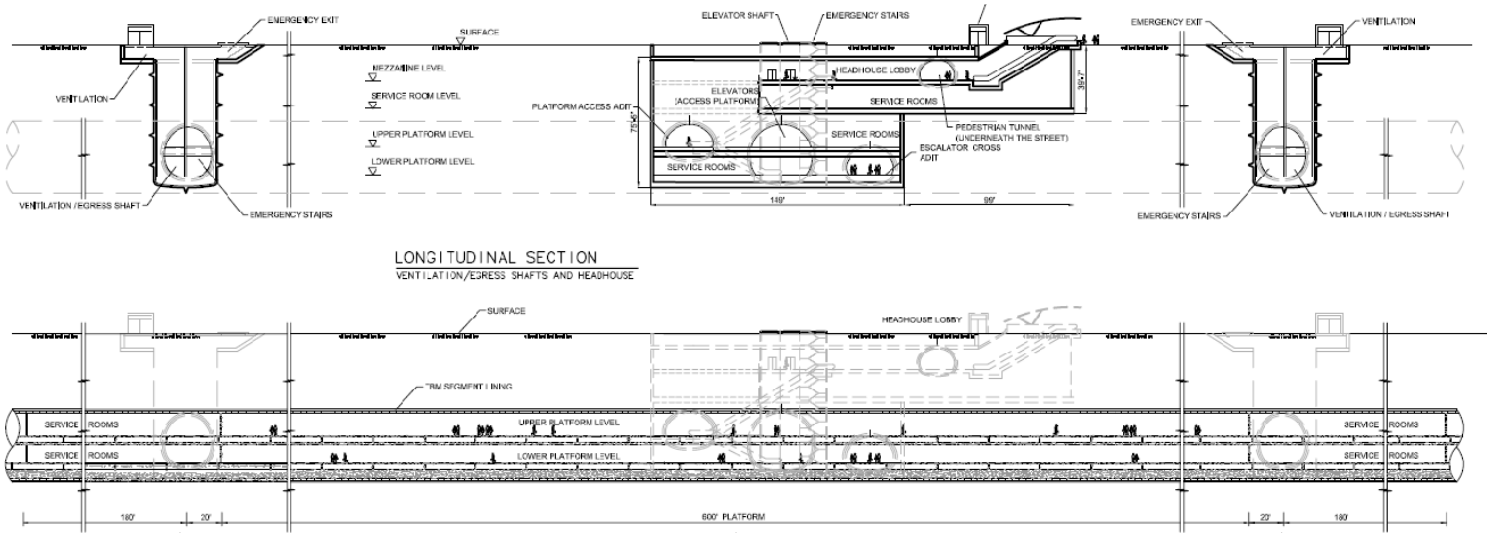

Figure 2.74 Side view of the mined station

shown in Figure 2.74. Upper and lower platforms were planned within the single large-bore tunnel (Figure 2.75). The continuous station scheme, which had first been introduced in Metro Line 9 in Barcelona, Spain, was employed. The platforms were to be 183-m long and elevators and escalators would have been used to provide access from the ground level to the platform level in the station.

Table 2.16 Depth of the station (at the lower level platform)

Station	Tyson East	Tyson Central 123	Tyson Central 7	Tyson West
Depth (m)	18.7	29.3	32.7	22.6

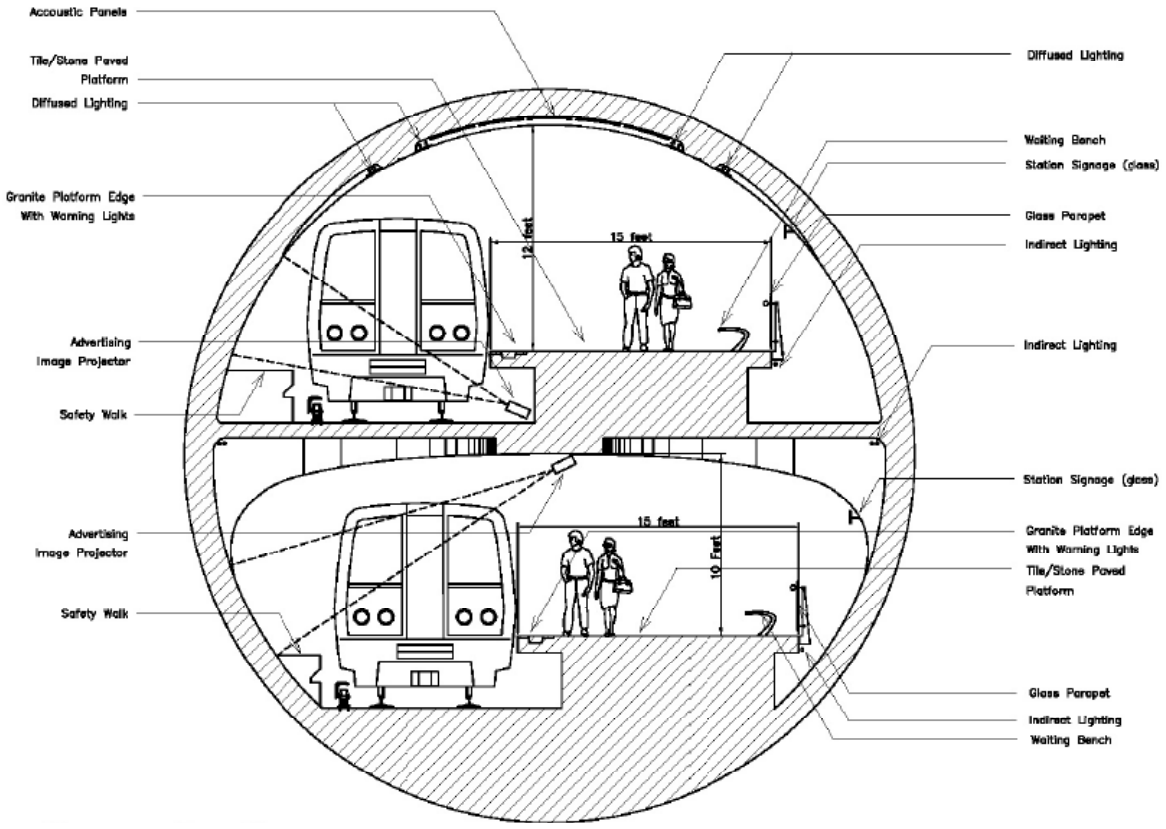

Figure 2.75 Cross sectional view of the tunnel at a station

Ventilation shafts were to be constructed at both ends of the platform. Emergency stairs were to be included within the ventilation shafts. The ventilation analyses were not carried out, thus the required ventilation capacity was not determined.

2.10.5. Construction planning

During the decision-making process, the Virginia Department of Transportation (VDOT) and Washington Metropolitan Area Transit Authority (WMATA) pointed out that the tunnel proposal failed to secure the land for storing precast lining segments (700 m^2) as well as slurry plant and muck pit acreage (12,000 m^2). Furthermore, the tunnel proposal failed to provide an effective logistics sequence plan, such as setting up of safe acceleration and deceleration lanes in the access highway for the muck transport trucks and temporary lane closure for the haulage of heavy construction equipment.

2.11. STATE ROUTE 99 TUNNEL

The Alaskan Way Viaduct and Seawall Replacement Program (AWVSRP) includes State Route 99 tunnel construction, demolition of the Alaskan Way Viaduct and seawall replacement in Seattle, WA. In this dissertation, only the SR99 tunnel is covered. As of July 2010, the design/build project is under the bidding process and the information described below is subject to change with the project's progress.

The Alaskan Way Viaduct is a 3.4-km long, 12-m wide, double-deck, reinforced-concrete aerial highway that was built along Seattle's Elliot Bay waterfront area in 1956. It was constructed upon the sand fill that is supported by the Alaskan Way Seawall, which is a sheet pile wall topped with a precast concrete platform. However, the viaduct

and the seawall were damaged in the February 2001 Nisqually Earthquake and a number of analyses showed that they should be reconstructed or demolished (Figure 2.76).

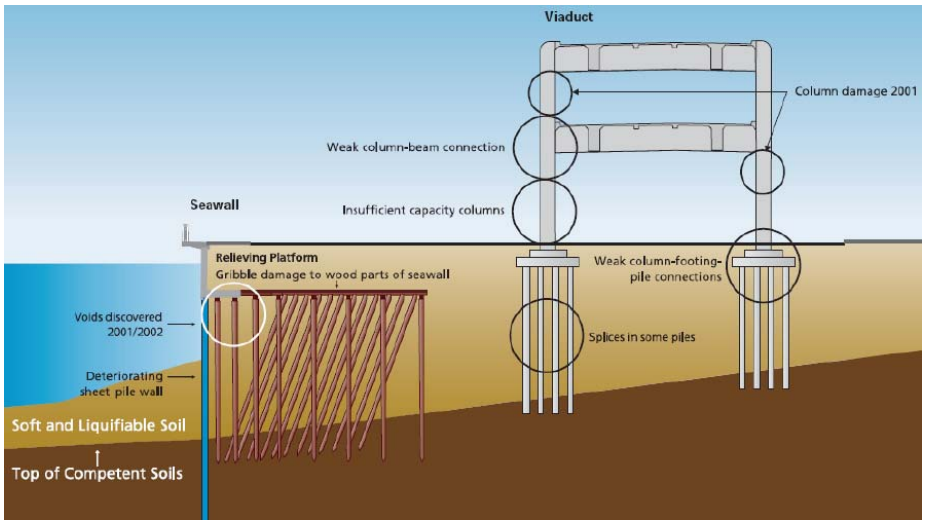

Figure 2.76 Damaged Viaduct and Seawall during earthquake (Washington Department of Transportation, 2008)

Since 2002, numerous proposals have been made including a cut-and-cover tunnel (Figure 2.77), where the west-side wall of the tunnel would serve as a seawall, as well. In 2007, the State government chose two options: reconstruct both the viaduct and the seawall; or demolish the viaduct and construct a two-level, cut-and-cover tunnel (Figure 2.77). However, the average daily traffic along the waterfront mainline was 103,000 trips/day and disruption to the traffic and the surface area during the construction of either a viaduct or a cut-and-cover tunnel was unacceptable (Parsons Brinckerhoff and Jacobs Engineering, 2009). Consequently, both options were discarded and the construction of a TBM-driven tunnel, which would minimally affect the surface area, was considered. In December 2008, construction of a single-bore, double-deck tunnel (Figure 2.79) was approved. The construction of the tunnel was expected to take 4-5

years and the viaduct would stay open to traffic during the construction. The tunnel is 2.7-km long and travels between 18 to 61 m below the surface.

Figure 2.77 Proposed cut-and-cover tunnel (Washington Department of Transportation, 2008)

2.11.1. Determining the tunnel grade

Two options were proposed for vertical alignment, as shown in Figure 2.78. The alignment must be chosen to minimize negative impact to the adjacent underground structures and surface settlement, right-of-way issues, and to allow for more favorable soil conditions. The following constraints were evaluated and Alternative 1 was chosen for vertical alignment (Parsons Brinckerhoff and Jacobs Engineering, 2009):

- Maintain a tunnel diameter (1D) clearance to adjacent underground structures.
- Avoid possible settlement and right-of-way issues by boring too close to the surface or near adjacent building foundations.
- Maintain a maximum 5 percent grade.
- Due to the TBM excavation process, mitigate unknown inherent risks by increasing depth from surface.

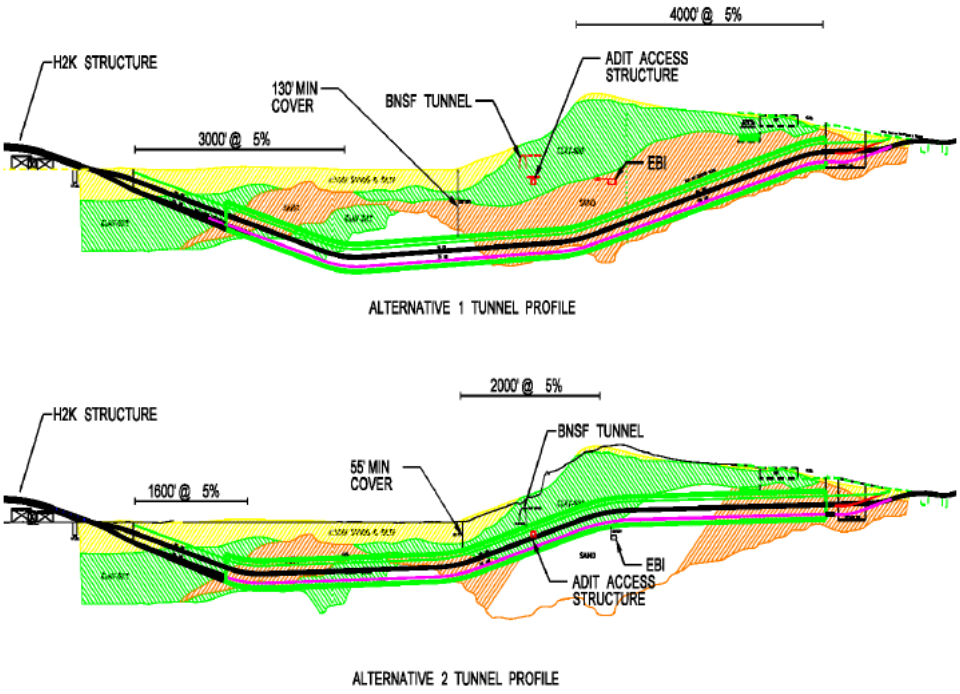

Figure 2.78 Vertical alignment options

2.11.2. Comparison between single bore and twin bore

As stated in the previous section, the driven tunnel option was chosen after years of study because other options (construction of a new viaduct structure or a cut-and-cover tunnel) were unacceptable based on their massive disruption to the city. Another study was carried out to evaluate the relative benefits of a twin-bore, single-deck tunnel and a single-bore, double-deck tunnel (Figure 2.79). The plan view of each option is shown in Figure 2.80.

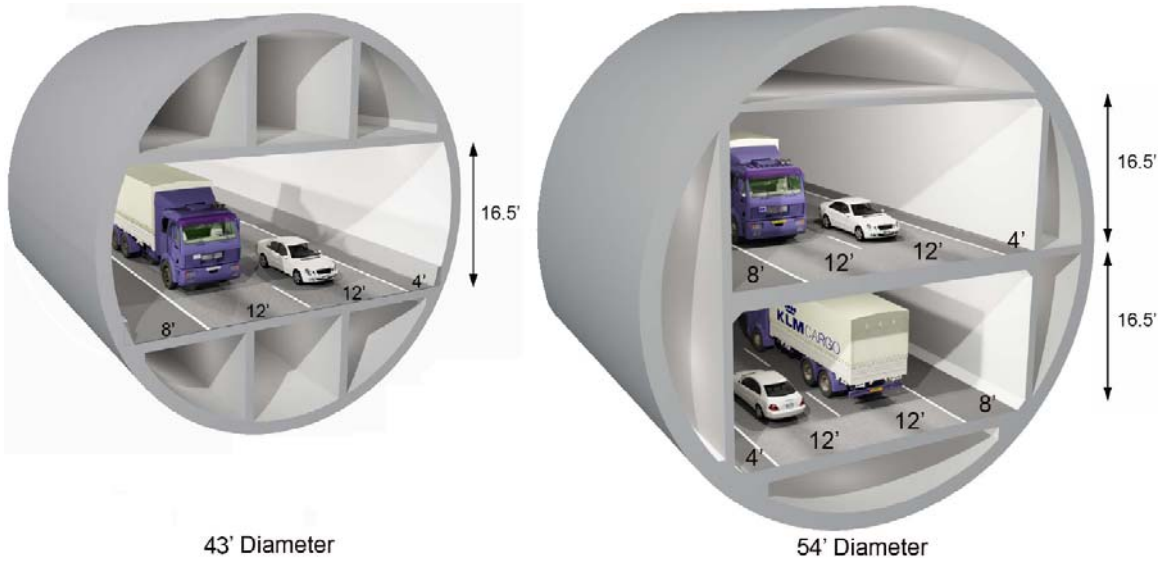

Figure 2.79 Twin-bore single-deck (13.1 m OD) and single-bore double-deck (16.5 m OD) option (Washington Department of Transportation, 2008)

Schedule and cost estimates for the twin-bore and single-bore options are shown in Figure 2.81 and Table 2.17. It was found that the single-bore, double-deck option was superior. The overall tunnel construction cost was estimated to be 2.8 billion USD for the twin-bore option and 2.1 billion USD for the single-bore option. The expected completion date of the single-bore tunnel was 1 year earlier than that of the twin-bore tunnel. It is notable that the right-of-way cost of the single-bore option is only 1/3 that of the twin-bore option because the corridor of a single-bore tunnel can remain under the public roads and does not interfere with privately owned properties. Extensive soil improvements, including inject grouting and soil mixing (jet grouting), were planned for sensitive areas such as historical sites and where cover-depth is small. Realtime monitoring devices will be employed to measure vertical and horizontal movement of the ground and structures along the tunnel corridor.

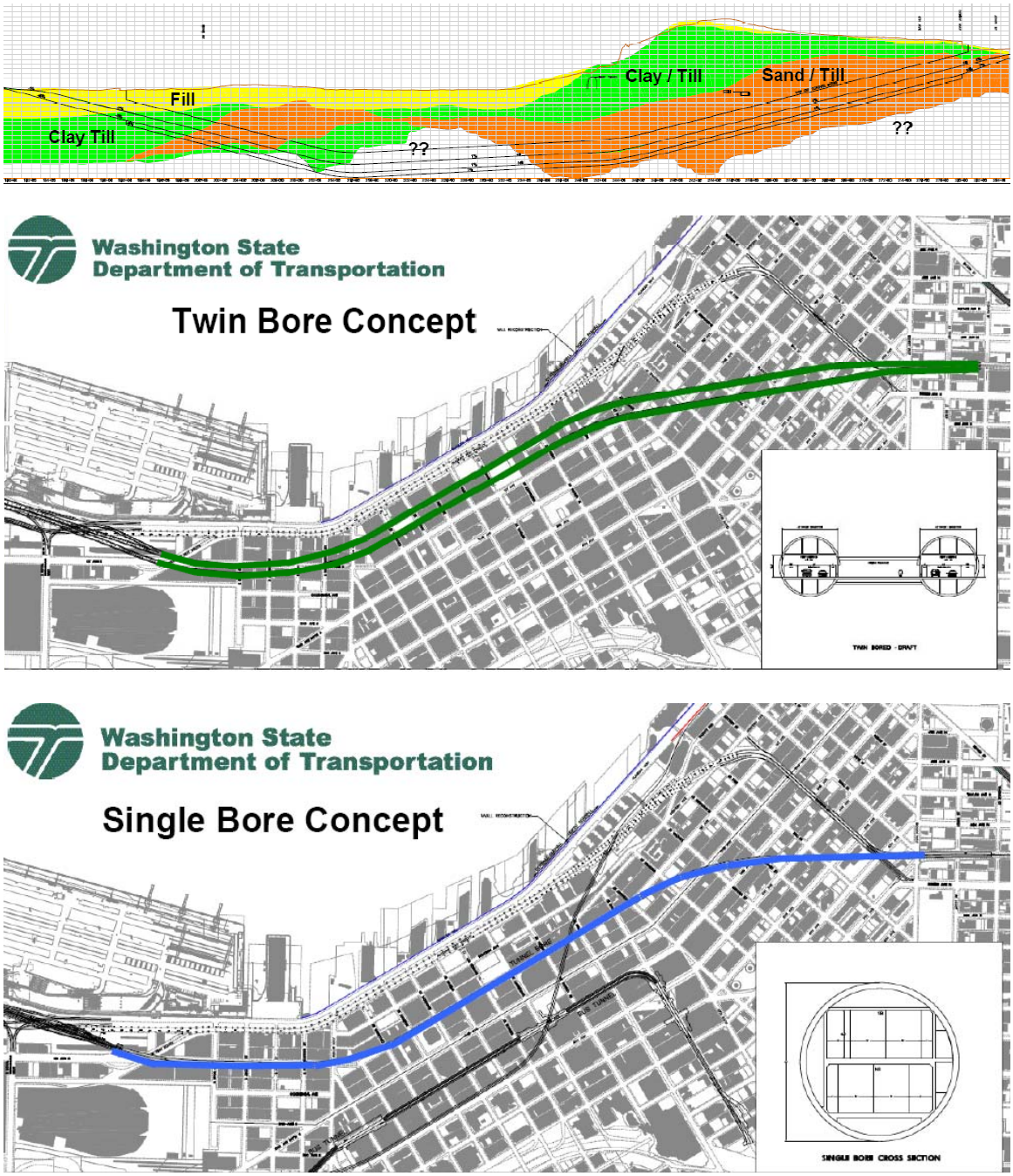

Figure 2.80 Twin-bore and Single-bore option plan views (Washington Department of Transportation, 2008)

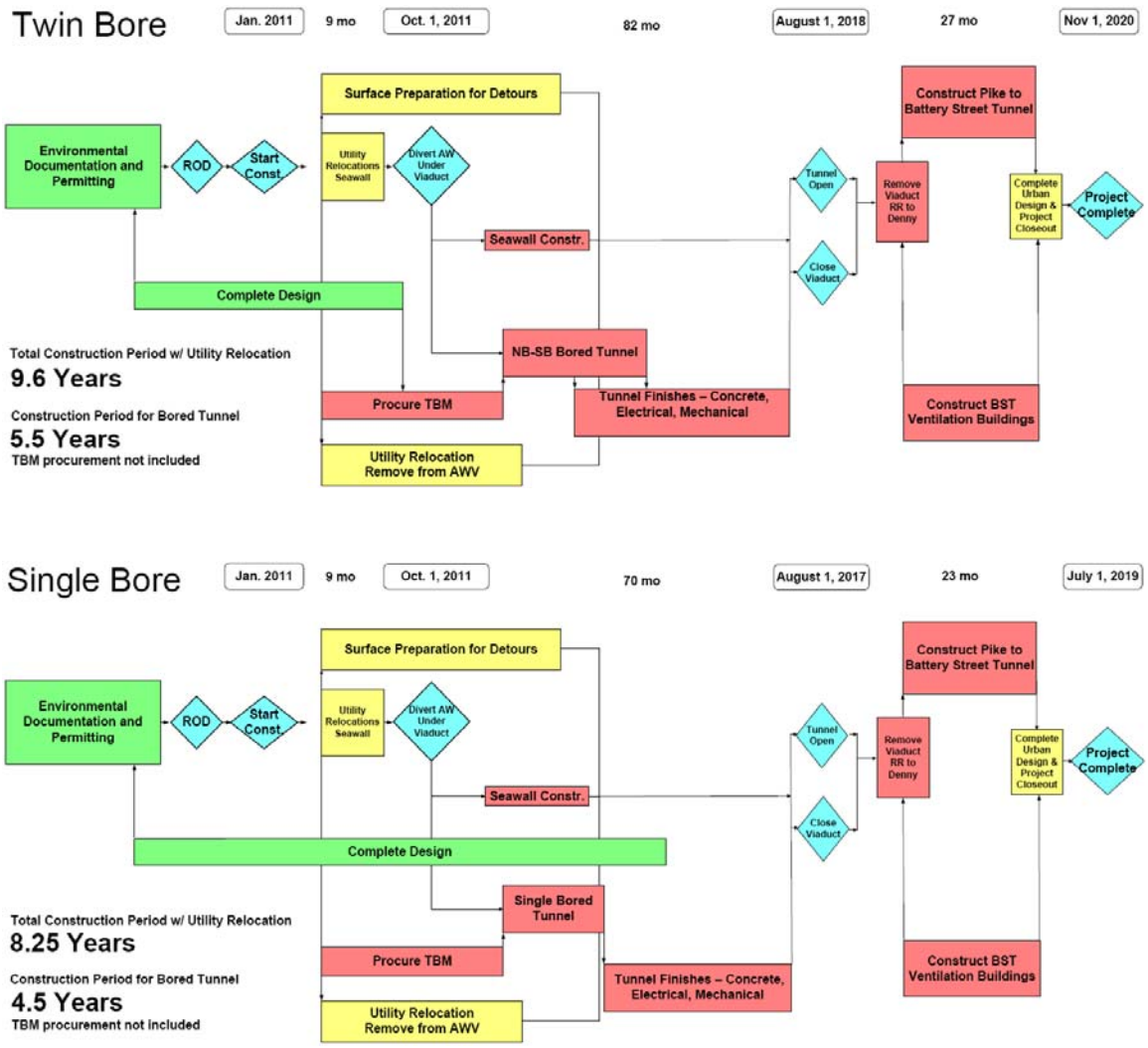

Figure 2.81 Construction schedule estimates for twin- and single-bore options (Washington Department of Transportation, 2008)

Table 2.17 Tunnel cost estimate (in million UDS; Washington Department of Transportation, 2008)

Item	Twin	Single
New city street	20	8
South tunnel entry	110	58
Bored tunnel	430	330
North tunnel entry	50	42
Utilities	50	47
Tunnel systems	173	159
Subtotal direct cost	833	644
Construction allowance for underdeveloped design (25%)	208	161
Contractor mobilization, overhead, and profit (24.25%)	202	156
Construction estimate	1,243	961
Contract management, administration, and construction management (15.5%)	193	149
Preliminary and final design	196	151
Tunnel cost without escalation, contingency and risk	1,632	1,262
Contingency (add 12%)	1,828	1,413
Risk (add 28%)	2,339	1,809
Escalation (per global insight) (add 15.55%)	2,703	2,090
Right-of-way costs	120	40
Program cost for tunnel	2,823	2,130

2.11.3. Safety issues

The tunnel will be designed to withstand a 2,500-year average-return-interval (ARI) earthquake (peak ground acceleration of 0.76 g). For a 100-year ARI earthquake the structure of the tunnel was designed to remain in its elastic range, and for a 2,500-year ARI earthquake, it was designed to form plastic hinges (Clark, 2006). The challenge is that the southern part of the tunnel will be constructed in a loose, silty, sand fill, which is extremely liquefiable during seismic events. Additionally, considerable groundwater inflow is expected because the tunnel is located beneath the mean sea level and the groundwater flows from a hill on the east.

2.12. SUMMARY

Case histories on large-diameter mechanically driven tunnels for transportation purpose were presented for the following tunnels:

- Stormwater Management And Road Tunnel, Kuala Lumpur, Malaysia (Section 2.2)
- Subway Line 9 Tunnel, Barcelona, Spain (Section 2.3)
- Highway M30 Tunnel, Madrid, Spain (Section 2.4)
- Socatop A86 Duplex Tunnel, Paris, France (Section 2.5)
- 4th Elbe Tunnel, Hamburg, Germany (Section 2.6)
- Lefortovo Tunnel, Moscow, Russia (Section 2.7)
- Silberwald Tunnel, Moscow, Russia (Section 2.8)
- Chongming Tunnel, Shanghai, China (Section 2.9)

A number of topics have been covered. First, the purpose(s) and the features of the tunnel are explained. When innovative schemes are used, such as multi-purpose usage of a tunnel and continuous station scheme, they are presented with proper figures and photos. Next, the specification of the TBM is given and factors, such as geological conditions, that considered during TBM selection process are described. Ventilation and safety features implemented in the tunnel are given. Special design and construction consideration are given when available and construction stages and schedules are briefly illustrated in a chronological order. Finally, decision making process that led to the bored tunnel option is given. The reason why tunnel option was chosen instead of other types of infrastructure, such as surface roads, aerial structures or

bridges is presented. Also reasons why TBM method was selected instead of cut-and-cover or conventional drill-and-blast method are given.

A number of factors are observed which are found in common from the case histories presented above are: The length of the tunnel was long enough (over 2 km) to justify the initial acquisition cost of the TBM. The ground was not composed of extremely hard rock where mechanical boring might become inefficient. They were constructed in urban environment where disruption of the surface area and noise- and visual-pollution is prohibited.

Large diameter mechanically driven tunnel cases that have been proposed in the U.S. were also presented for the following tunnels:

- Dulles Tyson Corner Tunnel (Section 2.10)
- State Route 99 Tunnel (Section 2.11)

Dulles Tyson Corner Tunnel was proposed by a group of residents who resisted against the construction of the aerial structure in the city center, but it was denied because of risk of delaying the opening of the entire metro transit system and additional expenses. State Route 99 Tunnel is expected to open to the public by 2015. A single-bore double-deck tunnel and a twin-bore single-deck tunnel were compared in terms of construction cost and schedule during, and the former option was found to be superior.

CHAPTER 3. STABILITY OF TUNNEL HEADING AND FACE SUPPORTING MECHANISM

3.1. INTRODUCTION

As tunneling in unfavorable geotechnical conditions and in heavily populated urban areas is becoming widespread, the importance of maintaining tunnel face stability is gaining more importance. Ensuring tunnel face stability is directly related to the safe and successful construction of a tunnel. In the conventional literature on tunneling, in fact, the face is seen as "the enemy". On the other hand, 800 km of tunnels excavated with and without Tunnel Boring Machines (TBMs) according to the ADECO (Analysis of COntrolled DEformations), have shown the success in using the ground *ahead* of the tunnel face (core) as a stabilization measure (Lunardi, 2008), and therefore as the "best friend" of the designer and contractor. Within this context, the analysis of an unlined and unsupported tunnel leads to the determination of the face/core behavior category (Figure 3.1).

Since the arrival of the tunnel face reduces the confinement of the ground to zero (Figure 3.2), in category B or C the designer may then act in two ways: artificially create confinement (σ_3 increase $\rightarrow$ decrease of Mohr circle diameter), or engineer the ground in the core to increase its strength and stiffness. With reference to Figure 3.3, countermeasures are then designed to either confine, protect, and/or reinforce the ground ahead of the tunnel face (preconfinement) or to confine the ground by acting on the walls of the cavity (excavated space) or in the ground behind the face (cavity confinement).

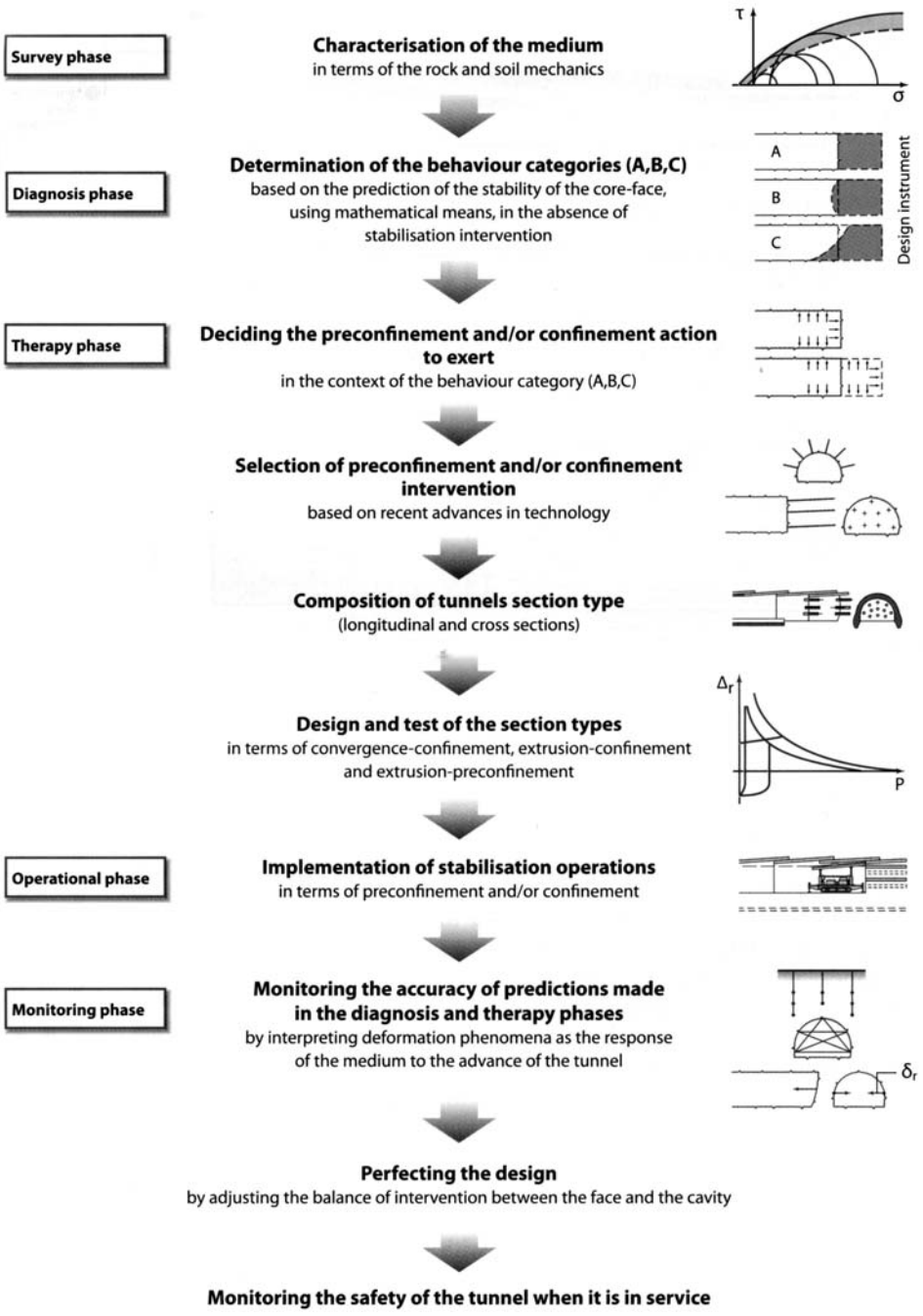

Figure 3.1 Tunnel face/core behavior category, After Lunardi (2008)

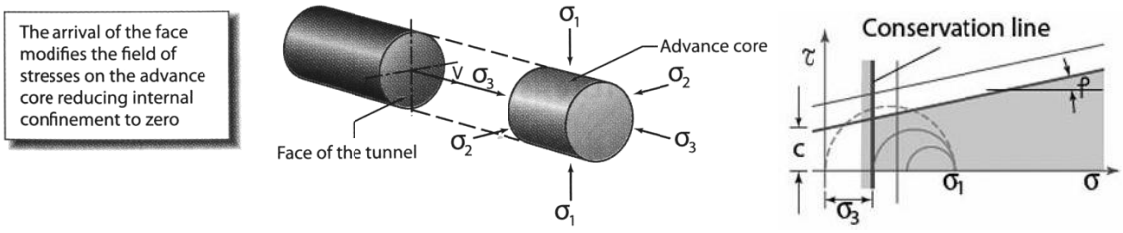

Figure 3.2 State of stress of a tunnel when tunnel face arrives, After Lunardi (2008)

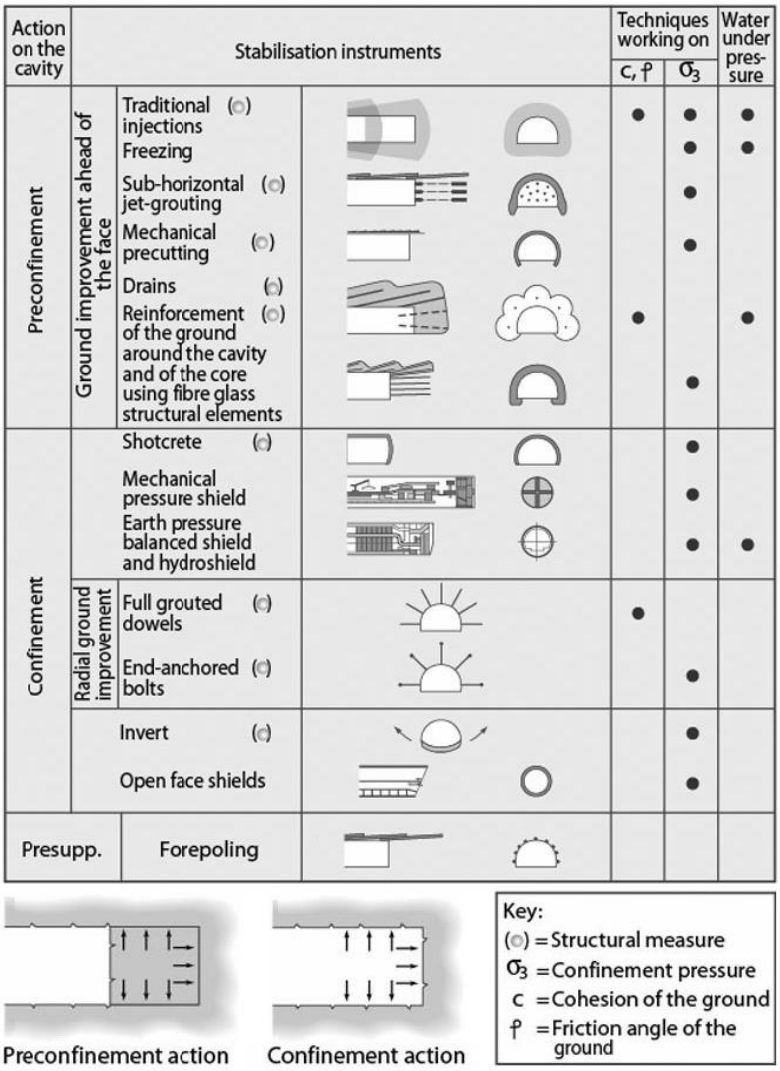

Figure 3.3 List of preconfinement/confinement techniques, After Lunardi (2008)

Face stabilization is one of the most critical issues that should be achieved during mechanical tunnel excavation. In a full face excavation using a TBM, the tunnel face is mechanically supported by the TBM cutterhead and by the pressure exerted by slurry or muck in the excavation chamber through openings in the cutterhead, whereas walls are radially supported by the shield and the final lining. As a consequence, TBM action is classified as cavity confinement in Figure 3.3. Two extreme cases of failure may occur due to the poor management of face support pressure: the formation of chimneys or the development of blow-outs in the ground above the tunnel face. The minimum pressure to avoid face instability is affected by various factors, such as cohesion, friction angle and permeability of the ground, type of the machine, advance rate, unit weight of slurry or conditioned soil, tunnel diameter, cover depth, and location of the ground water table. Generally speaking, it is beneficial to maintain the support pressure as small as possible to minimize the unfavorable effects large support pressure might induce, e.g., increased machine wear, arching of the muck in the excavation chamber and the reduced advance rate, as long as an excessive deformation of the ground, an unacceptable surface settlement and influx of groundwater do not take place. Face stability of a mechanically driven tunnel has attracted many scholars and engineers, and many publications are available today. Many researchers have proposed analytical approaches to determine the required pressure to stabilize the tunnel face. Most of them are based either on limiting equilibrium analysis (Jancsecz and Steiner, 1994; Anagnostou and Kovári, 1994 and 1996; Broere, 2001), or limit analysis (Atkinson and Potts, 1977; Davis et al., 1980; Leca and Dormieux, 1990). The detailed description for the analytical and empirical/ experimental solutions are described in Sections 3.3.1 to 3.3.3.

3.2. SHIELD TUNNELING AND FACE SUPPORT PRESSURE

Shield tunneling, as a tunnel excavation and construction principle, has a long tradition, and great progress has been made since its first development by Sir Marc Isambard Brunel in the early of 19th Century (Stack, 1982). The basic concept of shield tunneling involves pushing a shield, which is a rigid cylindrical frame, forward on the axis of the tunnel while, at the same time, excavating the ground at the face and erecting a preliminary or final tunnel lining at the shield tail. The shield must withstand the pressure of the surrounding ground and water pressure, if the tunnel is located beneath the water table. Figure 3.4 describes the methods of tunnel-face stabilizing and discharge of excavated material.

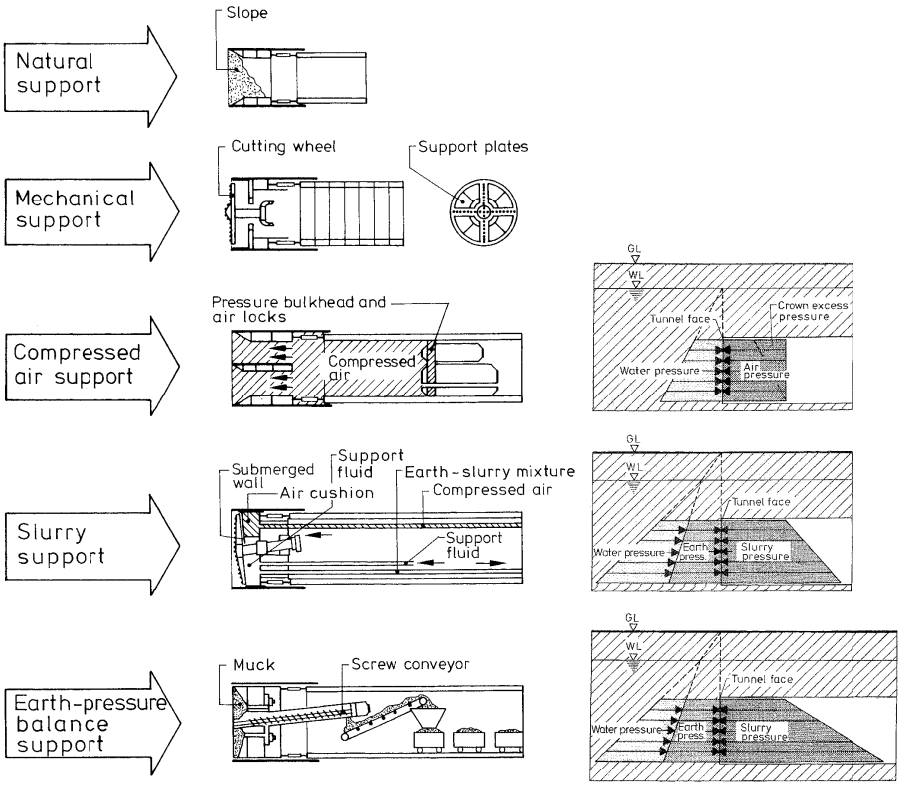

Figure 3.4 Types of TBMs and tunnel face support method (Maidl et al., 1996)

3.2.1. Face support during mechanized tunneling

The method of face support is categorized mainly by the supporting medium. It is summarized below.

- Natural support

  The tunnel face is stabilized by the inherent stability sustained temporarily and the support pressure provided by the slope of the soil made inside the excavation chamber. The volume of the slope formed inside the shield can be reduced (thereby reducing the amount of ground subsidence) by installing the intermediate shelves that separate the shield horizontally.

- Mechanical face support

  The tunnel face is supported passively by placing a steel plate (breast plate) in front of the excavation chamber. For the shield with breast plates and part-face excavation tools, such as a roadheader, the supports are removed only for the parts where excavation takes place. A closed cutting wheel supports the face by itself. This is often called the open-faced shield method, a term which refers to the tunneling machine without a closed pressure compensation system. Generally, these are only suitable for dry ground conditions, because ground water ingress is not controllable using an open-face shield.

- Compressed air support

  This method uses compressed air as a supporting medium to prevent the ingress of groundwater and surface settlement. A steel plate (pressure bulkhead) at the back of the excavation chamber divides the pressurized zone in the excavation chamber from the rest of the shield and the tunnel. The air pressure is normally kept in

balance with the hydrostatic pressure of the groundwater. When the cover depth is insufficient, the ground above cannot resist the force generated by the flow of air current, and the collapse of the tunnel face can be induced. Because of this risk, the compressed-air shield is rarely used in today's tunneling sites.

- Slurry shield

A slurry shield refers to a TBM that supports the tunnel face by means of a pressurized slurry, which is a viscous mixture of bentonite/clay and water with or without chemical agents or polymers. The prototype of the slurry shield was developed by Wayss & Freytag in 1972, when they introduced the submerged wall (also known as front bulkhead) between the cutting wheel and the pressure bulkhead (Figure 3.5). The support pressure is exerted to the tunnel face by means of the pressurized slurry and is regulated by the air pressure in the rear chamber (Maidl and et al., 1996).

Bentonite is used because of its swelling potential and high plasticity. In the ground, the bentonite suspension seals the tunnel face to form a thin impermeable film (filter cake). Consequently the support pressure exerted by the pressurized slurry is applied to the tunnel face more effectively. The excavated material is mixed within the excavation chamber by an agitator, and the screw conveyor and conveyor belt system transport it to the separation plant located on the surface for the reutilization of the slurry suspension after treatment.

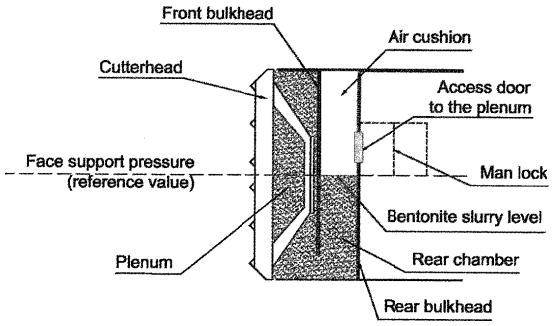

Figure 3.5 Excavation chamber of a slurry shield (Guglielmetti et al. 2007)

- Earth-pressure balance shield

Since this method was developed in the early 70's in Japan, it has become one of the most widely used mechanized tunneling methods, along with the slurry shield tunneling technique. Earth-pressure balance shields utilize the excavated ground as a supporting medium. In clayey ground, the muck, which is excavated material mixed with a conditioner (water, slurry, and/or polymer as foam), is extracted from the excavation chamber in a controlled manner to counterbalance the earth and water pressure acting on the tunnel face. The extraction of the muck takes place by means of a screw conveyor. Because the pressure is developed in the excavation chamber by controlling the advance rate and the extraction rate, the use of EPB technology is not advised for ground with fines content lower than 10% due to its high permeability coefficient. The conditioning agents, such as bentonite slurry, foam, and polymer, are often added in the excavation chamber to secure the continuous and homogeneous application of the face-support pressure, facilitate plug formation in the screw conveyor, and minimize machine wear (Vinai et al., 2007).

3.2.2. Extraction of spoil

The material removal from the excavation chamber has to be carried out without influencing the face-support pressure in the excavation chamber. The excavated material is transported from the excavation chamber to the surface for separation and deposition using various techniques, depending on the type of shield and the soil type. For the discharge of the excavated material out from the excavation chamber, either dry muck hauling, hydraulic mucking (slurry transport), or conditioned muck hauling is used. The dry muck hauling method is used for low water content excavated material in the compressed-air and open shields. Transport of the spoil is carried out by a belt conveyor or scraper conveyor. In the case of the compressed-air shield, the pressure difference must be overcome, and that is achieved by installing a material air lock or cellular wheel lock. Hydraulic mucking is used for the slurry shield and the hydroshield where the excavated material exists as a form of slurry. Screw conveyors or suction pipes are commonly used. Figure 3.6 shows the schematics of an earth-pressure balance shield using two stages of a muck transportation system: a screw conveyor (from the excavation chamber to the rear of shield) and a conveyor belt (from the rear of the shield to outside the tunnel). To prevent any oversized solids from entering the discharging system, a grill and a crusher are installed in front of them. The allowable solid size for a screw conveyor depends on the geometry of the screw, inclination, pressure difference, and soil properties. An agitator is installed to avoid the accumulation of heavy and fast sinking solids. For an earth-pressure balance shield, conditioned muck is transported in its plastic state. To improve the consistency and homogeneity that is required for transferring material in its plastic state, either a fluid or agent is supplied to the excavation chamber. Unlike the compressed-air shield or slurry shield, a sudden collapse of the tunnel face

into the excavation chamber is not possible with the earth-pressure balance shields where the excavation chamber is filled with pulpy and compacted material. This fact makes it unnecessary to have a grill or crusher in front of the discharge screw.

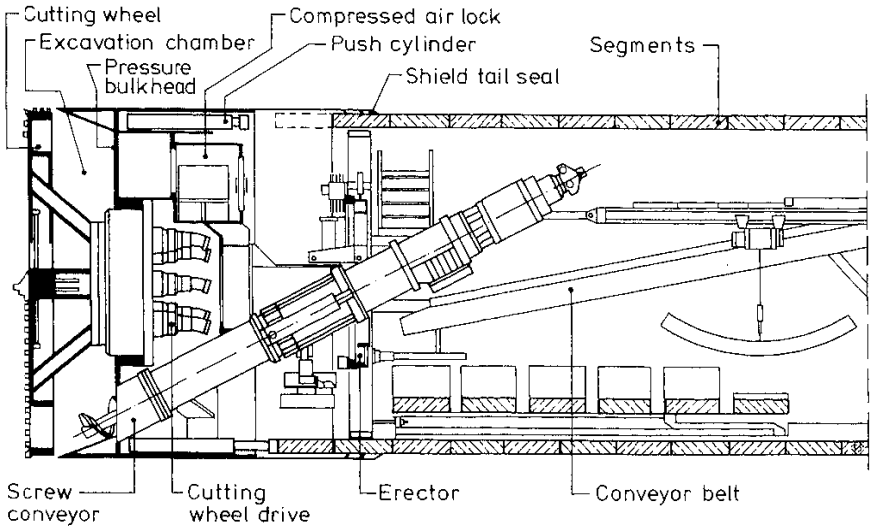

Figure 3.6 Schematics of muck discharge system of an earth-pressure balance shield (Maidl et al. 1996)

3.3. EXISTING ANALYTICAL STABILITY SOLUTIONS

The geotechnical analysis of conventional soil mechanics problems is divided into two groups – the stability problem and the elasticity problems: The ground should have suitable factor of safety and meet the serviceability requirements (Terzaghi et al., 1996). They are considered as two independent problems and they are approached in a different manner. It is the condition of the ultimate failure of the soil mass that is considered in the stability problems and solutions to these problems provide the engineer with a load that will cause failure of the soil mass under consideration. On the other hand, it is the

deformation of the soil mass under working load conditions that is considered in the elasticity problems.

The actual behavior of soils is very complicated and no mathematical model can completely describe the real behavior. Drastic idealization is necessary to only capture the essential features within the mathematical model for practical applications. It is well known that soils are not linearly elastic or perfectly plastic. However, the Hooke's law of linear elasticity has been used to describe the behavior of a soil mass under moderate working load conditions, and Coulomb's law of perfect plasticity has been used to describe the behavior of soil mass under ultimate strength condition because plastic flow becomes a dominant factor governing the overall soil behavior compared to elastic behavior. To assess the ultimate strength (collapse load), the perfect plasticity model has been extensively used in conventional soil mechanics (Chen and Liu, 1990; Davis and Selvadurai, 2002).

Stability solutions for a boundary value problem of a deformable continuum must satisfy three basic physical conditions. They are the stress equilibrium equations, the compatibility equations and the constitutive equations. In general, an infinite number of the stress states exist that do not violate the yield criteria and satisfy the equilibrium equations and stress boundary conditions. Likewise, an infinite number of displacement modes exist that satisfy the displacement boundary conditions. Finding a complete analytical solution that satisfies all three conditions is difficult and sometimes impossible for all but the simplest problems. To make the problem tractable, either limit equilibrium analysis or plastic limit analysis can be used as described in this section.

3.3.1. Limit equilibrium analysis

The limit equilibrium method is the most frequently used analysis technique for the stability of geotechnical structures, which applies a static equilibrium condition between forces and moments acting on the soil mass and the strength mobilized in the soil for the most critical collapse mechanism. It uses global equilibrium condition rather than equilibrium conditions at every point in the soil mass, and neglects the constitutive and compatibility conditions altogether.

Anagnostou and Kovári (1994 and 1996) and Jancsecz and Steiner (1994) stability solution use limit equilibrium method and drained soil properties. They employ a three dimensional wedge model that consists of a prism and a wedge with sliding planes.

Anagnostou and Kovári (1994) investigated the effects of slurry infiltration into the soil mass ahead of the tunnel face on the face stability of slurry shield driven tunnels, and quantified the loss of the face support pressure caused by slurry infiltration.

In 1996, the same authors proposed a solution for the required effective face support pressure that consists of four dimensionless factors that considers tunnel diameter, cohesion, piezometric head difference between the excavation chamber and the surrounding soil, and the cross effect of cohesion and head difference in the flow domain ahead of tunnel face and above the crown. They assessed the required face support pressure for EPBM using a model composed of a wedge and a prism (Figure 3.7) under drained conditions. Tunnel face is considered to be stable when the limit equilibrium condition is achieved for the wedge and prism. Forces acting on the wedge at the face are shown in Figure 3.8, where G' is the submerged weight of the wedge, V' is the vertical force acting on the wedge-prism interface, F_X and F_Z are the seepage forces, N' and T are the normal and shear forces acting on the slip plane, and the S' is the effective face

support force, effective face support pressure, σ'_T, multiplied by the face area, A. The force V' is obtained from silo theory (Janssen, 1895). The lateral earth pressure coefficient was assumed to be 0.4 for the wedge and 0.8 for the prism.

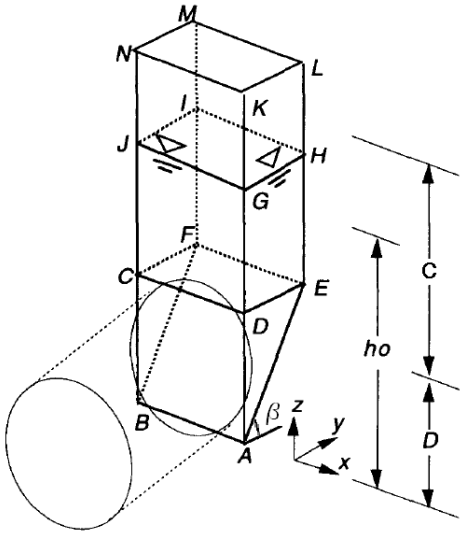

Figure 3.7 Wedge and prism model (Anagnostou and Kovári, 1996)

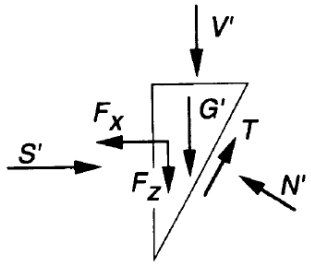

Figure 3.8 Force diagram on the wedge ahead of tunnel face
(Anagnostou and Kovári, 1996)

The required face support pressure is then a function of model geometry (tunnel diameter, cover depth, and inclination angle of slip surface) and ground properties (cohesion, friction angle, and unit weight of the ground). Based on force equilibrium of the system, required face support pressure is calculated, and the inclination angle, β, of

the slip surface is determined by iteration in such a way it is maximizing the support pressure. Required effective face support pressure at limit equilibrium state was obtained like Equation (3.1).

$$\sigma'_T = F_0\gamma' D - F_1 c + F_2\gamma'\Delta h - F_3 c\frac{\Delta h}{D} \tag{3.1}$$

The expression contains four dimensionless coefficients (F_0 to F_3). Coefficients F_0 and F_1 are shown in Figure 3.9. The Equation (3.1) takes the effect of seepage force into account by prescribing a constant piezometric head in the chamber and ahead of the face. This appears in the third and fourth terms of the right hand side of the equation. However the seepage force was not considered in the finite element simulation (Section 5.1.2) of this study, and these terms are disregarded in the calculation of the required face support pressure.

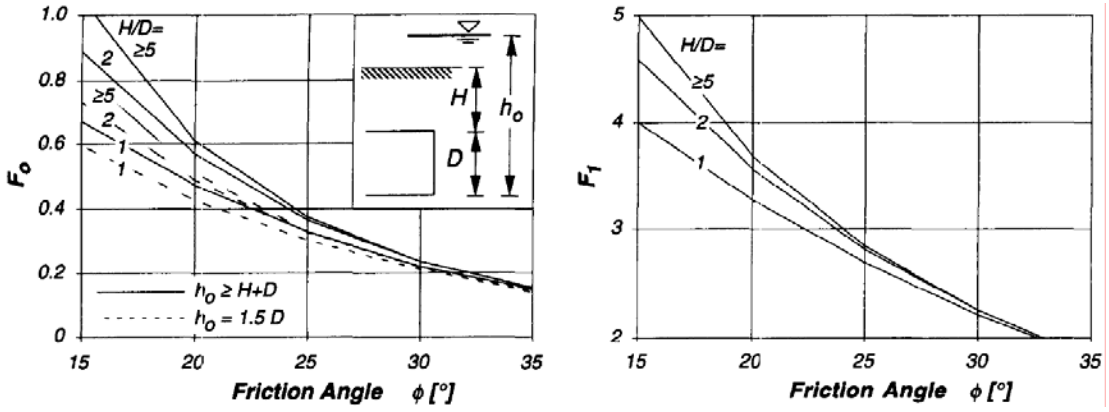

Figure 3.9 Nomograms for coefficient F_0 to F_1 (Anagnostou and Kovári, 1996)

Jancsecz and Steiner (1994) published a method that evaluates the required face support pressure for slurry shield using a model composed of a wedge and a prism (Figure 3.10)

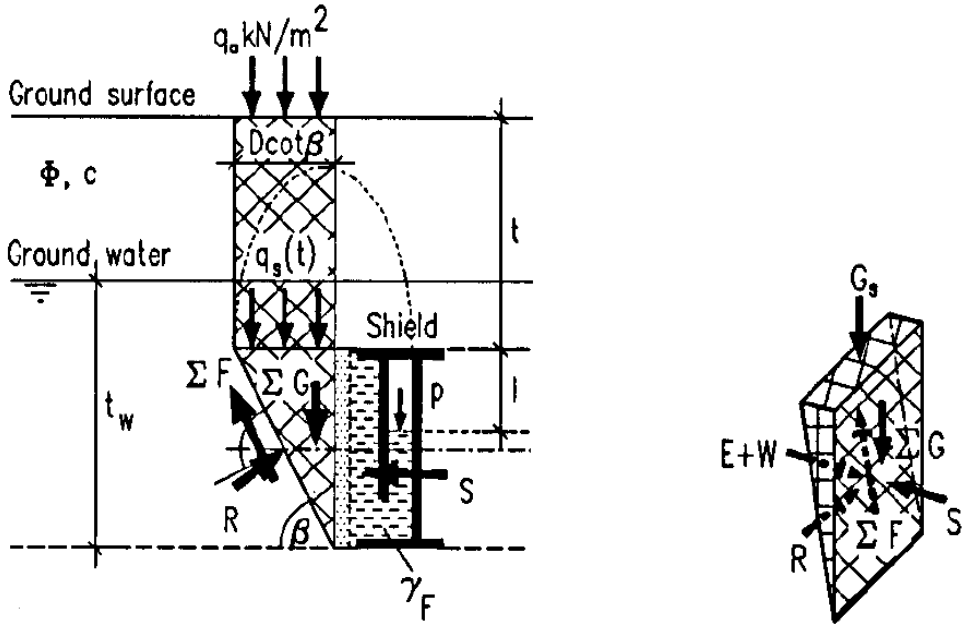

(a) Model description (b) Force diagram

Figure 3.10 Wedge and prism model and forces acting on the wedge
(Jancsecz and Steiner, 1994)

They investigated the effects of soil arching above the tunnel heading, and suggested a three dimensional earth pressure coefficient for different values of the friction angle. It seems that this model was originally developed by Jancsecz in 1987 and submitted to the government, but not published until 1994. It is based on the limit equilibrium method and forces acting on the wedge are shown in Figure 3.11, where Σ*G* is the unit weight of the wedge plus vertical force, Q_S, acting on the wedge, *R* is resultant due to the normal and shear force at the slip plane, and E is the horizontal earth pressure.

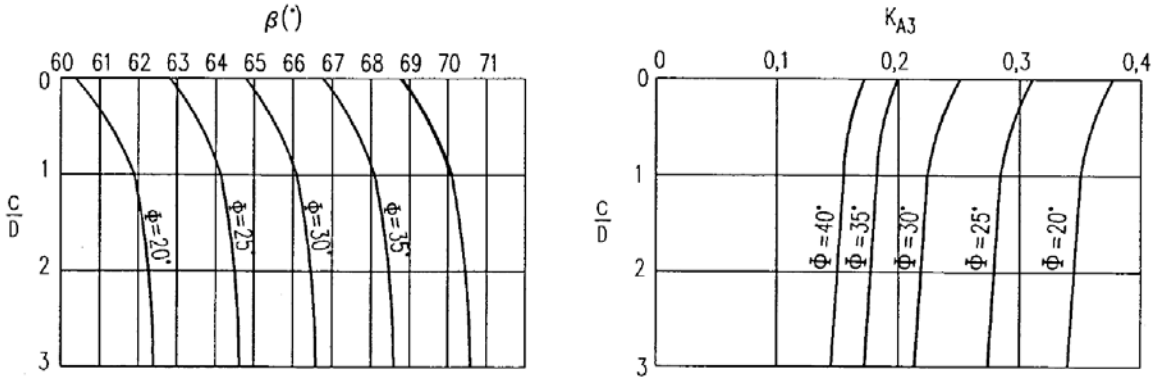

Figure 3.11 Nomograms for angle β and K_{A3} (Jancsecz and Steiner, 1994)

The magnitude of horizontal earth pressure, *E*, is dependent on the angle β, and the maximum value of *E* was obtained mathematically. By adding hydrostatic water pressure to the maximum *E*, the required face support pressure can be obtained.

$$\sigma'_T = K_{A3}\sigma'_v \tag{3.2}$$

Three-dimensional earth pressure coefficient, K_{A3}, is expressed as in Equation (3.3). The calculated values of β and K_{A3} according to friction angle, φ, is shown in Figure 3.11.

$$K_{A3} = \frac{\sin\beta\cos\beta - \cos^2\beta\tan\varphi - \frac{K\alpha}{1.5}\cos\beta\tan\varphi}{\sin\beta\cos\beta + \sin^2\beta\tan\varphi} \tag{3.3}$$

where,

$$K = \frac{1}{2}\left[1 - \sin\varphi + \tan^2\left(45 - \frac{\varphi}{2}\right)\right]$$

and

$$\alpha = \frac{1 + 3\frac{t}{D}}{1 + 2\frac{t}{D}}$$

3.3.2. Limit analysis

For most of geotechnical problems of fully saturated soils, drained and undrained conditions represent two extremes, where partially drained and consolidation analyses are encountered between them. The tunnel heading stability solutions employing limit analysis approach are based on dry material (Leca and Dormieux, 1990) or fully saturated material that follows either a drained (Atkinson and Potts, 1977) or an undrained condition (Davis et al, 1980). Leca and Dormieux (1990) method used three-dimensional sliding cones, and Atkinson and Potts (1977) and Davis et al (1980) employed two-dimensional plane strain conditions to derive the solutions based on the bound theorem. Atkinson and Potts (1977) investigated the required support pressure for an unlined tunnel cross section away from tunnel heading in a cohesionless soil. For purely cohesive material, Davis et al. (1980) derived upper and lower bound solutions against collapse and blow-out for a plane strain cross section of a tunnel in a longitudinal and in a transverse direction. The undrained shear strength, s_u, of the ground was assumed to be constant with depth (Tresca material). Their upper bound solution against collapse takes into account the effects of both tunnel depth and cover-to-diameter ratio. A three dimensional conical failure mechanism was introduced by Leca and Dormieux (1990) to develop upper and lower bound solutions against collapse and blow-out of a tunnel face in a ground that obeys Mohr-Coulomb yield criteria. Upper and lower bound solutions provide a range of required face support pressure.

Davis et al. (1980) derived kinematically admissible upper bound and statically admissible lower bound plasticity solutions for the idealized plane strain tunnel heading, assuming constant undrained shear strength with depth. The upper bound solution employed two sliding blocks composed of an isosceles triangle and a right trapezoid on

the plane of the longitudinal tunnel cross section; therefore, this model refers to an infinitely long slot, not to a circular tunnel. The lower bound solutions used the stress field calculated either in a thick cylinder or in thick sphere. Their stability solutions were expressed in terms of the derived stability number as shown in Figure 3.12. The stability number N is equal to the difference between total overburden stress and applied support pressure divided by the undrained shear strength s_u of the ground:

$$N = \frac{\sigma_S + \gamma\left(C + \frac{D}{2}\right) - \sigma_T}{s_u} \tag{3.4}$$

where σ_S is the surcharge pressure, γ is the total unit weight of the ground, C is the cover-depth, D is the tunnel diameter, σ_T is the applied face support pressure at the center of the face, and s_u is the undrained shear strength of the ground.

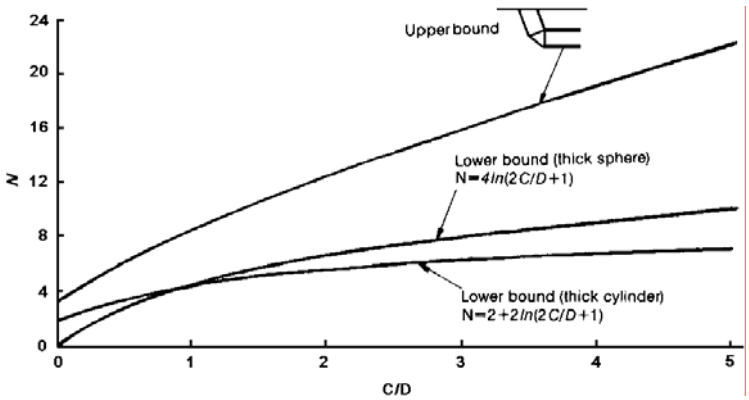

Figure 3.12 Stability number derived from upper and lower bound plasticity solutions for plane strain tunnel heading (after Davis et al., 1980)

Using numerical limit analysis, Sloan and Assadi (1993) and Augarde et al. (2003) presented bound solutions for the plane strain condition where the undrained shear strength increases with depth. They found that N is greater than 6 for deeper tunnels,

i.e. using N=6 may overestimate the support pressure in deeper tunnels, and showed that N depends on tunnel diameter, cover-depth, ground unit weight and normalized undrained shear strength ratio (s_u/σ_{vo}').

Leca and Dormieux (1990) have investigated the face stability of tunnel against collapse and blow-out cases. Bound solutions give bracketed estimate of required face support pressure: upper and lower bound solutions. The upper bound solution is found by considering a kinematically admissible failure mechanism. The external work done to the system exceeds the work dissipated inside the system. The lower bound solution is found by considering a statistically admissible stress distribution in equilibrium that does not violate the yield criterion. The external work done to the system cannot constitute an unconfined plastic flow. The model is composed of one or two conical blocks as shown in Figure 3.13

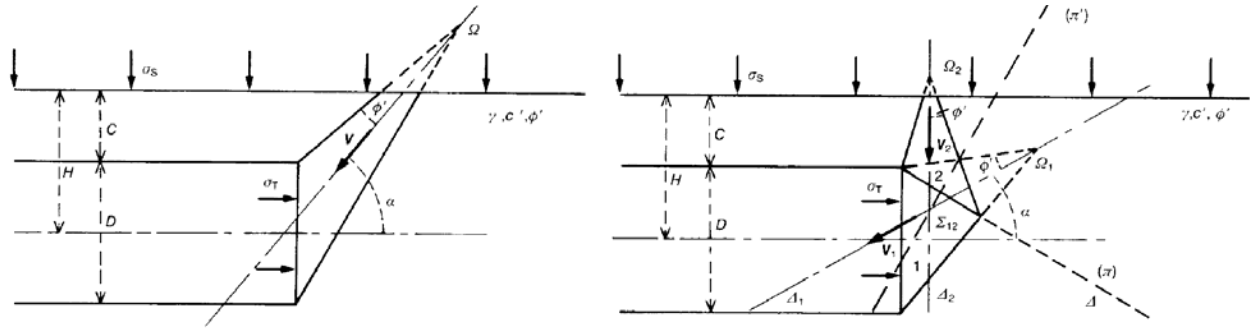

(a) 1 conical block failure mechanism (b) 2 conical block failure mechanism

Figure 3.13 Conical block model for upper bound solution for collapse case (Leca and Dormieux, 1990)

The upper bound solution for required face support pressure, σ_T, against collapse associated with mechanism I and II can be determined by finding the σ_T that satisfies inequality Equation (3.5).

$$N_S Q_S + N_\gamma Q_\gamma \leq Q_T \tag{3.5}$$

where loading parameters, Q_S, Q_T and Q_γ, are defined as follows:

$$\begin{aligned} Q_S &= (K_P - 1)\frac{\sigma_S}{\sigma_C} + 1 \\ Q_T &= (K_P - 1)\frac{\sigma_T}{\sigma_C} + 1 \\ Q_\gamma &= (K_P - 1)\frac{\gamma D}{\sigma_C} \end{aligned} \tag{3.6}$$

Weighting coefficients N_S and N_γ are dependent on the angle α and can be found from Figure 3.14. The lower bound solution for required face support pressure against collapse is obtained by calculating the force equilibrium within the mechanism shown in Figure 3.15. For lower bound solution, Q_S, Q_T and Q_γ are calculated using Equation (3.6) and N_S and N_γ are calculated as follows:

$$\begin{aligned} N_S &= K_A \\ N_\gamma &= K_A\left(\frac{C}{D} + 1\right) \end{aligned} \tag{3.7}$$

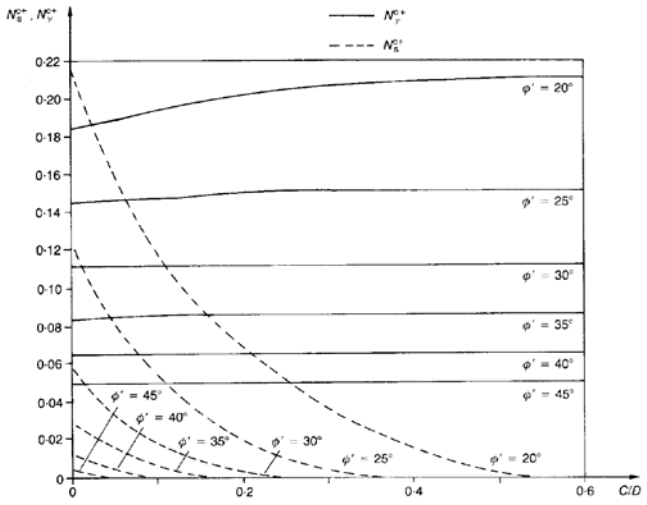

Figure 3.14 Upper bound values of weighting coefficients N_S and N_γ
(Leca and Dormieux, 1990)

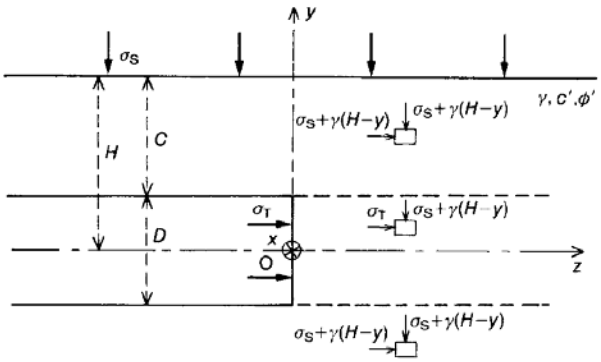

Figure 3.15 Geostatic model for lower bound solution for collapse case
(Leca and Dormieux, 1990)

3.3.3. Experimental/empirical approach for undrained conditions

To evaluate the stability of tunnel headings excavated under undrained ground conditions, a number of tunnel face instability mechanisms have been suggested. Among them, the stability number N suggested by Broms and Bennermark (1967) is one of the most frequently referred to criteria by engineers and researchers.

$$N = \frac{\sigma_S + \gamma\left(C + \frac{D}{2}\right) - \sigma_T}{s_u} \qquad (3.4)\ bis$$

They concluded that vertical openings became unstable when the stability number *N* was greater than 6-8 based on their experiments, where the undisturbed or remolded clay samples were loaded axially until the material extruded through a 10 mm or 20 mm diameter hole at the mid-height of the cylinder that was confined by a pressurized glycerin in a triaxial cell. The authors supported the idea of a stability number (derived experimentally) by using the actual data collected from a face failure case history. A face collapse occurred during the excavation of Tyholt tunnel in Norway, where a 7.9 m outer diameter compressed air shield was employed for a ground composed of silty clay and quick clay. As shown in Figure 3.16 the total overburden pressure was greater than six times the undrained shear strength of the ground at the site of collapse. Face support pressure of 1,940 psf (92.9 kPa) was applied before the tunnel excavation resumed successfully; under this condition N was equal to 5.3 at the tunnel invert.

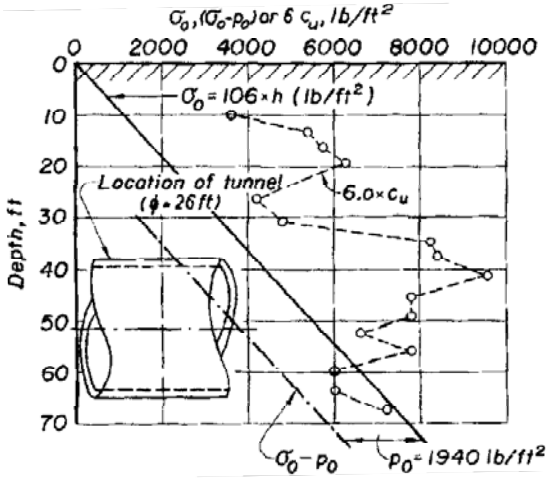

Figure 3.16 Face collapse in Tyholt tunnel, Norway (after Broms and Bennermark, 1967)

Mair (1979) and Kimura and Mair (1981) investigated the tunnel face stability using centrifugal model tests. 60 mm diameter circular tunnels were cut in the clay models with different C/D and P/D values, where P represents the distance between the face and the point where the stiff radial support is provided. Models were tested at 75g and 125g, which made the models equivalent to 4.5 m and 7.5 m diameter tunnels from a stability viewpoint. The model tunnel was radially supported by a brass tube. A rubber membrane was installed on the face and compressed air pressure was supplied into the tunnel. The air pressure in the tunnel was maintained equal to the total overburden pressure at the tunnel axis and it was reduced rapidly until failure of the tunnel occurred. The authors gave a range of curves showing the stability number N in terms of the dimensionless ratios P/D and C/D as shown in Figure 3.17. As P/D decreases and C/D increases, the stability number N decreases, i.e. the face support pressure necessary to maintain a stable tunnel heading decreases. When the shield is used, the distance P can be taken as equal to zero, unless the ground is composed of hard rock or very stiff clay where the gap between the ground and the shield can be maintained for an extended period of time. Since TBM-driven soft ground tunnels are considered in this paper, the case with P/D=0 in Figure 3.17 is applicable here.

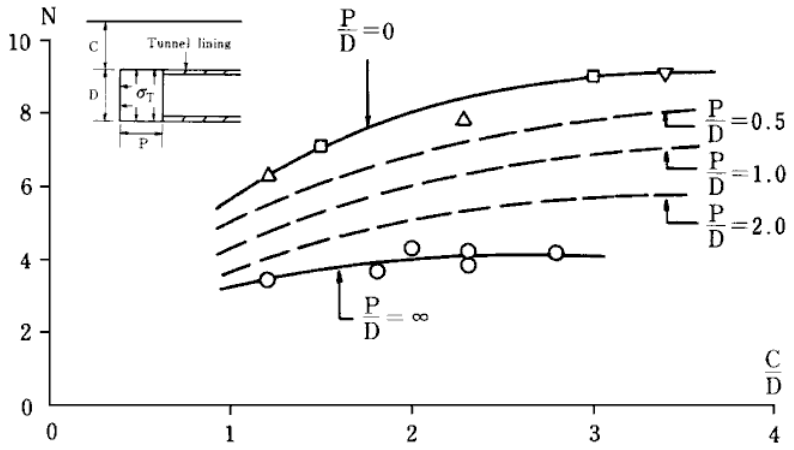

Figure 3.17 Stability number derived from centrifuge model test (Kimura and Mair, 1981)

CHAPTER 4. DEVELOPMENT OF SIMPLE PRISM-AND-WEDGE LIMIT ANALYSIS MODELS IN UNDRAINED CONDITIONS

4.1. INTRODUCTION

The theory of limit analysis was developed in the early 1950s by Prager and Hodge under the assumption of associated flow rule or normality rule for perfectly plastic metals. Then, the metal plasticity was extended to soil plasticity by Drucker and Prager in 1952. Typical limit analysis was developed based on perfect plasticity and associated flow rule. As already stated in the third paragraph of Section 3.3, finding a complete solution that satisfies three fundamental conditions (force equilibrium, constitutive and compatibility conditions) at the same time is too cumbersome, and therefore, in limit analysis, in order to ease the calculations, one ignores either the equilibrium conditions or the compatibility conditions (Chen and Liu, 1990). By ignoring the equilibrium condition we may calculate a kinematically admissible upper bound value to the true collapse load. When a system is loaded to the upper bound value, the system must collapse. In contrast, by ignoring the compatibility condition we may calculate a lower bound value to the true collapse load. This is a statically admissible solution and the system loaded to this value cannot collapse. The true collapse load must lie in between these upper and lower bounds.

When the loads determined from the upper bound theorem are applied to the system, it must collapse (unsafe solution), and when the loads determined from the lower bound theorem are applied to the system, it must not collapse (safe solution). When applied to tunnel face stability problems, the upper bound solution gives face pressure

values that are less than the true collapse pressure, and the lower bound solution gives face pressure values greater than the true collapse pressure.

4.2. PRISM-AND-WEDGE MODEL WITH RIGID BLOCKS

In this section, upper bound solutions for the tunnel face against collapse are derived using the upper bound theorem. The ground is assumed to behave in undrained condition with Tresca failure criterion characterized by the undrained shear strength, s_u. To describe the movement of the soil mass near the tunnel heading, an idealized prism-and-wedge model was used. For the sake of simplicity, the tunnel face was assumed to be a square that has the same cross sectional area as the circular tunnel heading as illustrated in Figure 4.1. The symbols C_e and D_e represent the equivalent cover-depth and tunnel diameter.

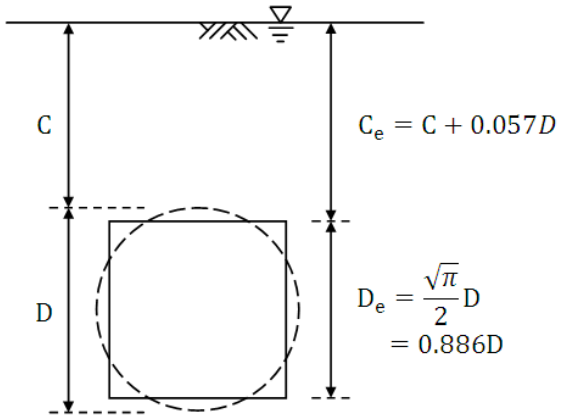

Figure 4.1 Equivalent cover-depth and tunnel diameter

Upper bound solutions against collapse were examined using four different assumptions. The problems presented in this chapter are provided in a series of stages beginning with the simplest case, where the undrained shear strength of the ground was assumed to be uniform and the shape of slip surface ahead of tunnel face was assumed to

be planar (Section 4.2.1). In order to represent more realistic situation, additional complexity was added one at time. The undrained shear strength of the ground was assumed to be uniform (Sections 4.2.1 and 4.2.3) or increasing with depth (Sections 4.2.2 and 4.2.4), and the shape of slip surface ahead of tunnel face was assumed to be planar (Sections 4.2.1 and 4.2.2) or circular (Sections 4.2.3 and 4.2.4). In Section 4.3, deformable soil blocks were used

4.2.1. Planar slip surface in a ground with uniform undrained shear strength

Figure 4.2 shows the model consisting of a prism and a wedge employed for the calculation of upper bound solutions. The entire domain was divided into three blocks. The prism and the wedge are marked by symbols P and W, respectively. The domain outside the prism and the wedge is represented by symbol O and it is stationary material. Ground water table is located at the surface. The unit weight of soil γ and the undrained shear strength s_u was assumed to be uniform for entire ground. The tunnel face □aa'e'e is pressurized by the uniform slurry or conditioned ground pressure σ_T. With undrained ground conditions, the angle of sliding plane, θ, is equal to 45°, so that $|\overline{ae}| = |\overline{be}|$. The arrows represent the direction and magnitude of the soil block movements.

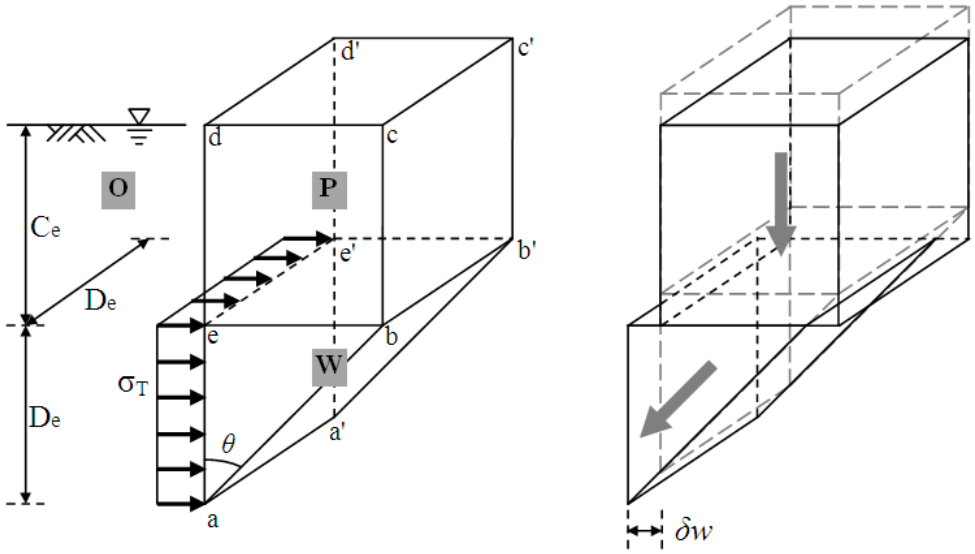

Figure 4.2 Prism-and-wedge model

Kinematic compatibility is examined using the corresponding displacement diagram given in Figure 4.3. The letters on the arrows represent the increment of displacement of soil blocks. OW is the relative increment of displacement of the soil wedge W with respect to the stationary soil block O. The horizontal component of the increment of displacement of the wedge OW represents the inward displacement of the tunnel face and its magnitude was taken as δw_F.

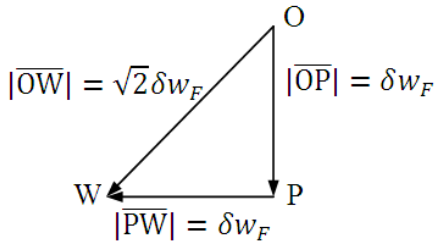

Figure 4.3 Displacement diagrams for undrained bound solution

To determine an upper bound solution of a kinematically compatible mechanism, it is necessary to calculate the work done by the internal stresses (the energy dissipated on

the slip planes) and the increment of the work done by the external loads during an increment of displacement. If the increment of work done during plastic deformation by the boundary tractions and body forces is greater or equals the rate of energy dissipated within the body, then collapse takes place (Davis and Selvadurai; p. 127). The increment of the work done by the internal stresses on the slip planes are tabulated in Table 4.1.

Table 4.1 Increment of work done by internal stresses for the compatible mechanism shown in Figure 4.1(s_u=uniform)

Slip planes	Shear strength	Area	Displacement	Work done δW_i
□aa'b'b	s_u	$\sqrt{2}D_e^2$	$\sqrt{2}\delta w_F$	$\delta W_1 = 2s_u D_e^2 \delta w_F$
Δabe Δa'b'e'	s_u	$\frac{D_e^2}{2}$	$\sqrt{2}\delta w_F$	$\frac{1}{2}\delta W_2 = \frac{1}{\sqrt{2}} s_u D_e^2 \delta w_F$
□bb'e'e	s_u	D_e^2	δw_F	$\delta W_3 = s_u D_e^2 \delta w_F$
□bb'c'c □dd'e'e □bcde □b'c'd'e'	s_u	$C_e D_e$	δw_F	$\frac{1}{4}\delta W_4 = s_u C_e D_e \delta w_F$

$$\sum_i \delta W_i = \left(\left(3+\sqrt{2}\right) D_e^2 + \frac{4C_e}{D_e} \right) s_u \delta w_F \qquad (4.1)$$

The increment of work done by internal forces is given in Equation (4.1). The increment of work done by external forces, δE, is the product of the displacement vector and the force vector in the direction of movement. In here, two external forces are acting on the system. The gravity force acts vertically on the bodies P and W and the support force acts horizontally on the block W. The external work is:

$$\delta E = \gamma C_e D_e^2 \delta w_F + \gamma \frac{D_e^3}{2} \delta w_F - \sigma_T D_e^2 \delta w_F \qquad (4.2)$$

$$= \left(\gamma C_e + \gamma \frac{D_e}{2} - \sigma_T\right) D_e^2 \, \delta w_F$$

By equating δW (Equation (4.1)) and δE (Equation (4.2)), the upper bound solution for the collapse load becomes:

$$\sigma_T = \gamma\left(C_e + \frac{D_e}{2}\right) - s_u\left(3 + \sqrt{2} + \frac{4C_e}{D_e}\right) \tag{4.3}$$

4.2.2. Plane slip surface in a ground with increasing undrained shear strength

The undrained shear strength of the ground varies with depth (Bjerrum, 1972). For normally consolidated soils, the undrained shear strength increases with depth and it can be idealized as shown in Figure 4.4 (Bjerrum, 1972). The normalized undrained shear strength ratio is represented by symbol ρ.

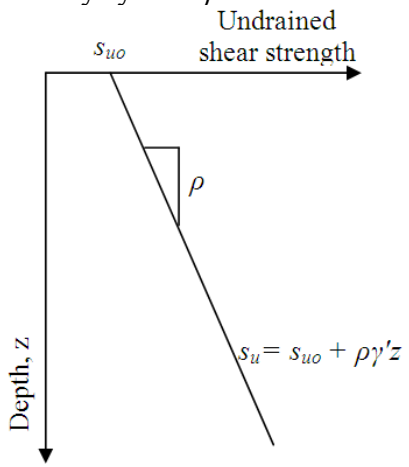

Figure 4.4 Undrained shear strength profile

The upper bound solution can be determined using the same displacement diagram shown in Figure 4.3 because there is no change in the kinematic compatible mechanisms. The increment of work done by external forces δE is dependent only to the load applied to the system and the corresponding increment of displacement. Since δE is independent to the material strength parameters, Equation (4.2) can be still used for

the calculation. Thus only the increment of the work done by the internal stresses, δW, needs to be recalculated as summarized in Table 4.2, where the undrained shear strength is evaluated at centroid of each face.

Table 4.2 Increment of work done by internal stresses for compatible mechanism shown in Figure 4.2 ($s_u = s_{uo} + \rho$)

Slip planes		Shear strength Work done δW_i	Area	Displacement
□aa'b'b		$s_u = s_{uo} + \rho\gamma'\left(C_e + \frac{D_e}{2}\right)$	$\sqrt{2}D_e^2$	$\sqrt{2}\delta w_F$
		$\delta W_1 = 2\left(s_{uo} + \rho\gamma'\left(C_e + \frac{D_e}{2}\right)\right)D_e^2\delta w_F$		
Δabe	Δa'b'e'	$s_u = s_{uo} + \rho\gamma'\left(C_e + \frac{D_e}{3}\right)$	$\frac{D_e^2}{2}$	$\sqrt{2}\delta w_F$
		$\frac{1}{2}\delta W_2 = \frac{1}{\sqrt{2}}\left(s_{uo} + \rho\gamma'\left(C_e + \frac{D_e}{3}\right)\right)D_e^2\delta w_F$		
□bb'e'e		$s_u = s_{uo} + \rho\gamma' C_e$	D_e^2	δw_F
		$\delta W_3 = (s_{uo} + \rho\gamma' C_e)D_e^2\delta w_F$		
□bb'c'c □bcde	□dd'e'e □b'c'd'e'	$s_u = s_{uo} + \rho\gamma'\frac{C_e}{2}$	$C_e D_e$	δw_F
		$\frac{1}{4}\delta W_4 = \left(s_{uo} + \rho\gamma'\frac{C_e}{2}\right)C_e D_e\delta w_F$		

$$\sum_i \delta W_i = \left(\left(3+\sqrt{2}\right)\left(s_{uo} + \rho\gamma'\left(C_e + \frac{D_e}{3}\right)\right)D_e + 4\left(s_{uo}C_e + \rho\gamma'\frac{C_e^2}{2}\right)\right)D_e\delta w_F \qquad (4.4)$$

By equating δW (Equation (4.4)) and δE (previously given in Equation (4.2)), the upper bound solution for the collapse load becomes:

$$\sigma_T = \gamma\left(C_e + \frac{D_e}{2}\right) - 4\left(\frac{C_e}{D_e}\right)\left(s_{uo} + \rho\gamma'\frac{C_e}{2}\right) - (3+\sqrt{2})\left(s_{uo} + \rho\gamma'\left(C_e + \frac{D_e}{3}\right)\right) \quad (4.5)$$

By substituting $s_u = s_{uo}$ and $\rho = 0$, Equation (4.5) reduces to Equation (4.3).

4.2.3. Circular slip surface in a ground with uniform shear strength

In this section, a circular slip surface was used to construct a kinematic compatibility mechanism illustrated in Figure 4.5. With the circular slip surface □aa'b'b, the arc wedge rotates about the axis ee'. As the block W rotates, block P deforms into a parallelepiped shape at constant volume.

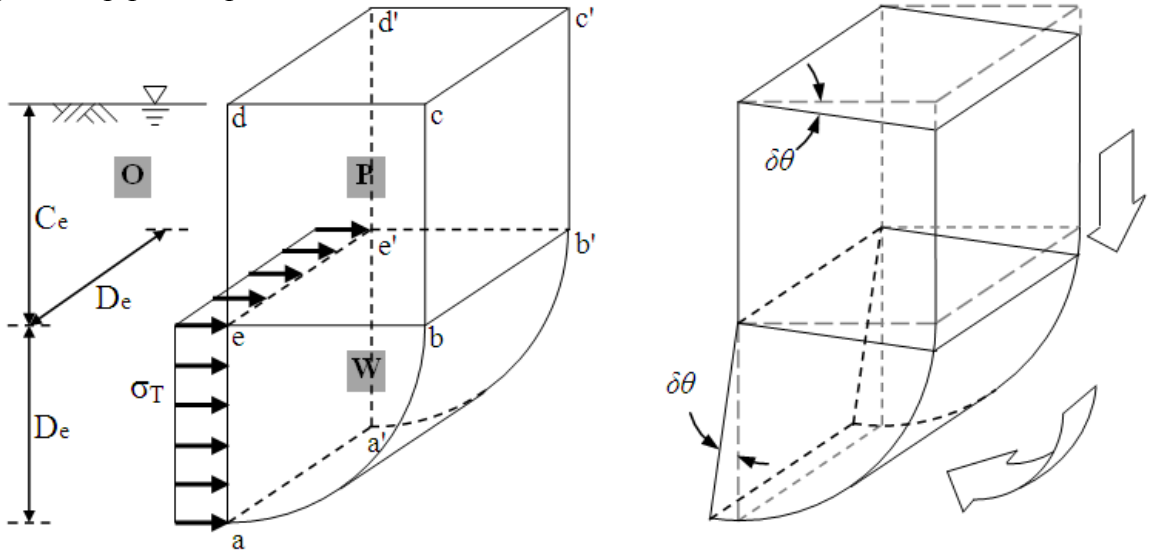

Figure 4.5 Circular wedge-and-plane model

The displacement value of circular sectors abe and a'b'e' due to the rotation of the wedge is shown in Table 4.3. The increment of internal energy dissipated by a plastic deformation due to pure shear in block P can be easily calculated because angle of rotation, $\delta\theta$, is achieved at constant stress (s_u). The work per untit volume is $s_u C_e D_e^2 \delta\theta$. Details of δW calculation are given in Table 4.3.

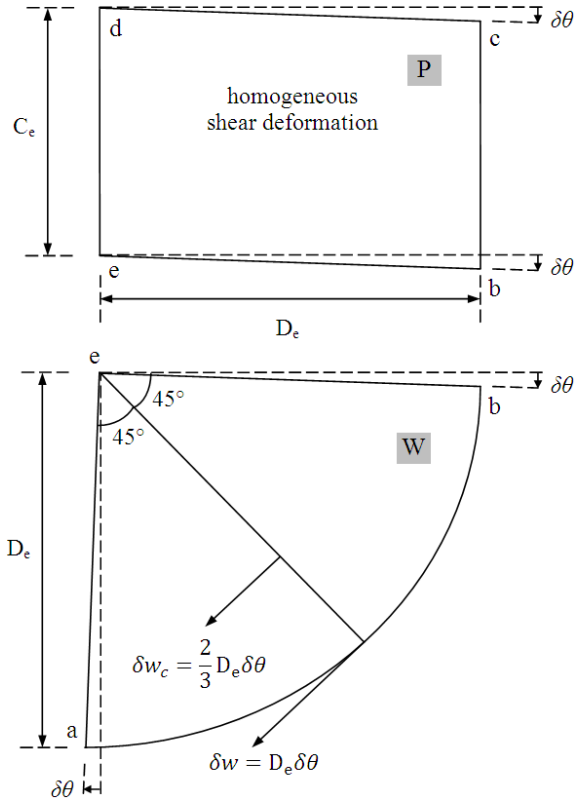

Figure 4.6 Rotation of block W and deformation of block P

Table 4.3 Increment of work done by internal stresses for compatible mechanism shown in Figure 4.5

Slip planes	Shear strength	Area	Displacement	Work done δW_i
□aa'b'b	s_u	$\frac{\pi D_e^2}{2}$	$D_e \delta\theta$	$\delta W_1 = \frac{\pi}{2} s_u D_e^3 \delta\theta$
Δabe Δa'b'e'	s_u	$\frac{\pi D_e^2}{4}$	$\frac{2}{3} D_e \delta\theta$	$\frac{1}{2}\delta W_2 = \frac{\pi}{6} s_u D_e^3 \delta\theta$
□bb'c'c □dd'e'e □bcde □b'c'd'e'	s_u	$C_e D_e$	$\frac{D_e}{2}\delta\theta$	$\frac{1}{4}\delta W_3 = \frac{1}{2} s_u C_e D_e^2 \delta\theta$
energy dissipated due to the shear deformation of block P		$\delta W_4 = s_u C_e D_e^2 \delta\theta$		
$\sum_i \delta W_i = s_u \left(\frac{5\pi}{6} + 3\frac{C_e}{D_e}\right) D_e^3 \delta\theta$				(4.6)

The increment of work done by the external forces is given by the gravity force and the support pressure applied on the face. The body forces of the soil wedge W due to gravity and the support pressure applied on the face are applied on the center of the gravity point (see centroid) of the block W:

$$\begin{aligned}\delta E &= (\gamma C_e D_e^2)\left(\frac{1}{2}D_e\delta\theta\right) + \left(\frac{\pi}{4}\gamma D_e^3\right)\left(\frac{4D_e}{3\pi}\delta\theta\right) - (\sigma_T D_e^2)\left(\frac{4D_e}{3\pi}\delta\theta\right) \\ &= \left(\frac{1}{2}\gamma C_e + \frac{1}{3}\gamma D_e - \frac{4}{3\pi}\sigma_T\right) D_e^3\delta\theta\end{aligned} \tag{4.7}$$

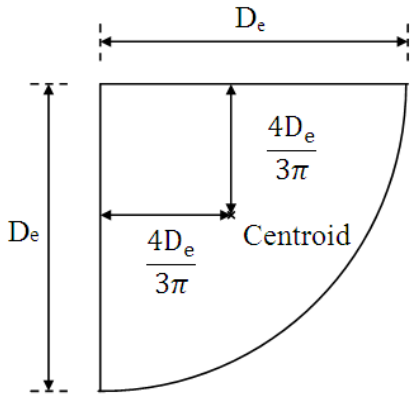

Figure 4.7 Center of gravity of a quarter circle

By equating δW (Equation (4.6)) and δE (Equation (4.7)), the upper bound solution for the collapse load becomes:

$$\sigma_T = \frac{3\pi}{4}\left(\frac{\gamma C_e}{2} + \frac{\gamma D_e}{3} - s_u\left(\frac{5\pi}{6} + \frac{3C_e}{D_e}\right)\right) \tag{4.8}$$

4.2.4. Circular slip surface in a ground with increasing undrained shear strength

When the shear strength profile follows Figure 4.4, the shear strength is a function of depth. Consider the cylindrical coordinates α and ξ as in Figure 4.8. For the soil wedge the undrained shear strength is:

$$s_u = s_{uo} + \rho\gamma'(C_e + \xi \sin\alpha) \tag{4.9}$$

where $(0 \leq \xi \leq D_e)$. For the soil prism the undrained shear strength is:

$$s_u = s_{uo} + \rho\gamma' z \tag{4.10}$$

where $(0 \leq z \leq C_e)$.

The face support pressure is calculated for a tunnel excavated in a ground where the undrained shear strength increases with depth using the failure model that was used in Section 4.2.3 (Figure 4.5 and Figure 4.6). With the circular slip surface □aa'b'b, the arc wedge rotates about the axis ee'. As the block W rotates, block P deforms into a parallelepiped shape at constant volume.

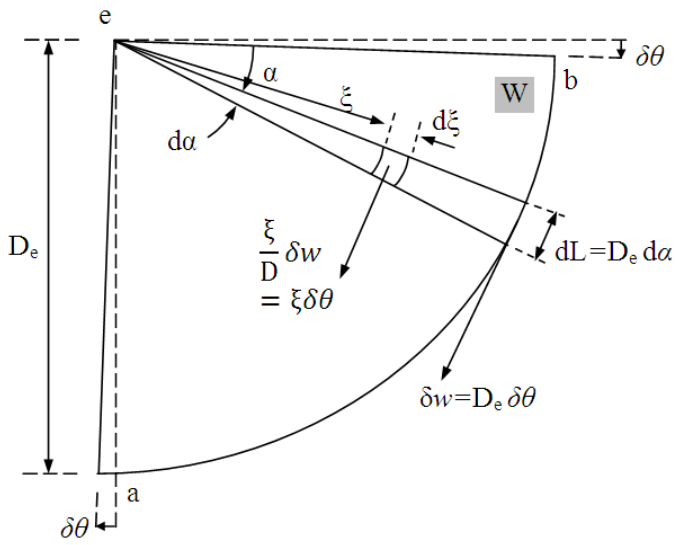

Figure 4.8 Kinematic compatibility condition

Table 4.4 Increment of work done by internal stresses for compatible mechanism shown in Figure 4.5.

Slip planes		Shear strength Work done δW_i	Area	Displacement
□aa'b'b		$s_u = s_{uo} + \rho\gamma'(C_e + D_e \sin\alpha)$	$D_e^2 d\alpha$	$D_e \delta\theta$
		$\delta W_1 = \int_0^{\frac{\pi}{2}} \left(\left(s_{uo} + \rho\gamma'(C_e + D_e \sin\alpha) \right) (D_e^3 \delta\theta) \right) d\alpha$ $= \left(\frac{\pi}{2} s_{uo} + \frac{\pi}{2} \rho\gamma' C_e + \rho\gamma' D_e \right) D_e^3 \delta\theta$		
Δabe	Δa'b'e'	$s_u = s_{uo} + \rho\gamma'(C_e + \xi \sin\alpha)$	$\xi \, d\xi \, d\alpha$	$\xi \, \delta\theta$
		$\frac{1}{2}\delta W_2 = \int_0^{\frac{\pi}{2}} \int_0^{D_e} \left(\left(s_{uo} + \rho\gamma'(C_e + \xi \sin\alpha) \right) \xi \delta\theta \right) \xi \, d\xi \, d\alpha$ $= \left(\frac{\pi}{6} s_{uo} + \frac{\pi}{6} \rho\gamma' C_e + \frac{1}{4} \rho\gamma' D_e \right) D_e^3 \delta\theta$		
□bb'c'c □bcde	□dd'e'e □b'c'd'e'	$s_u = s_{uo} + \rho\gamma' \frac{C_e}{2}$	$C_e D_e$	$\frac{D_e}{2} \delta\theta$
		$\frac{1}{4}\delta W_4 = \frac{1}{2} \left(s_{uo} + \rho\gamma' \frac{C_e}{2} \right) C_e D_e^2 \delta\theta$		
energy dissipated due to the shear deformation of block P		$\delta W_5 = \int_0^{C_e} (s_{uo} + \rho\gamma' z)(D_e dz)(D_e \delta\theta)$ $= \left(s_{uo} + \frac{1}{2} \rho\gamma' C_e \right) C_e D_e^2 \delta\theta$		
$\sum_i \delta W_i = \left\{ \left(\frac{5\pi}{6} + \frac{3C_e}{D_e} \right) s_{uo} + \left(\frac{5\pi}{6} + \frac{3}{2} \left(\frac{C_e}{D_e} + \frac{D_e}{C_e} \right) \right) \rho\gamma' C_e \right\} D_e^3 \delta\theta$				(4.11)

By equating δW (Equation (4.11)) and δE (previously given in Equation (4.7)), the upper bound solution for the collapse load becomes:

$$\sigma_T = \frac{3\pi}{4} \left\{ \frac{\gamma C_e}{2} + \frac{\gamma D_e}{3} - s_u \left(\frac{5\pi}{6} + \frac{3C_e}{D_e} \right) - \left(\frac{5\pi}{6} + \frac{3}{2} \left(\frac{C_e}{D_e} + \frac{D_e}{C_e} \right) \right) \rho\gamma' C_e \right\} \quad (4.12)$$

4.3. PRISM-AND-WEDGE MODEL WITH DEFORMABLE BLOCKS

4.3.1. Model description

In Section 4.2, the different support pressure at the crown and invert was not considered, and the soil wedge was assumed to be rigid. In this section, the soil wedge and the soil prism are considered as deformable bodies, and as a result, the effect of the non-uniform pressure distribution on the excavation face can be taken into account.

Figure 4.9 shows the side view of the deformed bodies. Local coordinates are defined for the soil wedge and the soil prism as shown in Figure 4.9. The symbol ξ represents the depth from the tunnel crown: at the crown ξ equals to zero and at the invert it is D_e; the symbol y represents the displacement value of a point on the tunnel face in horizontal direction; a negative displacement indicates that the tunnel face moved towards the cavity (active state), and a positive y value indicates that the face support pressure is pushing the tunnel face in the direction of advance (passive state). Because the curves ea and eb of the body W and the curve eb of the body P have the same shape and because the deformation occurs at constant volume, the equation that represents the face deformation profile (curve ea) can be applied to the curves eb by rotating the local coordinates of the body W by 90 degrees.

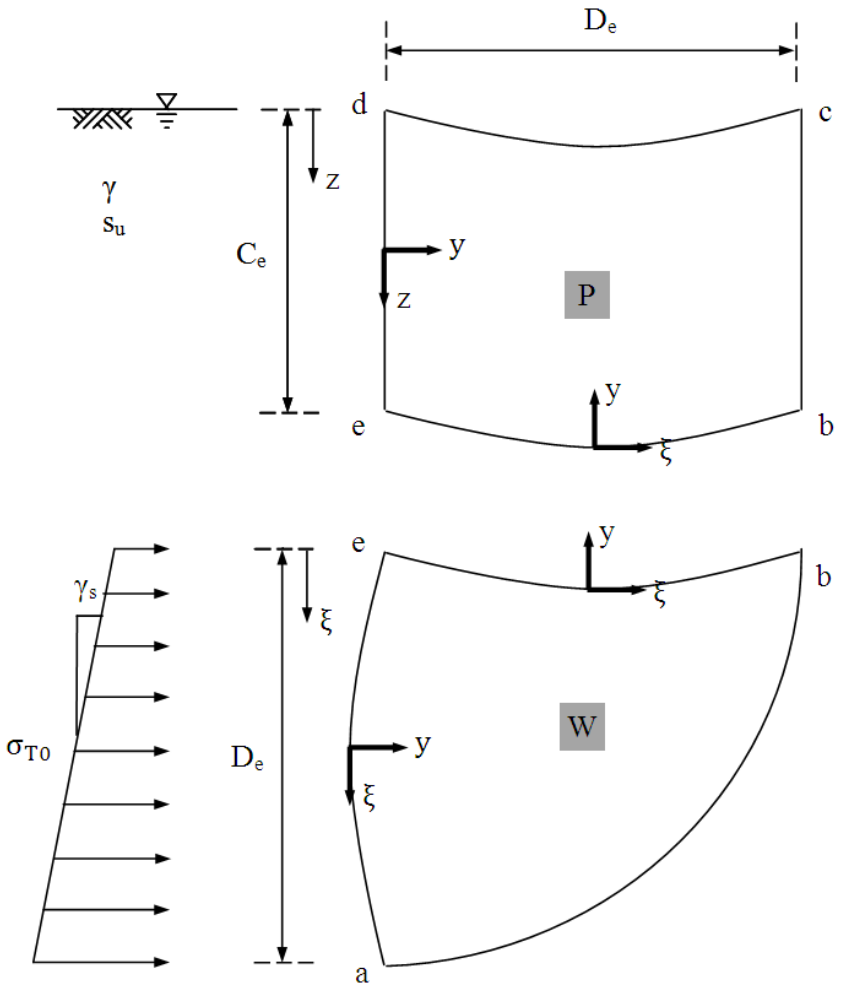

Figure 4.9 Deformed shape and the local coordinates

The undrained shear strength that was already discussed in Section 4.2.4 (Equations (4.9) and (4.10)) can be used here:

$s_u = s_{uo} + \rho\gamma'(C_e + \xi \sin\alpha)$ for soil wedge *bis* (4.9)

$s_u = s_{uo} + \rho\gamma' z$ for the soil prism. *bis* (4.10)

(a) (b)

Figure 4.10 shows the angle of rotation, $\delta\theta$, and the face deformation profile, and Figure 4.11 shows the circular soil wedge discretized into thin circular strips. The rotation angle of thin strips is initially assumed to decrease linearly with increasing ξ. The displacement value y is the product of the angle of rotation ($\delta\theta$) and the distance between from the pivot point O to the thin strip; therefore, y becomes a second order polynomial curve, as shown in the face deformation profile in

(a) (b)

Figure 4.10. The symbol $\delta\theta^*$ represents the angle of rotation of the first element (element [1]), and it is an arbitrary value. The last element [n] does not rotate at all.

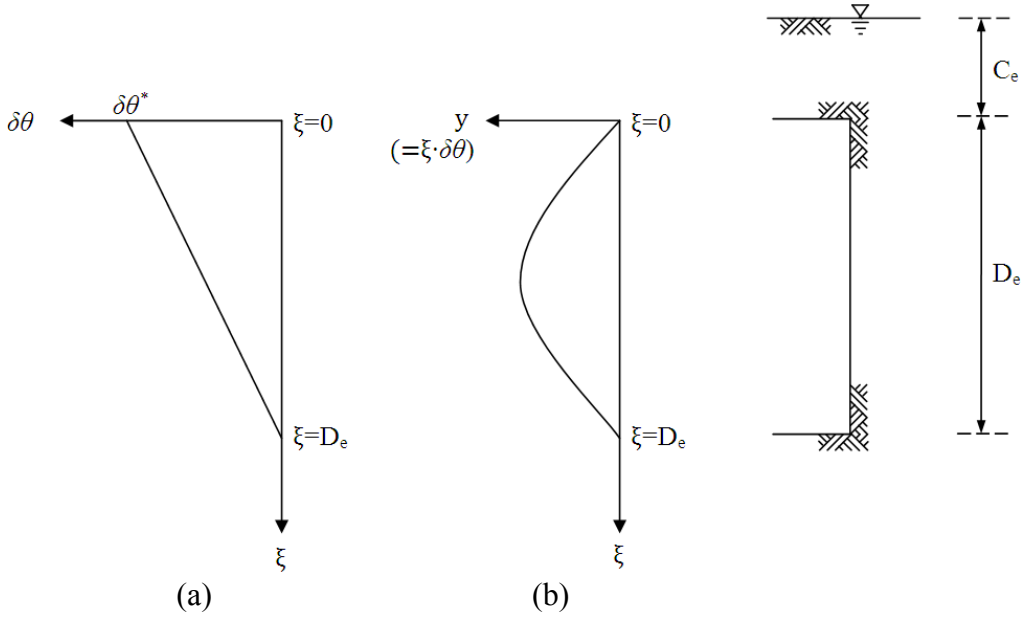

Figure 4.10 (a) angle of rotation and (b) face deformation profile

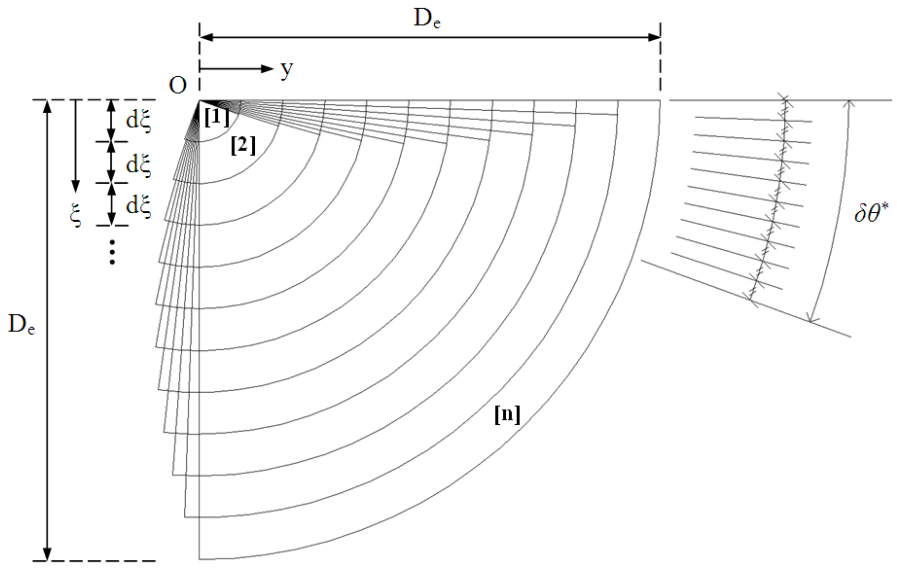

Figure 4.11 Shear deformation of soil wedge

From

(a) (b)

Figure 4.10, the angle of rotation can be expressed as:

$$\delta\theta = \delta\theta^* \left(1 - \frac{\xi}{D_e}\right) \tag{4.13}$$

Therefore, for a small $\delta\theta$*, the face deformation profile is expressed as follows:

$$y = -\delta\theta^* \left(1 - \frac{\xi}{D_e}\right)\xi \tag{4.14}$$

As previously stated, Equation (4.14) is an expression for a second order polynomial curve. The negative sign in Equation (4.14) indicates that the tunnel face moves toward the cavity when $\delta\theta$* is positive.

A more general expression for the angle of rotation and the face deformation profile is presented in Equations (4.15) and (4.16).

$$\delta\theta = \delta\theta^* \left(1 - \left(\frac{\xi}{D_e}\right)^{\beta}\right) \tag{4.15}$$

$$y = -\delta\theta^* \left(1 - \left(\frac{\xi}{D_e}\right)^{\beta}\right)\xi \tag{4.16}$$

Figure 4.12 shows how the angle of rotation and the face deformation profile are affected by the value of β. When β is equal to 0.1, the maximum face displacement takes place at the upper 1/3 point of the tunnel face. When β=1.0, the face deformation profile is symmetric at the tunnel axis and when β=10, the maximum displacement takes place at the lower 1/3 point of the tunnel face. Figure 4.13 shows the deformed shape of the soil wedge when β equals to 3. Compare the face deformation profile when β=1 (Figure 4.11).

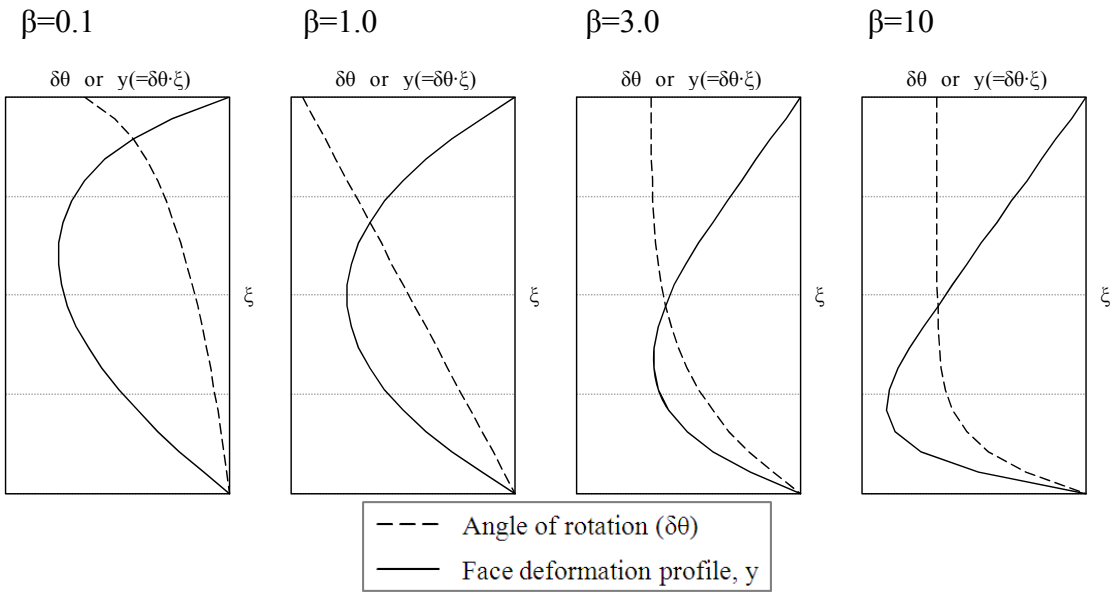

Figure 4.12 Effect of β on the angle of rotation and the face deformation profile

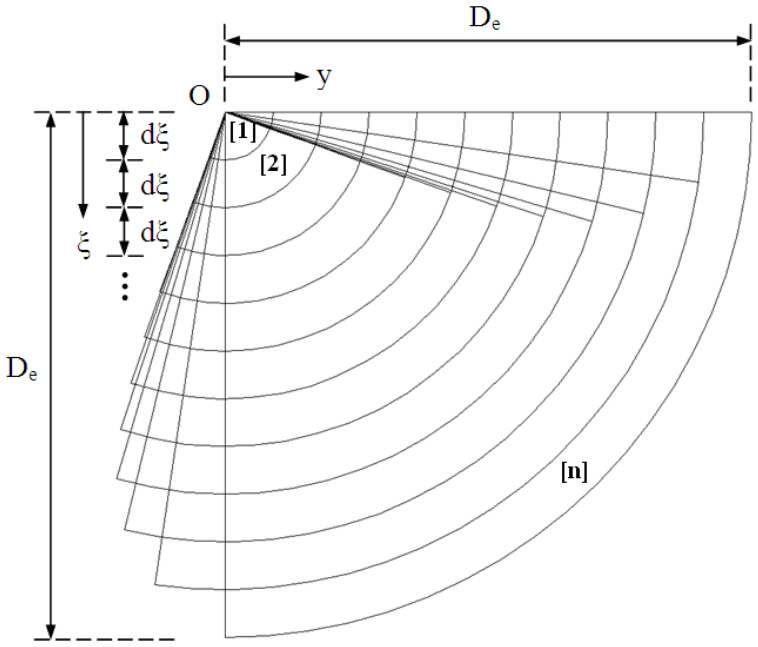

Figure 4.13 Shear deformation of soil wedge (β=3.0)

This paragraph shows the derivation of the relative displacement (Δy) between two adjacent thin strips. The Δy value is necessary to calculate the energy dissipated during the shear deformation of the soil wedge. Let's take two adjacent thin strips *i* and *i* +1 as shown in Figure 4.14. The relative displacement is then expressed as:

$$\Delta y = y_{i(\text{bottom})} - y_{i+1(\text{top})} \tag{4.17}$$

where,

$$y_{i(\text{bottom})} = -\delta\theta^* \left(1 - \left(\frac{\xi - \frac{d\xi}{2}}{D_e}\right)^{\beta}\right)\xi$$

$$y_{i+1(\text{top})} = -\delta\theta^* \left(1 - \left(\frac{\xi + \frac{d\xi}{2}}{D_e}\right)^{\beta}\right)\xi$$

Recall that according to the binomial theorem

$$\left(\xi+\frac{d\xi}{2}\right)^{\beta}=\sum_{k=0}^{\beta}\binom{\beta}{k}\xi^{\beta-k}\frac{d\xi}{2}^{k}$$
$$=\xi^{\beta}+\beta\xi^{\beta-1}\frac{d\xi}{2}$$

and

$$\left(\xi-\frac{d\xi}{2}\right)^{\beta}=\xi^{\beta}-\beta\xi^{\beta-1}\frac{d\xi}{2}$$

Therefore, the relative displacement (Δy) between two adjacent thin strips becomes:

$$\Delta y=\delta\theta^{*}\beta\left(\frac{\xi}{D_e}\right)^{\beta}d\xi \tag{4.18}$$

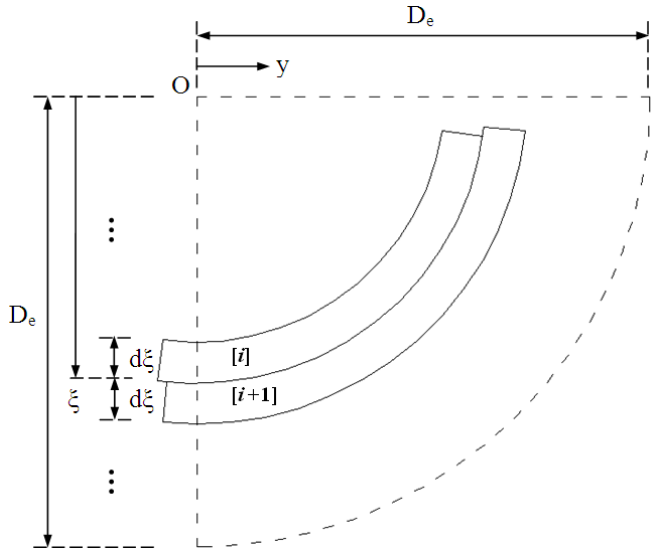

Figure 4.14 Calculatation of Δy

The compatibility mechanism is presented in Figure 4.15. The assumption of no volumetric strain in thin circular strip is valid owing to its undrained nature. As a result, the shape of the face deformation profile can be used to define the deformed shape of the soil prism at surfaces ebb'e' and dcc'd', and they are identical with each other. The face support pressure (σ_T) is non-uniform due to the unit weight of the support medium (γ_s).

Let σ_{T0} be the support pressure at the tunnel axis. Then the following expression between σ_T and γ_s is obtained:

$$\sigma_T = \sigma_{T0} + \left(\xi - \frac{D_e}{2}\right)\gamma_s \tag{4.19}$$

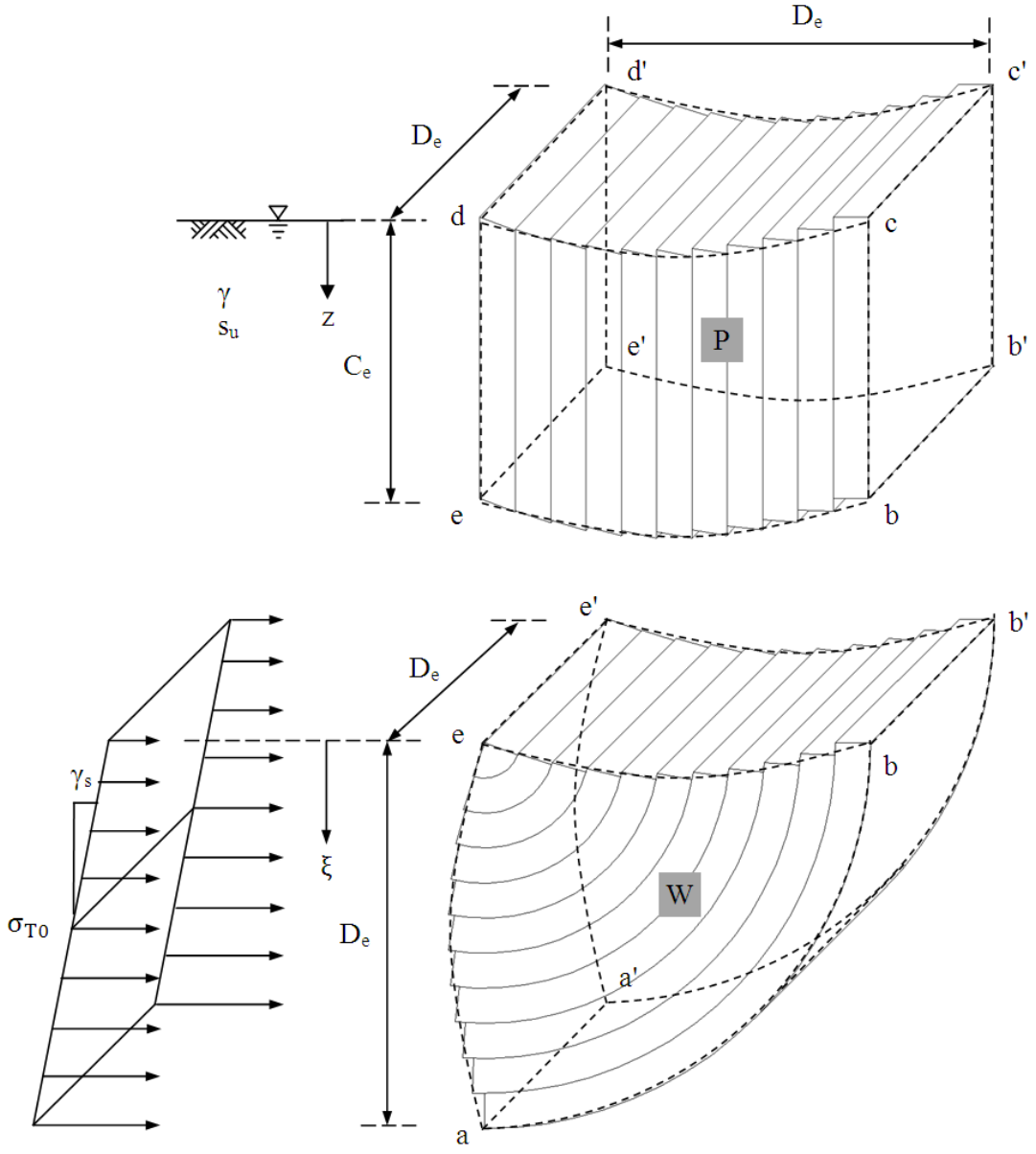

Figure 4.15 Kinematic compatibility

4.3.2. Increment of work done by external forces (δE)

The increment of work done by external forces (Σ(δE)) is the sum of the contributions shown in Table 4.5.

Table 4.5 List of increment of work done by external forces

δE_1: increment of work done to the body W by the support pressure
δE_2: increment of work done to the body W by the gravitational force
δE_3: increment of work done to the body P by the gravitational force

The increment of work done to the body W by the support pressure (δE_1) is expressed as a product of the face support force applied to the thin strip and the displacement value (y) as shown in Equation (4.16). Since the direction of the force vector and the displacement vector are opposite, δE_1 is negative:

$$\begin{aligned}\delta E_1 &= -\int_0^{D_e} \delta\theta^* \left(1-\left(\frac{\xi}{D_e}\right)^{\beta}\right)\xi \cdot \left(\sigma_{T0}+\left(\xi-\frac{D_e}{2}\right)\gamma_s\right) D_e d\xi \\ &= -\frac{\delta\theta^* D_e^3}{2}\left(\frac{\beta}{\beta+2}\sigma_{T0}+\frac{\beta(\beta-1)}{6(\beta+2)(\beta+3)}\gamma_s D_e\right)\end{aligned} \tag{4.20}$$

Figure 4.16 shows the shape of block W after the deformation. For a strip at a depth of ξ from the tunnel crown, the displacement in y-direction is y(ξ) that is expressed as Equation (4.14). Since there is no volumetric strain (undrained behavior), the value of y(ξ) is constant for the strip.

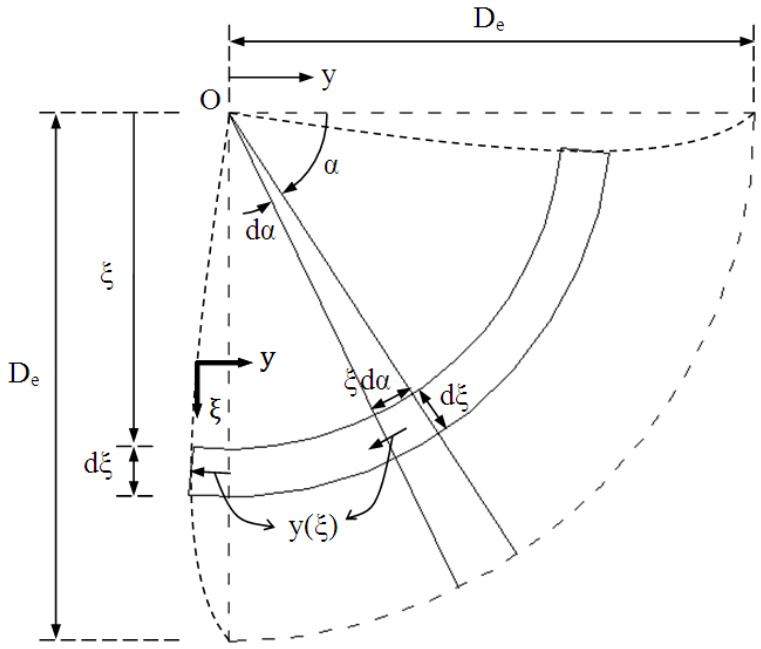

Figure 4.16 Movement of discretized element in the soil wedge W

The increment of work done to the body W by the gravitational force (δE_2) is the product of the body force acting on soil wedge due to the gravity and the displacement in the direction of gravity. Since the water is moving with the soil skeleton (undrained condition), the total unit weight of the ground γ is used:

$$\delta E_2 = \int_0^{\frac{\pi}{2}} \int_0^{D_e} \delta\theta^* \left(1 - \left(\frac{\xi}{D_e}\right)^{\beta}\right) \xi \cos\alpha \cdot \gamma D_e \xi \, d\xi \, d\alpha$$
$$= \delta\theta^* \frac{\beta}{3(\beta+3)} \gamma D_e^4 \tag{4.21}$$

The increment of work done to the body P by the gravitational force (δE_3) is:

$$\delta E_3 = \int_0^{D_e} \delta\theta^* \left(1 - \left(\frac{\xi}{D_e}\right)^{\beta}\right) \xi \cdot \gamma C_e D_e d\xi$$
$$= \delta\theta^* \frac{\beta}{2(\beta+2)} \gamma C_e D_e^3 \tag{4.22}$$

The total increment of work done by the external forces (Σ(δE)) is therefore:

$$\delta E = \sum_i \delta E_i = \delta\theta^* D_e^3 \left(\left(\frac{\beta}{\beta+2}\right)\left(\frac{\gamma C_e - \sigma_{T0}}{2}\right) + \left(\frac{\beta}{\beta+3}\right)\left(\frac{1-\beta}{12(\beta+2)}\gamma_s + \frac{1}{3}\gamma\right) D_e \right) \tag{4.23}$$

4.3.3. Increment of work done by internal stresses (δW)

The increment of work done by internal stresses (δW) is the sum of the contributions in Table 4.6. They represent energy dissipated by the shear deformation within the body and the shear displacement at the failure planes.

Table 4.6 List of increment of work done by internal stresses

δW_1: increment of work done by the shear deformation of the body W
δW_2: increment of work done by the shear deformation of the body P
δW_3: increment of work done at slip planes of the body W
δW_4: increment of work done at slip planes of the body P

The increment of work done by the shear deformation of the body W is expressed as a product of the undrained shear strength (Equation (4.9)) and the relative displacement (Equation (4.18)) at the slip surface between the neighboring thin strips. It is equal to the energy dissipated during the shear deformation of the body W:

$$\delta W_1 = \int_0^{D_e} \int_0^{\frac{\pi}{2}} \left(s_{uo} + \rho\gamma'(C_e + \xi\sin\alpha)\right)(D_e \xi\, d\alpha) \cdot \left(\delta\theta^* \beta \left(\frac{\xi}{D_e}\right)^{\beta} d\xi\right) = \delta\theta^* D_e^3 \left(\frac{\pi}{2}\frac{\beta}{\beta+2}(s_{uo} + \rho\gamma' C_e) + \frac{\beta}{\beta+3}\rho\gamma' D_e\right) \tag{4.24}$$

The increment of work done by the shear deformation of the body P is equal to the energy dissipated during the shear deformation of the body P. The undrained shear

strength (Equation (4.10)) and the relative displacement (Equation (4.18)) is used to calculate δW_2:

$$\begin{aligned}\delta W_2 &= \int_0^{D_e}\int_0^{C_e}(s_{uo}+\rho\gamma' z)(D_e dz)\cdot\delta\theta^*\beta\left(\frac{\xi}{D_e}\right)^{\beta}d\xi \\ &= \delta\theta^*\frac{\beta}{\beta+1}C_e D_e^2\left(s_{uo}+\frac{1}{2}\rho\gamma' C_e\right)\end{aligned} \tag{4.25}$$

The increment of work done at both sides of body W during shear displacement (δW_3) should be calculated for both plane abe and plane a'b'e':

$$\begin{aligned}\frac{1}{2}\delta W_3 &= \int_0^{D_e}\int_0^{\frac{\pi}{2}}\left(s_{uo}+\rho\gamma'(C_e+\xi\sin\alpha)\right)(\xi\, d\alpha\, d\xi)\cdot\delta\theta^*\left(1-\left(\frac{\xi}{D_e}\right)^{\beta}\right)\xi \\ &= \delta\theta^* D_e^3\left(\frac{\pi}{3}\frac{\beta}{\beta+3}(s_{uo}+\rho\gamma' C_e)+\frac{\beta}{2(\beta+4)}\rho\gamma' D_e\right)\end{aligned} \tag{4.26}$$

The increment of work done at both sides of body P during shear displacement (δW_4) should be calculated for both plane bcde and plane b'c'd'e':

$$\begin{aligned}\frac{1}{2}\delta W_4 &= \int_0^{D_e}\int_0^{C_e}(s_{uo}+\rho\gamma' z)(dz\, d\xi)\cdot\delta\theta^*\left(1-\left(\frac{\xi}{D_e}\right)^{\beta}\right)\xi \\ &= \delta\theta^*\frac{\beta}{\beta+2}C_e D_e^2\left(s_{uo}+\frac{1}{2}\rho\gamma' C_e\right)\end{aligned} \tag{4.27}$$

Therefore, the total increment of work done by the internal stresses is expressed:

$$\begin{aligned}\delta W &= \sum_i \delta W_i \\ &= \delta\theta^* D_e^3\left(\frac{\pi\beta(5\beta+13)}{6(\beta+2)(\beta+3)}(s_{uo}+\rho\gamma' C_e)+\frac{(3\beta+11)\beta}{2(\beta+3)(\beta+4)}\rho\gamma' D_e\right. \\ &\qquad \left.+\left(\frac{(2\beta+3)\beta}{(\beta+1)(\beta+2)}\right)\left(s_{uo}+\frac{1}{2}\rho\gamma' C_e\right)\frac{C_e}{D_e}\right)\end{aligned} \tag{4.28}$$

The upper bound solution is obtained when by δE= δW. By equating δE (Equation (4.23)) and δW (Equation (4.28)), the small angle of rotation $\delta\theta^*$ cancels out and the upper bound solution against face collapse is expressed as a function of C_e, D_e, s_{u0} and ρ, and β.

$$\sigma_{T0} = \gamma\left(C_e + \frac{2(\beta+2)}{3(\beta+3)}D_e\right) + \frac{1-\beta}{6(\beta+3)}\gamma_s D_e - \frac{\pi}{3}\frac{5\beta+13}{\beta+3}(s_{u0} + \rho\gamma' C_e) - \frac{(\beta+2)(3\beta+11)}{(\beta+3)(\beta+4)}\rho\gamma' D_e - \frac{2\beta+3}{\beta+1}(2s_{u0} + \rho\gamma' C_e)\frac{C_e}{D_e} \quad (4.29)$$

4.3.4. Sensitivity analysis and comparison with existing solutions

In this section, the value of the coefficient β is found that gives the maximum face support pressure (Equation (4.29)) for different unit weight of slurry, undrained shear strength profile and tunnel diameter and cover depth.

The relations between the calculated face support pressure and the coefficient β is shown in Figure 4.17 for different unit weight of slurry: 0 kN/m^3 (compressed air support), 10 kN/m^3 (clean water), 12 kN/m^3 (typical bentonite slurry), 14 kN/m^3 (typical conditioned muck), and 18 kN/m^3 (native ground). When γ_s is equal to 0, 10 or 12 kN/m^3, the calculated support pressures gradually approach a horizontal asymptote when coefficient β increases. The location of the asymptote is 158.9, 142.2, and 138.9 kPa for γ_s=0, 10 or 12 kN/m^3, respectively. As the unit weight of the slurry increases, the upper bound face support pressure against collapse decreases. The value of coefficient β when the maximum support pressure σ_T takes place is infinity. On the other hand, when γ_s is equal to 14 kN/m^3, the maximum support pressure σ_T (=135.8 kPa) is obtained when β=16. when γ_s is equal to the unit weight of the ground (18 kN/m^3), the maximum support pressure σ_T (=132.2 kPa) takes place when β=3.1. The angle of rotation and the

shape of the face deformation profile are shown in Figure 4.19. The unit weight of the medium used at the face affects the shape of face deformation profile at failure. When γ_s is smaller than or equal to 12 kN/m^3, β tends to be infinity and the circular soil wedge rotates as it were a rigid body. When γ_s=14 or 18 kN/m^3, the maximum face displacement occurred at the bottom 1/7 or 2/5 part, respectively.

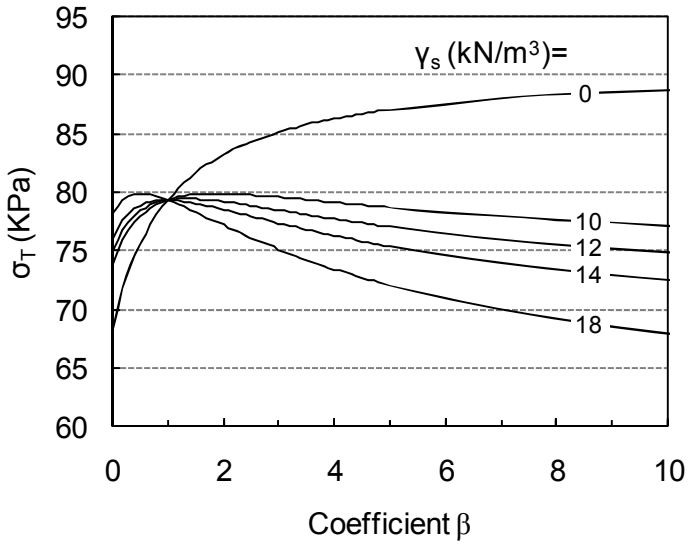

Figure 4.17 Face support pressure according to coefficient β
(D_e=10 m, C_e=10 m, γ=18 kN/m^3, s_u=0.25$\gamma'z$ (σ_{vo}=270 kPa at the tunnel axis))

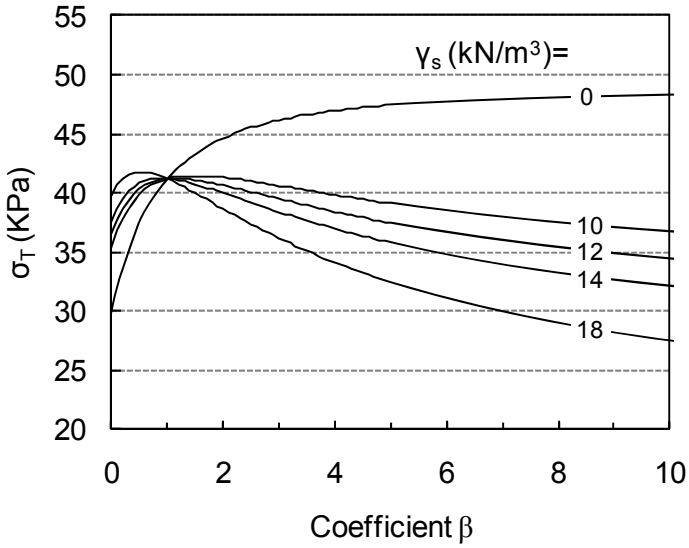

Figure 4.18 Face support pressure according to coefficient β

(D_e=10 m, C_e=10 m, γ=18 kN/m^3, s_u=0.30$\gamma'z$ (σ_{vo}=270 kPa at the tunnel axis))

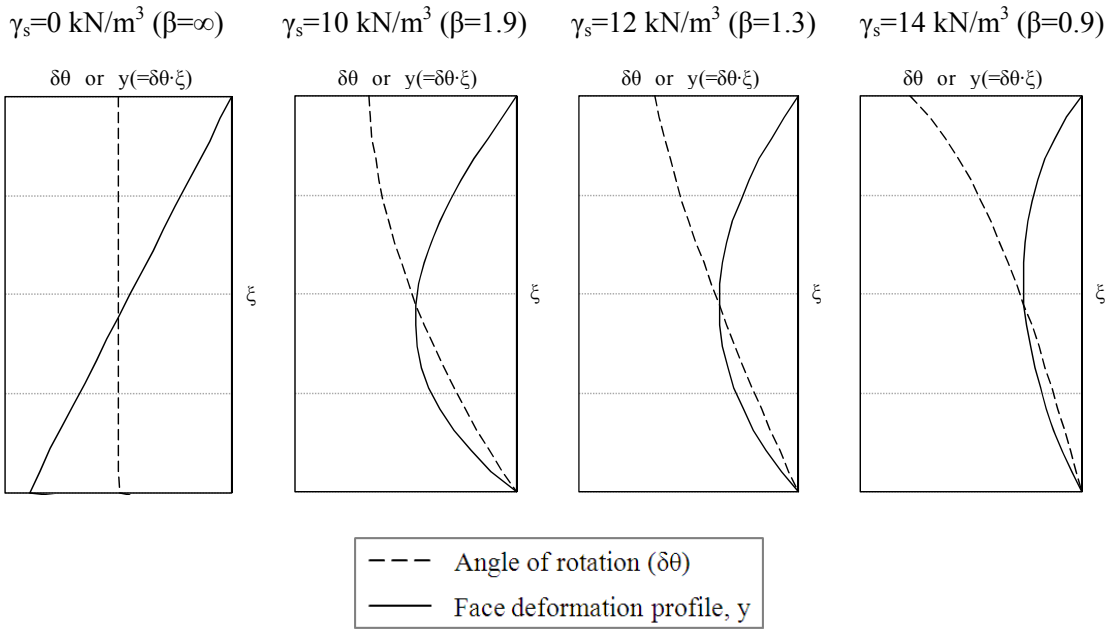

Figure 4.19 Angle of rotation and face deformation profile

(D_e=10 m, C_e=10 m, γ=18 kN/m^3, s_u=0.20$\gamma'z$ (σ_{vo}=270 kPa at the tunnel axis))

Figure 4.20 shows the face support pressure calculated using Equation (4.29) for different undrained shear strength profiles. The face support pressure decreases with increasing normalized undrained shear strength ratio ρ. The value of coefficient β where the maximum support pressure is obtained also decreases with increasing normalized undrained shear strength ratio.

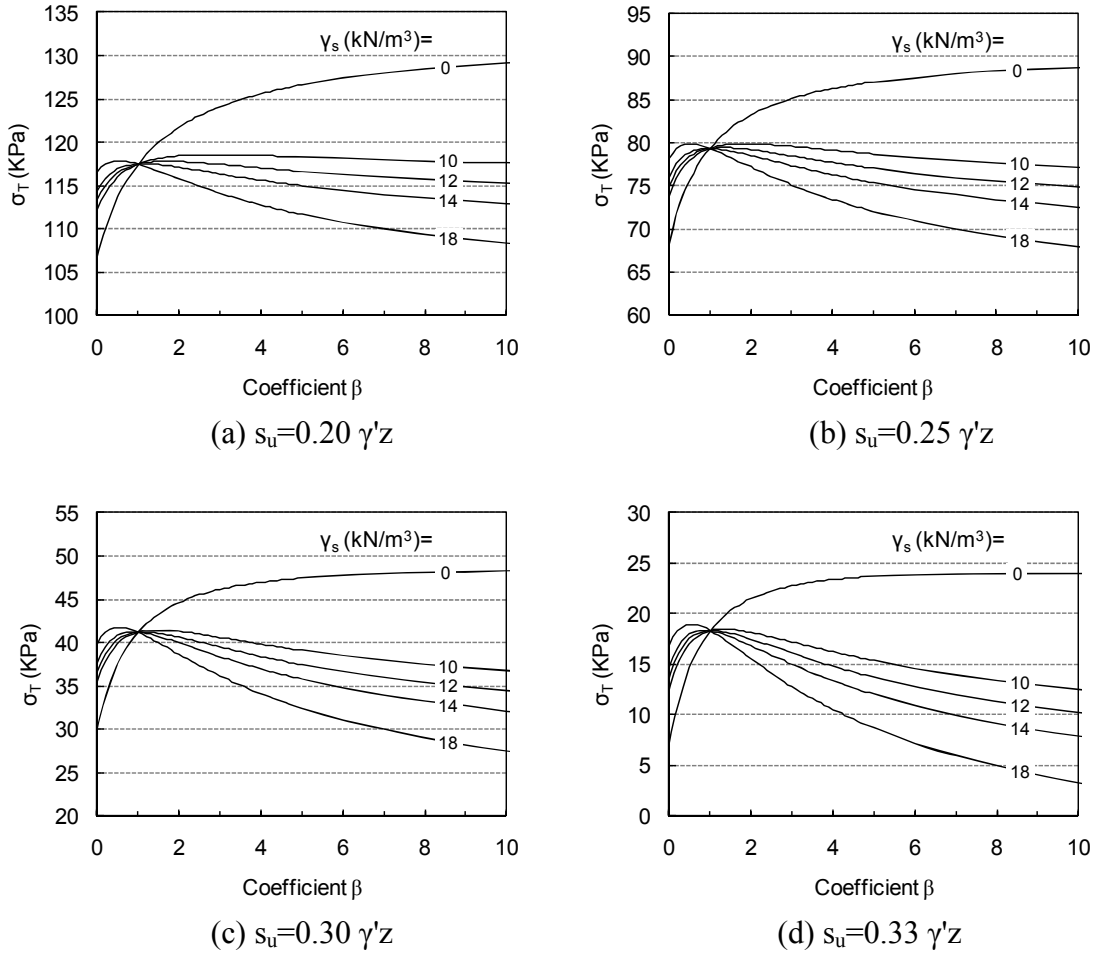

(a) s_u=0.20 γ'z (b) s_u=0.25 γ'z

(c) s_u=0.30 γ'z (d) s_u=0.33 γ'z

Figure 4.20 Undrained shear strength profile and face support pressure (D_e=10 m, C_e=10 m, γ=18 kN/m^3 (σ_{vo}=270 kPa at the tunnel axis))

The upper bound solution against collapse load calculated using Equation (4.29) is presented in Figure 4.21 for varying tunnel diameter when normalized undrained shear strength ratio is 0.25 and cover depth is 10 m. The effect of coefficient β was found to be minimal. Only 10 kPa difference is observed between β=1 (circular face deformation profile) and β=∞ (linear face deformation profile) for the entire range of the tunnel diameter under consideration. The face support pressure was compared with the two dimensional plane strain upper and lower bound solutions published by Davis et al in 1980, and with the experimental solution published by Broms and Bennermark in 1967. Equation (4.29) was found to give smaller support pressure than Davis et al. (1980)'s lower bound solution when tunnel diameter is smaller than 16 m and upper bound solution when D_e<10 m.

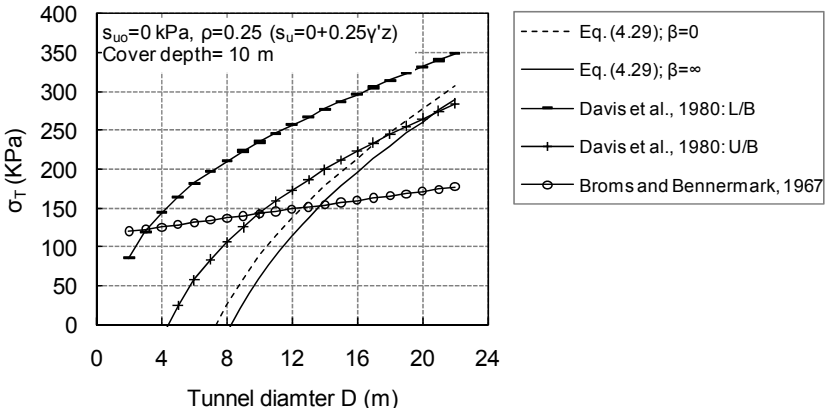

Figure 4.21 Upper bound solution (Equation (4.29)) vs. tunnel diameter

The comparison was also made for varying cover depth as shown in Figure 4.22. Tunnel diameter was fixed as 5, 10 or 15 m and the undrained shear strength of the ground was assumed to follow normalized undrained shear strength ratio ρ=0.25. Because undrained shear strenght of the ground proportionally increases with depth, at a certain point undrained shear strength becomes sufficient to make the tunnel heading self

support. Consequently, the upper bound solutions against collapse decreases with increasing cover depth. The value of cover depth where the face support pressure starts to decrease increases with increasing tunnel diameter. Equation (4.29) was found to give similar support pressure as Davis et al. (1980)'s upper bound solution when cover depth is equal to or smaller than 1D, whereas Equation (4.29) gives smaller value when cover depth is greater than 1D. The current solution is also compared with Kimura and Mair's (1981) model test result, where they investigated the required air pressure in the tunnel to support the face in undrained clay. It is shown that the current solution matches well with the Kimura and Mair's (1981) centrifuge model test result.

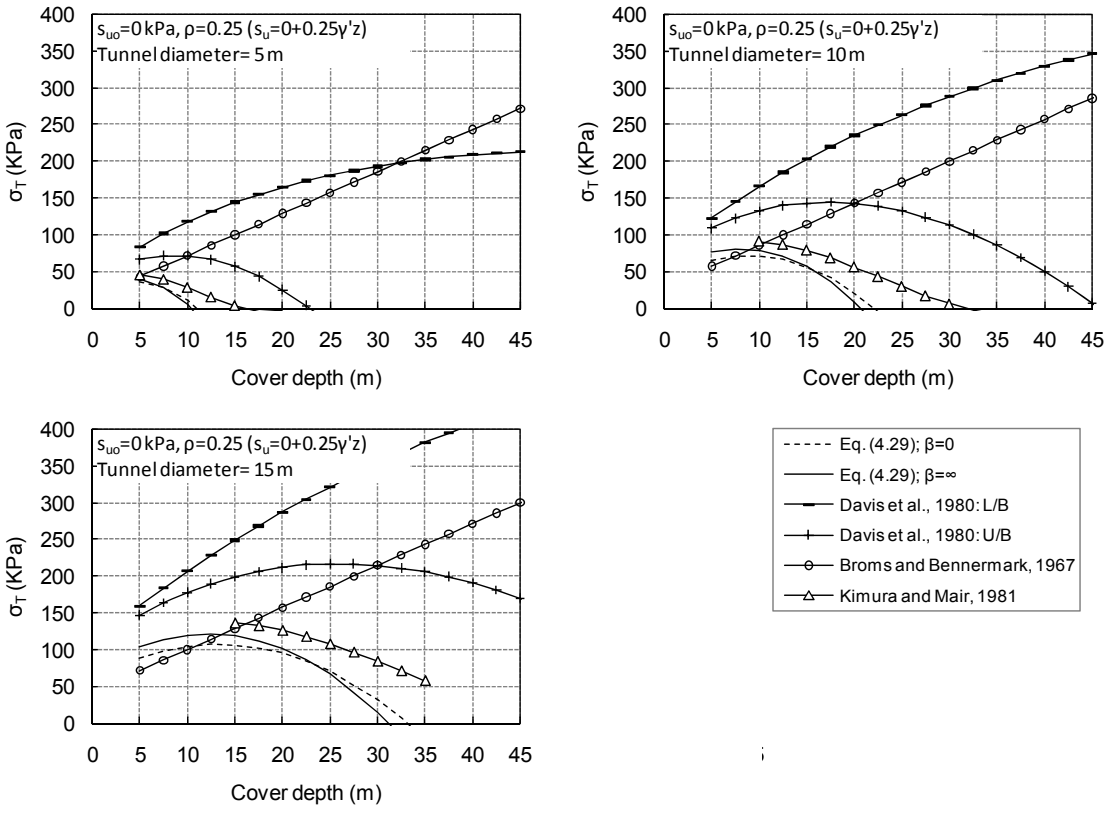

Figure 4.22 Upper bound solution (Equation (4.29)) vs. cover depth

Figure 4.23 shows the comparison of upper bound solutions derived in this chapter. Equation (4.5) was derived assuming that the soil blocks was rigid and Equation (4.12) was derived assuming the block W is deformable. For Equation (4.29), which was derived assuming the blocks P and W were deformable, the unit weight of the supporting medium was set to 12 kN/m^3. Equations (4.12) and (4.29) show a good agreement with the Kimra and Mair's centrifuge model test result (1981).

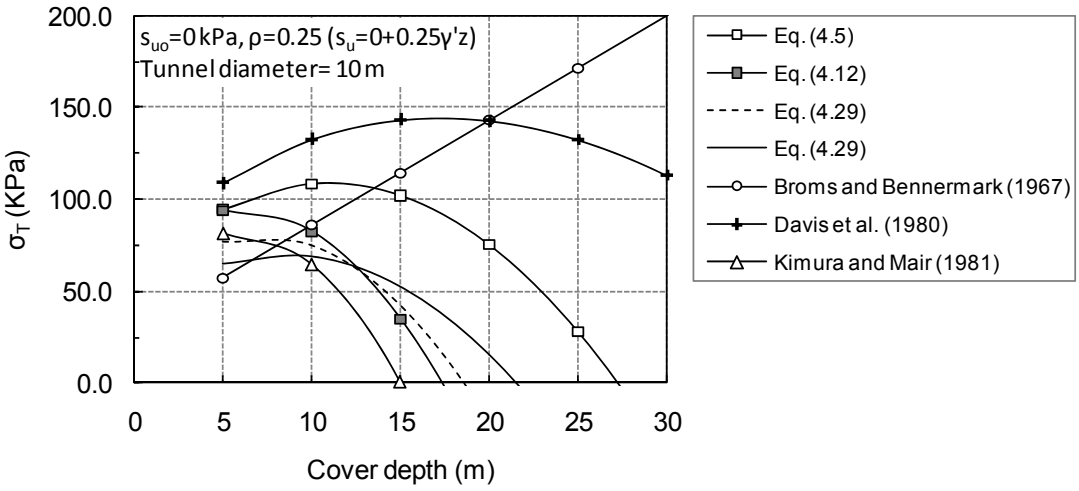

Figure 4.23 Comparison of upper bound solutions

4.4. SUMMARY

The upper bound solution load against collapse was obtained using a prism-and-wedge model. The linear and circular soil wedges which are rigid have been employed in Section 4.2. The face support pressure is expressed as a function of tunnel diameter and cover depth, and undrained shear strength and unit weight of the ground. To take into account the effect of non-uniform support pressure, the deformable circular soil wedge block has been employed in Section 4.3. The body was discretized into thin

strips with thickness of $d\xi$, and the face deformation profile was considered using a coefficient β. The smallest face support pressure was found when the unit weights of the supporting medium and the ground were identical. For a typical face support pressure gradient (12 kN/m^3/m to 14 kN/m^3/m) and a typical undrained shear strength (ρ=0.20-0.30), the face deformation profile was found to be linear and the body block W translated as it were a rigid body. However, when the face support pressure gradient was large (>14 kN/m^3/m) or the undrained shear strength is large (ρ=0.40), a curved face deformation profile was obtained and the maximum displacement of the tunnel face occurred at the bottom 1/7-2/5 location. The support pressure evaluated using Equation (4.29) was found to be smaller than Davis et al. (1980)'s upper bound value.

CHAPTER 5. FINITE ELEMENT SIMULATION OF TUNNEL FACE STABILIY AND PREDICTION OF REQUIRED FACE SUPPORT PRESSURE

In this chapter, finite element simulations were carried out for both drained (Section 5.1) and undrained (Section 5.2) ground to investigate the ground behavior due to tunneling. The necessary face support pressure evaluated from a series of finite element simulations is presented as a function of geometrical (tunnel diameter and cover depth) and geotechnical parameters for drained and undrained ground. The results from the finite element simulations were compared with the values obtained from the solutions available from the literature (Sections 5.1.5 and 5.2.5).

5.1. FINITE ELEMENT SIMULATION (DRAINED CASES)

As already described in Section 3.3, the two noteworthy limitations shared by the approaches using limit analysis and limit equilibrium method come from the fact that failure planes are predetermined or assumed, and these planes may not always realistically represent the actual situation, and from the fact that it is impossible to consider the displacement or deformation. To overcome this drawback, a series of 3-D finite element analyses were carried out based on the ideal membrane model. The description of ideal membrane model is presented in Section 5.1.1. A circular mechanically driven tunnel in a saturated homogeneous ground was modeled. To investigate the behavior of the tunnel face subjected to support pressures (ranging from 0% to 200% of lateral earth pressure) a parametric study was carried out to examine the effect of geotechnical and geometric conditions on the required face support pressure. The required face support pressure obtained as a result of finite element analyses was

compared with the following three analytical solutions: Anagnostou and Kovári (1996); Leca and Dormieux (1990); and Jancsecz and Steiner (1994), which are three dimensional face stability solutions derived based on a homogeneous Mohr-Coulomb material. Additionally, multi-variable regression analysis was carried out to express the required effective face support pressure ratio as a function of five parameters considered in this study.

5.1.1. Ideal face membrane

The face is supported by the pressurized slurry in case of slurry-shield machine and by the pressurized mixture of muck and bentonite slurry in case of earth-pressure balanced machine (EPBM). The tunnel face becomes unstable as the slurry penetrates into the ground due to the pressure build-up ahead of the tunnel face. The deteriorating effect of slurry infiltration on the face stability has been studied by a number of authors (for slurry shield driven tunnels, see: Anagnostou and Kovári, 1994; Kasper and Meschke, 2004; for earth pressure balanced shield, see: Anagnostou and Kovári, 1996; Broere, 2002; Babendererde et al., 2005). If the tunnel face were sealed by a thin impermeable layer (i.e. impervious membrane or ideal membrane), the slurry penetration may not take place. Figure 5.1 shows the role of the ideal membrane created on the excavation face in an EPB shield driven tunnel (Maidl and Cordes, 2003; Babendererde et al., 2005). In this case, the difference in pressure between the slurry and the ground water will act as an effective face support pressure. The impervious membrane develops when the small clay particles in the slurry form a filter cake on the excavation surface quickly enough to prevent slurry infiltration as soon as the soil mass is removed from the excavation face.

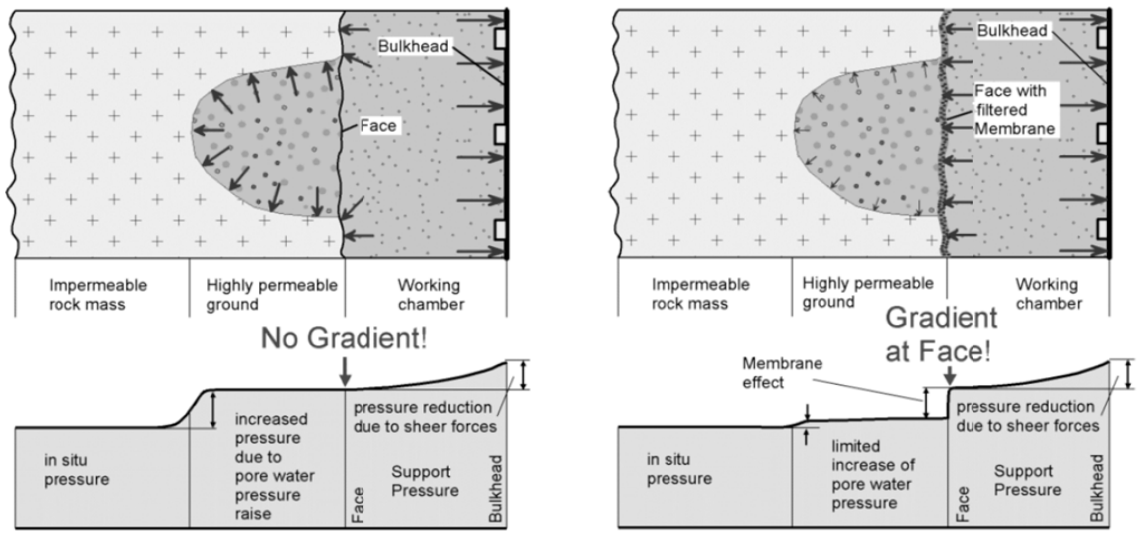

(a) No membrane (b) With membrane

Figure 5.1 Transfer of support pressure (Babendererde (2005))

For the ideal membrane model in a slurry or an earth pressure balanced shield to be valid, the following conditions should be satisfied. First of all, the pressure of the slurry or the muck in the excavation chamber should be greater than the water pressure of the surrounding ground. Otherwise, inward ground water flow will take place and the filter cake cannot be created and sustained. Secondly, the permeability of the ground should be low enough not to allow rapid influx of the slurry into the ground in front of the TBM, and the pore size of the ground should be small enough to inhibit the particles in the slurry or muck from infiltrating into the pores of the ground ahead of the tunnel face. Figure 5.2 shows that as the effective grain size d_{10} increases, the tunnel face safety factor decreases.

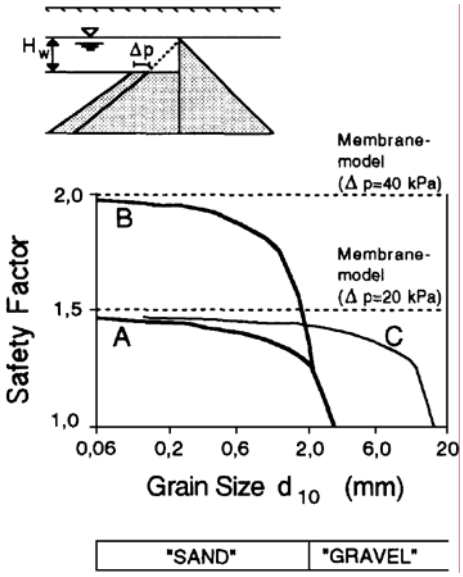

Figure 5.2 Membrane model (modified after Anagnostou and Kovári, 1994)

The dotted lines represent the safety factor when the slurry penetration does not take place at all (ideal membrane model) for a specific excess pressure Δp. Anagnostou and Kovári (1994) concluded that the slurry behaves as if the face were sealed when d_{10} is smaller than 0.6 mm based on the observation that the pressure transferred to the soil skeleton ahead of the tunnel face can be approximated by the ideal membrane model without a significant error. Thirdly, it is necessary to maintain a proper concentration of additives and polymers according to the ground conditions. In a fine grained soil, the filter cake is likely to build up, and therefore the face stability may be achieved by increasing the slurry pressure, because the increased excess pressure Δp would be transferred to the impermeable membrane and thus to the soil skeleton. On the other hand, in a coarse grained soil, where the filter cake is less likely to develop, the increased excess pressure Δp would only promote the slurry penetration rate and distance, and therefore the tunnel face will not gain the stability solely by increasing the slurry pressure. In order to aid the formation of the impermeable membrane in a coarse

grained soil, polymers with long strings or saw dust are frequently used since they create a micro-structure like a net and clog the pores on the tunnel face. From a lab test using a slurry composed of bentonite, polymers and saw dust, Steiner (1993) reported the creation of impermeable air-tight membrane that could withstand up to 100 kPa of air-pressure in a poorly graded gravelly ground (granular diameter of 4 to 8 mm).

5.1.2. Numerical model

The primary purpose of the numerical simulation was to evaluate the influence of the following five factors on the relationship between the required face support pressure and the consequent deformation of the face in the horizontal direction: D (tunnel diameter), C/D (cover-to-diameter ratio), K_0 (lateral earth pressure coefficient), c' (cohesion), and φ' (friction angle). For this purpose, 15,552 analyses were prepared using the finite element analysis software Midas GTS (Midas Information Technology, 2009). As summarized in Table 5.1, twelve different geometries and 144 different geotechnical properties were combined. To facilitate the otherwise tedious process, macro programs designed specifically for this project were developed for input file preparation and output file data collection.

Table 5.1 Analysis case

Tunnel geometry (12 cases)
4 sets of diameter (D): 5, 7, 10 and 14 m
3 sets of cover-to-diameter ratio (C/D): 1, 2 and 4
Geotechnical properties (144 cases)
4 sets of cohesionless soils (φ'=30°, 35°, 40° and 45°)
32 sets of c-φ soils (c'=5, 10, 20, 30, 40, 60, 80 and 100 kPa; φ'=20, 25, 30 and 35°)
4 sets of in situ stress condition (K_0=0.5, 0.75, 1.0, 1.5)
Effective face support pressure (σ'_T) applied normal to the face
9 sets of pressure (0, 10, 20, 40, 60, 80, 100, 140 and 200 % of σ'_h)

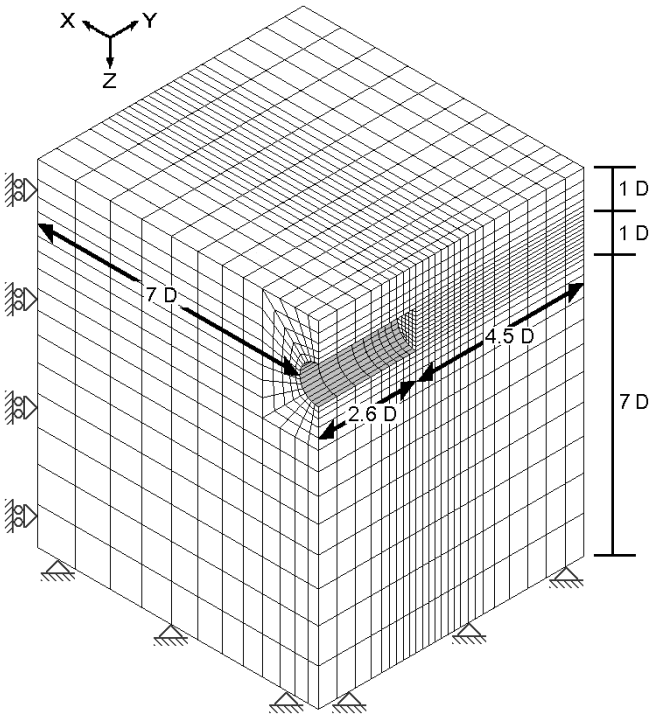

Figure 5.3 3-D finite element mesh

Figure 5.3 shows the finite element model with the cover-to-diameter ratio of 1. Owing to the symmetry of the geometry and the boundary conditions, only a half space was discretized. Four-node first-order shell elements were used to model the shield and the lining, and eight-node first-order solid elements were used for the ground. The number of elements is 7,344, 7,944 and 9,144 for the *C/D*=1, 2 and 4 models respectively. Sufficient distance was given between the model boundaries and the tunnel face to avoid any boundary effect. All translational and rotational degrees of freedom were restrained at the bottom of the model and translations in transverse direction and rotations were restrained at the vertical faces of the model. The water table is always located at the ground surface. A saturated unit weight of the ground of 18 kN/m^3 and a Young's modulus of 30 MPa were used for all analyses. A Poisson's

ratio equal to 0.3 was used regardless of the lateral earth pressure coefficient. The ground was assumed to be an elastic perfectly-plastic material conforming Mohr-Coulomb failure criterion. All models assumed associated plasticity, i.e. the dilation angle was assumed equal to the friction angle. The elastic modulus and Poisson's ratio were equal to 210 GPa and 0.15 for the shield, and 30 GPa and 0.25 for the lining, respectively. The shield and lining were modeled to behave lineally elastically. Using effective strength parameters, a drained analysis has been carried out.

Figure 5.4 shows how the magnitude of the face support pressure has been defined in this study. A non-uniform face support pressure was applied to consider the pressure difference between the tunnel crown and the invert due to the self weight of the slurry or the muck in the excavation chamber. The existence of the ideal membrane was reproduced by applying the entire slurry or conditioned muck pressure in the plenum to the tunnel face. σ'_T represents the effective stress at the tunnel axis (average effective stress over the entire face). σ'_h and u_o represent the in situ horizontal stress and the pore water pressure at the tunnel axis.

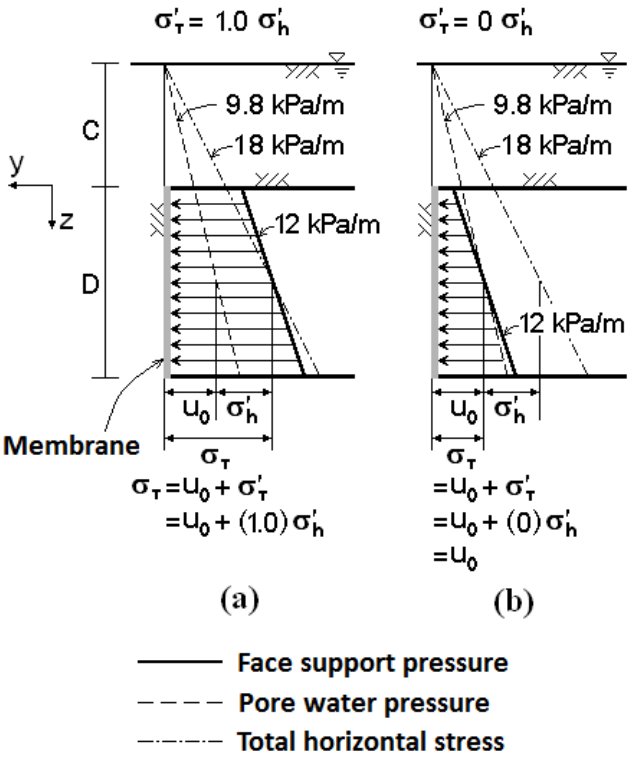

Figure 5.4 Face support pressure

As shown in Figure 5.4(a), when the effective face support pressure $\sigma'_T/\sigma'_h=1$ is applied, the magnitude of the support pressure is equal to the total horizontal earth pressure at the depth of tunnel axis. When the effective face support pressure applied to the face is zero ($\sigma'_T/\sigma'_h=0$), it indicates that the magnitude of the support pressure is equal to the ground water pressure at the depth of tunnel axis and the ground water pressure ahead of the tunnel face is compensated for by the face support pressure (Figure 5.4 (b)). It has to be noted that all of the simulations have been parameterized by *average effective* pressure applied on the face. The unit weight of slurry γ_S of the slurry was assumed to be 12 kN/m^3. (Anagnostou and Kovári, 1994; Chaffois et al., 1988; Li et al., 2008), and therefore the gradient of the support pressure became 12 kPa/m. It is typical that the unit weight of the slurry or the muck in the excavation chamber is slightly higher in earth

pressure balanced shield than in slurry shield. Also, the face support pressure distribution created by an earth pressure balanced shield is not clearly linear like that of slurry shields because the muck in the excavation chamber of the earth pressure balance shield is essentially a solid, even though it is very weak and easily deformable, whereas slurry shields use a liquid. Nevertheless, σ'_T was considered as a distributed pressure linearly increasing with depth, and its gradient was assumed to be equal to 12 kPa/m. Because of the gradient difference between the effective pressure applied to the face and the hydrostatic groundwater pressure, $\sigma'_T/\sigma'_h=0$ does not mean that the effective stress applied to the face is zero everywhere as shown in Figure 5.4(b).

The model did not reproduce several aspects of the TBM in detail. The cutterhead inclination, opening ratio and its mechanical supporting effect were not considered. The weight of the TBM and its backup parts was not accounted for and the shield was modeled as a straight cylinder rather than a conical shaped cylinder. The simulation consists of two steps: In the first stage of the simulation, the anisotropic *in situ* stress state was reproduced and the hydrostatic groundwater pressure was applied to the model. In the second stage, the solid elements in the tunnel were deactivated to simulate the excavation. At the same time, the shell elements for the shield and lining were activated and the face pressure distribution in Figure 5.4 was applied normal to the excavation surface. The tunnel excavation was modeled as a single-step process, assuming that the tunnel advances 2.6D instantaneously. This simplification has been successfully implemented in previous studies (Gioda and Swoboda, 1999; Li et al., 2008). presents the comparison between a single-step simulation and a multi-step simulation.

5.1.3. Numerical simulation result

When the total pressure applied on the face was zero, then the face collapsed as shown in Figure 5.5. Since the solution failed to converge, the deformation shown in the figure is drawn after 30 iterations.

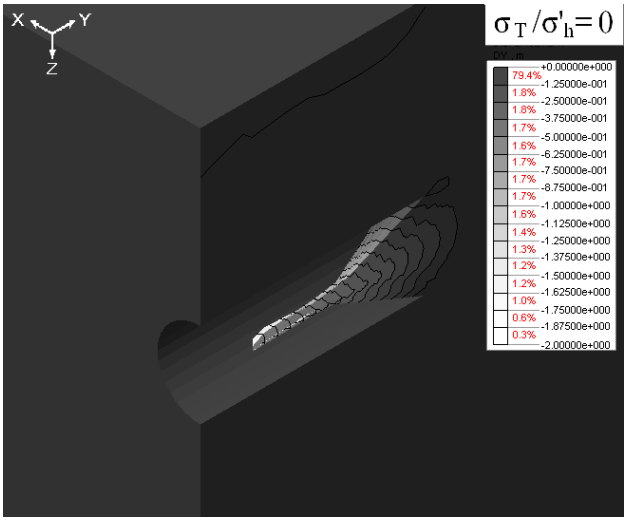

Figure 5.5 Displacement contour in y-direction (10/2; 0kPa/30°/0.5) when σ_T=0; deformation magnified 10 times (after 30 iterations)

Figure 5.6 shows the displacement contours in the *y*- and *z*-directions around the tunnel face when it is subjected to an average effective face support pressure equal to zero, i.e., when the face is supported by a total pressure equal to the pore water pressure. The formation of a chimney is clearly visible. The curve connecting the tunnel crown to the invert after the excavation takes place (line A-A in Figure 5.6(a)) is referred to as "tunnel face deformation profile". Figure 5.7 shows the deformation profile of the tunnel face when it is subjected to σ'_T/σ'_h of 1and 0.6. When $\sigma'_T=\sigma'_h$ at the center of the face (σ'_T/σ'_h =1), the applied face support pressure is greater than the horizontal earth pressure at the tunnel crown, and smaller at the tunnel invert because slurry is heavier than water (Figure

5.4). Therefore, the horizontal earth pressure is not completely balanced, and as a result, the tunnel face deformation profile becomes an s-shaped curve. The average face displacement is zero within 3 significant digits. When σ'_T/σ'_h =0.6, the maximum displacement is concentrated in the lower third part of the tunnel face. The quantity u_{Yavg} is the average face displacement and it will be explained in the following section in detail.

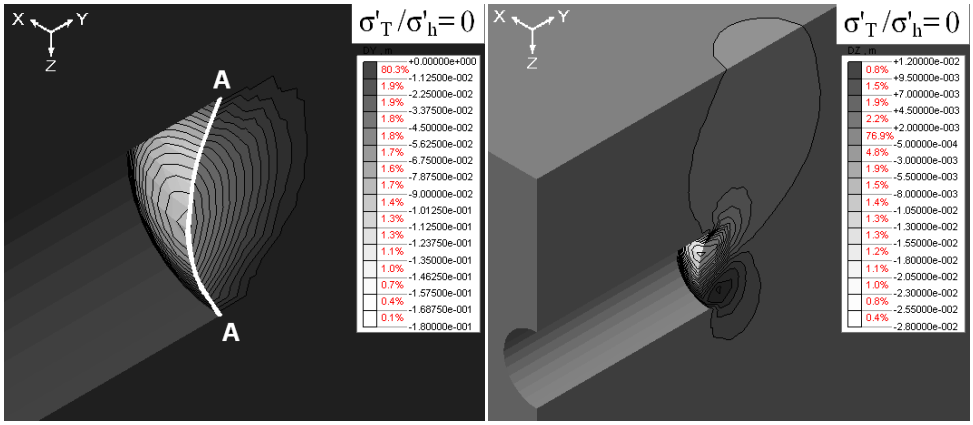

(a) Displacement in y-direction (b) Displacement in z-direction

Figure 5.6 Displacement contour of the ground around tunnel face (D=10 m; C/D= 2; c'=0 kPa; φ'=30°; K_0=0.5); deformation magnified 10 times

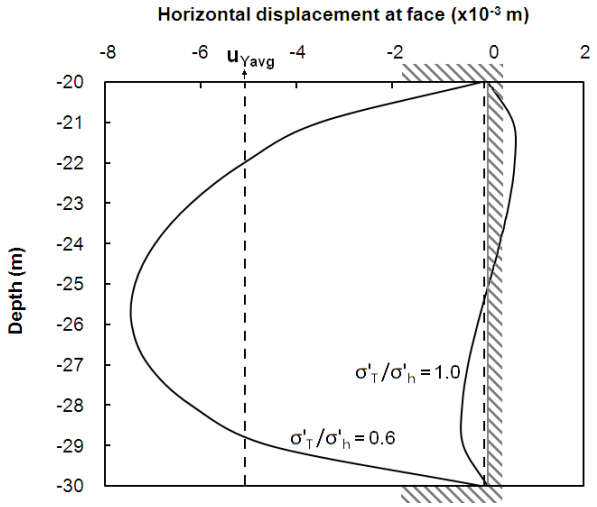

Figure 5.7 Typical face deformation profile
(D=10 m; C/D= 2; c'=0 kPa; φ'=30°; K_0=0.5)

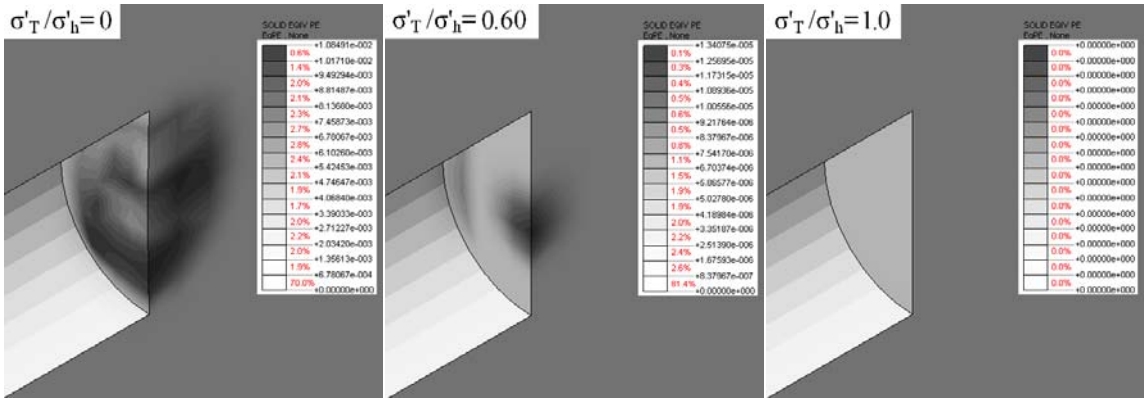

Figure 5.8 Equivalent plastic strain contour (D=5 m; C/D= 2; c'=0 kPa; φ'=30°; K_0=0.5)

Figure 5.8 shows a typical plot of the equivalent plastic strain (ε_p) which is a measure of the amount of permanent strain in a body, developed in a soil mass near the tunnel face. Positive equivalent plastic strain of an element indicates that the element's state of stress is on the yield surface. The figure illustrates that there is a plastic zone surrounded by an elastic zone (also known as confined yield zone), which may form a

local failure plane, but may not always lead to global instability (Kasper et al., 2004). As the face support pressure decreases, the confined yield zone extends from the tunnel face to the surrounding soil mass. It shows good agreement with the fact that the largest plastic strains, and hence the largest displacements, develop around the lower third part of the tunnel face.

When the tunnel diameter is fixed, Figure 5.9(a) shows that the maximum horizontal displacement increases linearly with increasing cover depth C. Figure 5.9 (b), drawn for a fixed C/D, shows that the maximum displacement increases with the square of the tunnel diameter. These two figures suggest that the tunnel face deformation profiles can be reduced to one curve by dividing them by D^2. The normalized plots are shown in Figure 5.10 for cohesionless soil and Figure 5.10(b) for cohesive soil. The vertical axis of the plot (z/D) is the depth from the crown normalized by the tunnel diameter. Figure 5.10(a) shows that when cohesion is equal to zero, the normalized face deformation profiles overlap with each other regardless of the tunnel diameter when the same σ'_T/σ'_h was applied. On the other hand, for the cohesive soils shown in Figure 5.10(b), the normalized face deformation profiles do not overlap with each other when the applied effective face support pressure is much smaller than the *in situ* effective horizontal stress ($\sigma'_T/\sigma'_h << 1$).

Figure 5.11 and Figure 5.12 show the relationship between the normalized average face displacement (u_{Yavg}/D^2) and the applied effective face support pressure ratios (σ'_T/σ'_h). The quantity u_Y represents the displacement in y-direction at a node on the tunnel face. The quantity u_{Yavg} is referred to as the average tunnel face displacement, and is defined by the area enclosed by the deformed tunnel face profile and the original tunnel face profile divided by the tunnel diameter (see Figure 5.7):

$$u_{Yavg} = \frac{1}{D}\sum_{i=1}^{n}((u_Y)_{i+1} + (u_Y)_i)((z)_{i+1} - (z)_i) \tag{5.1}$$

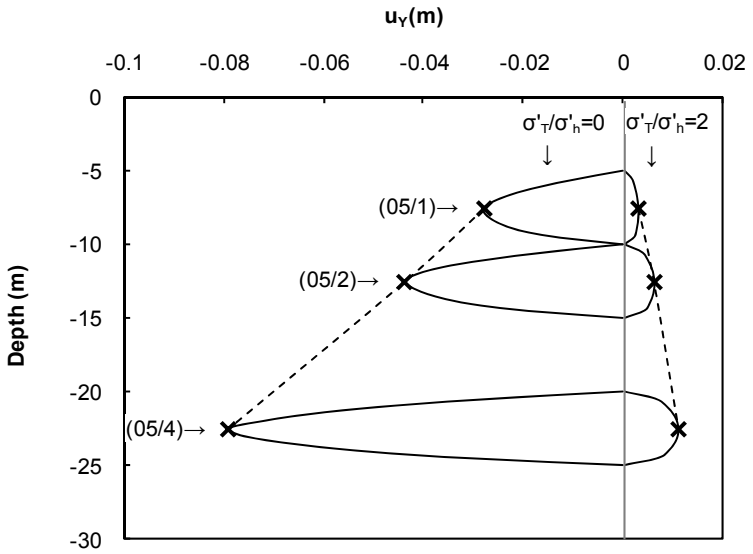

(a) Varying *C/D* (*D*=5 m, *φ′*=30°)

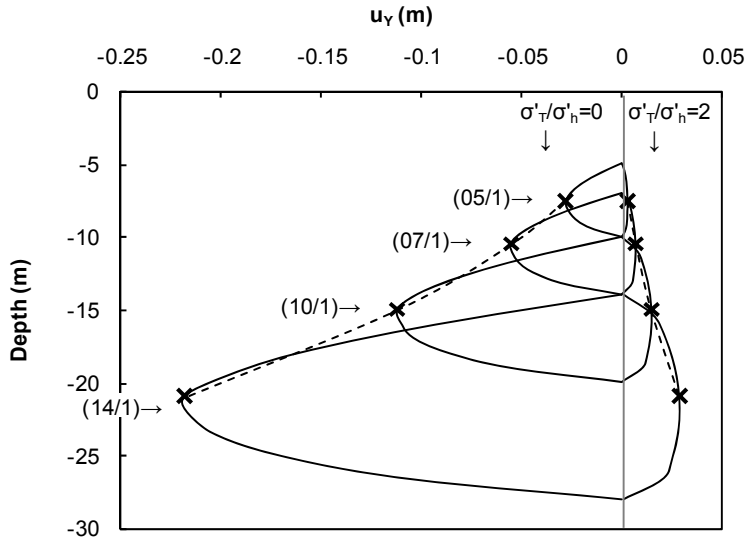

(b) Varying *D* (*C/D*=1, *φ′*=30°)

Figure 5.9 Face deformation profiles

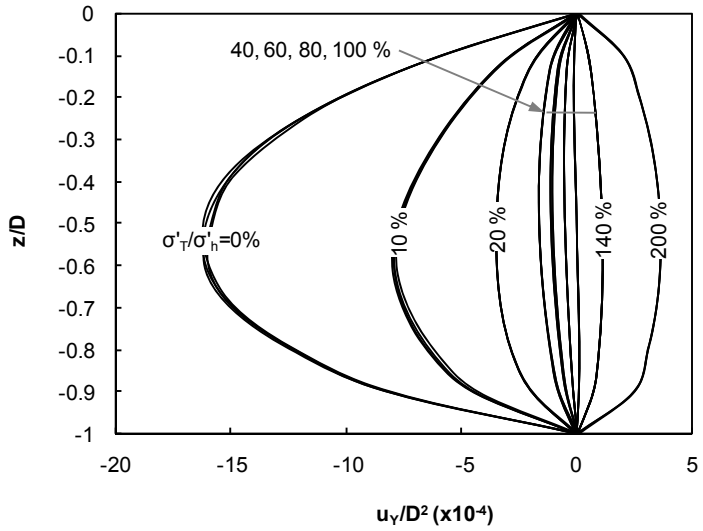

(a) Cohesionless soil (*C/D*=2; *c′*=0 kPa; *φ′*=30°; K_0=0.75)

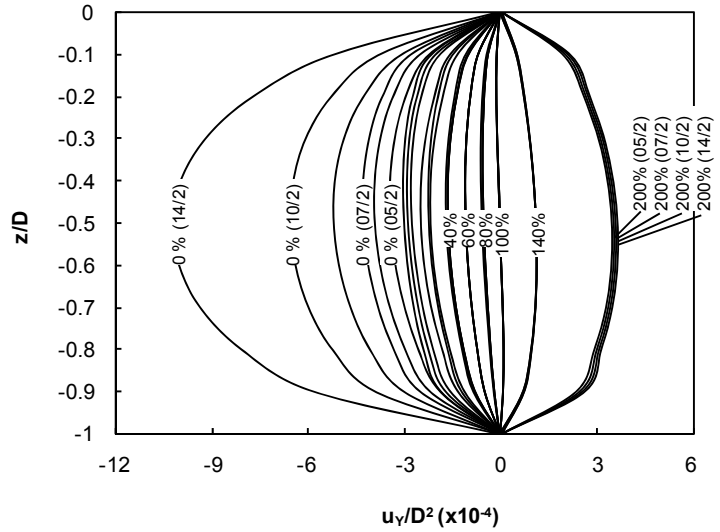

(b) Cohesive soil (*C/D*=2; *c′*=20 kPa; *φ′*=30°; K_0=0.75)

Figure 5.10 Face deformation profile normalized by D^2

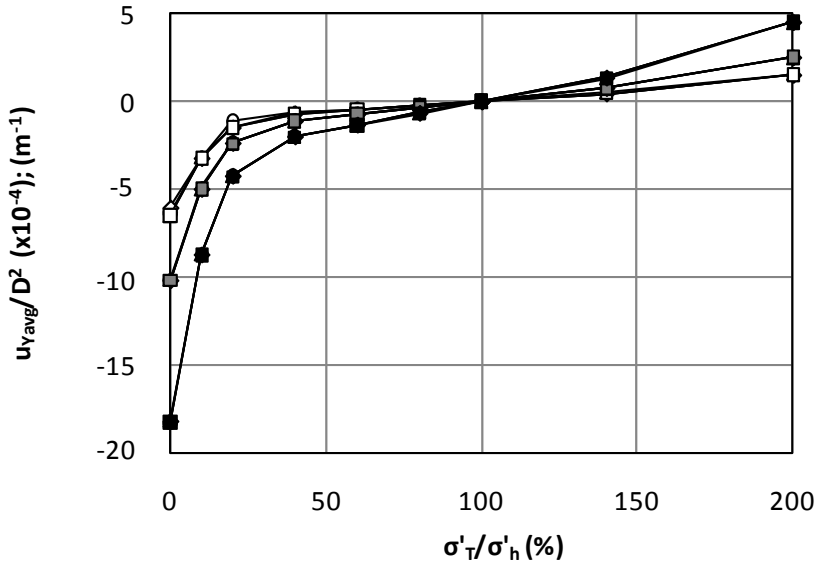

(a) c'=0 kPa; φ'=30°; K_0=0.75

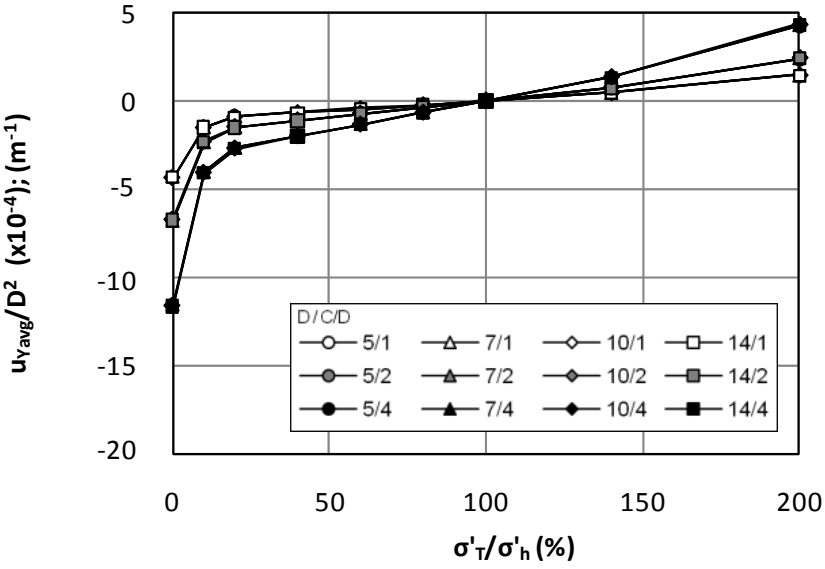

(b) c'=0 kPa; φ'=40°; K_0=0.75

Figure 5.11 Normalized characteristic curves for cohesionless soil

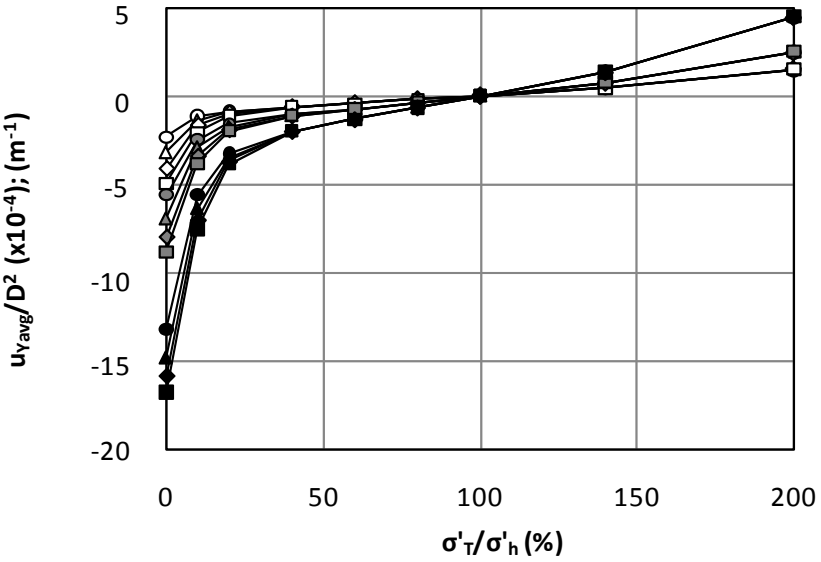

(a) c'=5 kPa; φ'=30°; K_0=0.75

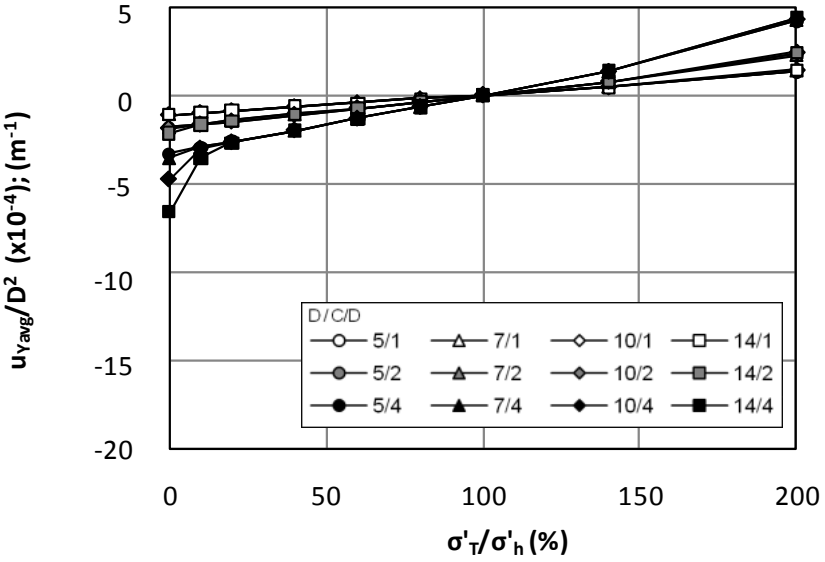

(b) c'=40 kPa; φ'=30°; K_0=0.75

Figure 5.12 Normalized characteristic curve for cohesive soil

Lines that connect the peak displacement points at each deformation profile are drawn in Figure 5.13. It is observed that the peak displacement increases linearly with

increasing cover depth when diameter is fixed (solid lines). The extrusion or contraction of core material under given amount of face support pressure is proportional to the cover depth.

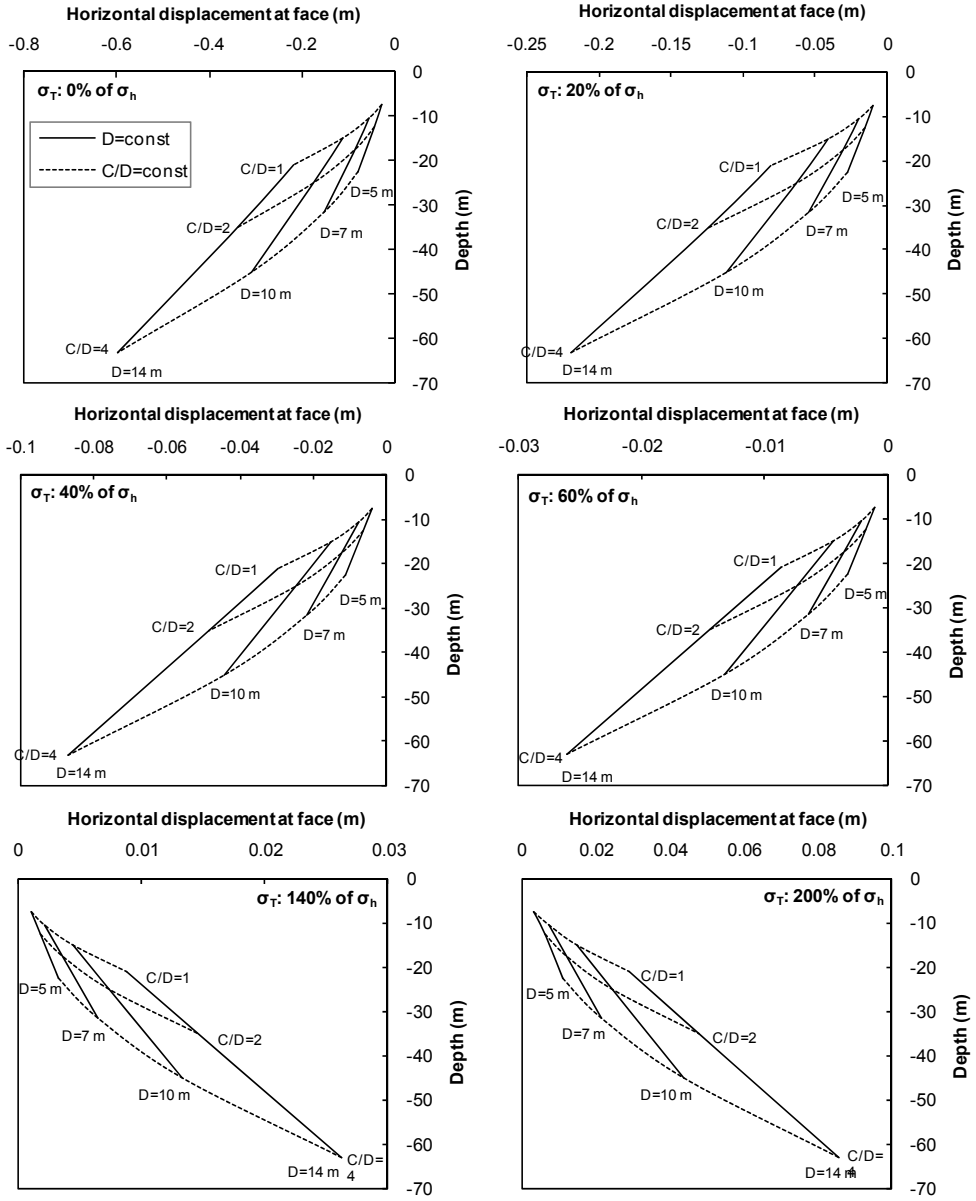

Figure 5.13 Horizontal displacement according to tunnel diameter and depth (c'=0 kPa, φ'=30°)

Negative u_{Yavg} indicates that the tunnel face moved towards the cavity (active state), and the positive u_{Yavg} indicates that the face support pressure is pushing the tunnel face in the direction of advance (passive state). Chaffois et al. (1988) called "characteristic curve" the relation between the displacement of the face center point ($u_{Ycenter}$) and the pressure applied to the face (σ'_T). In this paper the relationship (σ'_T/σ'_h-u_{Yavg}/D^2) is called "normalized characteristic curve".

The normalized characteristic curves are shown for various strength parameters, c' and φ' for cohesionless soil in Figure 5.11 and for cohesive soil in Figure 5.12. In general, the normalized average face displacement decreases with increasing friction angle and cohesion. However, the way the tunnel face behaves under different σ'_T/σ'_h is affected by various factors.

Let us consider the active part of the plot first, i.e. the part to the left of σ'_T/σ'_h=1.0. Figure 5.11(a) and (b) consider the normalized characteristic curves for cohesionless soils. The normalized average face displacement when φ'=40° is about 65% of that when φ'=30° regardless of D and C/D. Figure 5.12(a) and (b) are the normalized characteristic curves for c'-φ' ground. When σ'_T/σ'_h is low, the effect of additional cohesion is clearly visible. When the cohesion is sufficiently large, the tunnel face can stand without a positive effective face support pressure as shown in Figure 5.12(b) where no sudden increase in the face movement is observed as σ'_T/σ'_h drops to zero. In Figure 5.12(b) for tunnel faces with larger D and larger C/D, e.g., (10/4), (14/2) and (14/4) tunnels, yielding is observed as face support pressure decreases unlike for the tunnels with small D and small C/D. When cohesion increases from 0 to 5 kPa, u_{Yavg}/D^2 decreases by 8 % for (14/4) tunnel and 28 % for (14/1) tunnel. For a fixed C/D, u_{Yavg}/D^2 decreases by 23% for (05/4) tunnel and by 64% for (05/1) tunnel. Therefore, the face of

a deep and large tunnel in a cohesive ground is less likely to be self-supporting compared to the shallow tunnels with smaller diameter in the analogous ground with the same friction angle and cohesion (recall that, at least in homogeneous normally consolidated clay, s_u increases with depth). This is because the confining effect provided by the rim of the tunnel diminishes with distance from the outer rim.

When σ'_T/σ'_h is within the range of 0.6~1.4, say, the normalized characteristic curves in Figure 5.11 and Figure 5.12 are independent of the ground strength parameters, c' and φ', and thus there is no difference between cohesive and cohesionless soils. As already shown in Figure 5.8, this is due to the fact that the majority of the soil mass ahead of tunnel face remains elastic and the ground behavior is governed only by the elastic properties of the ground.

Now, let us turn our attention to the passive part of the plot. The failure of the ground in a passive state ($\sigma'_T/\sigma'_h>1$) was never achieved in this analysis. Unlike in the active state ($\sigma'_T/\sigma'_h<1$), the tunnel face displacement changes linearly with σ'_T/σ'_h until σ'_T/σ'_h reaches a value of 2. As a result, it is much easier to control the face displacement when $\sigma'_T/\sigma'_h>1$, as long as the displacement-support force relationship is concerned.

Let us define the tunnel face stiffness as the inverse of the tangent to the curves in Figure 5.11 and Figure 5.12, i.e.

$$\text{Tunnel face stiffness} = \frac{\Delta(\sigma'_T/\sigma'_h)}{\Delta(u_{Yavg}/D^2)} \tag{5.2}$$

where $\Delta(\sigma'_T/\sigma'_h)$ represents an increment in normalized face support pressure, and $\Delta(u_{Yavg}/D^2)$ represents the increment in normalized face displacement.

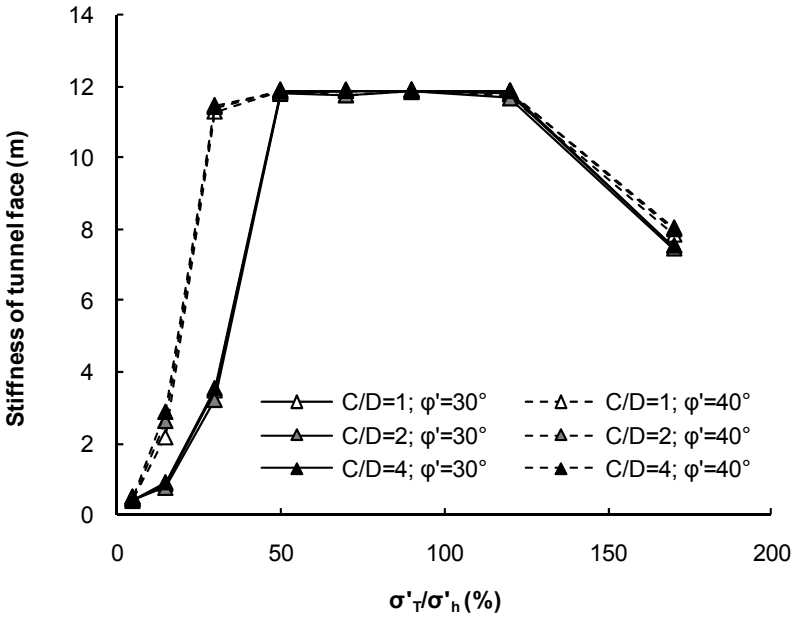

(a) Effects of C/D and φ' (D=7m, K_0=0.75, c'=0 kPa)

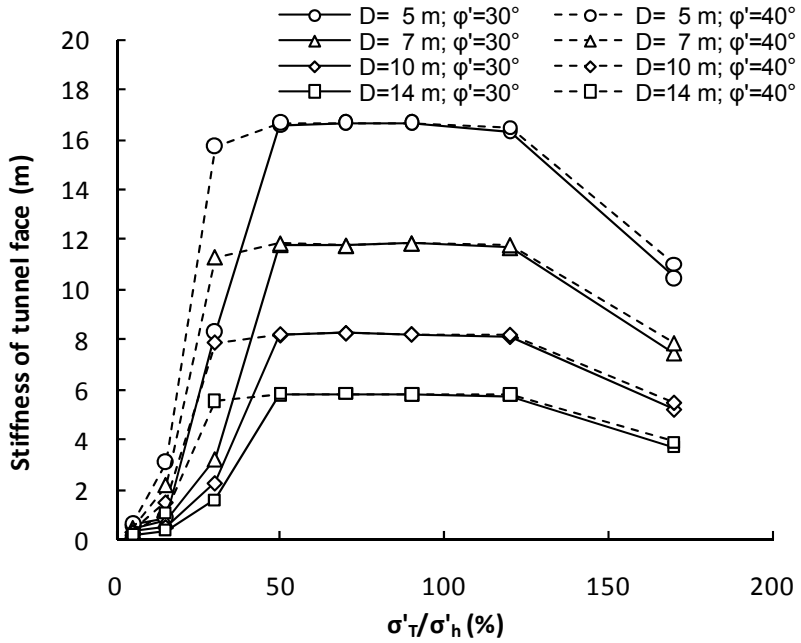

(b) Effects of D and φ' (C/D=1, K_0=0.75, c'=0 kPa)

Figure 5.14 Stiffness of tunnel face in cohesionless ground

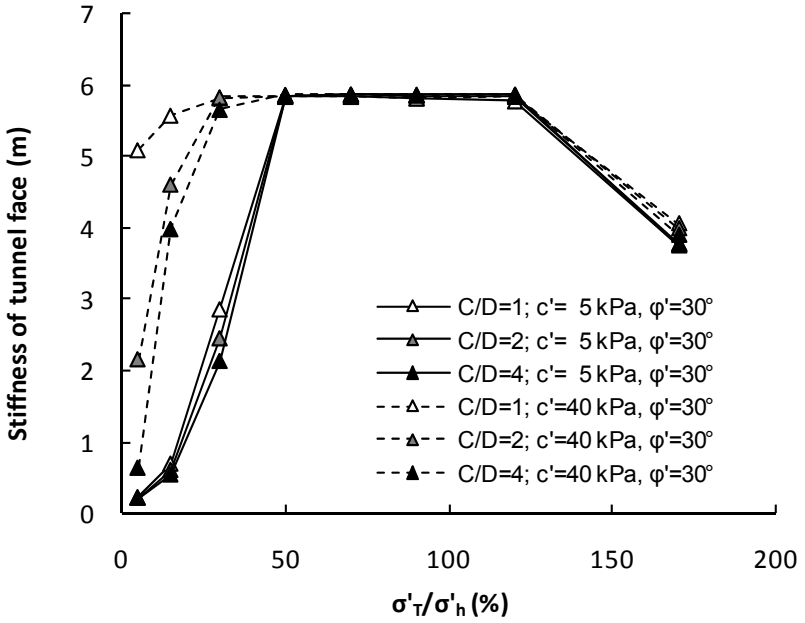

(a) Effects of *C/D* and *c′* (*D*=14m, K_0=0.75, *φ′*=30°)

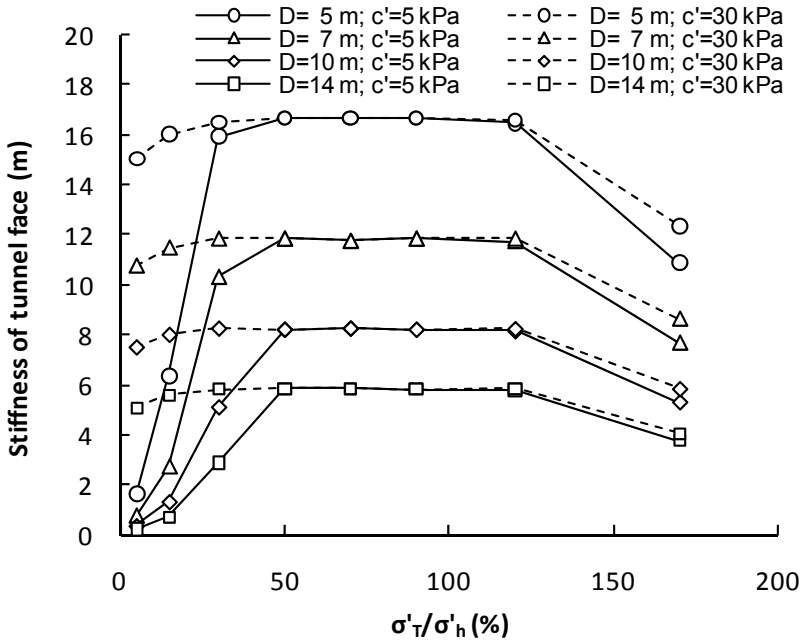

(b) Effects of *D* and *c′* (*C/D*=1, K_0=0.75, *φ′*=30°)

Figure 5.15 Stiffness of tunnel face in cohesive ground

The tunnel face stiffness is shown in Figure 5.14 and Figure 5.15. Because its dimension is length, it should be understood not as a way providing an absolute quantity but as a way to provide a normalized value. As already discussed, c' and φ' do not play a role in the behavior of the tunnel face when it is subjected to the normalized effective face support pressure close to 1. Around the normalized face support pressure of 1, the stiffness of the tunnel face is independent of C/D, K_0, and c' and φ'. From Figure 5.15(a) we see again that the uncontrollable movement of the face is more likely to happen when the tunnel is located deep from the ground surface. For a D=14m C/D=1 tunnel, 30 kPa cohesion is found to be sufficient to prevent the tunnel face from losing the majority of its face stiffness. Figure 5.15(b) shows that the effect of increased cohesion on the tunnel face stiffness is independent of the tunnel diameter so long as the cohesion intercept is large enough to make the tunnel face self-supporting. When c'=5 kPa, the tunnel face stiffness decreases with increasing tunnel diameter. In large diameter tunnels, the tunnel faces lose their stiffness more rapidly with decreasing σ_T'/σ_h' than the smaller diameter tunnels do.

5.1.4. Required face support pressure

In this paper, the "required effective tunnel face support pressure ratio" (σ'_{Tf}/σ_h') refers to the ratio between the minimum average pressure that should be applied on the tunnel face to avoid sudden increase in the tunnel face movement in the case of a small pressure change and the effective in situ horizontal stress. The σ'_{Tf}/σ_h' was defined as a point in a normalized characteristic curve where the sudden change in tunnel face movement takes place. It was determined as the intersection of two straight lines tangent to the normalized characteristic curve at points where the normalized face support

Table 5.2 Required face support pressure from finite element analysis

c'(kPa)	0	0	0	0	5	5	5	5	10	10	10	10	20	20	20	20	30	30	30	30	40	40	40	40	60	60	60	60	80	80	80	80	100	100	100	100
D/(C/D);K_0 $\Phi'(^{\circ})$	30	35	40	45	20	25	30	35	20	25	30	35	20	25	30	35	20	25	30	35	20	25	30	35	20	25	30	35	20	25	30	35	20	25	30	35
05/1; 0.5	28.1	24.6	21.7	19.3	27.8	24.7	20.6	16.5	17.4	12.2	8.3	0	0	0	0	0	0	0	0	0	0	0	0	0	0	0	0	0	0	0	0	0	0	0	0	0
05/2; 0.5	27	24.5	21.4	19	28.9	26.9	23.6	20.3	27.2	22.9	17.9	14.2	11.4	6.9	0	0	0	0	0	0	0	0	0	0	0	0	0	0	0	0	0	0	0	0	0	0
05/4; 0.5	26.8	24.5	21.5	18.9	29.8	27.6	25.3	22.2	29.8	26.9	23.7	19.8	27	21.2	16.4	12.9	17.3	12.1	8.3	0	7.9	0	0	0	0	0	0	0	0	0	0	0	0	0	0	0
05/1; 0.75	20.7	18.9	17.7	17.3	19.3	16.8	14.7	12.2	10.4	6.8	0	0	0	0	0	0	0	0	0	0	0	0	0	0	0	0	0	0	0	0	0	0	0	0	0	0
05/2; 0.75	20.4	18.5	17.4	16.6	21.5	19.6	17.2	15.4	18.1	14.5	11.9	9.2	6.1	0	0	0	0	0	0	0	0	0	0	0	0	0	0	0	0	0	0	0	0	0	0	0
05/4; 0.75	20.3	18.4	17.3	16.3	22.7	20.9	18.7	16.9	21.5	19.2	16.6	14.6	16.6	13.2	10.5	6.9	10.1	6.5	0	0	0	0	0	0	0	0	0	0	0	0	0	0	0	0	0	0
05/1; 1.0	18.5	17.7	16.7	16	18.1	16.2	14.3	11.7	10.1	6.2	0	0	1.2	0	0	0	0	0	0	0	0	0	0	0	0	0	0	0	0	0	0	0	0	0	0	0
05/2; 1.0	18.3	17.5	16.4	15.3	19.9	17.9	16.4	14.8	16.7	14.6	11.9	9	6.5	0	0	0	0	0	0	0	0	0	0	0	0	0	0	0	0	0	0	0	0	0	0	0
05/4; 1.0	18.2	17.5	16.2	15.1	20.7	18.9	17.4	15.7	19.3	17.5	16.1	14.2	15.9	13.4	9.9	0	9.9	5.8	0	0	5.1	1.3	0	0	1.2	0.5	0	0	0	0	0	0	0	0	0	0
05/1; 1.5	18.8	17.7	16.5	15.1	19.4	17.8	16	13.7	15.9	13.1	10	5.9	5.6	0	0	0	0	0	0	0	0	0	0	0	0	0	0	0	0	0	0	0	0	0	0	0
05/2; 1.5	18.8	17.6	16.3	14.7	20.4	18.9	17.3	15.7	18.9	17	14.9	12	13.8	10.4	7	0	6.9	3.5	0	0	3.3	1.3	0	0	1.1	0.5	0	0	0	0	0	0	0	0	0	0
05/4; 1.5	18.7	17.6	16.2	14.4	21.1	19.5	18	16.6	20.4	18.7	17	15.3	18.5	16.5	14	11	15.8	13	9.8	5.2	12.2	8.8	5	1.4	5.5	3	1.3	0.5	2.5	1.3	0.6	0	1.4	0.7	0	0
07/1; 0.5	28.2	24.6	21.7	19.4	28.5	26.3	22.9	19.5	23.7	19.9	15.3	12.2	5.2	0	0	0	0	0	0	0	0	0	0	0	0	0	0	0	0	0	0	0	0	0	0	0
07/2; 0.5	27.1	24.5	21.5	19	29.6	27.3	24.7	21.6	28.6	26.1	21.9	18	21.5	16	11.8	8.8	9.2	0	0	0	0	0	0	0	0	0	0	0	0	0	0	0	0	0	0	0
07/4; 0.5	26.8	24.5	21.5	18.9	30.4	28	25.8	22.8	30.4	27.3	24.7	21.3	30	25.7	20.9	16.9	25.8	19.9	15.3	12	18.7	13.4	9.5	0	5.3	0.5	0	0	0	0	0	0	0	0	0	0
07/1; 0.75	20.6	18.9	17.6	17.3	20.9	19	16.8	15.4	15.9	12.7	9.8	6.8	0	0	0	0	0	0	0	0	0	0	0	0	0	0	0	0	0	0	0	0	0	0	0	0
07/2; 0.75	20.4	18.5	17.4	16.7	22.2	20.5	18.2	16.7	20.4	17.8	15.4	12.9	12.6	9.8	6.1	0	0	0	0	0	0	0	0	0	0	0	0	0	0	0	0	0	0	0	0	0
07/4; 0.75	20.3	18.4	17.3	16.3	23.2	21.4	19.2	17.3	23	20.3	17.9	16.3	20.1	16.9	14.3	11.7	15.6	12.4	9.5	5.5	11	7.7	0	0	1.7	0.6	0	0	0.6	0	0	0	0	0	0	0
07/1; 1.0	18.5	17.7	16.7	16.1	19.4	17.6	16.1	14.5	15.5	12.8	9.4	6	3.1	0	0	0	0	0	0	0	0	0	0	0	0	0	0	0	0	0	0	0	0	0	0	0
07/2; 1.0	18.3	17.4	16.5	15.3	20.5	18.5	17.2	15.6	18.6	16.7	15	12.5	12.9	9.4	0	0	5.2	0	0	0	1.6	0	0	0	0.5	0	0	0	0	0	0	0	0	0	0	0
07/4; 1.0	18.2	17.5	16.2	15.1	21.2	19.2	17.7	16.6	20.3	18.3	16.8	15.2	18.2	16.1	14.2	10.6	15.2	12.4	8.4	0	10.8	6.9	0	0	3.7	1.1	0.5	0	1.3	0.6	0	0	0.6	0	0	0
07/1; 1.5	18.8	17.7	16.5	15.1	20.1	18.6	17.1	15.4	18.2	16.2	13.7	10.9	11.2	7.9	0	0	3.2	0	0	0	1.5	0	0	0	0.7	0	0	0	0	0	0	0	0	0	0	0
07/2; 1.5	18.7	17.6	16.3	14.7	20.7	19.3	17.8	16.3	20	18.1	16.5	14.2	17	14.7	11.6	8.2	12.8	9.4	5.5	0	7.6	5.3	2	0	2.8	1.4	0.6	0	1.3	0.6	0	0	0.5	0	0	0
07/4; 1.5	18.7	17.6	16.2	14.4	21.2	19.7	18.2	16.9	21.2	19.2	17.6	16.3	19.8	17.8	16.2	13.3	18.1	16.1	13.4	10.4	16.2	13.6	10.3	6.2	11	7.7	3.7	1.5	6.1	3.4	1.6	0.6	3.5	1.8	0.8	0
10/1; 0.5	28.2	24.6	21.8	19.6	29.2	27.2	24.3	21.2	28.1	24.8	20.4	16.7	17.6	12.3	8.5	0	0	0	0	0	0	0	0	0	0	0	0	0	0	0	0	0	0	0	0	0
10/2; 0.5	27.2	24.5	21.5	19	30	28.1	25.5	22.4	29.3	27	23.9	20.4	27.4	23	18	14.2	20.3	14.9	10.8	7.6	11.5	7	0	0	0	0	0	0	0	0	0	0	0	0	0	0
10/4; 0.5	26.8	24.5	21.5	18.9	30.5	28.8	26.1	23.2	30.5	27.8	25.2	22.3	30.5	26.9	23.7	19.8	29.8	25.3	20.3	16.4	27	21.3	16.5	12.1	17.3	12.2	8.4	4	7.9	3.1	0	0	0	0	0	0
10/1; 0.75	20.6	18.8	17.6	17.2	21.9	20.2	18.1	16.6	19.8	16.7	14.6	12.1	10.1	6.5	0	0	0	0	0	0	0	0	0	0	0	0	0	0	0	0	0	0	0	0	0	0
10/2; 0.75	20.3	18.7	17.4	16.6	22.9	21.1	19.1	17.2	21.8	19.6	17.1	15.6	18	14.4	11.9	9.2	11.8	8.8	0	0	6	0	0	0	0.5	0	0	0	0	0	0	0	0	0	0	0
10/4; 0.75	20.3	18.4	17.2	16.3	23.6	21.7	19.6	17.7	23.4	20.9	18.7	16.9	21.5	19.1	16.6	14.6	19.7	16.3	13.8	11.1	16.6	13.2	10.5	6.9	10	6.4	1.4	0.5	3.1	0.6	0	0	0.7	0	0	0
10/1; 1.0	18.4	17.6	16.7	16	20.1	18.3	17.2	15.7	18	16.2	14.2	11.6	10	6.1	0	0	6.8	0	0	0	0	0	0	0	0	0	0	0	0	0	0	0	0	0	0	0
10/2; 1.0	18.3	17.4	16.4	15.2	21.1	19	17.6	16.3	19.7	17.8	16.4	14.8	16.8	14.6	11.8	6.3	12	8.3	0	0	6.3	3.8	0	0	1.5	0.7	0	0	0.7	0	0	0	0	0	0	0
10/4; 1.0	18.2	17.5	16.2	15.1	21.7	19.6	17.8	16.8	21	18.8	17.4	16	19.5	18.7	16.1	14.1	17.9	15.9	13.7	9.8	15.9	13.3	9.8	4.8	9.8	5.7	1.4	0.5	4.6	1.6	0.6	0	2	0.8	0	0
10/1; 1.5	18.7	17.7	16.5	15.1	20.5	19.1	17.7	16.2	19.6	17.7	16	13.7	15.8	13	10	5.9	10.1	6.8	3	0	5.6	2.8	1	0	1.9	1	0.5	0	0.8	0	0	0	0	0	0	0
10/2; 1.5	18.7	17.6	16.3	14.7	21	19.5	18.1	16.8	20.7	18.9	17.3	15.7	19	17	14.9	12	16.7	14.2	11	7.4	13.7	10.3	6.9	3	6.9	4	1.9	0.7	3.4	1.7	0.8	0	1.8	0.9	0	0
10/4; 1.5	18.7	17.5	16.2	14.4	21.5	19.9	18.3	17.2	21.4	19.4	18	16.6	20.7	18.7	17	15.2	19.6	17.6	16	13	18.5	16.4	14	10.9	15.8	12.9	9.7	5.1	12.1	8.7	4.6	1.9	8	5	2.3	0.9
14/1; 0.5	28.4	24.7	21.8	19.4	29.9	28.1	24.9	22	28.8	26.4	22.9	19.5	25	20	15.4	12.4	15.4	10.4	6.5	0	5.6	0	0	0	0	0	0	0	0	0	0	0	0	0	0	0
14/2; 0.5	27.3	24.5	21.5	19	30.3	28.5	25.8	22.8	30.1	27.4	24.7	21.6	29.8	26.1	21.9	18	27.5	21.9	17	13.5	21.5	16	11.8	9	9.2	4.5	0	0	0	0	0	0	0	0	0	0
14/4; 0.5	27	24.5	21.5	18.9	30.8	28.8	26.2	23.7	30.8	28.3	25.8	22.8	30.7	27.2	24.6	21.3	30.4	26.9	23.4	19.3	29.9	25.6	20.8	17.3	25.7	19.9	15.2	12	18.7	13.4	9.5	5.8	11.6	7.2	2.5	0
14/1; 0.75	20.5	18.8	17.6	17.2	22.8	20.9	18.9	17.2	21.3	19	16.7	15.3	15.7	12.6	9.6	6.6	8.7	0	0	0	0	0	0	0	0	0	0	0	0	0	0	0	0	0	0	0
14/2; 0.75	20.3	18.5	17.4	16.6	23.7	21.5	19.4	17.5	22.8	20.5	18.3	16.6	20.5	17.7	15.4	12.8	17.1	13.6	11	8	12.5	9.7	5.9	0	4.1	0.7	0	0	0.6	0	0	0	0	0	0	0
14/4; 0.75	20.3	18.4	17.2	16.3	24.6	22	19.8	17.8	24	21.4	19.1	17.3	23.5	20.2	17.8	16.2	22.2	18.8	16.3	14.1	20	16.8	14.2	11.6	15.5	12.3	9.4	5.4	10.8	7.6	2.8	0.7	6.2	1.3	0	0
14/1; 1.0	18.5	17.7	16.7	16	20.8	18.9	17.5	16.5	19.2	17.5	16.1	14.4	15.4	12.7	9.3	0	8.5	3.9	0	0	2.7	1.2	0	0	1	0.5	0	0	0	0	0	0	0	0	0	0
14/2; 1.0	18.2	17.4	16.4	15.2	21.6	19.4	17.7	16.7	20.7	18.4	17.2	15.5	18.5	16.7	15	12.4	16.2	13.8	10.7	0	12.7	9.3	5.2	0	5.1	1.9	0.6	0	1.7	0.7	0	0	1	0	0	0
14/4; 1.0	18.2	17.5	16.2	15.1	22.2	19.8	17.9	17	21.8	19.2	17.6	16.5	20.9	18.2	16.7	15.2	19.2	17.2	15.7	13.7	18.1	16.1	14.1	10.5	15.1	12.3	8.3	1.6	10.7	6.8	1.8	0.6	6.4	2.7	0.7	0
14/1; 1.5	18.7	17.6	16.4	15.1	21	19.5	18	16.7	20.5	18.6	17.1	15.3	18.1	16.1	13.5	10.8	15.1	12	8.9	3.8	11	7.6	4	1.1	4.6	2.3	1	0.5	2	1	0.5	0	1.1	0.5	0	0
14/2; 1.5	18.7	17.6	16.2	14.7	21.4	19.7	18.2	17.1	21.2	19.2	17.8	16.2	20.1	18.1	16.5	14.2	18.6	16.6	14.3	11.4	17	14.6	11.5	8.2	12.7	9.2	5.4	2.1	7.5	4.5	2.1	0.8	4.5	2.3	1.1	0.5
14/4; 1.5	18.7	17.5	16.2	14.4	21.8	20	18.4	17.3	21.7	19.6	18.1	16.9	21.3	19.1	17.6	16.2	20.5	18.5	16.8	14.9	19.8	17.7	16.1	13.2	18	16	13.3	10.2	16.1	13.4	10.2	6.1	13.7	10.3	6.9	2.6

pressure is 0 and 1.0 (Figure 5.16). In case the normalized characteristic curve is straight and the yield point is not apparent, the required face support pressure was set to zero. The σ'_{Tf}/σ_h' values found from a series of FE analysis are summarized in Table 5.2.

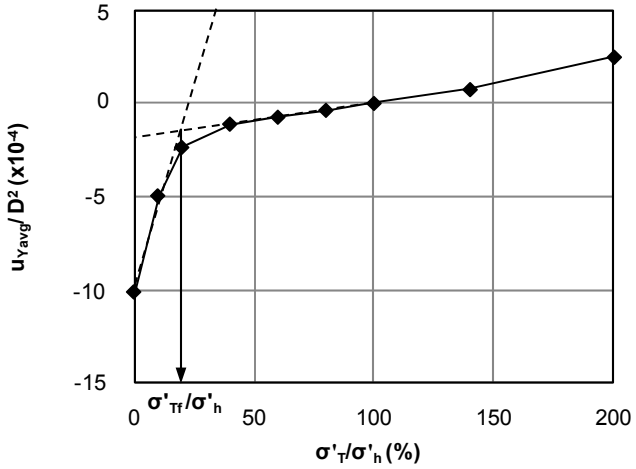

Figure 5.16 Definition of σ'Tf/σ'h on a characteristic curve

Equation (5.3) estimates σ_{Tf}'/σ_h' values in Table 2 using four dimensionless quantities: $|1-K_0|/K_0$, $\tan(\varphi')$, $c'/\gamma' C$ and $c'/\gamma' D$.

$$\frac{\sigma'_{Tf}}{\sigma'_h} = 0.3 + \frac{|1-K_0|}{K_0}\left(\frac{14-9\sqrt{\tan(\varphi')}}{100}\right) - \sqrt{\frac{\tan(\varphi')}{45}} + \frac{c'}{7\gamma'}\left(\frac{2}{C}+\frac{1}{D}+\frac{1}{3C}\frac{|1-K_0|}{K_0}\right) \quad (5.3)$$

Without prior knowledge on the form of the best-fit expression, the derivation of the equation was carried out on a trial-and-error basis. The first step was to evaluate the effects of each dimensionless quantity and their cross effects on the value of σ'_{Tf}/σ_h'. From this analysis, a model equation with unknown multipliers and exponents was

proposed. The second step was finding the unknown multipliers and exponent values, using a multi-variable regression analysis technique. The multipliers and exponents were determined by minimizing the sum of square of errors and maximizing the Pearson's coefficient. As for the multipliers, real numbers within predetermined ranges were tried. As for the exponents, only -1, -0.5, 0.5, 1 and 2 were tried in order to keep the expression simple. Equation (5.3) gives fairly good estimation of σ'_{Tf}/σ_h' and its R^2 is 0.90 for both cohesionless and cohesive ground. Equation (5.3) should not be extrapolated beyond its range of validity, i.e. ideal face membrane; fully saturated with ground water table at the top surface; drained condition; homogeneous soft ground; D from 5 to 14 m; C/D from 1 to 4; K_0 from 0.5 to 1.5; c' from 0 to 100 kPa; and φ' from 30 to 45° for sand and from 25 to 35° for clay.

5.1.5. Comparison with analytical solutions

In this section, the σ'_{Tf}/σ_h' values obtained using finite element analyses are compared with the analytical solutions available from the literature. Three methods have been selected: Leca and Dormieux (1990), Jancsecz and Steiner (1994) and Anagnostou and Kovári (1996). All of them assume drained conditions and are capable of taking c' and φ' into account. Leca and Dormieux (1990) solution, developed based on limit analysis, suggests a range of face support pressures, comprised between a kinematically admissible upper bound value and a statically admissible lower bound value. As for upper bound solutions, MI and MII models were used. MI and MII lead to similar results when C/D is greater than 1.0. As for lower bound solutions, SI model was used because it represents a geostatic stress field and applies to general cases of a soil with weight. SII and SIII solutions were not considered since they deal with

weightless (γ=0) soil. Since Leca and Dormieux (1990) solution refers to a dry condition, the support pressure was obtained using effective parameters and the hydrostatic water pressure was added. Both Jancsecz and Steiner (1994) solution and Anagnostou and Kovári (1996) solution are limit equilibrium solutions using a 3-D silo-and-wedge model and are derived by equating the forces acting upon a soil wedge ahead of the tunnel face. Jancsecz and Steiner (1994) solution takes the arching effect above the excavation face into account. Anagnostou and Kovári (1996) solution considers seepage forces acting on the face. The purpose of making a direct comparison between the FE solution and the three aforementioned solutions should be limited to a comparative study only, even though they are focusing on the same problem, because the methodology each solution employs is different: the FE solution is a result of a load-displacement analysis while the others belong to the category of stability analyses.

Figure 5.17 to Figure 5.20 compare the FE results to the analytical solutions. The FE results are presented as a range since we have simulated various cases with K_0 ranging from 0.5 to 1.5. This range covers typical values for a normally- or over-consolidated ground. The hatched areas in the figures represent envelopes composed of the upper limit and the lower limit with K_0 of 0.5 to 1.5. It is notable that the required effective face support pressures do not exceed 30% of the horizontal effective earth pressure in any case. The increase of the required effective face support pressure (σ'_{Tf}) is not as large as the increase of the *in situ* horizontal earth pressure caused by the increase of K_0 because the required effective face support ratio (σ'_{Tf}/σ_h') decreases with increasing lateral earth pressure coefficient. The analytical solutions considered here use different K_0 values. Leca and Dormieux (1990) and Jancsecz and Steiner (1994) employed a one-to-one relationship between φ' and K_0. Jancsecz and Steiner (1994)

uses a three-dimensional earth pressure coefficient depending on *C/D* and angle of internal friction. Anagnostou and Kovári assumed a constant K_0 value of 0.8 in their solution for slurry shield published in 1994, and K_0=0.4 for the wedge and K_0=0.8 for the prism in their solution for earth pressure balance shield in 1996.

Figure 5.17 refers to cohesionless soil with friction angles ranging from 30 to 45° for *C/D*=1, 2 and 4. Even though Figure 5.17 is drawn for tunnel diameter of 10 m and plots drawn for other tunnel diameters are not shown here, plots for different diameter tunnels are not significantly different from Figure 5.17. Therefore, Figure 5.17 is still valid for tunnels with different diameters. When compared to the FE results, Jancsecz and Steiner (1994) solution is found to give greater values by a factor of 1.5 to 2 regardless of the friction angle, tunnel diameter and cover-to-diameter ratio. Anagnostou and Kovári (1996) solution is found to give smaller values when *C/D*=2 and when *C/D*=4, i.e. for *C/D*>1. Leca and Dormieux (1990) upper bound solution is found to give greater values when *C/D* is equal to 1 and smaller values when *C/D* is equal to 4 and in agreement with FE results when *C/D*=2. The FE results are *not* comprised between Leca and Dormieux (1990) upper bound and lower bound solutions when *C/D* is equal to 1.

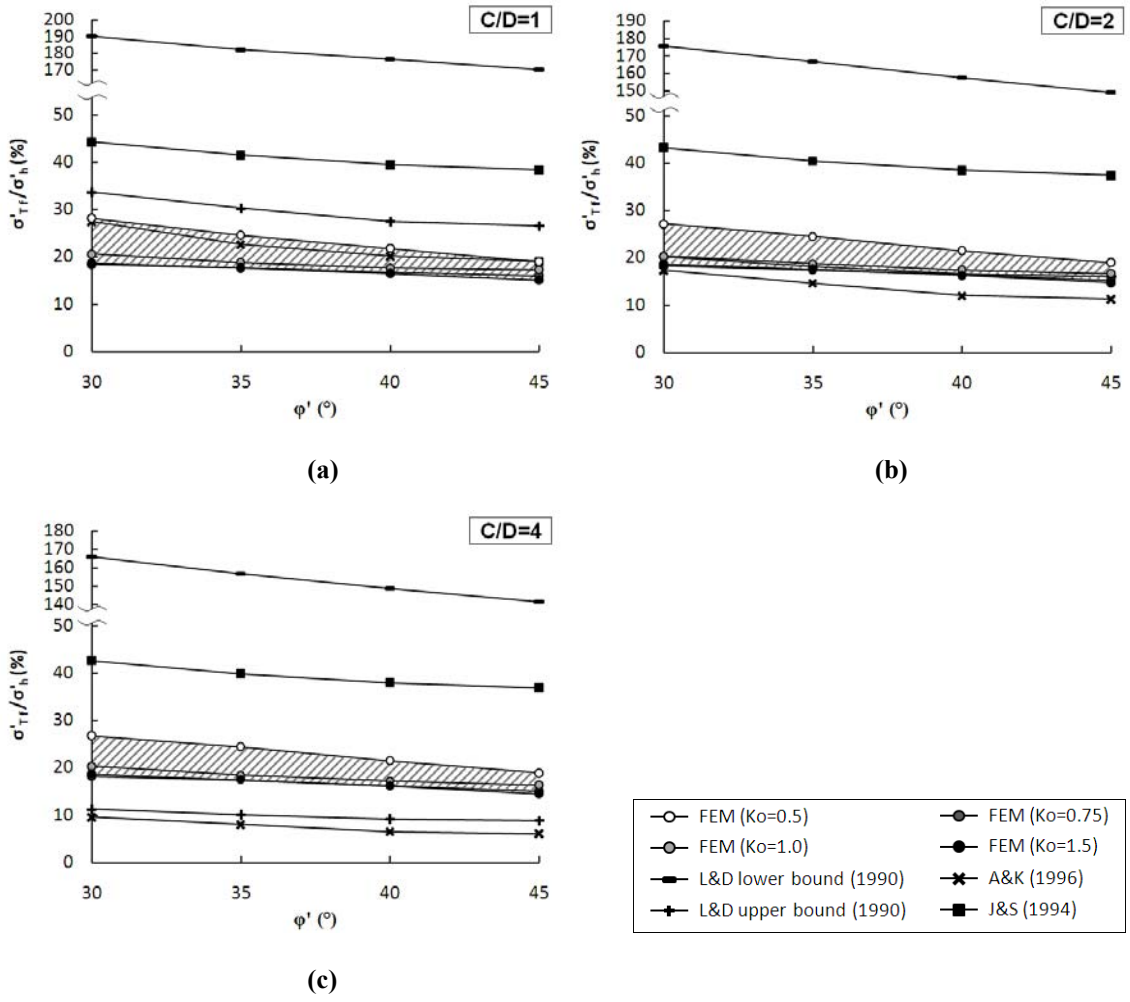

Figure 5.17 Comparison of required face support pressure for cohesionless soil (D=10 m, K_0=0.5)

Figure 5.18 to Figure 5.20 refer to the cohesive-frictional soils. The FE results are shown for various friction angles (Figure 5.18), tunnel diameters (Figure 5.19), and *C/D* (Figure 5.20). As the cohesion intercept increases, the minimum pressure required to support the tunnel face drops quickly and when cohesion reaches a certain value, which depends on various factors like tunnel diameter, cover-to-diameter ratio, lateral earth pressure coefficient and shear strength parameters, then tunnel face stability is

achieved by just compensating the ground water pressure in front of the TBM (i.e. σ'_T/σ_h' =0). Figure 5.18 shows the effect of friction angle on the required face support pressure for a cohesive-frictional material. When the cohesion is greater than 10 kPa, both Leca and Dormieux (1990) upper bound and Anagnostou and Kovári (1996) solutions give σ'_{Tf}/σ_h' values close to zero. The required face support pressure from FE solution was higher than the values from both analytical solutions, especially when the friction angle is high. Figure 5.19 shows the influence of tunnel diameter on the required effective face support pressure and indicates that, when c'<10 kPa, the FE estimated support pressure is greater when the tunnel diameter is small (5 m) and smaller when the tunnel diameter is large (14 m) compared to both analytical solutions; when the tunnel diameter is 7 m or 10 m, the FE results and both analytical solutions show a good agreement. When c'>10 kPa, the FE pressures are higher than both analytical solutions. Figure 5.20 compares the effect of cover-to-diameter ratio for a 10 m diameter tunnel. When *C/D* is equal to 1, the FE solutions and both analytical solutions show a good agreement for c'=0 (see Figure 5.17) and, as the tunnel gets deeper, the FE solution gives higher values than the analytical solutions.

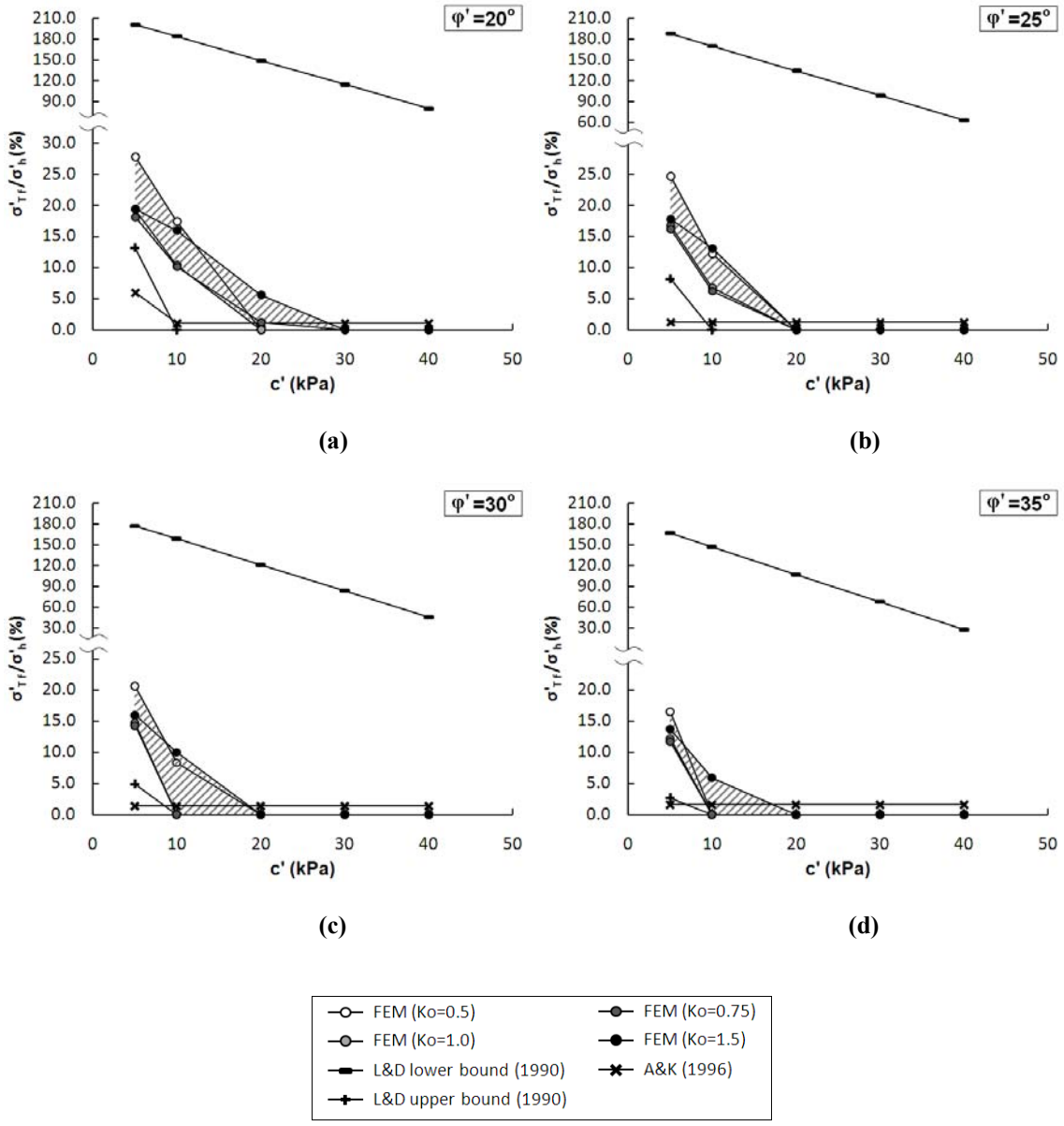

Figure 5.18 Comparison of required face support pressure for cohesive soil (D=5 m; C/D=1)

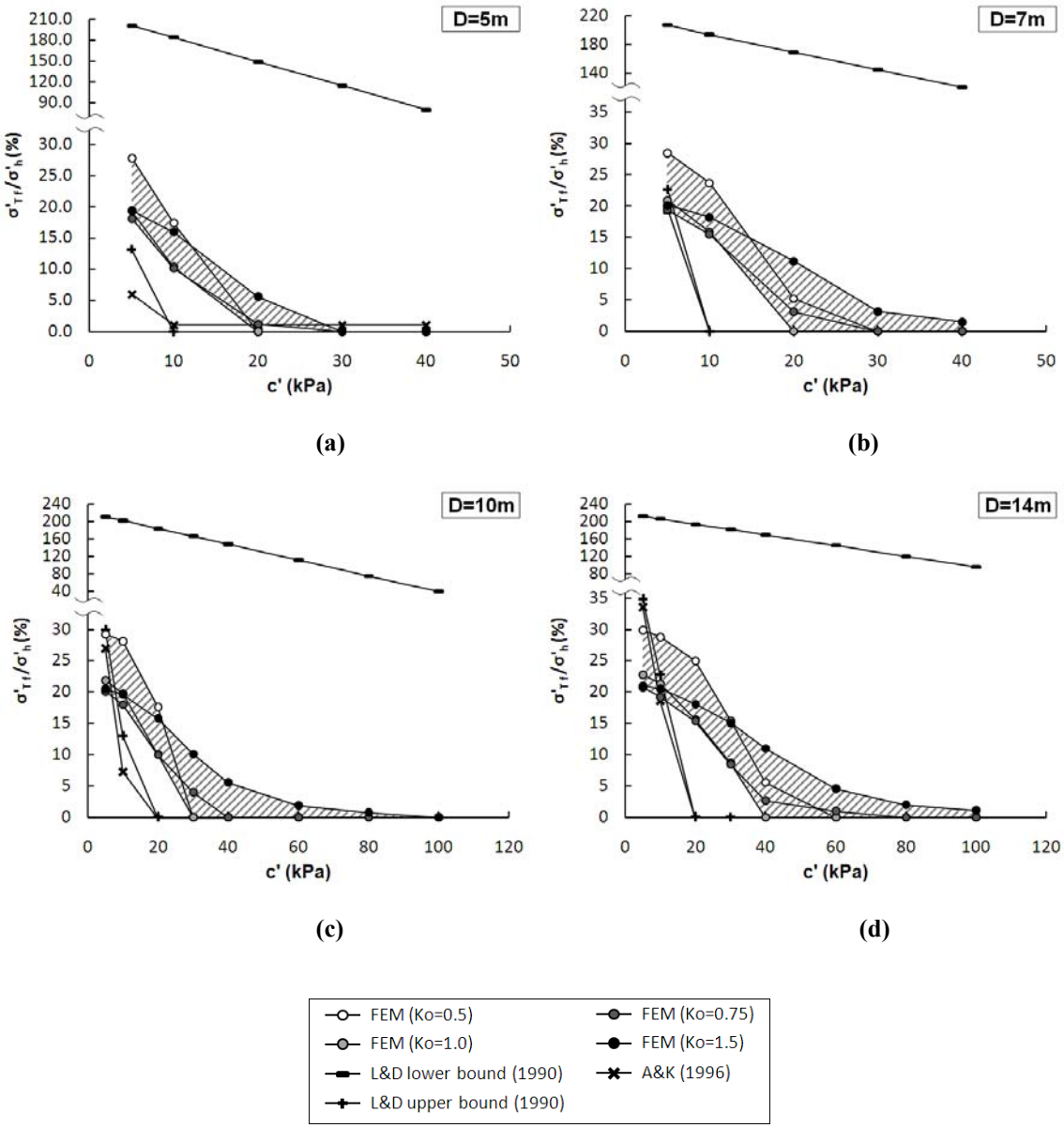

Figure 5.19 Comparison of required face support pressure for cohesive soil (C/D=1; K_0=0.5; φ'=20°)

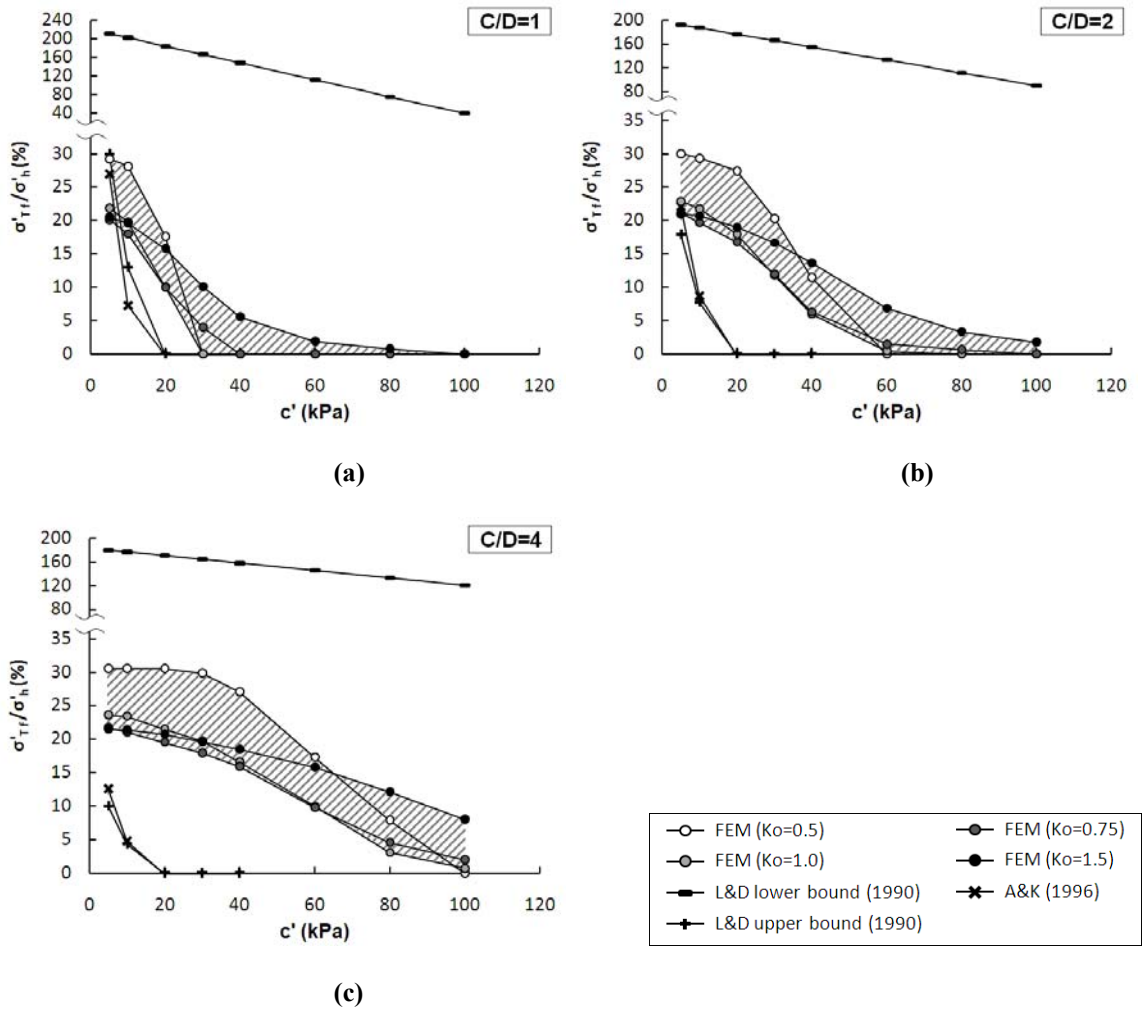

Figure 5.20 Comparison of required face support pressure for cohesive soil (D=10 m; K_0=0.5; φ'=20°)

It is clear that the required face support pressure will decrease as the ground becomes stronger (i.e. shear strength parameters c' and φ' increase). The effect of increasing the shear strength parameters on the required face support pressure is different in the FE solution and in the analytical solutions. Figure 5.18 to Figure 5.20 show that as the cohesion increases, the σ'_{Tf}/σ_h' values evaluated from the FE analyses decreases

more slowly compared to the values calculated from the analytical solutions. In Figure 5.18, we have already seen that as the friction angle increases, the FE solution gives higher support pressure than the analytical solutions. Therefore, the influence of increasing shear strength parameters of the ground on the required effective face support pressure is considered to be overly estimated in both Anagnostou and Kovári (1996) and Leca and Dormieux (1990) upper bound solutions compared to the FE solution.

As for the effect of tunnel diameter and cover-to-diameter ratio on the required face support pressure, the FE solution and the analytical solutions show a similar trend. As the tunnel diameter or *C/D* increases, σ'_{Tf}/σ_h' values increase (Figure 5.19 and Figure 5.20). This trend is observed in both FE solution and the analytical solutions, however, the effect of increasing tunnel diameter and increasing *C/D* on the σ'_{Tf}/σ_h' values is not as strong as indicated by the analytical solutions.

A bird-eye view of the comparison between the FE results and the analytical solutions is presented in Table 5.3 and Table 5.4. If the σ'_{Tf}/σ_h' values from the analytical solution fall on the hatched area of Figure 5.17 and Figure 5.20 (good agreement between the analytical solutions and the FE results), then the symbol '0' is used. If the values from the FE solution are higher than the values from the analytical solutions, then the symbol 'H' is used. 'L' indicates that the values from the FE solution are smaller than the analytical solutions.

Table 5.3 Comparison of FE result with the analytical solutions for cohesionless soil.

C/D	D	A&K (1996)				J&S (1994)				L&D (1990)			
	φ':	30	35	40	45	30	35	40	45	30	35	40	45
1	5	0	0	0	0	L	L	L	L	L	L	L	L
	7	0	0	0	0	L	L	L	L	L	L	L	L
	10	0	0	0	0	L	L	L	L	L	L	L	L
	14	0	0	0	0	L	L	L	L	L	L	L	L
2	5	H	H	H	H	L	L	L	L	0	0	0	0
	7	H	H	H	H	L	L	L	L	0	0	0	0
	10	H	H	H	H	L	L	L	L	0	0	0	0
	14	H	H	H	H	L	L	L	L	0	0	0	0
4	5	H	H	H	H	L	L	L	L	H	H	H	H
	7	H	H	H	H	L	L	L	L	H	H	H	H
	10	H	H	H	H	L	L	L	L	H	H	H	H
	14	H	H	H	H	L	L	L	L	H	H	H	H

*'H' and 'L' represents that the FE results are higher/lower than the support pressure obtained from the analytical solutions.

Table 5.4 Comparison of FE result with the analytical solutions for cohesive soil

	φ':	20								25								30								35							
	c':	5	10	20	30	40	60	80	100	5	10	20	30	40	60	80	100	5	10	20	30	40	60	80	100	5	10	20	30	40	60	80	100
C/D	D	A&K (1996)																															
1	5	H	H	0	L	L	L	L	L	H	H	L	L	L	L	L	L	H	0	L	L	L	L	L	L	H	0	L	L	L	L	L	L
	7	0	H	H	H	H	H	H	H	H	H	H	H	H	H	H	H	H	H	H	H	H	H	H	H	H	H	H	H	H	H	H	H
	10	0	H	H	H	H	H	H	H	0	H	H	H	H	H	H	H	H	H	H	H	H	H	H	H	H	H	H	H	H	H	H	H
	14	L	H	H	H	H	H	H	H	0	H	H	H	H	H	H	H	H	H	H	H	H	H	H	H	H	H	H	H	H	H	H	H
2	5	H	H	H	0	0	0	L	L	H	H	0	0	0	L	L	L	H	H	0	L	L	L	L	L	H	H	L	L	L	L	L	L
	7	H	H	H	0	0	0	0	0	H	H	H	0	0	0	0	L	H	H	0	0	0	0	L	L	H	H	0	L	L	L	L	L
	10	0	H	H	H	H	H	H	H	H	H	H	H	H	H	H	H	H	H	H	H	H	H	H	H	H	H	H	H	H	H	H	H
	14	0	H	H	H	H	H	H	H	H	H	H	H	H	H	H	H	H	H	H	H	H	H	H	H	H	H	H	H	H	H	H	H
4	5	H	H	H	H	0	0	0	0	H	H	H	H	0	0	0	0	H	H	H	0	0	0	0	L	H	H	0	0	0	0	L	L
	7	H	H	H	H	H	H	H	H	H	H	H	H	H	H	H	H	H	H	H	H	H	H	H	H	H	H	H	H	H	H	H	H
	10	H	H	H	H	H	H	H	H	H	H	H	H	H	H	H	H	H	H	H	H	H	H	H	H	H	H	H	H	H	H	H	H
	14	H	H	H	H	H	H	H	H	H	H	H	H	H	H	H	H	H	H	H	H	H	H	H	H	H	H	H	H	H	H	H	H
C/D	D	L&D (1990)																															
1	5	H	H	0	0	0	0	0	0	H	H	0	0	0	0	0	0	H	0	0	0	0	0	0	0	H	0	0	0	0	0	0	0
	7	0	H	0	0	0	0	0	0	H	H	0	0	0	0	0	0	H	H	0	0	0	0	0	0	H	H	0	0	0	0	0	0
	10	L	H	H	0	0	0	0	0	0	H	H	0	0	0	0	0	0	H	0	0	0	0	0	0	0	H	0	0	0	0	0	0	0
	14	L	0	H	H	0	0	0	0	0	H	H	0	0	0	0	0	0	H	H	0	0	0	0	0	0	H	0	0	0	0	0	0	0
2	5	H	H	H	0	0	0	0	0	H	H	0	0	0	0	0	0	H	H	0	0	0	0	0	0	H	H	0	0	0	0	0	0
	7	H	H	H	0	0	0	0	0	H	H	H	0	0	0	0	0	H	H	0	0	0	0	0	0	H	H	0	0	0	0	0	0
	10	H	H	H	H	H	0	0	0	H	H	H	H	0	0	0	0	H	H	H	0	0	0	0	0	H	H	H	0	0	0	0	0
	14	H	H	H	H	H	H	0	0	H	H	H	H	H	H	0	0	H	H	H	H	H	0	0	0	H	H	H	0	0	0	0	0
4	5	H	H	H	H	0	0	0	0	H	H	H	H	0	0	0	0	H	H	H	0	0	0	0	0	H	H	0	0	0	0	0	0
	7	H	H	H	H	H	H	0	0	H	H	H	H	H	H	0	0	H	H	H	H	0	0	0	0	H	H	H	0	0	0	0	0
	10	H	H	H	H	H	H	H	0	H	H	H	H	H	H	H	0	H	H	H	H	H	H	0	0	H	H	H	H	H	H	0	0
	14	H	H	H	H	H	H	H	H	H	H	H	H	H	H	H	H	H	H	H	H	H	H	H	0	H	H	H	H	H	H	H	0

*'H' and 'L' represents that the FE results are higher/lower than the support pressure obtained from the analytical solutions.

Figure 5.21 is an extended version of the plot that shows the σ'_{Tf}/σ_h' values for a (10/1) tunnel in cohesionless ground (Figure 5.17(a)). Additional FE analyses were carried out for friction angles of 20° and 25°. Due to convergence problems, simulation using a material with 15° friction angle could not be executed. Figure 5.21 compares Anagnostou and Kovári (1994) solution and the FE results. Both Anagnostou and Kovári (1994) solution and the FE models considered similar conditions: *C/D* equal to 1, ground water table at the surface, and assumption of ideal membrane. The FE-calculated required effective face support pressure increases rapidly with decreasing friction angle especially when the friction angle is smaller than 30°. The FE estimated support pressure was found to be greater than the value from Anagnostou and Kovári (1994) solution in a cohesionless soil over the entire range investigated, i.e. φ'=20° to 45° compared to the FE solution.

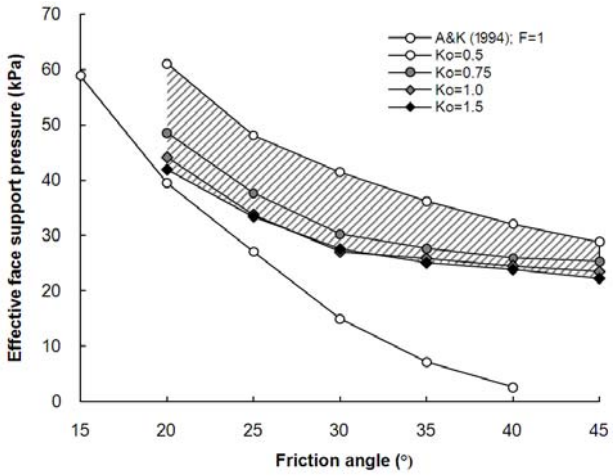

Figure 5.21 Comparison of FE results to limiting equilibrium solution

5.2. FINITE ELEMENT SIMULATION (UNDRAINED CASES)

Using the same framework that was employed for the drained case (Section 5.1), the present study attempts to extend its scope to the ground that shows undrained behavior. Undrained condition is defined as the condition whereby water cannot move in and out of a soil element. In practice, undrained condition may apply because of a combined effect of the permeability of the ground, the TBM advance rate, and the size of the tunnel that leads to an undrained behavior (Negro and Eisenstein, 1991); Anagnostou and Kovári (1996) concluded that drained conditions are expected when the permeability of the ground is higher than 10^{-7} to 10^{-6} m/sec and the advance rate is less than 0.1 to 1 m/hr. When an external force is applied to a soil in undrained condition, because the bulk modulus of water (K_w≈2 GPa) is much larger than that of the soil skeleton, the water entrapped within the pores takes the majority of the load and generates changes in pore water pressure. This change in pore water pressure is controlled by the change in volume caused by: i. changes in the hydrostatic component of the stress tensor; ii. the dilatancy (or contraction) caused by changes in the deviatoric component of the stress. When failure occurs before the shear-induced excess pore water pressure dissipates, undrained shear strength is mobilized. In this study, total stress Mohr-Coulomb models with linearly varying undrained shear strength profile and effective stress Modified Cam-clay models are employed to investigate the response of tunnel headings under undrained conditions. Indeed, when considering an undrained ground behavior, the time rate of consolidation should be accounted for. In a highly sheared zone in a normally consolidated ground, as the positive pore water pressure dissipates and the pore water migrates away from the sheared zone, the soil experiences a local increase of shear strength over time. In over consolidated ground, as the negative pore pressure generated

during shear straining dissipates and the pore water migrates toward the shear zone, the soil experiences a local reduction of shear strength (Broms and Bennermark, 1967; Davis et al, 1980). In a squeezing ground with low permeability, as negative excess pore pressure developed after the excavation of tunnel dissipates with time, it triggers a transient flow and increases the load on the lining (Anagnostou and Kovári, 2005). The study presented in this paper does not include the observation of the excess pore pressure generation due to the tunnel excavation and assumes constant ground response regardless of time. Therefore, the results of this study are limited to the immediate undrained response of the tunnel heading rather than long-term or time-dependent behavior.

5.2.1. Numerical model

The ground was assumed to be fully saturated with the ground water table at the ground surface. The undrained analysis was carried out using two different constitutive models: Mohr-Coulomb model (6,864 analyses) and Modified Cam-clay model (Roscoe and Burland, 1968) (4,620 analyses). Finite element analysis software Midas GTS was used. Finite element models are shown in Figure 5.3 (Mohr-Coulomb model) and Figure 5.22 (Modified Cam-clay model). Table 5.5 describes the detailed features of the model. The input ranges for the parameters are shown in Table 5.6 and Table 5.7. In determining the geotechnical parameters for both Mohr-Coulomb and Modified Cam-clay models, plasticity index I_P was used as independent variable from which the other soil parameters were derived by using a number of published correlations as described in the following.

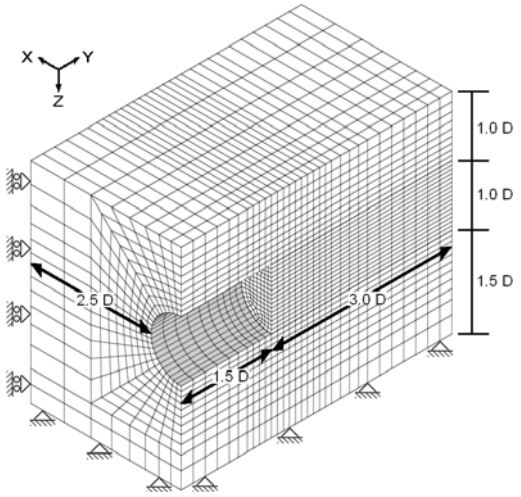

Figure 5.22 Finite element mesh (Modified Cam-clay model (MCC))

Table 5.5 FE model details

Figure	Yield criterion	Number of the elements							Element types
4	Mohr-Coulomb	*C*/*D*=1 7,344		*C*/*D*=2 7,944		*C*/*D*=4 9,144			Shield, lining: four-node first-order shell
5	Modified Cam-clay	*C*=5 m 11,648	7 m 11,896	10 m 12,392	14 m 12,888	20 m 13,632	28 m 15,386	40 m 16,608	Ground: eight-node first-order solid

Table 5.6 Analyses using the total stress Mohr-Coulomb constitutive model

Tunnel geometry (12 cases)

4 sets of diameter (*D*): 5, 7, 10 and 14 m

3 sets of cover-to-diameter ratio (*C*/*D*): 1, 2 and 4

Total stress constitutive model (52 cases)

4 sets of in situ stress condition defined by at-rest lateral earth pressure coefficient K_0=0.5, 0.75, 1.0 and 1.5

16 sets of undrained shear strength ratio and Young's modulus according to Plasticity Index

I_P (%)	10*	15*	20*	25*	30*	35*	40	45	50	60	70	80	90	100	110	120
s_u/σ_{vo}'	0.147	0.166	0.184	0.203	0.221	0.240	0.258	0.277	0.295	0.332	0.369	0.406	0.443	0.480	0.517	0.554
E_u/s_u	1,250	1,000	800	660	550	460	400	360	330	280	250	220	200	180	160	150
E_u/z (KPa/m)	1,500	1,350	1,200	1,100	1,000	900	850	820	790	770	750	730	710	700	690	680

*: cases with $s_u/\sigma_{vo}' < 0.25$ were not considered for K_0=0.5 and 1.5.

Total face support pressure (σ_T/σ_{ho}) applied normal to the face (11 cases)

σ'_T/σ'_{ho}	0	0.1	0.2	0.3	0.4	0.5	0.6	0.8	1.0	1.4	2.0
K_0=0.5	0.706	0.735	0.764	0.794	0.823	0.853	0.882	0.941	1.000	1.118	1.294
0.75	0.615	0.653	0.692	0.73	0.769	0.807	0.846	0.923	1.000	1.154	1.385
1.0	0.545	0.591	0.636	0.682	0.727	0.773	0.818	0.909	1.000	1.182	1.455
1.5	0.444	0.500	0.555	0.611	0.666	0.722	0.778	0.889	1.000	1.222	1.556

Table 5.7 Analyses using the effective stress Modified Cam-Clay (MCC) model

Tunnel geometry (28 cases)

4 sets of diameter (D): 5, 7, 10 and 14 m

3 sets of cover-depth (C): 5, 7, 10, 14, 20, 28, 40 m

Geotechnical properties for normally consolidated soft ground (64 cases)

1 set of isotropic in situ stress condition (K_0=1.0)

15 sets of undrained shear strength ratio and Young's modulus according to Plasticity Index

I_P (%)	10	15	20	25	30	35	40	45	50	55	60	70	80	90
φ'	35.5	32.7	30.7	29.3	28.1	27.1	26.2	25.5	24.8	24.2	23.6	22.7	21.9	21.1
(M)	1.44	1.32	1.23	1.17	1.12	1.07	1.04	1.00	0.975	0.949	0.926	0.885	0.850	0.820
λ	0.0586	0.0879	0.117	0.147	0.176	0.205	0.234	0.264	0.293	0.322	0.352	0.410	0.469	0.527
(C_C)	0.135	0.202	0.270	0.337	0.405	0.472	0.540	0.607	0.675	0.742	0.810	0.945	1.080	1.21
κ	0.0117	0.0176	0.0234	0.0293	0.0352	0.0410	0.0469	0.0527	0.0586	0.0645	0.0703	0.0820	0.0938	0.105
(C_R)	0.0270	0.0405	0.0540	0.0675	0.0810	0.0945	0.108	0.121	0.135	0.148	0.162	0.189	0.216	0.243
N_{MCC}	$N_{MCC} = \upsilon + \lambda \ln(p'_c)$													
Γ	$\Gamma = N_{MCC} - (\lambda - \kappa)\ln 2$													

Effective face support pressure (σ'_T) applied normal to the face (11 cases):

0, 10, 20, 30, 40, 50, 60, 70, 80, 90 and 100 % of σ'_{ho}

Table 5.6 summarizes the parameters used in the Mohr-Coulomb model. The parameters include four diameters (5, 7, 10 and 14 m), three cover-to-diameter ratios (1, 2 and 4), four at-rest lateral earth pressure coefficients (0.5, 0.75, 1.0 and 1.5) and sixteen different normalized undrained shear strength ratios. As for undrained shear strength, the paper used Skempton's (1957) correlation (Equation (5.4)) between plasticity index I_P and normalized undrained shear strength ratio s_u/σ_{vo}' determined from field vane shear tests:

$$s_u/\sigma'_{vo} = 0.11 + 0.0037 I_P \tag{5.4}$$

The undrained shear strength profile was assigned to the model based on the value of s_u/σ_{vo}'. The undrained elastic modulus, E_u, was modeled to be linearly increasing with the depth; the value of E_u/z was calculated from the normalized undrained modulus (E_u/s_u), which was taken from Duncan and Buchignani's (1976) relation between normalized undrained modulus (E_u/s_u), over consolidation ratio, and plasticity index given in Figure 5.23.

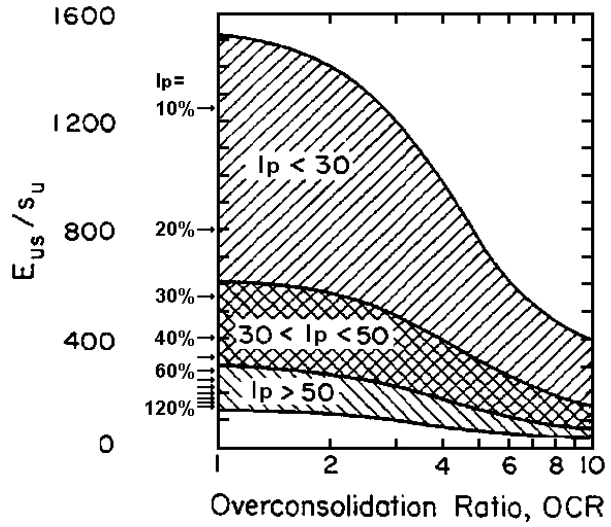

Figure 5.23 Normalized undrained modulus according to the plasticity index I_P (after Duncan and Buchignani,

The ground was assumed to be normally consolidated and therefore, the E_u/s_u values were taken for OCR=1 depending on the plasticity index as shown by an arrow mark in Figure 5.23. Both E_u/s_u and E_u/z values are presented in Table 5.6. In particular, when K_0=0.5 and 1.5, the cases with s_u/σ_{vo}' smaller than 0.25 (marked with an asterisk) were not simulated because the initial state of the stress would violate the yield criterion as follows:

$$s_u/\sigma'_{vo} < |1 - \mathrm{K}_0| \frac{\gamma'}{2} \tag{5.5}$$

The initial stress state that violates Equation (5.5) is inadmissible since the maximum shear stress exceeds the shear strength of the ground at any point.

Table 5.7 shows the Modified Cam-clay (MCC) model parameters. The values of two Cam-clay parameters, the critical friction angle φ' and the slope λ of the normal compression line, were determined using the following equations:

$$\varphi' = \text{asin}(0.35 - 0.1\ln(I_P)) \tag{5.6}$$

$$\lambda = 0.586 I_P \tag{5.7}$$

Equation (5.6) that correlates I_P to φ' was suggested by Mitchell (1976: p.335) using data from undisturbed or remolded clays and Equation (5.7) that correlates I_P to λ was suggested by Wood (1990: p.264). They were derived using data collected from insensitive or remolded soils. The slope κ of the recompression line was taken as one fifth of λ (Wood, 1990: p.264). The specific volumes of the normal compression and the critical state line at unit pressure (N_{MCC} and Γ) were determined based on their definitions as shown in Table 5.7. The symbol p_c' in the table represents the mean normal stress at the depth of the tunnel axis.

The normalized undrained shear strength ratio (s_u/σ_{vo}') is not one of the Cam-clay model parameters. However, by assuming no volume change at the critical state, the undrained shear strength s_u can be determined as follows (Wood, 1990: p.181):

$$s_u = \frac{M}{2}\exp\left(\frac{\Gamma - \upsilon}{\lambda}\right) \tag{5.8}$$

In this paper, the undrained shear strength s_u for the Modified Cam-clay models refers to the calculated value using Equation (5.8) at the depth of the tunnel axis.

It should be noted that the simulations used in this research employ several assumptions and simplifications. The mechanical supporting effect of the cutterhead was not considered. The lining and the shield was modeled as if they were a straight hollow cylinder. Annular grouting pressure and thrust force was not included in the simulation. The excavation was a single-step excavation procedure rather than a step-

by-step excavation procedure, assuming that the entire tunnel length in the model is excavated instantaneously. The single-step excavation procedure is a cost-effective method because it consists of only two steps (initial stage and excavation stage) and requires less elements. Because high deformation and high stress gradient exist near the tunnel heading, mesh refinement is necessary throughout the entire range of the tunnel when a step-by-step procedure is employed, whereas the mesh refinement is only necessary for the region close to the tunnel face. The favorable comparison between both procedures in terms of a characteristic curve and required face support pressure was given in a previous study for the drained case (Kim and Tonon, 2010). Similar results were obtained for undrained analysis.

5.2.2. Numerical simulation results

The equivalent plastic strain (ε^p) and the displacement contours are presented in Figure 5.24 to Figure 5.26 for the Modified Cam-clay model when the normalized undrained shear strength ratio (s_u/σ_{vo}') equals 0.184. The equivalent plastic strain is a scalar measure of the amount of permanent strain in a body defined through time integration of the equivalent plastic strain rate ($\dot{\varepsilon}^p$), which is expressed as $\sqrt{\frac{2}{3}\dot{\varepsilon}_{ij}^p\dot{\varepsilon}_{ij}^p}$.

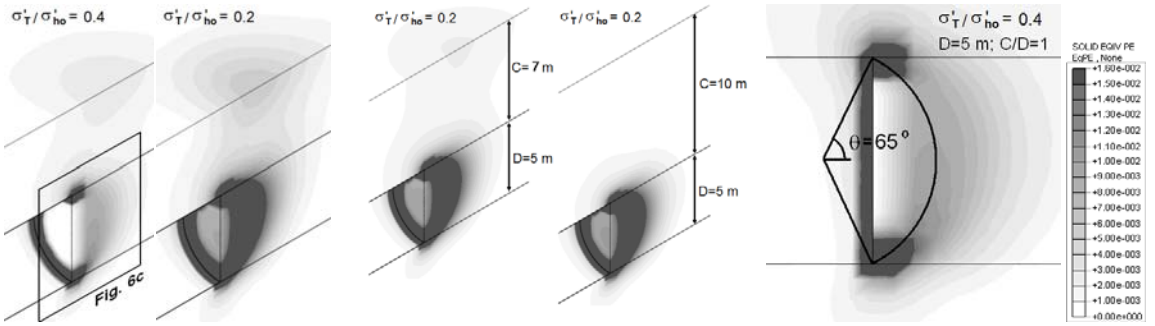

(a) Cover-depth=5 m (b) Cover-depth=7 and 10 m (c) Rotation of tunnel heading

Figure 5.24 Equivalent plastic strain contours (MCC; D=5 m; s_u/σ_{vo}'=0.184)

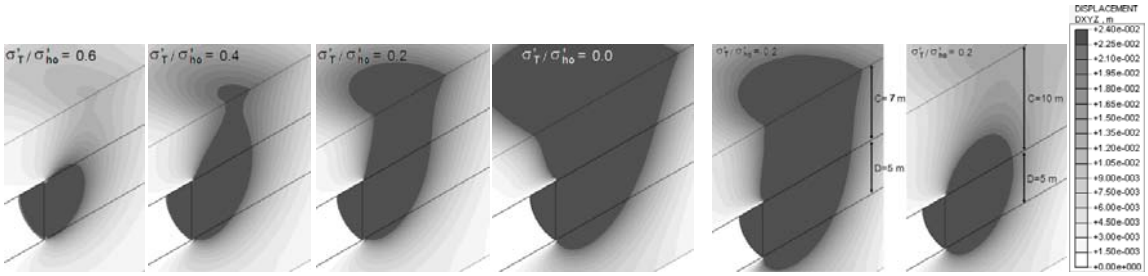

(a) Cover-depth=5 m b) Cover-depth=7 and 10 m

Figure 5.25 Displacement contours (MCC; D=5 m; s_u/σ_{vo}'=0.184)

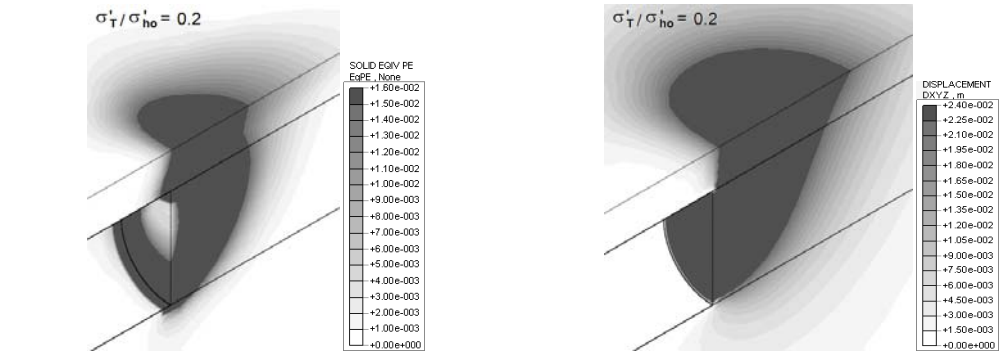

(a) Equivalent plastic strain contour (b) Displacement contour

Figure 5.26 Deformation of shallow tunnel heading
(MCC; D=14 m, C=5 m; s_u/σ_{vo}'=0.184)

Figure 5.24a shows the equivalent plastic strain that develops ahead and above of tunnel face when the applied support pressure ratio (σ'_T/σ'_{h0}) is equal to 0.4 and 0.2. With decreasing support pressure, the yield zone expands and plastic strain increases. Equivalent plastic strain larger than 0.0016 was marked as a dark grey. The same legend was used to facilitate the comparison between cases. Figure 5.24b shows the effect of the cover-depth on the equivalent plastic strain and the yield zone developed close to the tunnel heading. As the distance from the tunnel face increases, the equivalent plastic strain decreases rapidly. The yield zone reaches the ground surface

when C=5 m and 7 m, whereas it does not when C=10 m. This observation matches well with the well known fact that the risk of global instability, such as the formation of a chimney, reduces with increasing cover-depth. It is interesting that, in contrast to the yield zone development *above* the tunnel heading, the equivalent plastic strain and the yield zone development *ahead* of tunnel face are almost identical regardless of the cover-depth. Figure 5.24c compares the equivalent plastic strain contour with Li et al.'s (2008) finding. Li et al. (2008) investigated the tunnel face instability when a non-uniform face support pressure is applied with a unit weight of γ_S. When the rotation of the soil mass in the tunnel heading takes place due to the pressure gradient, the failure circle has its center on the tunnel axis and its aperture is 65° for any value of C/D. Figure 5.24c shows that the shear zone with the largest equivalent plastic strain falls on the failure circle predicted by Li et al. (2008).

Figure 5.25 shows the ground displacement contours. Displacements larger than 2.4 cm were marked with a dark grey contour for all displacement contour plots. Figure 5.25a shows the formation and the growth of the chimney with decreasing support pressure. Figure 5.25b illustrates that, as the cover-depth increases, the zone of large displacement is confined within a limited region, termed confined yield zone, which does not always lead to global instability (Kasper et al., 2004). As a consequence, the formation of a chimney becomes unlikely with increasing cover-depth.

Figure 5.26 shows the equivalent plastic strain and the displacement contour for a comparatively shallow large diameter tunnel (D=14 m and C=5 m) when it is subjected to a support pressure ratio σ'_T/σ'_{h0}=0.2. Even though the cover-depth is the same as in Figure 5.24a (where D=5 m), Figure 5.26a shows that the large equivalent plastic strain extended all the way to the ground surface when D=14 m. As a result, a deeper and

wider settlement trough developed at the surface (Figure 5.26b). The pressure imbalance at the crown and the invert of a tunnel due to the unit weight difference between the supporting medium and the ground plays an important role in local and global stability of the tunnel heading and this is especially true for the large diameter tunnels and the shallow tunnels.

5.2.3. Characteristic curves

The characteristic curve is basically a load-displacement diagram drawn from the relations between the applied support pressure and the resulting average face displacement. The characteristic curves are presented for the Mohr-Coulomb model in Figure 5.27 and for the Modified Cam-clay model in Figure 5.28. Figure 5.27a shows the characteristic curves for D=5, 7, 10 and 14 m and C/D=1, 2 and 4, when K_0=1 and s_u/σ_{vo}' =0.184. When the face is in the active state (σ'_T/σ'_{h0}<1.0), the characteristic curves were found to be independent of the cover-to-diameter ratios because, for a fixed diameter, the curves are overlapping regardless of the cover-to-diameter ratios. Additionally, since a linear relationship was found between the tunnel diameter and the average tunnel face displacement, the characteristic curves will coalesce to a single curve when the average tunnel face displacement is normalized by the tunnel diameter, as shown in Figure 5.27b. In the active state, a single characteristic curve regardless of D and C/D was obtained. To prevent confusion, it should be noted that the normalized tunnel face displacement is defined in different manners for drained and undrained cases. In the previous study conducted for drained cases (Kim and Tonon, 2010), the average tunnel face was divided by D^2 because in this way the characteristic curves overlapped.

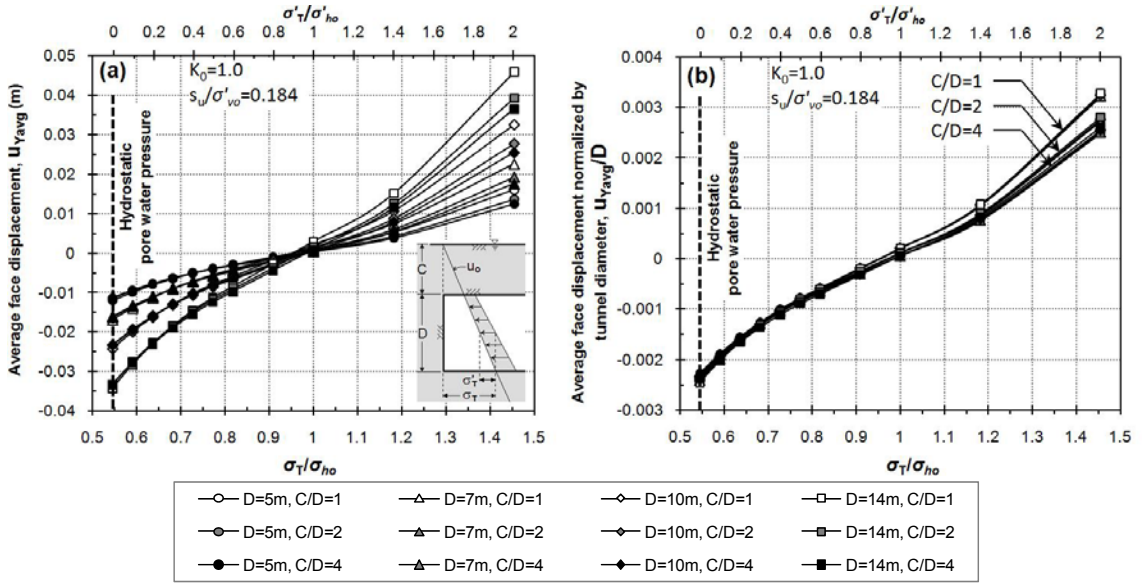

Figure 5.27 (a) Characteristic curves and (b) characteristic curves normalized by D (Mohr-Coulomb)

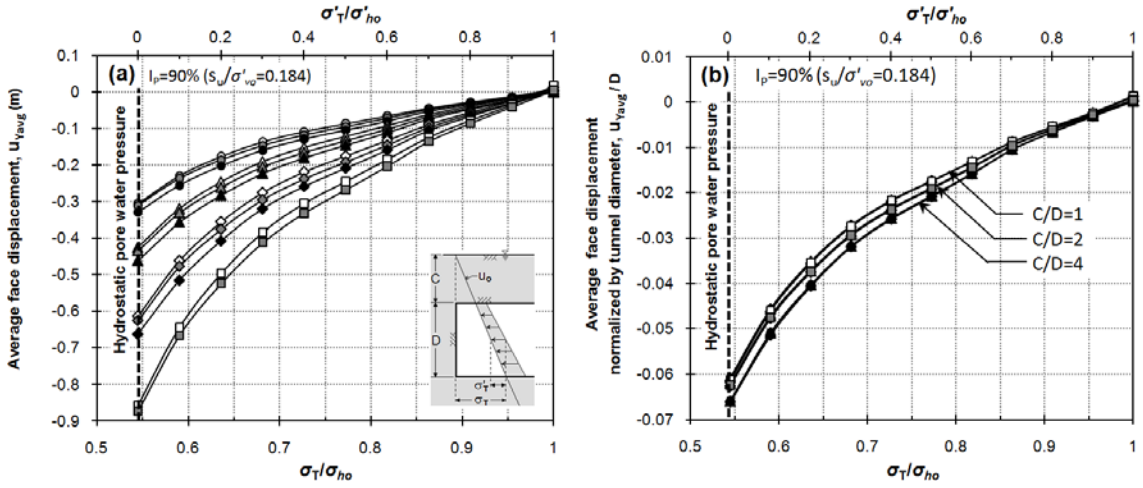

Figure 5.28 (a) Characteristic curves and (b) characteristic curves normalized by D (Modified Cam-clay)

Unlike for the Mohr-Coulomb model, FE analyses were carried out only for the active part for the Modified Cam-clay model. The characteristic curves shown in Figure 5.28a indicate that there is a slight dependency of the characteristic curves on the cover-

to-diameter ratio *C*/*D* and a strong dependency on the tunnel diameter *D*. Figure 5.28b shows that the normalized characteristic curve is slightly dependent on *C/D*.

Figure 5.29 shows the normalized face stiffness. The normalized tunnel face stiffness is defined as the inverse of the tangent to the normalized characteristic curves, i.e.

$$\text{Normalized face stiffness} = \frac{\Delta(\sigma'_{\mathrm{T}}/\sigma'_{\mathrm{ho}})}{\Delta(u_{\mathrm{Yavg}}/\mathrm{D})} \tag{5.9}$$

where $\Delta(\sigma'_T/\sigma'_{ho})$ represents the increment of the normalized face support pressure, and $\Delta(u_{Yavg}/D)$ represents the increment of the normalized face displacement. Because of the difference in the definition of normalized face displacement between drained and undrained analysis cases, the definition of the normalized tunnel face stiffness are not exactly same as in Kim and Tonon (2010).

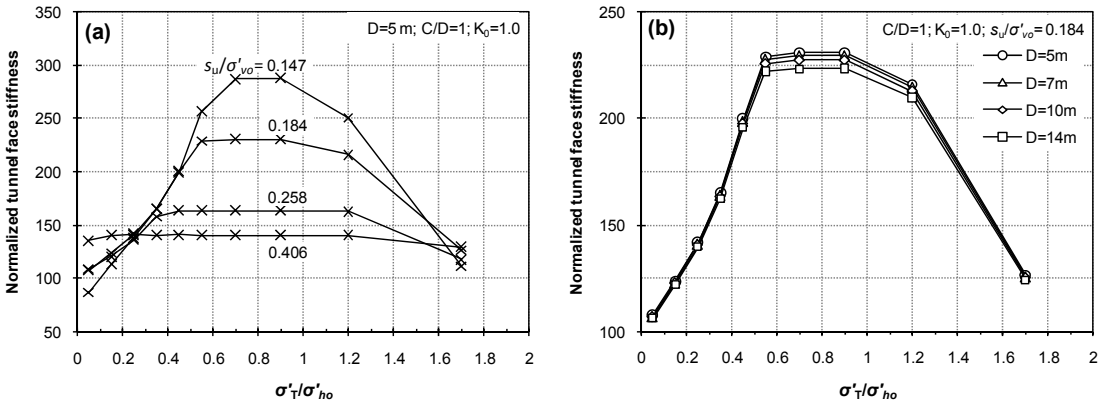

Figure 5.29 Normalized tunnel face stiffness (Eq. (8)) showing the influence of: (a) s_u/σ_{vo}'; (b) *D* (Mohr-Coulomb)

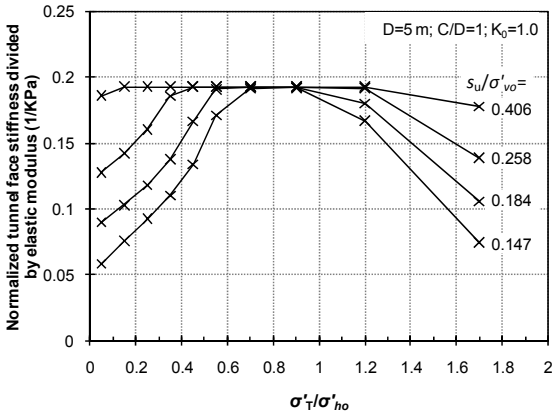

Figure 5.30 Normalized tunnel face stiffness divided by the elastic modulus of the ground

The tunnel face stiffness quantifies the rate of face deformation with respect to the support pressure change, and identifies the face support pressure at which a major portion of the ground ahead of the tunnel face behaves plastically and large plastic flow is initiated. The tunnel face stiffness decreases as the applied support pressure drops. Notice that different normalized tunnel face stiffness values are obtained in the region close to σ'_T/σ'_h =1.0 where the tunnel heading is mainly within its elastic range. This is because different elastic moduli were used for different cases (seeTable 5.7). Indeed, Figure 5.30 shows that the normalized face stiffness divided by the undrained modulus E_u is constant (independent of s_u/σ_{vo}') and equal to 0.19/KPa as long as yielding does not occur (compare with Figure 5.29a). Figure 5.29b shows that the normalized face stiffness is independent of the tunnel diameter; the slight lack of overlap in the range $0.6 \leq \sigma'_T/\sigma'_{ho} \leq 1.2$ is due to the divergence of the normalized characteristic curves in the passive state (see Figure 5.27b). The plots drawn for the other values of C/D show the same trends (figures not presented), and it is concluded that the normalized face stiffness of a tunnel is not influenced by the tunnel diameter and the cover-to-diameter ratio.

5.2.4. Required face support pressure

In defining the required face support pressure based on the characteristic curve, of outmost importance is a precise determination of the yield point. In the previous study for drained cases (Kim and Tonon, 2010), the yield point of a tunnel face was defined as the intersection of the two lines tangent to the characteristic curve at σ_T'/σ_{ho}'=0 and 1.0. Figure 5.31 compares the typical shapes of the characteristic curves from different models and drainage conditions and highlights a major difference between the drained and the undrained ground response in terms of the tunnel heading deformation upon unloading (reduction of σ_T'/σ_{ho}').

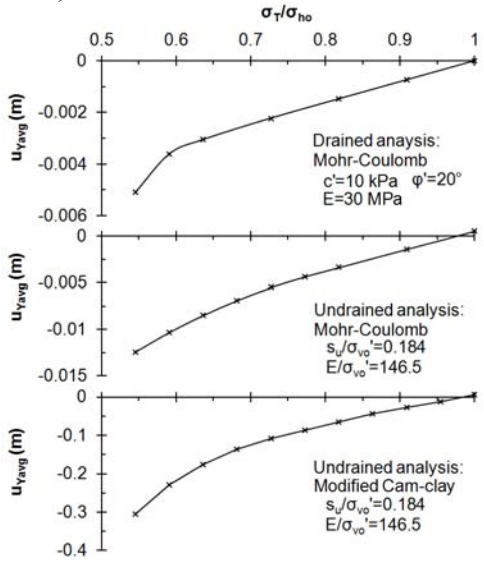

Figure 5.31 Typical shape of characteristic curves for drained and undrained analysis

The characteristic curve for drained analyses shows an apparent point where a sudden change in slope occurs. As a consequence, a consistent comparison of the yield point could be obtained among cases with different geometric and geotechnical parameters. On the other hand, for undrained cases, slope changes occur gradually. One possible explanation for this phenomenon might be the zero volumetric strain

constraint on the plastic behavior of the undrained element. In the undrained cases, when the undrained shear strength was high, the characteristic curve was quite close to a straight line, in which case determining a yield point as the intersection of tangents was not a suitable approach. In this light, besides the required face support pressure determined by the intersection of tangents (σ_{Tf}/σ_{h0}), this research also considers the relation between the applied support pressure (σ_T/σ_{h0}) and the average tunnel face displacement (u_{Yavg}/D), which quantifies the force-displacement relationship for the tunnel face under the given conditions.

Table 5.8 and Figure 5.32a show the required face support pressure ratios (σ_{Tf}/σ_{ho}) defined as the intersection of tangents derived from the Mohr-Coulomb models.

Table 5.8 Required face support pressure σ_T/σ_{ho} (Mohr-Coulomb model)

s_u/σ_{vo}'		0.147	0.165	0.184	0.202	0.221	0.239	0.258	0.276	0.295	0.332	0.369	>0.406
K_0=	0.5	0.871	0.86	0.848	0.836	0.825	0.811	0.798	0.782	-	-	-	-
	0.75	0.754	0.745	0.736	0.726	0.715	0.704	0.693	0.681	0.663	-	-	-
	1.0	0.665	0.653	0.644	0.634	0.625	0.615	0.603	0.59	0.58	0.556	-	-
	1.5	0.539	0.527	0.517	0.509	0.498	0.489	0.479	0.472	0.465	0.444	0.418	-

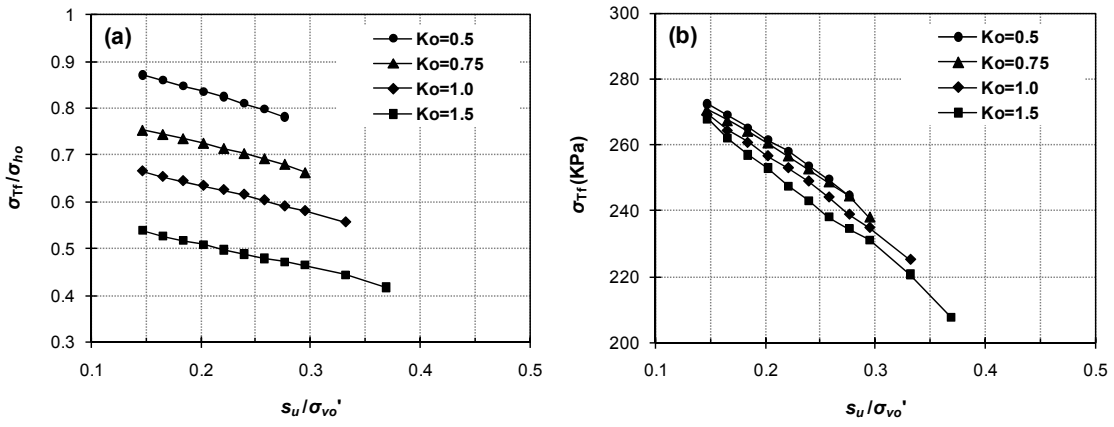

Figure 5.32 Required face support pressure (Mohr-Coulomb)

It was found that σ_{Tf}/σ_{ho} is independent to D and C/D. The value of σ_{Tf}/σ_{ho} decreases with increasing K_0 and increasing s_u/σ_{vo}'. When σ_{Tf} is not divided by σ_{ho} as in Figure 5.32b, σ_{Tf} changes only by 4% when K_0 changes between 0.5 and 1.5. When the characteristic curve is very close to a straight line, i.e. when the tangents slopes at both ends differ by less than 10%, the yield point was not calculated and omitted here due to the following two reasons. The yield point does not necessarily identify an acceleration of the face deformation as the support pressure drops. As one of the tangent lines becomes close to parallel to another tangent line, the coordinate of the intersection point is significantly affected by even the smallest change in the slope value. A multi variable regression technique was used to find a correlation between σ_{Tf}/σ_{ho}, K_0, and s_u/σ_{vo}':

$$\frac{\sigma_{Tf}}{\sigma_{ho}} = \frac{1}{3}(2 - \ln(K_o)) - \frac{3}{5}\left(1 + \frac{\ln(K_o)}{4}\right)(s_u/\sigma'_{vo} - 0.11) \quad (5.10)$$

(MC)

It gives fairly good estimation of σ_{Tf}/σ_{ho} and the correlation coefficient R^2 was 0.927. When K_0=1, Equation (5.10) reduces into a simpler form:

$$\frac{\sigma_{Tf}}{\sigma_{vo}} = \frac{2}{3} - \frac{3}{5}(s_u/\sigma'_{vo} - 0.11) \quad (5.11)$$

(MC; valid for K_0=1)

The required face support pressure ratio (σ_{Tf}/σ_{ho}) from the Modified Cam-clay model is presented in Table 5.9 and Figure 5.33. The σ_{Tf}/σ_{ho} value did not show a significant variation. The maximum and the minimum values were 0.781 and 0.718 respectively. Unlike the results obtained with the Mohr-Coulomb model, both D and C were found to have a slight influence on σ_{Tf}/σ_{ho}: σ_{Tf}/σ_{ho} increases with increasing C/D, and the effect of D on σ_{Tf}/σ_{ho} is minimal when C is larger than 20 m (Figure 5.33a). For

the cases with higher undrained shear strength, σ_{Tf}/σ_{ho} was found to be almost independent (1 % variation) of D and C/D (Figure 5.33b).

Table 5.9 Required face support pressure σ_{Tf}/σ_{ho} (Modified Cam-Clay model)

I_P (%)		10	15	20	25	30	35	40	45	50	55	60	70	80	90	100
s_u/σ_{vo}'		0.323	0.296	0.277	0.262	0.251	0.241	0.233	0.225	0.219	0.213	0.208	0.199	0.191	0.184	0.178
D(m)	C/D(m)															
	5	0.778	0.777	0.777	0.775	0.774	0.773	0.772	0.771	0.770	0.768	0.766	0.766	0.765	0.766	0.767
	7	0.776	0.776	0.775	0.773	0.771	0.770	0.769	0.767	0.765	0.764	0.761	0.760	0.759	0.759	0.758
	10	0.774	0.773	0.773	0.771	0.769	0.767	0.764	0.762	0.759	0.756	0.752	0.749	0.747	0.744	0.745
5	14	0.771	0.770	0.770	0.768	0.765	0.763	0.760	0.757	0.752	0.746	0.740	0.733	0.726	0.720	0.718
	20	0.779	0.778	0.778	0.777	0.776	0.775	0.774	0.773	0.773	0.771	0.770	0.770	0.770	0.772	0.773
	28	0.778	0.777	0.776	0.776	0.774	0.773	0.772	0.771	0.770	0.769	0.766	0.766	0.766	0.766	0.767
	40	0.776	0.776	0.775	0.774	0.771	0.770	0.769	0.767	0.766	0.764	0.761	0.760	0.759	0.759	0.758
	5	0.774	0.774	0.773	0.771	0.769	0.766	0.764	0.761	0.758	0.756	0.752	0.749	0.746	0.744	0.744
	7	0.779	0.779	0.778	0.778	0.776	0.776	0.775	0.774	0.774	0.773	0.772	0.772	0.772	0.774	0.776
	10	0.779	0.778	0.778	0.777	0.776	0.775	0.774	0.773	0.773	0.771	0.770	0.770	0.770	0.772	0.773
7	14	0.778	0.777	0.776	0.775	0.774	0.773	0.772	0.771	0.770	0.768	0.766	0.765	0.765	0.766	0.767
	20	0.776	0.776	0.774	0.773	0.771	0.770	0.768	0.766	0.765	0.763	0.760	0.759	0.758	0.758	0.757
	28	0.779	0.779	0.778	0.778	0.777	0.776	0.775	0.775	0.775	0.773	0.773	0.773	0.773	0.775	0.777
	40	0.779	0.779	0.778	0.778	0.776	0.776	0.775	0.774	0.774	0.773	0.772	0.772	0.772	0.774	0.776
	5	0.779	0.778	0.777	0.777	0.775	0.774	0.773	0.772	0.772	0.770	0.769	0.769	0.769	0.771	0.772
	7	0.778	0.777	0.777	0.776	0.774	0.773	0.772	0.771	0.770	0.769	0.767	0.766	0.766	0.767	0.768
	10	0.780	0.779	0.779	0.778	0.777	0.777	0.776	0.776	0.776	0.775	0.774	0.775	0.775	0.777	0.779
10	14	0.779	0.779	0.778	0.778	0.777	0.776	0.776	0.775	0.775	0.774	0.773	0.774	0.774	0.776	0.778
	20	0.779	0.779	0.778	0.778	0.776	0.776	0.775	0.774	0.774	0.773	0.772	0.772	0.772	0.774	0.776
	28	0.779	0.778	0.778	0.777	0.776	0.775	0.774	0.773	0.773	0.771	0.770	0.770	0.770	0.772	0.773
	40	0.780	0.780	0.779	0.779	0.778	0.777	0.777	0.776	0.777	0.776	0.776	0.776	0.776	0.778	0.781
	5	0.779	0.779	0.779	0.778	0.777	0.777	0.776	0.776	0.776	0.775	0.774	0.774	0.775	0.777	0.779
	7	0.780	0.779	0.779	0.778	0.777	0.777	0.776	0.776	0.776	0.775	0.774	0.774	0.775	0.777	0.779
	10	0.779	0.779	0.778	0.778	0.777	0.776	0.775	0.774	0.774	0.773	0.772	0.772	0.772	0.775	0.776
14	14	0.780	0.779	0.779	0.778	0.777	0.777	0.776	0.776	0.776	0.775	0.775	0.776	0.776	0.778	0.780
	20	0.780	0.779	0.779	0.778	0.777	0.777	0.776	0.776	0.776	0.775	0.775	0.775	0.776	0.778	0.780
	28	0.779	0.779	0.779	0.778	0.777	0.776	0.776	0.775	0.775	0.774	0.774	0.774	0.774	0.777	0.778
	40	0.780	0.779	0.779	0.778	0.777	0.776	0.776	0.775	0.775	0.774	0.773	0.774	0.774	0.776	0.778

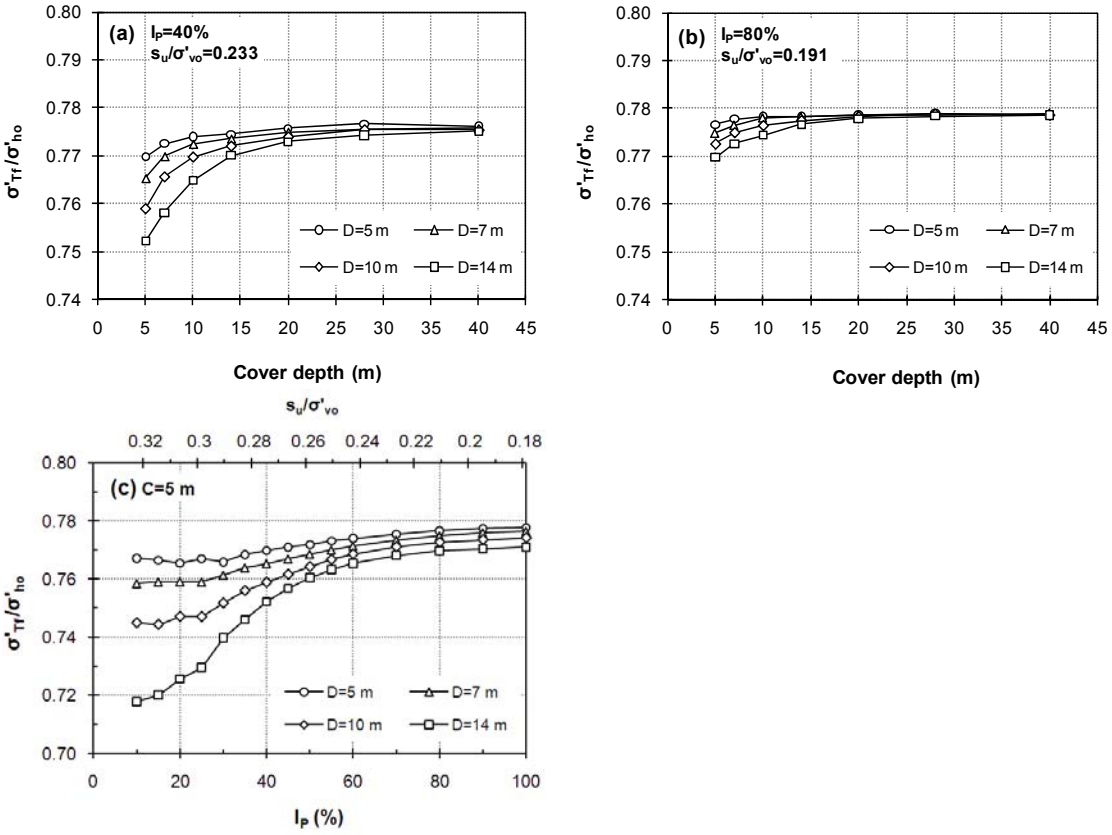

Figure 5.33 Required face support pressure (Modified Cam-clay)

The effect of s_u/σ_{vo}' on σ_{Tf}/σ_{ho} is shown in Figure 5.33c: for a fixed cover-depth the values of σ_{Tf}/σ_{ho} decrease with increasing s_u/σ_{vo}' for large diameter tunnels, but only a slight drop in σ_{Tf}/σ_{ho} occurs in small diameter tunnels when s_u/σ_{vo}' increases. The following equation correlates σ_{Tf}/σ_{ho} with D/C and I_P:

$$\frac{\sigma_{\mathrm{Tf}}}{\sigma_{ho}} = 0.58 + 0.09\frac{D}{C} - \left(0.46 + 0.57\frac{D}{C}\right)\left(\frac{1}{\ln(I_P)}\right) + \left(0.76 + 0.65\frac{D}{C}\right)\left(\frac{1}{\ln(I_P)}\right)^2 \quad (5.12)\ (\mathrm{MCC})$$

Equation (5.12) was obtained by multi-variable regression on the data shown in Table 5.9. It gives a reasonable approximation with the correlation coefficient R^2 equal to 0.740.

In the first paragraph of this section, the need for a more generalized approach was highlighted. By analyzing the results obtained with the Modified Cam-clay model, relations between the applied support pressure and the resulting average face displacement were obtained for the cases where the characteristic curves do not give an evident value for the yield point. For D=5 and 10 m tunnels, Figure 5.33 presents the magnitude of σ_T/σ_{ho} that should be applied on the face to limit the normalized face displacement (u_{Yavg}/D) to a specified value. For a given u_{Yavg}/D value, σ_T/σ_{ho} increases with increasing D, C/D and I_P, and decreasing s_u/σ_{vo}'. The following equation correlates σ_T/σ_{ho} with u_{Yavg}/D, C, D, and I_P:

$$\frac{\sigma_T}{\sigma_{ho}} = \frac{23}{22} - \frac{1}{7}\sqrt{u_{Yavg}/D} - \left(5.5 + 13.4\left(u_{Yavg}/D\right)\right)\left(1.4\frac{C^{0.3}}{D} + \frac{1}{C^{0.7}}\right)\left(\frac{1}{I_P}\right) \quad \text{(MCC)} \tag{5.13}$$

The relations shown in Figure 5.34 can be approximated as shown in Figure 5.35 using Equation (5.13). It was derived using a multi variable regression analysis. It gives a reasonable approximation and the correlation coefficient R^2 is 0.889.

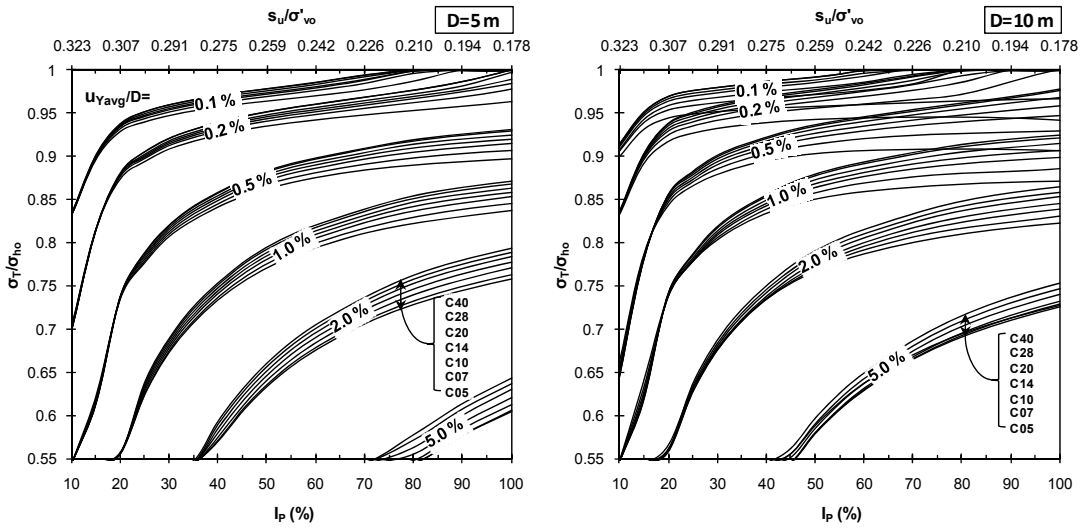

Figure 5.34 Relations between applied face support pressures and average tunnel face displacement values (Modified Cam-clay)

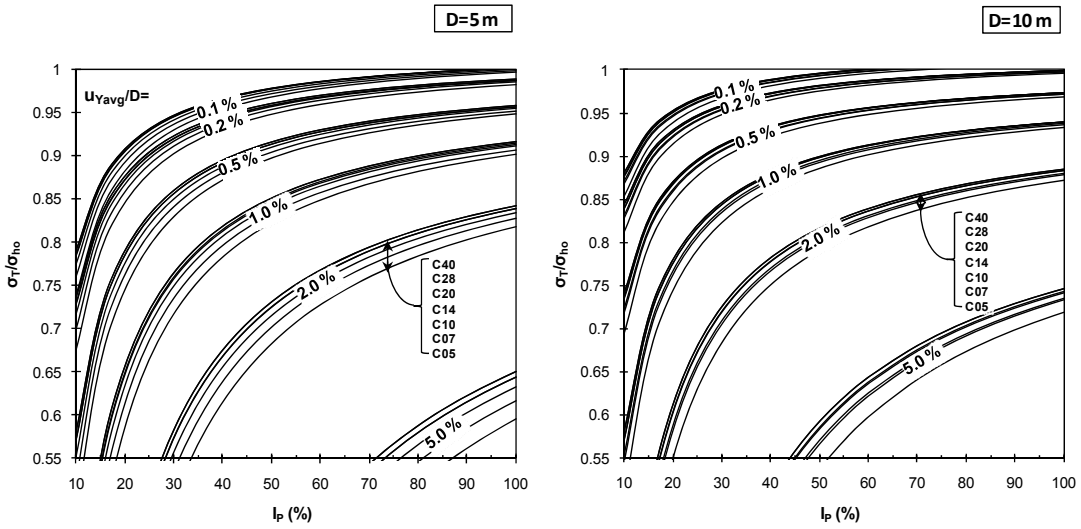

Figure 5.35 Approximation of u_{Yavg}-σ_T/σ_{ho} relationships using Equation (5.13) (Modified Cam-clay)

5.2.5. Comparison with analytical solutions

The face support pressure values obtained in Section 5.2.4 are here compared to the values available from the literature. The stability number N (Equation (3.4)) was calculated by using σ_{Tf}/σ_{ho} obtained from Mohr-Coulomb model (Table 5.8) and presented in Figure 5.36 and Table 5.10.

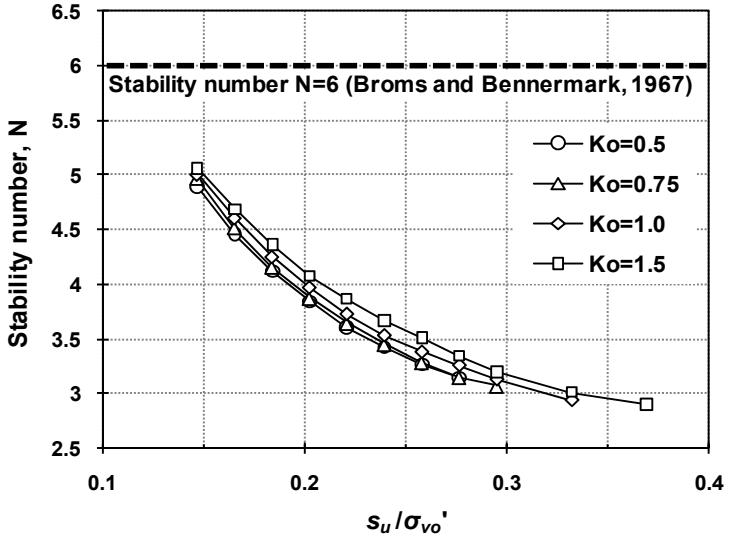

Figure 5.36 Stability number N calculated from the FE analysis result (Mohr-Coulomb)

Table 5.10 Stability number N according to the FE result

s_u/σ_{vo}'	0.147	0.165	0.184	0.202	0.221	0.239	0.258	0.276	0.295	0.332	0.369	0.406	0.443	>0.48
K_0=0.5	4.89	4.46	4.12	3.84	3.61	3.43	3.27	3.15	3.06	0	0	0	0	0
0.75	4.96	4.51	4.15	3.87	3.64	3.45	3.29	3.15	3.07	2.9	0	0	0	0
1.0	5.08	4.67	4.31	4.03	3.78	3.58	3.42	3.3	3.17	2.97	2.82	0	0	0
1.5	5.21	4.82	4.48	4.18	3.96	3.76	3.59	3.42	3.27	3.08	2.96	2.83	2.73	0

The value of σ_S in Equation (3.4) was taken as zero because no surcharge pressure was modeled. Since σ_{Tf}/σ_{ho} is independent of D and C/D, the stability number N was plotted against s_u/σ_{vo}' only for different K_0's. Note that the stability number N was found to have a quite similar value regardless of K_0 because σ_{Tf} is barely affected by K_0 (see Figure 5.32b). The stability number N is always smaller than six and ranges from 3 to 5.

As a consequence, the required support pressure ratio (σ_{Tf}/σ_{ho}) defined by the intersection of tangents is higher compared to Broms and Bennermark's (1967) recommendation: the face support pressure determined from the stability number N=6 might be insufficient to confine the tunnel heading in its elastic region, especially in a stiff ground with higher undrained shear strength.

Figure 5.37 presents the same plot as Figure 5.36 but for the Modified Cam-clay model. It shows the calculated stability number N when the σ_{Tf}/σ_{ho} values shown in Table 5.9 are applied to the face. The stability number N is always smaller than 6 and N decreases with increasing undrained shear strength. Similar to the Mohr-Coulomb model, the support pressure determined from N=6 might be insufficient, leading to an excessive deformation of the tunnel heading especially for a stiff ground. This conclusion (the required face support pressure determined as the intersection of tangents from load-displacement diagram is greater than the values from the stability solutions) was also observed in the previous study carried out for a drained ground condition (Kim and Tonon (2010)).

In Figure 5.38, the face support pressure and the stability number are shown for D=10 m and C=10 m excavation. Figure 5.38a shows the support pressure that should be applied to the face to maintain the average inward face displacement at 2% of the tunnel diameter. As the undrained shear strength increases, the necessary support pressure decreases until it reaches the hydrostatic pore water pressure at the depth of the tunnel axis. The pressure obtained from Figure 5.35 (Equation(5.13)) was also used to calculate N as shown in Figure 5.38b. The dotted line represents N when the applied support pressure is equal to the horizontal earth pressure ($\sigma_T = \sigma_{ho}$) and the dashed line represents N when the applied support pressure is equal to the hydrostatic pore water

pressure at the tunnel axis ($\sigma_T=u_0$). When imposing that u_{Yavg}/D=2 %, the stability number increases until it touches the curve that represents N when σ_T' =0. This suggests that when the undrained shear strength of the ground is large enough, then the tunnel heading may not show an excessive deformation even when the face support pressure is smaller than the ground water pressure.

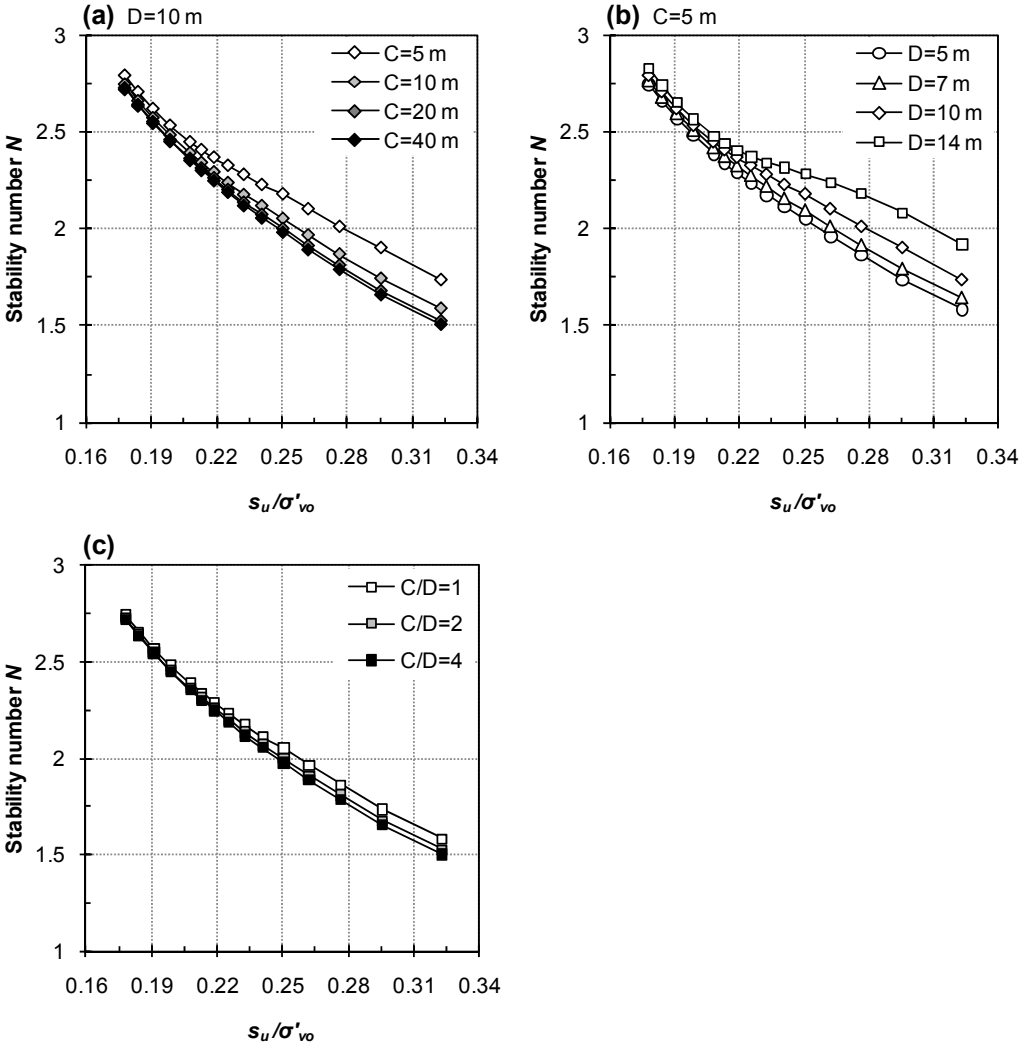

Figure 5.37 Variation of stability number N (Modified Cam-clay)

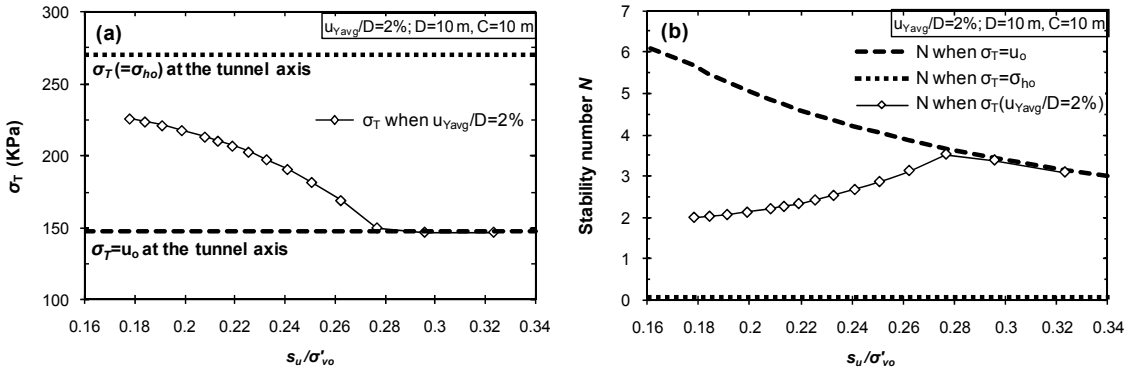

Figure 5.38 (a) σ_T when u_{Yavg}/D=2% and (b) calculated stability number (D=10 m, C=10 m; Modified Cam-clay)

Figure 5.39 and Figure 5.40 compare the stability number N with the lower and upper bound solutions of Davis et al. (1980). When the support pressure is calculated using the safe lower bound solution, the stability number is independent of the tunnel diameter and of the undrained shear strength of the ground, and equal to 3.4, 4.2, 5.2 and 6.39 when C/D=0.5, 1, 2 and 4, respectively. When the support pressure necessary to maintain u_{Yavg}/D to a certain value is applied to the face, the stability number N is far below 6 for most of the cases analyzed and it is also smaller than N obtained by using the safe lower bound. It means that, even if the support pressure is determined using the safe lower bound solution, excessive face deformation may take place. This is especially true for tunnels with large undrained shear strength (see Figure 5.39) and large cover-to-diameter ratio (see Figure 5.40).

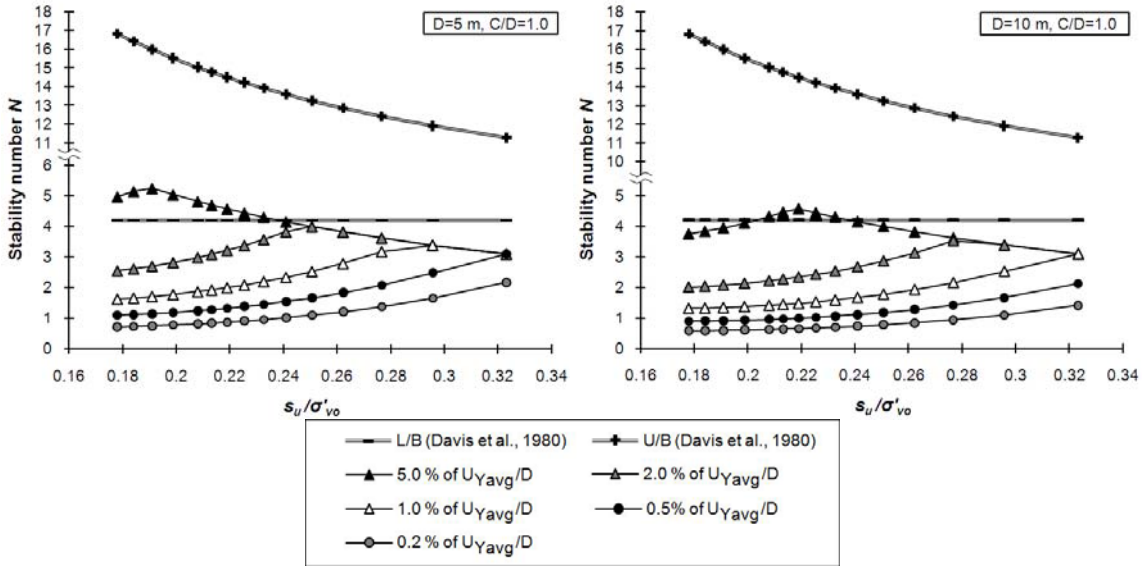

Figure 5.39 Calculated N from FE results and bound theorems (Davis et al., 1980)

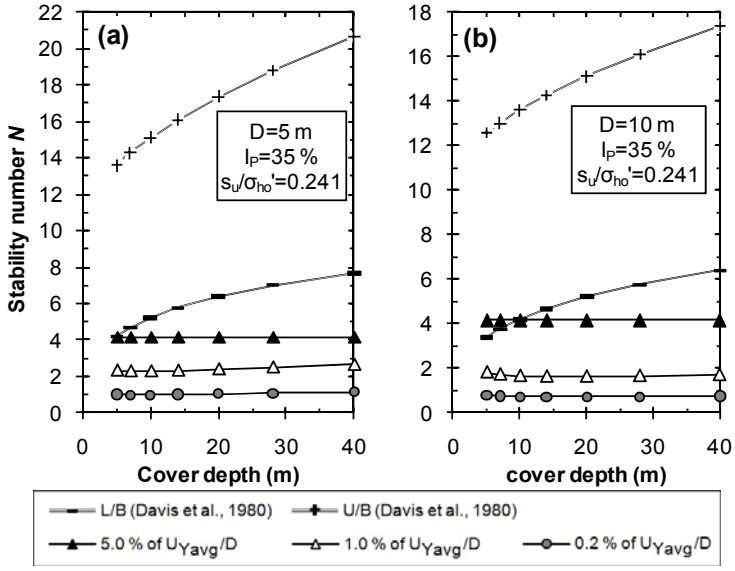

Figure 5.40 Calculated *N* from FE results and bound theorems (Davis et al., 1980)

The stability number *N* obtained analytically and experimentally by Davis et al. (1980) increases with increasing cover-depth (Figure 3.12 and Figure 3.17). It means

that, when the cover-depth increases, the required support pressure does not increase as fast as the *in situ* stress. On the other hand, the stability number *N* determined from the FE results is almost unaffected by the cover-depth (Figure 5.37c and Figure 5.40). It means that the required support pressure increases as fast as the *in situ* stress increases with increasing cover-depth, as already shown in Figure 5.33b. This observation highlights an important aspect of tunneling from a ground deformation point of view that should be considered when using the face support pressure determined by the stability solutions. When the tunnel face is supported by the pressure determined by the analytical stability solutions, substantial ground deformation and yielding of the soil mass may be induced near the tunnel face especially for deep tunnels. With increasing cover-depth, the yield zone does not reach the ground and it becomes a confined yield zone (see Figure 5.24a and b). However, the analytical stability solutions employ a failure plane that reaches the ground surface. When cover-depth increases, the support pressure determined by the analytical solutions becomes smaller than the values determined by the FE approach. Therefore, in terms of the global stability of the tunnel heading, e.g. formation of chimney or blow-out, the use of analytical stability solutions may be considered appropriate. However, using the analytical stability solutions may be inappropriate when controlling the ground deformation near the tunnel heading is of primary interest, such as when the TBM excavates in an urban environment.

Figure 5.41 compares current FE solluition with the upper bound solutions (Section 4.2 and 4.3) shown in Figure 4.23 and theoretical stability/experimental solutions (Chapter 3). As already discussed previously, it is shown that the FE solutions give greater values compared to the theoretical/experiemental stability solutions.

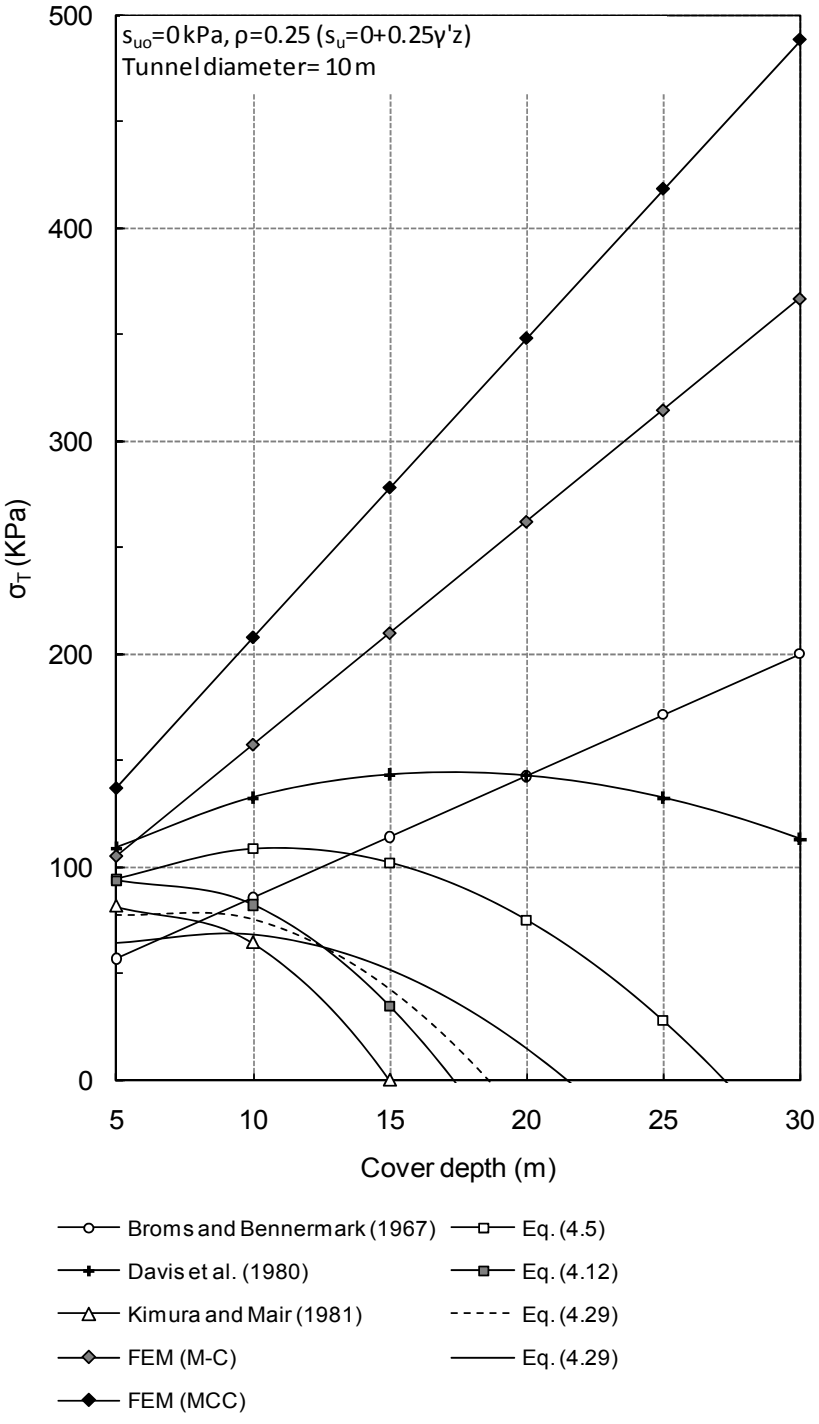

Figure 5.41 Comparison of face support pressure from FE solutions with theoretical/experimental stability solutions

5.2.6. Local instability depending on K_0

Figure 5.42 illustrates the growth of the yield zone when the applied support pressure ratio σ'_T/σ'_{h0} decreases from 1.0 to 0.7 in a Mohr-Coulomb model where the yield criterion is defined by the normalized undrained shear strength ratio s_u/σ_{vo}' of 0.258. The at-rest lateral earth pressure coefficient K_0 of the ground determines which part of the tunnel face yields first. When K_0<1, yielding first occurs in the invert (Figure 5.42a), whereas it first occurs in the crown when K_0>1 (Figure 5.42b), which may be explained by the different pressure gradient between the supporting medium and the ground.

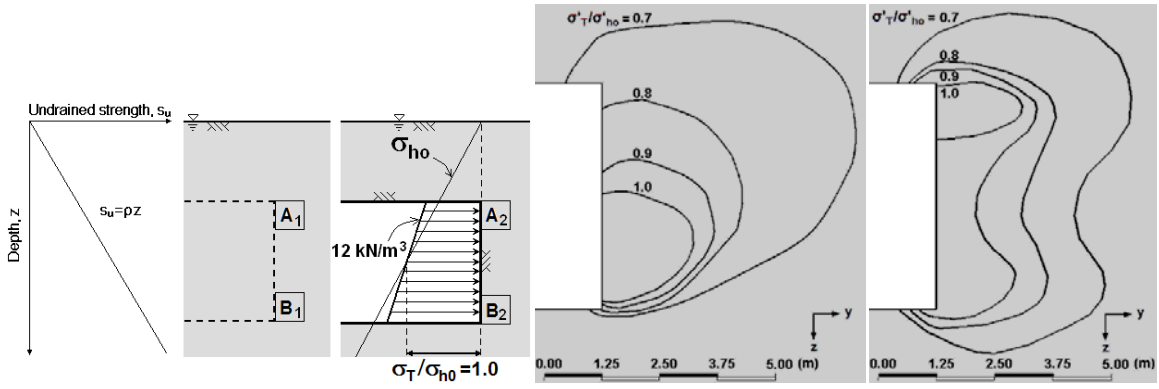

(a) K_0=0.5 (b) K_0=1.5

Figure 5.42 Growth of the yield zone with decreasing face support pressure ratio (D=5, C/D=1, I_P=40% (s_u/σ_{vo}'=0.258))

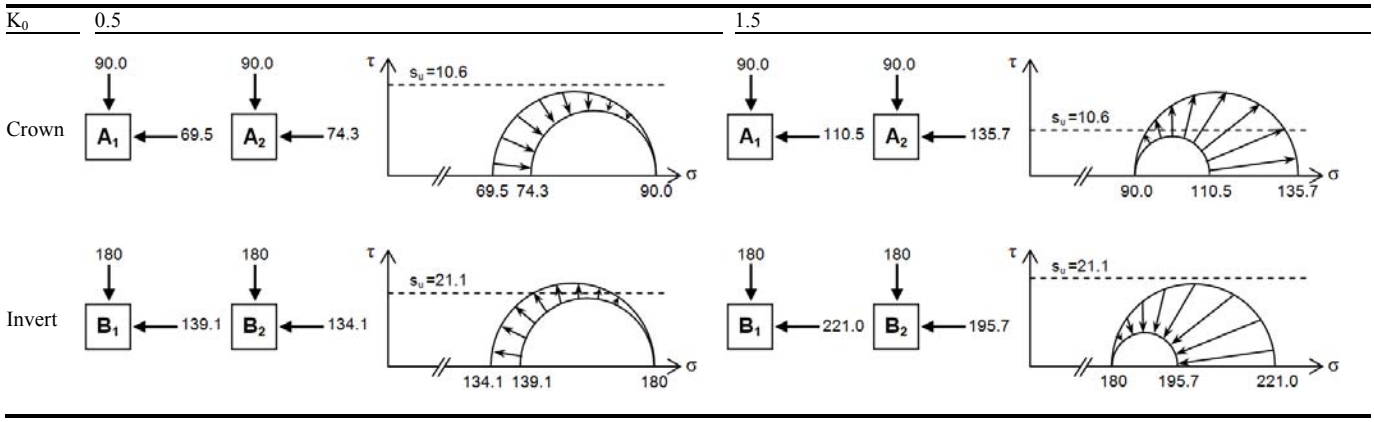

Figure 5.43 Stress state of an element on tunnel face
(D=5 m, C/D=1, I_P=40% (s_u/σ_{vo}'=0.258); stresses in kPa)

Simple and approximated Mohr circles shown in Figure 5.43 are provided to describe this phenomenon. Elements A and B in Figure 5.42 represent the soil elements at the crown and at the invert ahead of tunnel face. Suffix numbers 1 and 2 were used to distinguish before and after the excavation. The principal stress directions were assumed to remain the same after the excavation of the tunnel, because a support pressure close to the in situ horizontal pressure was applied to the face. Then the descriptions shown in Figure 5.43 are possible. When K_0=0.5, for the element A2 at the crown, it is the minor principal stress that increases (69.5→74.3 kPa), resulting in a reduction of the radius of the Mohr circle. On the other hand, when K_0=1.5, it is the major principal stress that increases (110.5→135.7 kPa), resulting in an increase of the Mohr circle radius and subsequent yielding of the element. The same explanation applies to the element at the invert.

5.3. SUMMARY

A series of three-dimensional finite element simulations was carried out to investigate the drained and undrained behavior of the ground near the tunnel heading for different tunnel diameters, cover-to-diameter ratios, at-rest lateral earth pressure coefficients and normalized undrained shear strength ratios. Several simplifications were made. The mechanical supporting effect of the cutterhead was not considered. Gap parameters and annular grouting pressure was not modeled in the simulation. TBM advance rate, penetration of the bentonite slurry into the ground ahead of the tunnel face, and the effects of pore pressure generation and dissipation, consolidation of the ground were not taken into account. Therefore, the results presented in Chapter 3 are only applicable to the immediate drained and undrained response of the tunnel heading.

The deformation of the ground near the tunnel heading was investigated. In drained ground, when the cover-to-diameter ratio is constant, the face deformation profiles normalized by the square of the tunnel diameter were independent of tunnel diameter, ground strength parameters, and lateral earth pressure coefficient. This statement holds its validity so long as either the material is purely frictional and the applied effective face support pressure is close to the *in situ* horizontal earth pressure. In undrained ground, the face deformation profiles normalized by the tunnel diameter were found to be independent of tunnel diameter, ground strength parameters, and lateral earth pressure coefficient. As the cover-to-diameter ratio increases, the chances for the yield zone to reach the ground surface decrease significantly. This fact questions the applicability of the analytical stability solutions to deep tunnels (C>2D), which employ failure planes that reach the ground surface.

From the load-displacement relations between the non-uniformly distributed support pressure and the face displacement, the required face support pressure was evaluated. For both drained and undrained cases, the required face support pressure ratio was given as a function of the controlling parameters. In cohesionless soils, the effect of the tunnel diameter on the required face support pressure was negligible, whereas the effect of the tunnel diameter was quite significant in cohesive soils. Both for cohesionless and cohesive soils, the ratio between the required effective face support pressure and horizontal effective stress decreases as K_0 increases (Equation (5.3)).

In drained conditions, when the values from the FE results were compared to the values available from the literature, the FE solution gives larger support pressure than Anagnostou and Kovári (1994 and 1996) solution does. The FE solution was found to give smaller values ($^1/_2$~$^2/_3$) compared to Jancsecz and Steiner (1994) solution. Compared to Leca and Dormieux (1990) upper bound solution, the FE solution gives larger values when C/D=1, similar when C/D=2, and smaller values when C/D=4. For ground with cohesion and friction, the FE solution gives larger values than Anagnostou and Kovári (1996) and Leca and Dormieux (1990) solutions do when c'>10 kPa. As for the undrained analyses, the required support pressure was correlated to D, C/D, K_0 and s_u/σ_{vo}' (Equation (5.10) for Mohr-Coulomb model and Equation (5.12) for Modified Cam-clay model). In addition to these two equations, the support pressure was also expressed as a function of the average tunnel face displacement (Equation (5.13)). The calculated stability number N was compared to the analytical stability solutions and found to be lower than N calculated with the safe lower bound solutions and always smaller than 6.

In general, for both drained and undrained cases, the analytical stability solutions were found to give smaller support pressures compared to the values from the FE results.

The support pressure calculated using the analytical stability solutions might be insufficient to constrain the movement of the ground ahead of the tunnel face so that the ground remains in its elastic condition. This indicates that large ground deformation around the tunnel heading will take place if analytical stability solutions are used, especially for deep tunnels where $C/D>2$. From the stability point of view, the support pressure obtained using analytical stability solutions might be sufficient to maintain the global stability of the ground ahead of and above of the excavation face. However, it should be stressed that satisfying global stability condition does not necessarily indicate that it can prevent the excessive tunnel heading deformation, which may lead to a costly consequences for urban tunneling where other underground and surface structures exist in close proximity.

CHAPTER 6. SUMMARY AND CONCLUSION

6.1. SUMMARY

In Chapter 2, case histories on large-diameter mechanically driven tunnels for transportation purpose were collected and summarized. The purpose and features of the tunnel, TBM specifications, construction method and schedule, and geological conditions were presented with appropriate drawings and photos. For applicable case histories, the reason why bored tunnel option has been selected was explained. Comparisons were given between a single-bore tunnel with large diameter and a twin-bore tunnel with relatively smaller diameter.

In Chapter 3, the tunnel face supporting mechanism and widely adopted theoretical and empirical methods to predict the necessary face support pressure were presented. Tunnel face

In Chapter 4, upper bound solution against collapse load was obtained using an undrained prism-and-wedge model. Deformable blocks have been employed to take into account the effect of non-uniform support pressure due to unit weight of the supporting medium. Upper bound solution was derived as a function of tunnel diameter and cover depth, normalized undrained shear strength ratio, and unit weight of the supporting medium. The calculated upper bound value against collapse load was compared with the values available from the literature.

In Chapter 5, three-dimensional finite element simulations were carried out to investigate the immediate drained and undrained behavior of the ground near the tunnel heading, and to establish a relationship between the required face support pressure (the necessary pressure to confine the tunnel heading in its elastic region) and various

geotechnical and geometrical parameters, such as tunnel diameter, cover-to-diameter ratio, at-rest lateral earth pressure coefficient and soil shear strength parameters. First, the deformation characteristics of the ground near the tunnel heading were investigated. Second, database on average face displacement depending on the applied face support pressure was established for the ground that obeys various geotechnical models. Third, the required face support pressure was expressed as a function of the controlling parameters. Lastly, the support pressure obtained as a result of the FE analyses was compared with the values obtained from the literature.

6.2. CONCLUSION

1. Despite of its relatively high cost, TBM driven tunnel option is preferred in urban environment where disruption of the surface area and noise- and visual-pollution is prohibited. However, TBM driven tunnel option can be an economical option when tunnel is very deep.

2. A single-bore double-deck tunnel is superior to a twin-bore single-deck tunnel in terms of construction cost and schedule.

3. In drained ground, when the cover-to-diameter ratio is constant, the face deformation profiles normalized by the square of the tunnel diameter are independent of tunnel diameter, ground strength parameters, and lateral earth pressure coefficient.

4. In undrained ground, the face deformation profiles normalized by the tunnel diameter are independent of tunnel diameter, ground strength parameters, and lateral earth pressure coefficient.

5. In cohesionless soils, the effect of the tunnel diameter on the required face support pressure is negligible, whereas the effect of the tunnel diameter is quite significant in cohesive soils.

6. As a result of numerical simulations, a number of equations that can be used to evaluate the required face support pressure have been proposed (Equations (5.3), (5.10), (5.12), and (5.13)).

7. As the cover-to-diameter ratio increases, the formation of a chimney becomes less likely. This fact questions the applicability of the analytical stability solutions to deep tunnels (C>2D), which employ failure planes that reach the ground surface.

8. In general, for both drained and undrained cases, the analytical stability solutions are found to give smaller support pressures than the values from the FE results. This indicates that large ground deformation around the tunnel heading will take place, if analytical stability solutions are used, especially for deep tunnels where C/D>2.

9. The values of support pressure evaluated using the upper bound solution (Equation (4.29)) are found to be similar to or smaller than Davis et al. (1980)'s upper bound values.

10. The upper bound solution using the deformable prism-and-wedge model shows that, for a typical face support pressure gradient (12 kN/m^3/m to 14 kN/m^3/m) and a typical undrained shear strength (ρ=0.20-0.30), the face deformation profile at failure is found to be linear rather than a polynomial curve.

References

Abdullah, H., 2004b. Stormwater Management and Road Tunnel (SMART) a lateral approach to flood mitigation works. *International Conference on Bridge Engineering & Hydraulic Structures.* Selangor, Malaysia, pp.59-79.

Almar, J.F., 2006. Planning system of metro networks: comparison between Copenhagen and Barcelona. *M.S. thesis*: *Polytechnical University of Catalunya*. p.114.

Anagnostou, G., Kovári, K., 1994. The face stability of slurry-shield-driven tunnels. *Tunnelling and Underground Space Technology* 9(2), pp.165-174.

Anagnostou, G., Kovári, K., 1996. Face stability conditions with Earth-Pressure-Balanced shield. *Tunnelling and Underground Space Technology* 11(2), pp.165-173.

Anagnostou, G., Kovári, K., 2005. Tunnelling through geological fault zones. *Proceedings of International Symposium on Design, Construction and Operation of Long Tunnels*, Taipei, Taiwan. pp.509-520.

Asian Development Bank, M-30 ring-road project, available at http://www.adb.org/Documents/Events/2008/Madrid-Urban-Management/MC30. p.10.

Atkinson, J., Potts, D.M., 1977. Stability of a shallow circular tunnel in cohesionless soil. *Géotechnique* 27(2), pp.203-215.

Augarde, C.E., Lyamin, A.V., Sloan, S.W., 2003. Stability of an undrained plane strain heading revisited. *Computers and Geotechnics* 30(5), pp.419-430.

Bezuijen, A., van Seters, A., 2006. The stability of a tunnel face in soft clay. *Tunnelling: a decade of progress* (GeoDelft 1995-2005). Eds.: Bezuijen, A., van Lottum, H. Taylor & Francis, London, pp.149-155.

Bin, Z., 2009. On the Analysis Methods of Face Stability in Shield Tunnel Excavation. *International Conference on Information Management: Innovation Management and Industrial Engineering*, vol. 1, pp.433-436

Bjerrum, L. 1972. Embankment on soft ground, state of the art report. *Proceedings of the ASCE Specialty Conference on Performance of Earth and Earth-Supported Structures*, Lafayette, Indiana, 11–14 June 1972. *American Society of Civil Engineers (ASCE)*, New York. Vol. 2, pp.1–54.

Broere, W., 2001. Tunnel face stability and new CPT applications. *Ph.D. Dissertation*, *Delft University of Technology*, *Delft University Press*, The Netherlands.

Broere, W., 2003. Influence of excess pore pressure on the stability of the tunnel face. *(Re)Claiming the Underground Space*. Balkema, pp.759-765.

Broms, B.B., Bennermark, H. 1967. Stability of clay in vertical openings. *Journal of the Soil Mechanics and Foundations Division* 93 (1), pp.71-94.

Carter and Burgess Inc., 2007. Review of large bore tunnel engineering and environmental studies from Tysons Tunnel, Inc., p.38.

Cascadia Center, 2008. Large diameter soft ground bored tunnel review. p.36

Chaffois, S., Laréal, P., Monnet, J., Chapeau, C., 1988. Study of tunnel face in a gravel site. *Proceedings of the Sixth International Conference on Numerical Methods in Geomechanics*. Innsbruck, Austria. pp.1493-1498.

Chambon, P., Corté, J.F., 1994. Shallow Tunnels in Cohesionless Soil: Stability of Tunnel Face, *Journal of Geotechnical Engineering* 120(7), pp.1148-1165.

Chen, W.F., Liu, X.L., 1990. Limit Analysis in Soil Mechanics. New York: Elsevier.

Craig, R., 2000. Under the Elbe to the Port of Hamburg. *World Tunnelling*, April 2000.

Clark, G., 2006. Alaskan Way Viaduct and Seawall Replacement Project: project overview.

Darby, A., and Wilson, R., 2005. Design of the SMART project, Kuala Lumpur, Malaysia. available at http://www.tunnels.mottmac.com/UC_2005_Paper_350_-_SMART.pdf.

Datuk, Y., Abdullah, H., 2004a. Kuala Lumpur: Re-engineering a flooded confluence, 14th Professor Chin Fung Kee Memorial Lecture. Kuala Lumpur, Malaysia. p.11.

Davis, E.H., Gunn, M.J., Mair, R.J., Seneviratne, H.N., 1980. The stability of shallow tunnels and underground openings in cohesive material. *Géotechnique* 30(4), pp.397-416.

Davis, R.O., Selvadurai, A.P.S., 2002. Plasticity and geomechanics. Cambridge: Cambridge University Press.

de Buhan, P., Cuvillier, A., Dormieux, L., Maghous, S., 1999. Face stability of shallow circular tunnels driven under the water table: A numerical analysis. *International Journal for Numerical and Analytical Methods in Geomechanics*, Vol. 23, pp.79-95.

Dr. G Sauer Corporation, 2006. Geological Profile Prestentation: Vertical Alignment, p.1.

Dragados and Dr. G Sauer Corporation, 2006. Dulles Corridor Rapid Transit Project

Drucker, D.C., Prager, W., 1952. Soil mechanics and plastic analysis or limit design. *Quarterly of applied mathematics* 10(2), pp. 157-165

Duncan, J.M., Buchignani, A.L., 1976. An engineering manual for settlement studies. Department of Civil Engineering, University of California, Berkeley, June 1976, p. 26.

Fernandez, E., 2007. The Madrid renewal inner ring Calle 30 with the largest EPB machines – planning and result. *Proceedings of Rapid Excavation and Tunneling Conference*, pp.769-782.

Gabarro, X., Frech, R., Maidl, B., Della Valle., N., 2003. Metro Barcelona Linea 9-Europe's greatest metro project with shield tunnel boring machines of large diameters. *Proceedings of Claiming the Underground Space*, pp.637-643.

Gioda, G., Swoboda, G., 1999. Developments and applications of the numerical analysis of tunnels in continuous media. *International Journal for Numerical and Analytical Methods in Geomechanics* 23, pp.1393-1405.

Guglielmetti, V., Grasso, P., Mahtab, A., Xu, S., 2008. Mechanized Tunnelling in Urban Areas. London: Taylor & Francis.

Grantz, W.C., 2001. Immersed tunnel settlements, Part 2: case histories. *Tunnelling and Underground Space Technology* 16(3). pp.203-210.

Herrenknecht, M., Bappler, K., 2008, Tunnel boring machine development. *Proceedings of North American Tunneling*, pp.52-57.

Jancsecz, S., Steiner, W., 1994. Face support for a large Mix-Shield in heterogeneous ground conditions. *Tunnelling* 94, pp.531-550.

Kanayasu, S., Kubota I., Shikibu N., 1995. Stability of face during shield tunneling – A survey on Japanese shield tunneling. *Underground Construction in soft ground*. Balkema, Rotterdam, pp. 337-343.

Kasper, T., Meschke., 2004. A 3D finite element simulation model for TBM tunneling in soft ground. *International Journal for Numerical and Analytical Methods in Geomechanics* 28, pp. 1441-1460.

Kim, S.H., Tonon, F., 2010. Face stability and required support pressure for TBM driven tunnels with ideal face membrane – Drained case. *Tunnelling and Underground Space Technology* 25(5), pp.526-542.

Kimura, T., Mair, R.J., 1981. Centrifugal testing of model tunnels in soft clay. *Proceedings of Tenth International Conference on Soil Mechanics and Foundation Engineering*, vol. 1, pp.319–322.

Klados, G., Kok. Y.H., 2004. Selection & performance of TBM in Karstic Limestone SMART case. *International Congress on Mechanized Tunnelling "Challenging Case Histories",* Torino.

Klados, G., Parks., D.R., 2005. Stormwater Management And Road Tunnel (SMART) overview: TBM selection and construction

Klar, A., Osman, A.S., Bolton, M., 2007. 2D and 3D upper bound solutions for tunnel excavation using 'elastic' flow fields. *International Journal for Numerical and Analytical Methods in Geomechanics* 31, pp.1367-1374.

Leca, E., Dormieux, L., 1990. Upper and lower bound solutions for the face stability of shallow tunnels in frictional material. *Géotechnique* 40(4), pp.581-606.

Lee, I.M., Nam, S.W., 2001, The study of seepage forces acting on the tunnel lining and tunnel face in shallow tunnels. *Tunnelling and Underground Space Technology* 16(1), pp.31-40.

Lee, I.M., Nam, S.W., 2000, Evaluation of face stability with the consideration of seepage forces in shallow tunnels. *Tunnels and Underground Structures*, Balkema, Rotterdam. pp.199-204.

Li, Y., Emeriault, F., Kastner, R., Zhang, Z.X., 2008. Stability analysis of large slurry shield-driven tunnel in soft clay. *Tunnelling and Underground Space Technology* 24(4), pp.472-481.

Lunardi, P., 2008. Design and construction of tunnels: analysis of controlled deformation in rock and soils (ADECO-RS). Heidelberg: Springer.

Madrid City Government, 2007. M-30 Ring Road Project, p.10.

Turner, D.L., 2007. Madrid Calle 30: Un proyecto de transformación urbana, p.311.

Maidl, U., Cordes, H., 2003. Active earth pressure control with foam. *World Tunnel Congress* 2003, Amsterdam, pp.791-797.

Maidl, B., Herrenknecht, M., Anheuser, L., 1996. Mechanized Shield Tunneling. Berlin: Ernst & Sohn.

MasterBuilder, 2005. Cover Story: SMART-A novelty in the making: an innovation coming true, *Master Builder*, pp 16-20.

Midas Information Technology Co., Ltd., 2009. GTS Analysis Reference manual (GTS Version 3.00).

Mitchell, J.K., 1976. Fundamentals of soil behavior, New York: John Wiley & Sons.

Monzon, A., Pardeiro, A.M., Vega, L.A., 2007. Reducing car trip and pollutant emissions through strategic transport planning in Madrid, Spain, *Proceedins of the 8th Highway and Urban Environment Symposium*, pp.81-90.

Mollon, G., Dias, D., Soubra, A.H., 2010, Face Stability Analysis of Circular Tunnels Driven by a Pressurized Shield, *Journal of Geotechnical and Geoenvironmental Engineering* 136(1), pp.215-229.

Mori, A., Kurihara, K., Mori, H., 1995. A study on face stability during slurry-type shield tunnelling. *Underground Construction in Soft Ground*. pp.261-264.

Negro, A., Eisenstein, Z., 1991. Shallow tunnels in soft ground: State-of-the-art report. *Ninth Pan American Conference on soil mechanics and foundation engineering*, Villa Del Mar, Chile. pp.23–42.

Parsons Brinckerhoff and Jacobs Engineering, 2009. Alaskan Way Viaduct and Seawall Replacemet Program: SR 99 bored tunnel alternative.

Personal communication with Xavier Delgado: engineer of GISA.

Prager, W., Hodge, P.G., 1950. Theory of perfectly plastic solids. New York: Wiley

Reid, R.L., 2008. Paris ring road will feature bi-level tunnel, *Civil Engineering*, June 2008, pp.17-18.

Romo-Alcañiz, P., 2007. Description of tunnels and constructive methods used during M-30 transformation works. p.85.

Roscoe, K.H., Burland, J.B., 1968. On the generalized stress–strain behaviour of 'wet' clay. *Engineering Plasticity Conference*, Cambridge. pp. 535–607.

Russo, G., 2003. Evaluating the required face-support pressure in EPBS advance mode. *Gallerie e Grandi Opere Sotterranee* 71. pp. 27-32.

Skempton, A.W., 1957. Discussion on the planning and design of the new Hong Kong Airport. *Proceedings of the Institution of Civil Engineers* 7, pp. 305–307.

Stack, B. (1982). Handbook of Mining and Tunneling Machinery, Chichester: Wiley.

Steiner, W. 1993. Experience with an 11.6 m diameter Mix-Shield: The importance of the ground machine interface, *Proceedings of Rapid Excavation & Tunneling Conference*, Boston, pp.759-779.

Terzaghi, K., Peck, R.B., Mesri, G., 1996. Soil mechanics in engineering practice (3rd edition). New York: Wiley.

Thompson, J., Chai, J., Biggart, A., Young, D., 2008. Earth pressure balance machines for the Silicon Valley Rapid Transit project - basis of design, *Proceeding of North American Tunneling* 2008, pp.168-176.

Tunnel-news I, 2008, The smarter way of fire fighting, pp.1-2.

Tunnels and Tunnelling International, 2005. Feature story-SMART, *Tunnels and Tunnelling International*. May 2005. p. 38.

Tunnels and Tunnelling International, 2003. Barcelona's mega machine in transit, *Tunnels and Tunnelling International*. Jan 2003. p.7.

Tunnels and Tunnelling International, 2005. The Barcelona TBM's learning curves, *Tunnels and Tunnelling International*. Feb 2005. pp.26-28.

Tunnels and Tunnelling International, 2005. Mixed fortunes on Barcelona's metro *Tunnels and Tunnelling International*. March 2005. p.7.

Tunnels and Tunnelling International, 2007. Optimizing Line 9's EPBM parameters, *Tunnels and Tunnelling International*. Apr 2007. pp.40-45.

Tunnels and Tunnelling International, 2002. Speedy mega TBM in Moscow, *Tunnels and Tunnelling International*. Dec 2005. pp.24-27.

Tunnels and Tunnelling International, 2005. Silberwald's first tube completed. *Tunnels and Tunnelling International*. May 2005. p.12.

Tunnels and Tunnelling International, 2004. Forming the French connection – A86 *Tunnels and Tunnelling International*. Mar 2004. pp.40-43.

Tunnels and Tunnelling International, 2003. Forming A86 – The path to fire safety *Tunnels and Tunnelling International*. Nov 2003. pp.42-45.

Tunnels and Tunnelling International, 2002. Following the French connection - A86 *Tunnels and Tunnelling International*. Oct 2002. pp.40-42.

Tunnels and Tunnelling International (2006) Mega EPBMs lead the way for Madrid's renewal. *Tunnels and Tunnelling International*. Jun 2006. pp.23-25.

Tunnels and Tunnelling International (2006) Madrid's massive M30 challenge. *Tunnels and Tunnelling International*. Dec 2006. pp.36-37.

US Department of Transportation Federal Highway Administration, 2009. Technical manual for design and construction of road tunnels – civil elements (publication no.: FHWA-NHI-10_034), December 2009, p.704.

Vinai, R., Peila, D., et al. (2007). Laboratory Tests for EPB Tunneling Soil Conditioning. *World Tunnel Congress and 31st ITA Assembly*, Prague.

Washington Department of Transporation. 2008. The Alaskan Way Viaduct and Seawall Replacement Program: Bored Tunnel Briefing.

Wood, D.M., 1990. Soil behaviour and critical state soil mechanics, Cambridge: Cambridge University Press.

Zell, S., 1999. Focus on Germany, *ITA- AITES newsletter* no. 9, pp.11-13.

http://www.roadtraffic-technology.com /projects/a86

Vita

Seung Han Kim earned degree of Bachelor of Science and degree of Master of Engineering from Korea University in February 2005 and February 2007, respectively. In August 2007, he started the graduate study in geotechnical and tunnel engineering at The University of Texas at Austin.

Permanent address: Woobang APT 106-1101, Tap-dong, Suwon-si
Gyunggi-do 441-440, Korea

This manuscript was typed by the author.